REPORT DOCUMENTATION PAGE

AFRL-SR-AR-TR-05-

0164

REPORT DATE (DD-MM-YYYY) 04-14-2005	2. REPORT TYPE Paper/PDF-file	3. DATES COVERED 05-01-2001 – 12-31-2004

Development of Formation Flight Control Algorithms Using 3 YF-22 Flying Models

5a. CONTRACT NUMBER

5b. GRANT NUMBER F49620-01-1-0373

5c. PROGRAM ELEMENT NUMBER

6. AUTHOR(S)
Marcello R. Napolitano, PI, Professor

Mechanical and Aerospace Engineering Department – PO Box 6106
West Virginia University, Morgantown, WV 26506/6106
Tel. (304) 2934111 Ext. 2346 – E-mail: *Marcello.Napolitano@mail.wvu.edu*

5d. PROJECT NUMBER

5e. TASK NUMBER

5f. WORK UNIT NUMBER

7. PERFORMING ORGANIZATION NAME(S) AND ADDRESS(ES)

West Virginia University Research Corporation
Alan Martin, Director, Office of Sponsored Programs
886 Chestnut Hill Road, P.O. Box 6845
Morgantown, WV 26506
Tel:(304) 293-3998, Fax:(304) 293-7435

8. PERFORMING ORGANIZATION REPORT NUMBER

9. SPONSORING / MONITORING AGENCY NAME(S) AND ADDRESS(ES)
Lt Col Sharon Heise, USAF, PhD
Program Manager, Dynamics & Control, AFOSR/NM
4015 Wilson Blvd, Rm 713
Arlington, VA 22203
l:(703) 696-7796

10. SPONSOR/MONITOR'S ACRONYM(S) AFOSR

11. SPONSOR/MONITOR'S REPORT NUMBER(S)

12. DISTRIBUTION / AVAILABILITY STATEMENT

Unclassified - Unlimited

13. SUPPLEMENTARY NOTES
This document was prepared for the AFOSR, Dynamics and Control Program.

14. ABSTRACT
The main objective of this project was to provide a flight demonstration of formation control using UAV research aircraft models. This document will describe the efforts leading to the design, construction, and flight-testing of formation control laws using three YF-22 research UAVs designed, built, and instrumented at West Virginia University (WVU). In the selected formation configuration, a radio control (R/C) pilot maintains ground control of the 'leader' aircraft while two autonomous 'follower' aircraft are required to maintain a pre-defined position and orientation with respect to the 'leader' aircraft. The report is organized as follows. First, a description of the aircraft test-bed construction and on-board payload systems will be provided. The following sections will describe the overall design of the formation control laws. Specifically, this design was based on a set of inner and outer loop control laws using a NLDI (Non Linear Dynamic Inversion) approach. The implementation of the controller design featured a mathematical model obtained directly from flight data through a PID (Parameter Identification) study. Additional sections will provide a description of the on-board flight control software and simulation work prior to the flight-testing activities. A final section will describe the results from an extensive flight-testing program. The flight-testing activities were articulated in several phases starting from the evaluation of the hardware and control laws, the testing of a 'Virtual Leader' configuration, up to the flight-testing of 2-aircraft and 3-aircraft formations.

15. SUBJECT TERMS
Flight Testing, Formation Flight, UAV, NLDI, Autonomous Control, Flight Controls, On-Board Computer

| 16. SECURITY CLASSIFICATION OF:			17. LIMITATION OF ABSTRACT	18. NUMBER OF PAGES	19a. NAME OF RESPONSIBLE PERSON Marcello R. Napolitano
a. REPORT Unclassified	b. ABSTRACT Unclassified	c. THIS PAGE Unclassified	none	167+ Appendix	19b. TELEPHONE NUMBER (include area code) (304) 293-4111 Ext.2346

20050624 028

Final Report

Development of Formation Flight Control Algorithms Using 3 YF-22 Flying Models

AFOSR GRANT F49620-01-1-0373
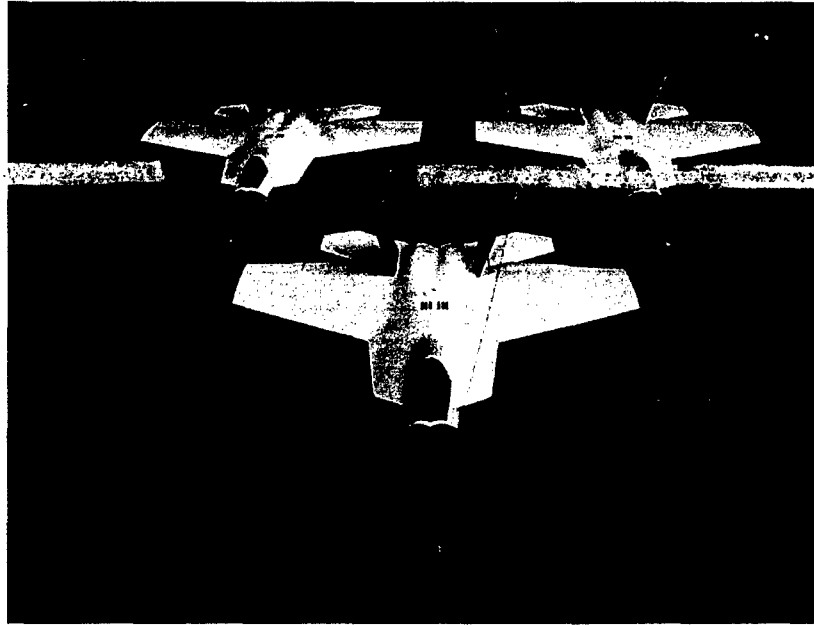
Marcello R. Napolitano, PI, Professor
Department of Mechanical and Aerospace Engineering
West Virginia University
P.O. Box 6106, Morgantown, WV 26506/6106
Tel. (304) 2934111 Ext. 2346, Fax (304) 2936689
Email: *Marcello.Napolitano@mail.wvu.edu*

Submitted to:

April 2005

Abstract

The main objective of this project was to provide a flight demonstration of formation control using UAV research aircraft models. This document will describe the efforts leading to the design, construction, and flight-testing of formation control laws using three YF-22 research UAVs designed, built, and instrumented at West Virginia University (WVU). In the selected formation configuration, a radio control (R/C) pilot maintains ground control of the 'leader' aircraft while two autonomous 'follower' aircraft are required to maintain a pre-defined position and orientation with respect to the 'leader' aircraft. The report is organized as follows. First, a description of the aircraft test-bed construction and on-board payload systems will be provided. The following sections will describe the overall design of the formation control laws. Specifically, this design was based on a set of inner and outer loop control laws using a NLDI (Non Linear Dynamic Inversion) approach. The implementation of the controller design featured a mathematical model obtained directly from flight data through a PID (Parameter Identification) study. Additional sections will provide a description of the on-board flight control software and simulation work prior to the flight-testing activities. A final section will describe the results from an extensive flight-testing program. The flight-testing activities were articulated in several phases starting from the evaluation of the hardware and control laws, the testing of a 'Virtual Leader' configuration, up to the flight-testing of 2-aircraft and 3-aircraft formations.

Table of Contents

List of Figures

List of Tables

Nomenclature

English

b	=	wingspan (m)
C	=	aerodynamic coefficients
$\bar{c}$	=	mean aerodynamic chord (m)
f	=	forward distance between 'leader' and 'follower' aircraft (m)
F	=	aerodynamic forces (N)
g	=	gravitational acceleration (m/s^2)
h	=	altitude (m)
h	=	vertical distance error (m)
I	=	inertial (kg/m^2)
l	=	lateral distance between 'leader' and 'follower' aircraft (m)
m	=	aircraft mass (kg)
M	=	aerodynamic moments (N m)
p	=	roll rate (deg/s)
q	=	pitch rate (deg/s)
r	=	yaw rate (deg/s)
S	=	wing platform area (m^2)
T	=	thrust (N)
V	=	speed (m/s)
x	=	position of an object along the x axes (m)
y	=	position of an object along the y axes (m)
z	=	position of an object along the z axes (m)

Greek

α	=	angle of attack (deg)
β	=	angle of sideslip (deg)
δ	=	command input
θ	=	pitch angle (deg)
ϕ	=	roll angle (deg)
χ	=	azimuth angle (deg)
Ω	=	angular turn rate (rad/s)
ρ	=	air density (kg/m3)
ω	=	washout filter constant

Subscripts

A	=	aileron
d	=	desired value
e	=	error between desired and measured variable
F	=	'follower'
f	=	forward
i_H	=	stabilator
l	=	lateral
L	=	'leader'

R	=	rudder
s	=	speed
T	=	throttle
x	=	projection along the x axis
xy	=	projection along the horizontal plane
y	=	projection along the y axis
z	=	projection along the z axis

<div align="center"><u>Acronyms</u></div>

A/D	=	Analog to Digital
BLS	=	Batch Least Square
CAD	=	Computer Aided Design
CFD	=	Computational Fluid Dynamics
CPU	=	Central Processing Unit
CRC	=	Cyclic Redundancy Check
CSDS	=	Control Signal Distribution System
DAQ	=	Data Acquisition
DCS	=	Data Communication System
DIO	=	Digital Input/Output
DOF	=	Degree of Freedom
ECU	=	Electronic Control Unit
EMI	=	Electromagnetic Interference
FCS	=	Flight Control System
FD	=	Forward Distance
G.M	=	Gain Margin
GPS	=	Global Positioning System
GUI	=	Graphical User Interface
LD	=	Lateral Distance
LED	=	Light Emitting Diode
IMU	=	Inertial Measurement Unit
LS	=	Least Square
NLDI	=	Non-linear Dynamic Inversion
OBC	=	On-Board Computer
PCB	=	Printed Circuit Board
PID	=	Parameter Identification
P.M	=	Phase Margin
PWM	=	Pulse Width Modulation
R/C	=	Radio Controlled
RF	=	Radio Frequency
RMS	=	Root Mean Square
RPM	=	Revolutions Per Minute
RTW	=	Real Time Workshop
S/N	=	Signal Noise Ratio
SQP	=	Sequential Quadratic Programming
STD	=	Standard Deviation
T/W	=	Thrust/Weight Ratio

UAV =   Unmanned Aerial Vehicle
VD   =   Vertical Distance
VL   =   Virtual Leader
VRT =   Virtual Reality Toolbox
W/S =   Weight/Wing Surface Ratio
WVU =   West Virginia University

Chapter 1 - Introduction

1.1 - Technical Objectives

The main objective of this research effort was to provide a flight demonstration of formation control using YF-22 research aircraft models. These models were designed, built, and instrumented by a group of faculty members, graduate research assistants, and undergraduate students in the Mechanical and Aerospace Engineering (MAE) Department at West Virginia University (WVU).

This report will provide detailed information about the different phases of the project, starting from the aircraft test-bed development, to the design of the on-board electronic payload and software systems, leading to simulation studies and flight testing activities.

In the formation flight configuration, a radio control (R/C) pilot maintained ground control of the 'leader' aircraft while 2 'follower' aircraft were required to maintain a pre-defined position and orientation with respect to the 'leader'. Each of the 'follower' aircraft was essentially an autonomous vehicle once engaged into the formation flight mode. Individual pilots controlled each aircraft from a ground transmitter during takeoff and up to formation engagement, as well as after formation disengagement and landing procedures. Autonomous formation was engaged after all aircraft reached a pre-determined altitude at a pre-selected rendezvous point. Due to safety issues, the UAVs were always flown within visual range so that the ground pilots could retain manual control of the UAVs, if necessary. This restriction, in turn, required that each UAV to be flown at high roll and heading angles and, thus, substantial angular rates for most of the mission. Therefore, a specific goal was to design a set of formation control laws with desirable performance under these specific conditions. An additional objective was to limit the amount of information exchanged between the 'leader' and 'follower' to maintain the pre-defined formation geometry.

The flight-testing program associated with this effort was quite substantial and involved approximately 100 sorties divided among all 3 of the UAV test-beds. The flight-testing activities involved the following phases:

- assessment of the aircraft handling qualities;
- assess the performance of the data acquisition system and electronic payload;
- PID (Parameter Identification) flights;

Chapter 2 - Aircraft Test-bed

2.1 - Aircraft Test-bed Overview

The WVU YF-22 aircraft fleet was developed as the main test-bed for carrying the formation flight payload and performing the closed-loop formation flight experiments. One of the 3 WVU YF-22 UAVs is shown in Figure 2-1 during takeoff at the WVU Jackson Mill flight-testing research facility. This chapter will provide detailed information about the aircraft design and construction.
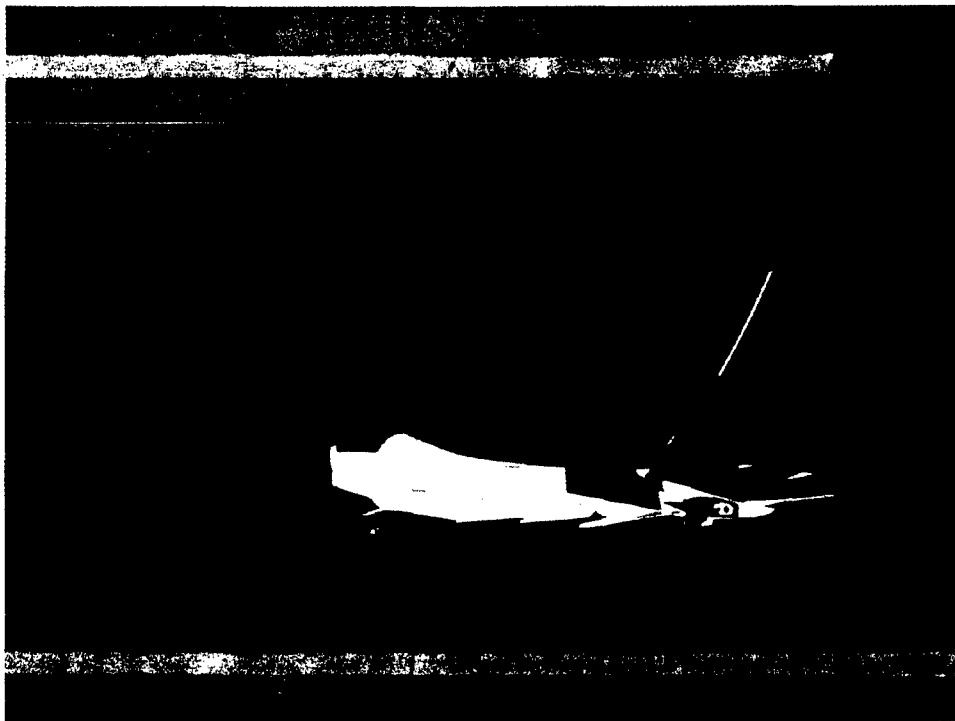
Figure 2-1: WVU YF-22 Model Aircraft (Formation Flight Green Aircraft)

The aircraft frames were manufactured with a number of products and materials, including fiberglass, composite materials (ex. carbon fiber, Kevlar), foam, and a variety of wood products. Although the WVU YF-22 model featured similarities with the 'actual' USAF YF-22 aircraft, the WVU research team did not wish to use for this effort a 'perfectly scaled' YF-22 model. In fact, it was very clear from a preliminary design analysis that a scaled model would not exhibit desirable handling qualities due to unacceptable values of the W/S (Weight/Wing Surface ratio - also known as wing load) parameter. An additional design requirement was to maintain the take-off and landing airspeeds within a desirable range. Therefore, the research team focused on

designing a model which provided desirable ranges for two very critical design parameters, that is the T/W (Thrust/Weight ratio) and W/S. The final result was the manufacturing of the 3 aircraft models shown in Figure 2-2. Detailed information about the aircraft construction will be provided in Section 2.2.
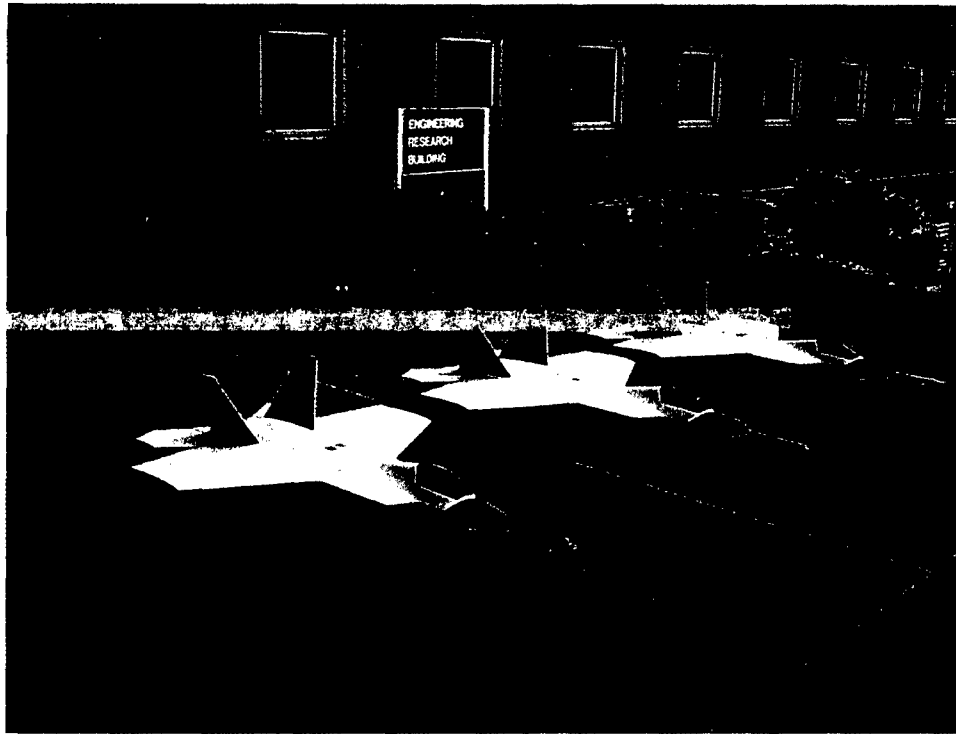
Figure 2-2: WVU YF-22 Aircraft Models (Formation Flight Fleet)

2.2 - Aircraft Construction

The design of the 'formation flight' YF-22 model evolved from the design of a smaller model used for a previous AFOSR/DoD EPSCoR research project (Grant # F49620-98-1-0136). This smaller research UAV featured a 3.6 Kg. electronic payload. A preliminary 5.5 Kg electronic payload target was originally set for the development of the new test-bed. A re-design process was performed to accommodate additional hardware components (necessary for formation flight) along with larger fuel capacity for longer missions. The additional hardware components included a GPS receiver, RF-modem, and a vertical gyro leading to an electronic payload under 5.4 Kg (per early design specifications). Since the previous smaller model had excellent handling qualities, a specific goal was to try to retain the same desirable handling

4

qualities. The resulting 'formation flight', 'new' WVU YF-22 design vs. the smaller, 'old' WVU YF-22 design is shown in Figure 2-3.
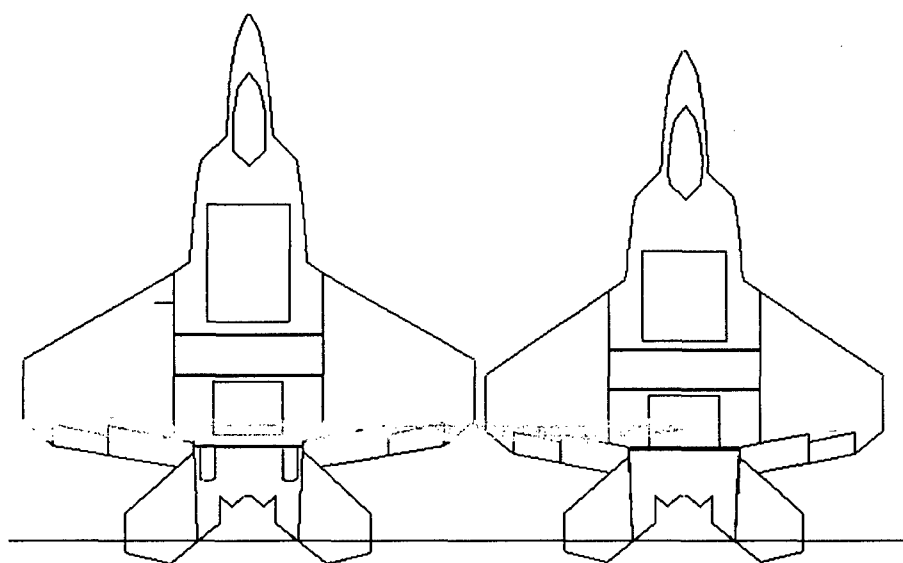
Figure 2-3: 'Formation Flight' vs. 'Old' WVU YF-22 Design

The main characteristics of the 'new' WVU YF-22 aircraft are listed Table 2-1.

Parameter	Value	Units
Length	2.2352	m
Wingspan	1.98	m
Wing Surface	1.52	m^2
Wing Aspect Ratio	2.53	---
Wing Sweep Angle	29°	degrees
Payload (maximum target)	5.44	Kg
Est. takeoff weight (w/ payload)	20.86	Kg
Est. wing load (with payload)	13.73	Kg/m^2
Est. Thrust/Weight (with payload)	0.6	---

Table 2-1: Design Parameters for the 'Formation Flight' WVU YF-22 Model

In addition to a larger wing size, the wing design was substantially different with respect to the previous model. The introduced modifications included the use of a different wing section (with increased curvature for additional lift at lower speeds), larger control surfaces (for enhanced maneuverability at slower speeds), and structural reinforcement for surfaces (due to the increased airspeeds). In addition to the wing aerodynamic modifications, the air intakes were also closed – where the previous design had open air-intakes in the front of the aircraft. In fact, it was determined that the propulsion system received enough air flow from the landing gear wells and

additional slots placed on top of the main hatch of the fuselage body. This modification allowed for a substantial reduction in drag, which, in turn allowed substantial savings in fuel consumption as well as an increased airspeed.

Following a detailed aircraft design, drawings were produced for the manufacturing of a fuselage plug and mold system, which was then used to produce the fuselage aircraft shell. CAD drawings of the top and side views were produced using 5 cm cross-sectional views. From the cross-sectional views, a number of templates were produced for the production of the fuselage plug. The manufacturing of the plug involved a labor-intensive handcrafting process to obtain a smooth and accurate form, which was necessary for the final shape of the fuselage. Figure 2-4 shows a rear view of the final fuselage plug.
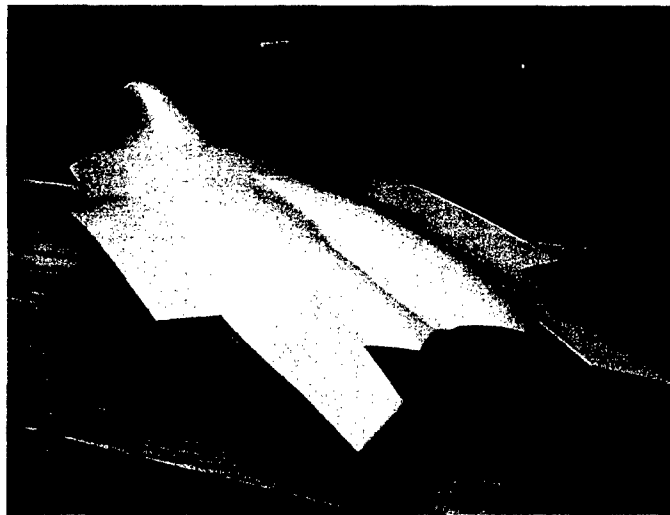
Figure 2-4: WVU YF-22 Plug (Rear View)

In forming the fuselage plug, an intermediate step was to prepare the plug for the creation of a two-section mold. These two 'sandwich halves' created the top/bottom mold section, which were later used for manufacturing the aircraft shells. Figure 2-5 shows the initial stage of the preparation of the production mold in the WVU 'UAV Construction' lab.
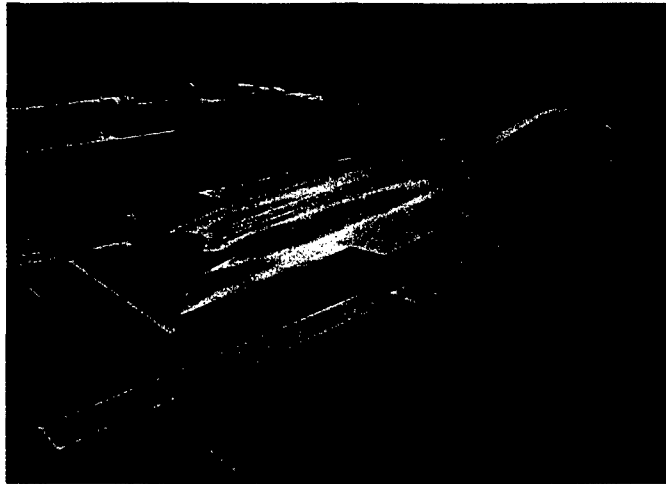
Figure 2-5: Creation of Mold from Plug (Initial Stage)

The mold was developed using a variety of materials, including a release agent and gel-coat, along with epoxy resin and fiberglass. The resulting mold produced a '2-piece' top and bottom section as shown in Figure 2-6.
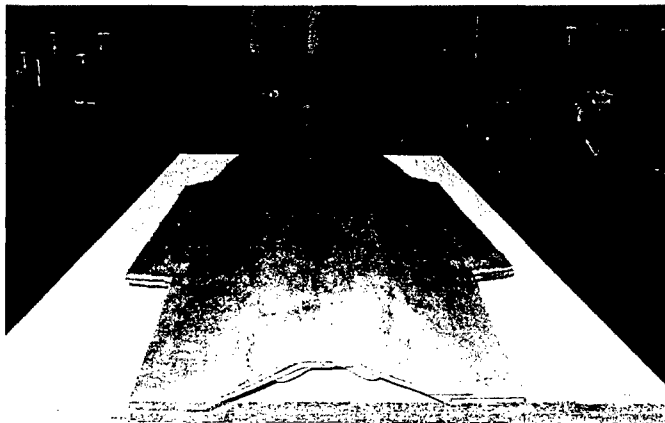
Figure 2-6: WVU YF-22 Mold (Rear View)

Once the mold was cured, the separation of the two components was then performed, leading to the 'top' and 'bottom' molds shown in Figure 2-7.
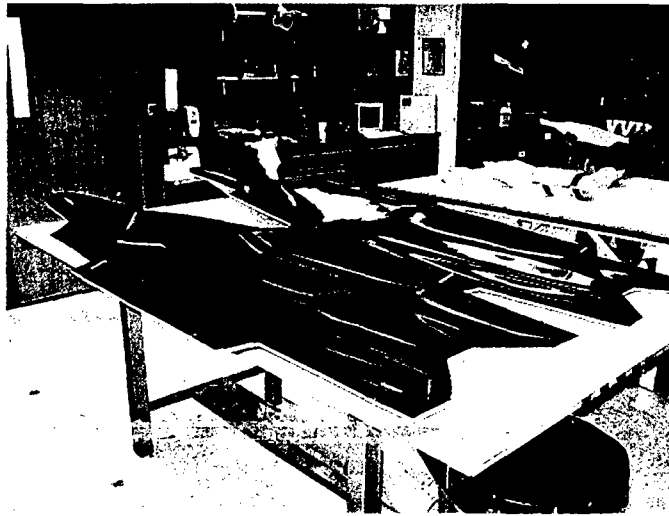
Figure 2-7: Top and Bottom Mold Sections Used to Produce Aircraft Shells

Next, the '2-piece' mold system was used for the fabrication of each YF-22 shell. Each shell was produced using a combination of fiberglass and composite materials. Particularly, carbon fiber in the fuselage shell was used in areas of high-level structural stress (such as bulkheads and tail section areas). Figure 2-8 shows the early development stage of the bottom fuselage shell.

Figure 2-8: Early Shell Development

The 'dark' areas represent the 'wetted' fiberglass while the white areas are the 'dry' edges of the raw material around the edges of the mold. Wood strips were then introduced as mounting

8

brackets for the installation of the electronic payload. Figure 2.9 shows a cured lay-up of the bottom fiberglass shell. The use of carbon fiber strips can be seen around 'high stress' areas, such as structural bulkheads, vehicle access hatches, landing gears, and at the intersection with the tail sections.
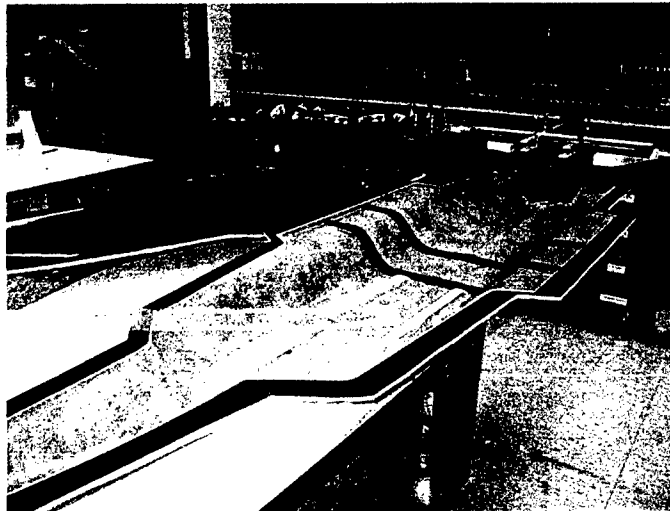
Figure 2-9: Cured Lay-up Shell

Figure 2.10 shows a test fitting of the aircraft bulkheads, propulsion, and computer package prior to laying the top shell on the bottom shell.
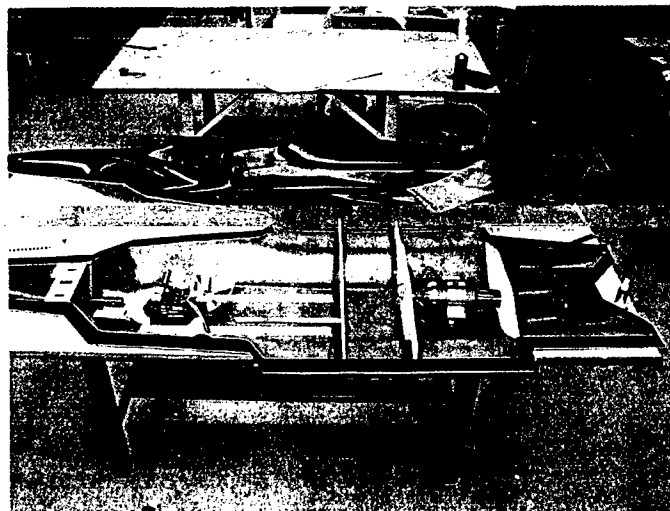
Figure 2-10: Test Fit of Internal Bulkheads

Figure 2-11 shows the 'merging' of the top and bottom shells prior to installation of the structural bulkheads separating the different bays inside the fuselage.
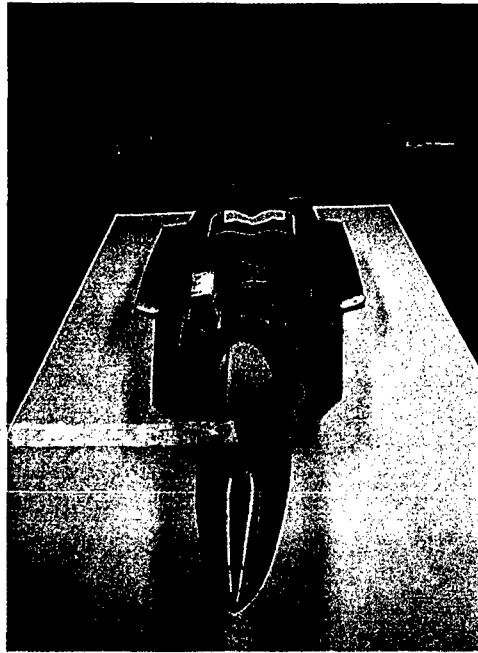
Figure 2-11: Assembly of Top and Bottom Shells

After the completion of the fuselage shell, the structural bulkheads, the wing and the tail sections were assembled with the fuselage body. Each wing and tail section was then manufactured using a foam and balsa wood combination, including structural supports (spars) covered by fiberglass. Figure 2-12 shows a top view of the 'raw' YF-22 for the formation flight project side-by-side with the 'old' YF-22 model.
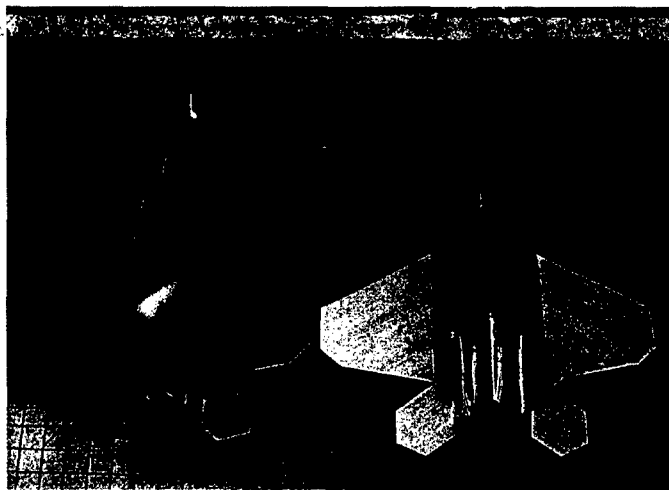
Figure 2-12: Side-by-Side Top View of the 'Old' YF-22 (Left) and 'Formation Flight' YF-22 Model (Right)

The next phase involved the manufacturing and installation of the control surfaces for both the wing and vertical tail sections; followed by the installation of the R/C aircraft hardware. The R/C aircraft hardware included the following items:

- the R/C receiver (radio system);
- the control surfaces and servo installations;
- the propulsion system;
- the landing gear systems (including wheels, brakes, and retracts).

Details about the propulsion and landing gear systems will also be discussed in Sections 2.3 and 2.4.

For the assessment of the handling qualities, flight tests were performed for the 1st aircraft model, the manufacturing process was repeated for the development of two additional aircraft. It should be noted that the flight-testing activities with the 1st aircraft for the performance assessment - which will be described in a later section - did not show any need for major design modifications. The pilot reported nominal handling qualities in terms of both the longitudinal and lateral directional dynamics as well as desirable takeoff and landing performance. Figure 2-13 shows an early photograph of the entire WVU aircraft fleet, prior to the application of the painting scheme.

Figure 2-13: Aircraft Fleet (Prior to Painting and Hardware Installation)

Following the completion of the entire fleet - including installation of the R/C and electronic payload systems - all of the aircraft were painted with a specific color scheme for maximizing visibility. Figure 2-14 shows the final paint scheme used for the formation flight aircraft.

11

Throughout the program, the 'blue' ship served as the 'leader' aircraft while the 'red' and 'green' aircraft acted as the 'follower' aircraft.
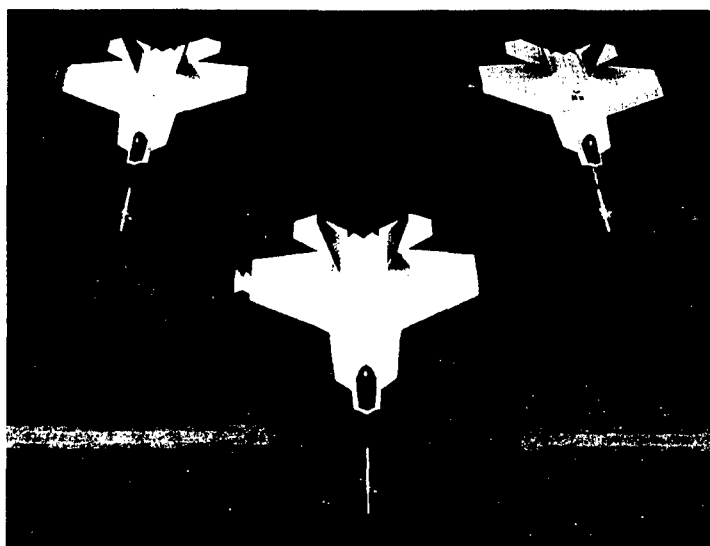
Figure 2-14: WVU 'Formation Flight' Fleet

2.3 - Aircraft Propulsion

The turbine propulsion system was manufactured by R.A Microjets, Inc. (Medley, FL). The selected engine model was the RAM 1000 system, shown in Figure 2-15. The engine was manufactured using a single stage centrifugal compressor driven by a single axial flow turbine wheel. The shaft was supported by two lubricated, pre-loaded angular contact bearings. An Electronic Control Unit (ECU) monitored the exhaust gas temperature and engine compressor pressure in addition to controlling the pump drive voltage. The miniature pump in turn controls the turbine speed by varying its RPM and, conversely, the fuel supplied to the turbine.
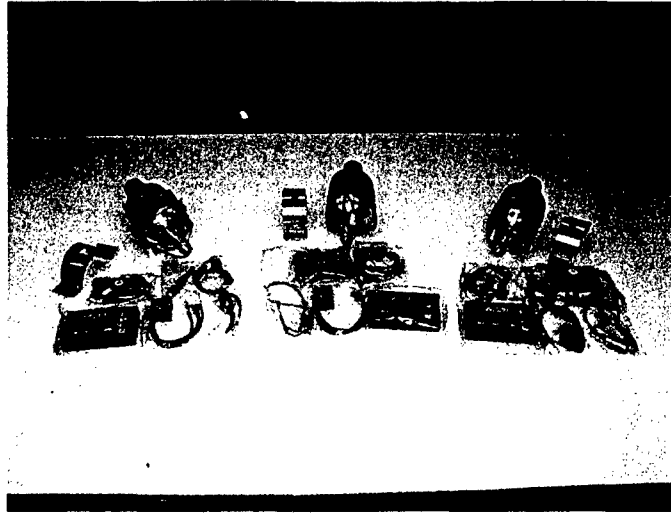
Figure 2-15: RAM 1000 Propulsion System

One of the important features of this engine - which was a primary factor for the selection of this specific propulsion system - was the safe and efficient start-up procedure. In fact, the turbine system featured an auto start (via the R/C throttle command) system using a small amount of starting fuel for the engine ignition sequence. Following startup procedure, the engine could then run on a variety of fuels, including Jet A, A1, or Kerosene. Jet A fuel was selected due to its availability at a local airport.

In terms of performance, the RAM 1000 provided up to 125 N of thrust. The fuel consumption was rated at approximately 0.35 liters/minute for a maximum RPM (127,000) setting. Maximum RPM setting was typically used only during the takeoff sequence. Once the aircraft was at altitude, the throttle setting was typically within the (½ - ¾) range, with fuel consumption in the range of (0.15-0.3) liters/minute.

A custom-designed by-pass cover system was purchased to streamline the airflow of the propulsion system. An additional advantage of the cover system was for protection purposes; in the event of a fire or engine malfunction because of the composite material used in construction. The by-pass system, shown in Figure 2.16, was manufactured by Jet-Tech which utilized Kevlar and carbon fiber materials. The propulsion system also featured customized Kevlar fuel tanks (photo is shown in Figure 3-32) also manufactured by Jet-Tech.
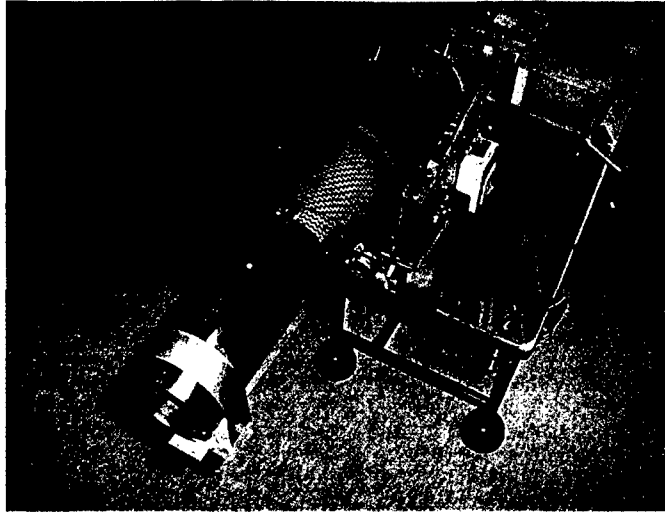
Figure 2-16: By-Pass System and Exhaust Tube

2.4 - Landing Gear Systems

The aircraft landing gear setup was assembled using a retract wheel and brake system (manufactured respectively by 'Spring Air Retracts and 'Glennis') along with struts (manufactured by 'Robart'). Each attachment point for the main left/right gear, as well as the nose wheel, was manufactured using wood with carbon laminated plating structures. The added strength of the carbon fiber allowed for additional protection against the structural stresses associated with the take-off and landing phases. Views for both the main and nose landing gear systems are shown in Figures 2-17 and 2-18.
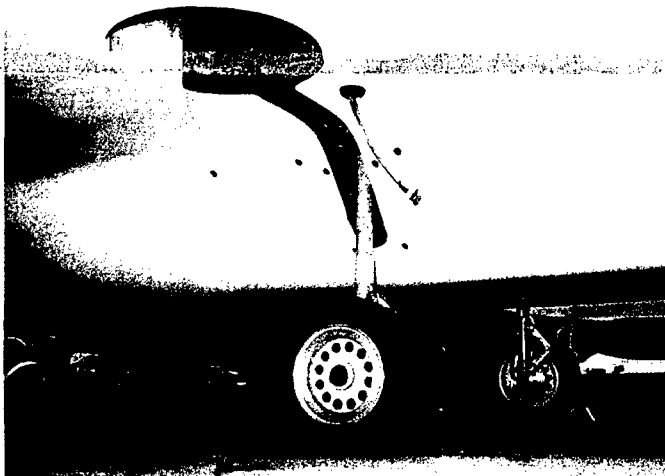
Figure 2-17: Main Landing Gear
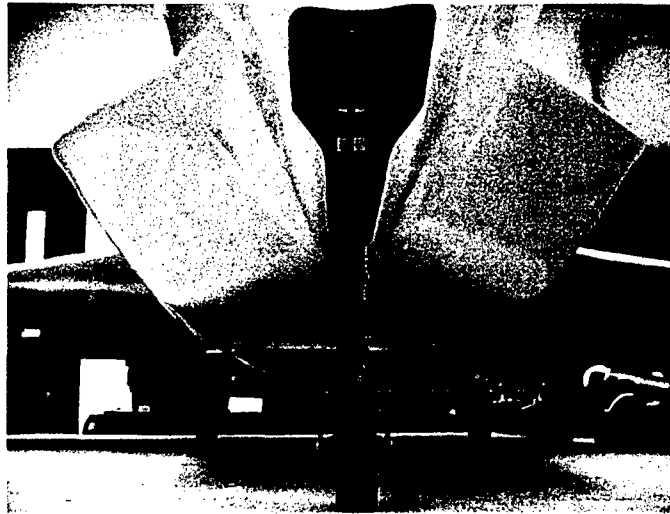
Figure 2-18: Nose Gear

2.5 - Aircraft Specifications

A top view of a completed aircraft test-bed is shown in Figure 2-19. Potentiometers were installed for measuring the deflection of each primary control surface. This included the left/right stabilators, left/right ailerons, and left/right rudders. Flaps were installed only for R/C control use during takeoff and landing purposes and were not used by the flight control laws.

Measured Surfaces (Stabilator, Aileron, Rudder) with Potentiometers

Propulsion System

GPS Antenna

RF Modem

Main Payload Bay
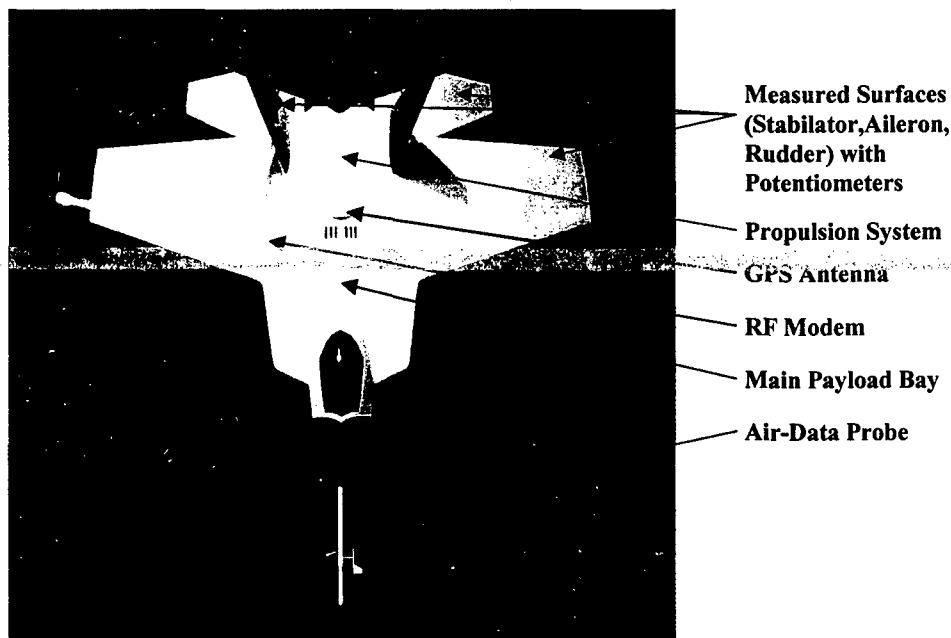
Air-Data Probe

Figure 2-19: WVU YF-22 Top View

An air-data nose probe - for measuring flow angles and pressure data - was installed. The nose hatch (front hatch) section provided the R/C control hardware and air-data sensors. The main payload bay (center hatch) contained the formation flight payload and fuel. The GPS antenna

was located near the center of the aircraft, directly behind the air intakes. The rear hatch provided access to the engine by-pass system, propulsion, and tail section components. A listing of the main aircraft specifications and geometric characteristics are listed in Table 2-2.

Aircraft Parameters	Values
Wingspan	1.98m
Length	3m with probe
Height	0.6 m
Wing Area	1.36 m^2
Weight	22.5 kg
Payload Capability	5.4 kg
Fuel Capability	3 kg
Duration	12 minutes
Cruse Airspeed	144 km/hr
Takeoff Speed	96 km/hr
Top Speed	200 km/hr
Takeoff Distance	150m
Radio	JR 10X 10 channel SPCM
Engine	RAM 1000
Average Fuel Consumption	0.25kg/minute
Thrust	125N
T/W ratio	0.56
W/S ratio	16.5 kg / m^2

Table 2-2: YF-22 Research UAV Specifications

Additional details about the on-board payload components will be provided in the next chapter.

Chapter 3 - On-Board Electronic Payload

3.1 - General Architecture of the Electronic Payload System

The on-board electronic payload system was designed to perform the following tasks:

- data acquisition;
- data storage;
- communication;
- execution of the formation control laws.

The on-board sensors provided measurements for all the major aircraft parameters. Six control channels were used to control respectively the left stabilator, right stabilator, left aileron, right aileron, dual rudders, and engine throttle. For formation flight purposes, the following six requirements were used to define the overall system architecture:

1. different commands (control commands, start/stop of formation control) can be sent from the ground pilot to each of the aircraft;

2. once formation control is engaged, the On-Board Computer (OBC) has full control of the aircraft primary control surfaces (stabilators, ailerons, and rudder) and propulsion system;

3. at any time the pilot - for any aircraft - can regain direct R/C control;

4. GPS information can be transmitted from the 'leader' aircraft to the 'follower' aircraft;

5. the electronic payload should be able to tolerate substantial levels of vibration and able to operate in cold/hot/humid environments with a combined weight not to exceed 5.5 Kg;

6. the electronic payload should exhibit desirable robustness to Electromagnetic Interference (EMI).

Using the above requirements, the flight control system was designed to operate in three separate modes:

1. "Manual" Mode;
2. "Manual – Partial Automatic" Mode;
3. "Automatic Formation Control" Mode.

17

In the "Manual" mode, the pilot had complete control of the aircraft. The pilot could switch to this mode at any time when operating in the other two modes. This mode was designed to provide a safe operating condition before engaging the controller. This mode can also be used for emergency recovery in the event of the occurrence of unstable dynamic conditions. During the takeoff and landing phases of the mission, the aircraft was required to be in the manual-operating mode.

Within the "Manual - Partial Automatic" mode, the pilot had control over a subset of the aircraft primary control surfaces while the on-board controller directed the remaining surfaces. The pre-programmed on-board software decides which control channels to be allocated to the OBC. This mode was used for intermediate testing of the formation control laws to minimize risks during flight tests.

Within the "Automatic Formation Control" mode, the OBC had complete control of all the primary control surfaces and aircraft propulsion. This mode was used for the evaluation of the design of the individual components of the control laws and for the final phases of the formation flight tests.

3.2 - On-board Payload Subsystems

According to the requirements and selected architecture, the on-board payload system was designed to receive pilot commands, collect flight data with the on-board instrumentation, perform data communication, generate on-board control commands, and distribute control signals to the primary control surfaces and propulsion. Thus, the 4 main components of the on-board electronic payload were given by:

1. R/C system;
2. Data acquisition system;
3. Data communication system;
4. Control signal distribution system.

A view of the main payload bay is shown in Figure 3-1. An overview of these major subsystems is provided next, while a more detailed description of the hardware components will be provided in Section 3.3.

GPS — Compact Flash

Vertical Gyro — OBC

IMU — Battery Pack

Sensor cables — Power Supply
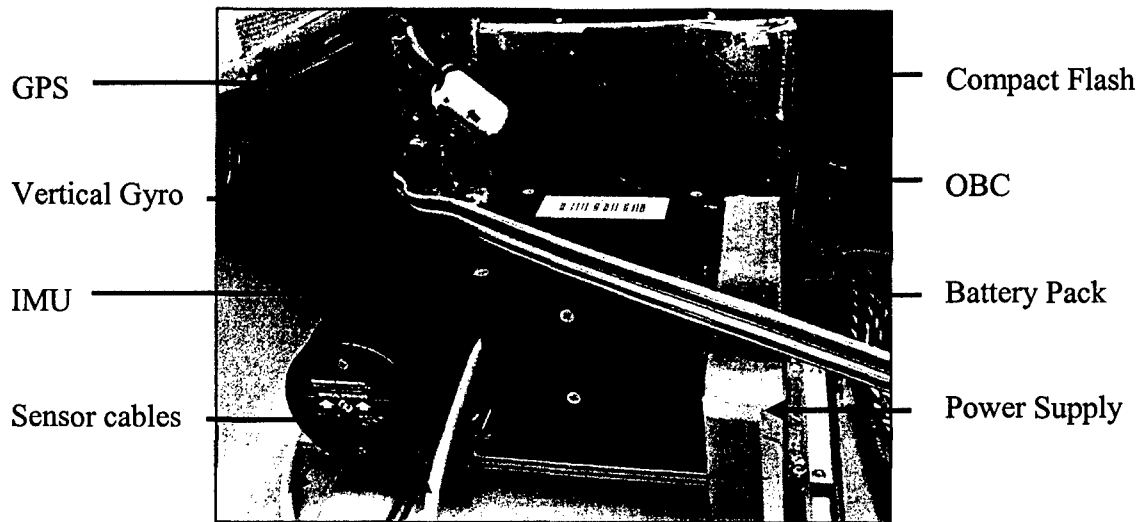
Figure 3-1: On-Board Electronic Payload

3.2.1 - R/C System

The R/C radio system was based on a JR-PCM 10X transmitter and receiver radio package, manufactured by JR Corp. This radio system featured a 10-channel capability for increased flexibility with the R/C system. A photo of the JR transmitter is shown in Figure 3-2.
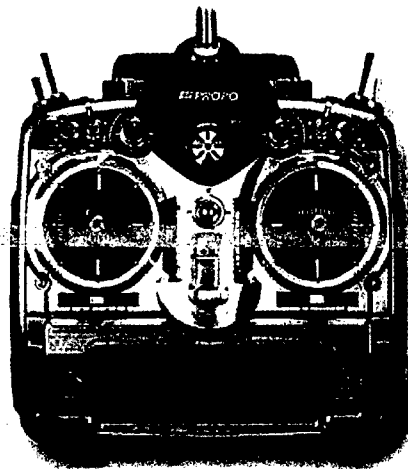
Figure 3-2: R/C Transmitter

This system featured digital servo technology, which allowed for faster control surface response, higher torque, and increased accuracy to control the aircraft's control surfaces with respect to analog servos. Through each of the R/C channels, the pilot had control of the aircraft primary control surfaces (stabilators, ailerons, and rudders), secondary control surfaces (flaps), engine

19

throttle, brakes, retractable landing gear, and, finally, a controller switch to activate the on-board control laws (used for formation flight purposes). The R/C receiver - shown in Figure 3-3 - was installed at a certain distance from the computer box to reduce potential EMI issues.
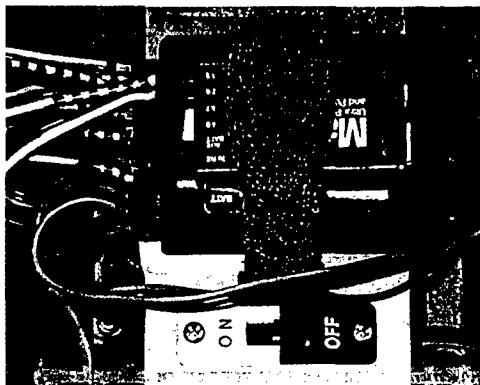
Figure 3-3: R/C Receiver

A total of nine cables were introduced to transmit the receiver control signals to the OBC. The Control Signal Distribution System (CSDS) - located within the OBC box - distributes the control signals, as allocated by the formation control laws coded in the on-board software, and sends the commands to the individual servos of the primary control surfaces.

3.2.2 - Data Acquisition System

The data acquisition system collected data for both on-line real time control purposes (for formation flight) and post-flight analysis purposes. The data acquisition system included the OBC and a suite of sensors. The suite of vehicle sensors included:

- air-data probe;
- pressure sensors;
- Inertial Measurement Unit (IMU);
- vertical gyro;
- potentiometers on primary control surfaces (stabilators, ailerons, rudders);
- Global Positioning System (GPS);
- temperature sensor.

The sensors listed above provided measurements for the following parameters:

- angle of attack;
- angle of sideslip;
- static and dynamic pressure;
- temperature;
- roll and pitch Euler angles;
- roll, pitch, and yaw angular rates;
- longitudinal, lateral, and vertical linear accelerations;
- GPS-based position and linear velocity along the x, y, z axes;
- angular deflections of the primary control surfaces.

The general architecture of the data acquisition system is shown in Figure 3-4.
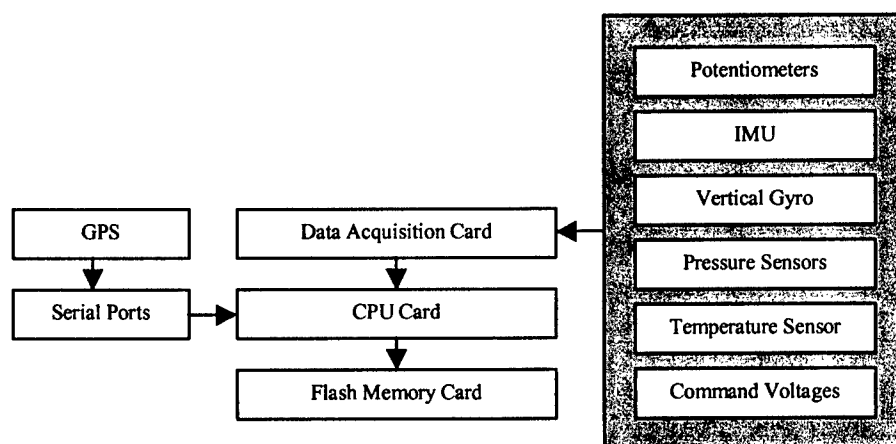
Figure 3-4: Data Acquisition System

The data acquisition card features 32 analog/digital channels; 22 channels were actually used with the remaining channels reserved for eventual future expansions.

3.2.3 - Data Communication System

The 'leader' aircraft's position and velocity information were required by the 'follower(s)' on-board controller to perform formation control. The 'Data Communication System' (DCS) is designed to perform this function. Two configurations of the communication scheme were considered:

Configuration #1: The 'leader' aircraft sends its position/velocity information to the ground station; next, the ground station relays the information to both 'follower' aircraft, as shown in Figure 3-5. The advantage of using the ground station is essentially in the possibility of using higher transmission power and providing more degrees of freedom in the selection of the antenna.
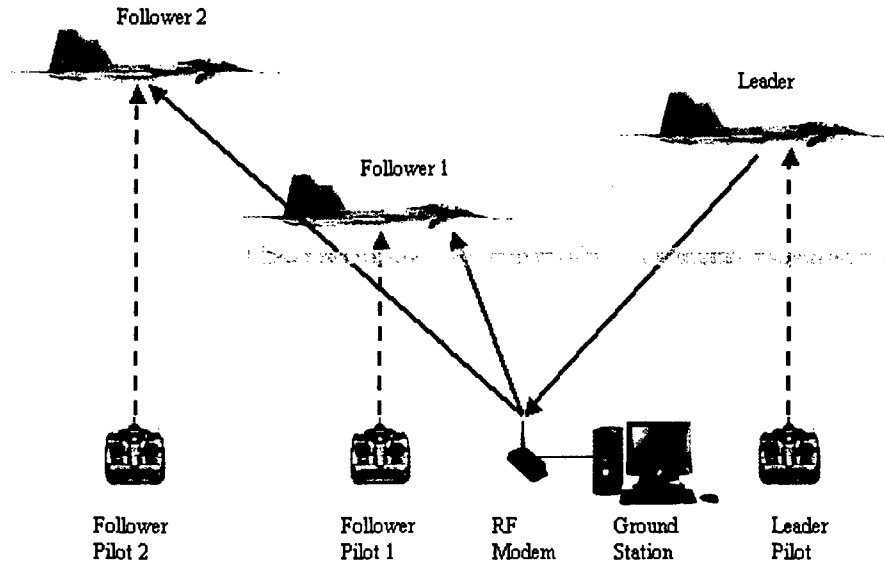
Figure 3-5: Communication Configuration #1

Configuration #2: The 'leader' sends the information directly to the 'follower' aircraft, as shown in Figure 3-6. This configuration is more flexible since it does not require a ground station. However, the selection of a suitable on-board antenna is a critical factor.
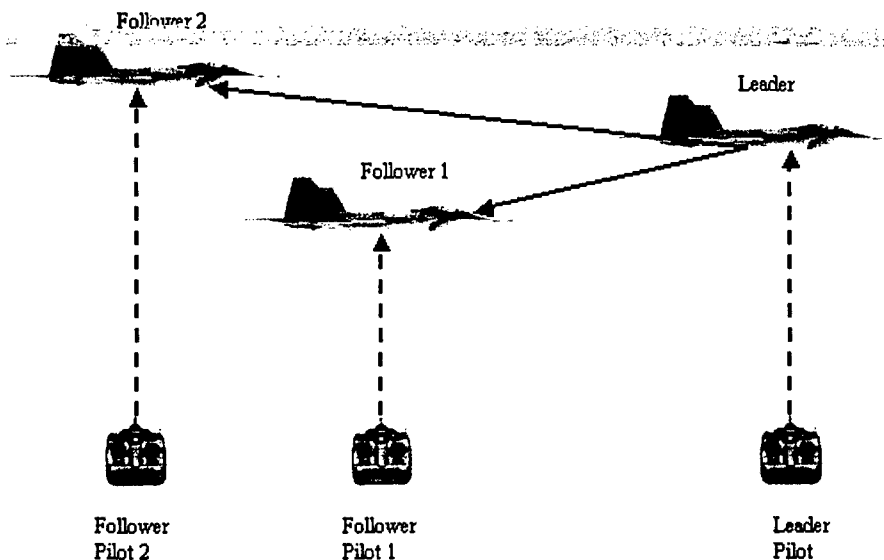
Figure 3-6: Communication Configuration #2

22

Both communication configurations were flight-tested. Various antenna positions for configuration #1 modems were considered and tested. However, at the end configuration #2 was selected since it provided the smallest amount of interference.

The communication devices used for data transmission from the 'leader' to the 'follower' aircraft were 900 MHz RF modems. The MRX-900, 900 MHz modem - shown in Figure 3-7 - was manufactured by Microhard Systems, Inc.
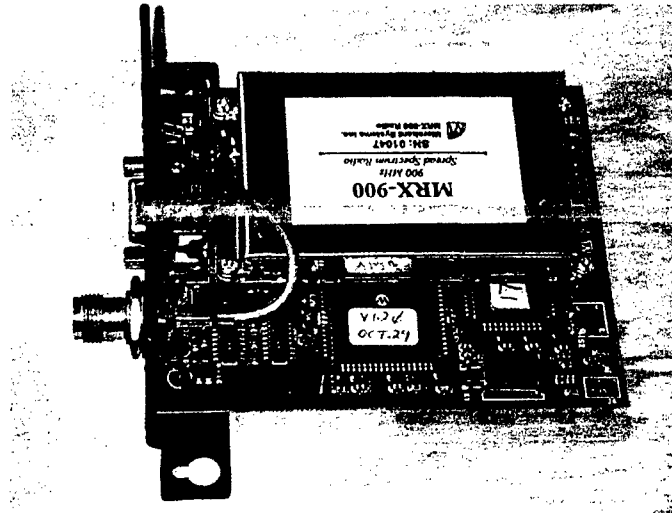
Figure 3-7: RF-Modem

The MRX-900 is a 900 MHz frequency hopping spread spectrum communications transceiver. The key features of the MRX-900 includes the following:

- transmission within a public, license-exempt band of the radio spectrum;
- fully compliant RS-232 serial I/O data port with handshaking and hardware flow control;
- 20 different user selectable pseudo random hopping patterns providing the possibility of separately operating multiple networks;
- encryption key with 65536 user selectable values for security purposes;
- built-in CRC-16 error detection and auto re-transmit for accuracy and reliability.

23

A brief listing of the MRX-900 modem technical specifications is provided in Table 3-1:

Bandwidth / Data Rate	2400 – 115, 200 bps, uncompressed half-duplex,
Communications Range	30 Kilometers (19 miles), with clear line-of-sight, elevated high-gain antennas
Power Requirements	9-14 VDC, 1.0 Amp
Power Consumption	600 mA at 1W transmit, 200 mA in receive
Operating Frequency	902-928 MHz
System Gain	135 dB
Sensitivity	-105 dBm
Output Power	1mW, 10mW, 100mW, 1W
Spreading Code	Frequency Hopping
Hopping Patterns	20 pseudo-random, user-selectable
Error Detection	CRC-16 with auto re-transmit
Dimensions (WxDxH)	94.5 mm x 108.0 mm x 43.7 mm
Weight (original case removed)	272 grams (included antenna)
Operating Environment	Temperature: -30 to +55°C

Table 3-1: MRX-900 Modem Specifications

3.2.4 - Control Signal Distribution System (CSDS)

The main component of the CSDS was the controller board, which acted as a hub for the entire flight control hardware. In total there were six functions included in the CSDS:

1. Receiving control signals from the pilot;

2. Receiving control signals from the OBC;

3. Transferring the command from the OBC into PWM signals;

4. Selecting the current operation mode of the aircraft ('Manual' or 'Automatic' mode);

5. Selecting the channels to be controlled by the OBC;

6. Distributing the control signals to individual servos.

The pilot used 'Channel #7' of the transmitter to enter the 'Automatic' mode; however, the pilot could reverse to 'Manual' mode at any time. The block diagram for the CSDS is shown in Figure 3-8.
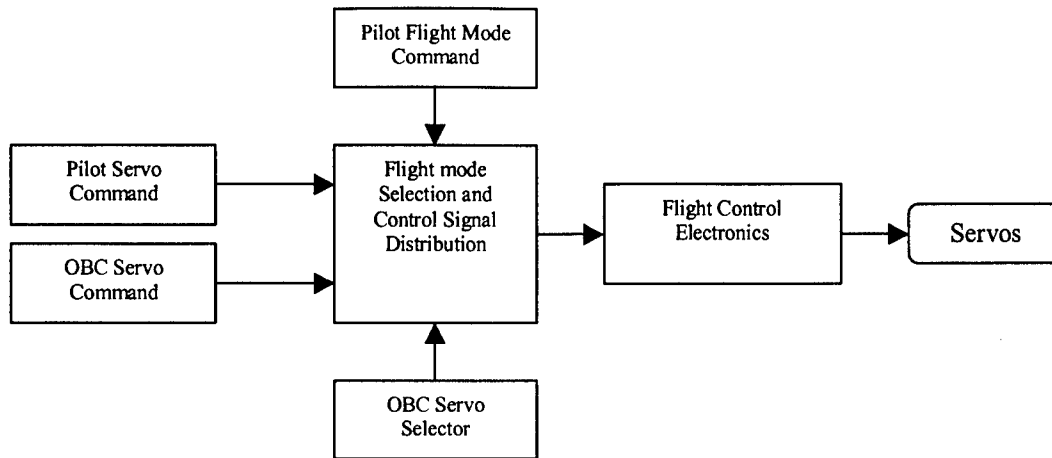
Figure 3-8: Control Signal Distribution System

3.3 - Major Payload Components

This section provides detailed descriptions of the main components of the payload.

3.3.1 - On-Board Computer (OBC) Modules

The OBC, shown in Figure 3-9, was based on a PC-104 stack system, which contained a CPU module, a data acquisition module, a power supply module, and supporting components. The PC-104 format was selected because of its reduced size, lightweight, and low power consumption.
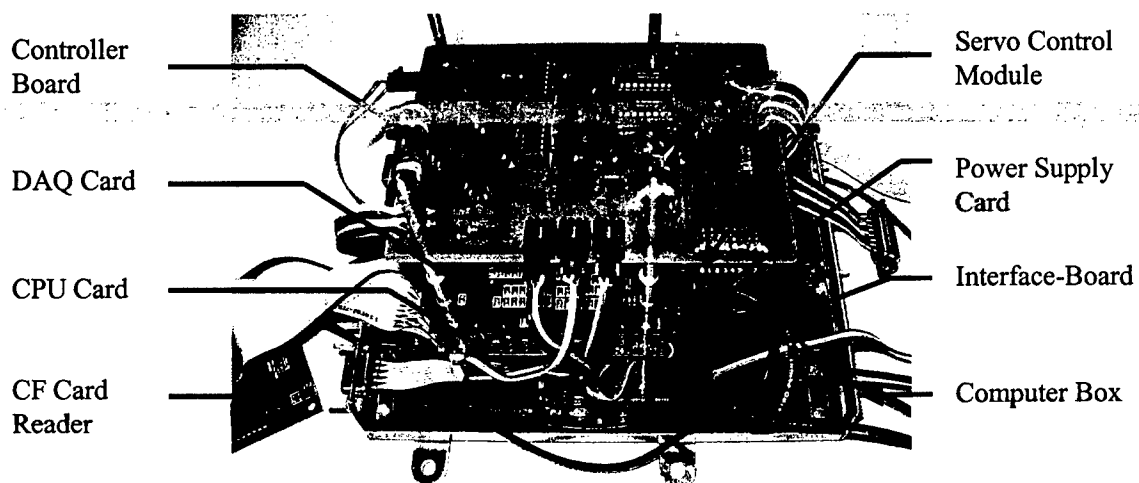
Figure 3-9: YF-22 On-Board Computer

25

The overall system included a CPU board, a data acquisition board, a power supply card, a set of customized sensor connection cards, and a top interface panel for connections to video/keyboard, etc. A layout diagram of the OBC is shown in Figure 3-10.
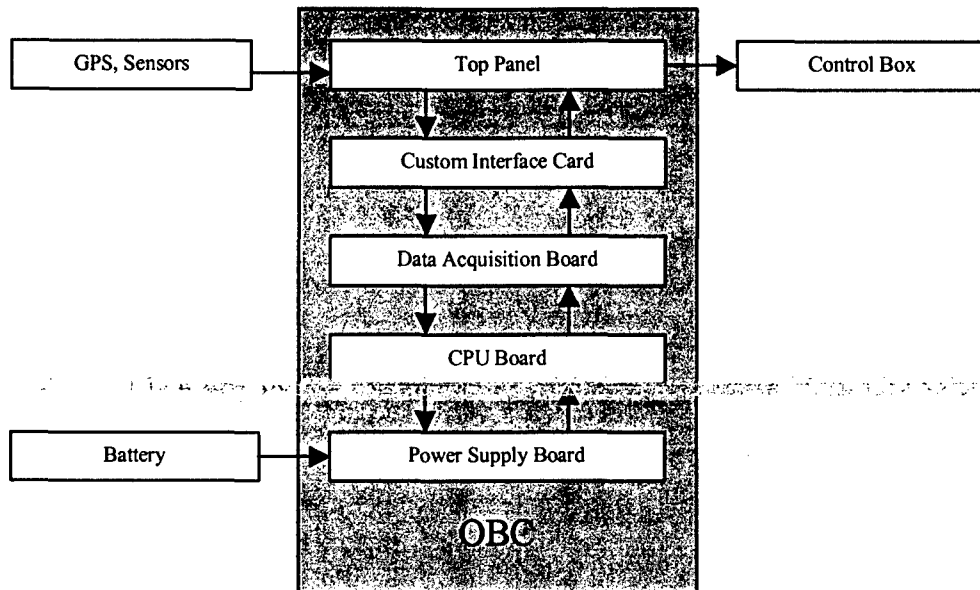
Figure 3-10: Layout of the OBC

A description of the 'off-the-shelf' individual components will be provided next while the custom-designed and custom-built boards (controller board and interface board) will be described in Section 3.3.3.

CPU Module (model: MSI-CM588)

The CPU card was the "brain" of the aircraft payload. The card collected the flight data from the data acquisition card and executed the control laws. It sent out control commands via a customized controller board, which in turn sent signals directly to the aircraft servos. The selected CPU card was the MSI-CM588 shown in Figure 3-11, manufactured by Microcomputer Systems.
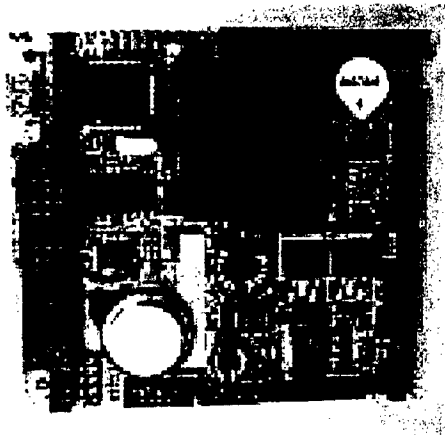
Figure 3-11: CPU Module

The MSI-CM588 is a low power PC/104 CPU card featuring a NS GXLV/GX1 processor and a GX5530 chipset with a built-in 6x86 300 MHz CPU operating from 0 to 85° C without a fan from a single +5V power supply. The speed of the CPU was a necessary design requirement for the on-board formation controller and execution of the control laws. The MSI-CM588 supported on-chip VGA display and two serial ports. 128 MB memory was installed on the CPU card for each aircraft system.

Data Acquisition Module (model: Diamond-MM-32-AT)

The main function of the data acquisition card was to collect signals from the individual aircraft sensors. It also sent channel selection commands to a servo driving circuit through the digital output capability. The accuracy of the flight control command was directly dependent on the speed and accuracy of the data acquisition card. The selected data acquisition card was the Diamond-MM-32-AT shown in Figure 3-12, manufactured by Diamond Systems.
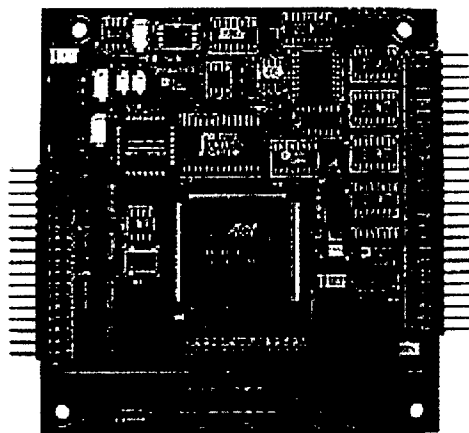
Figure 3-12: Data Acquisition Module

27

The card featured 32 analog input channels with 16 bits resolution. The maximum sampling rate is 200 KHz (although the on-board computer system used only up to 100 Hz). The card was also capable of providing 24 high-current digital I/O; 8 of them were used to send the channel selection signal to the controller board.

Power Supply and Communication Module (model: Jupiter-MM-SIO)

The selected power supply card was the Jupiter-MM-SIO, shown in Figure 3-13, also manufactured by Diamond Systems.
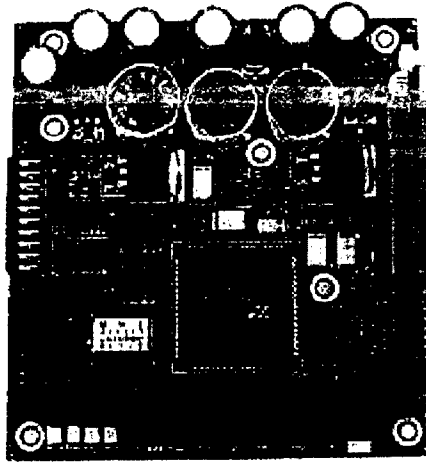
Figure 3-13: Power Supply Module

This module provided different voltage levels to power the OBC and the on-board sensors. It also featured two additional serial ports, which can be used for both communication and control purposes.

Servo Control Module (model: Mini SSC II)

The servo control module converted the OBC control commands (or serial signals) into the Pulse Width Modulation (PWM) signal to drive the aircraft servos. The servo control module used for the electronic payload was the Mini SSC II, shown in Figure 3-14.

28
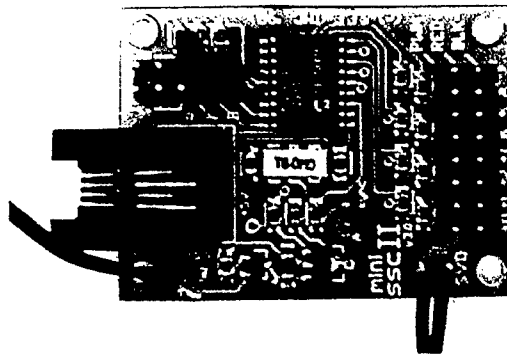
Figure 3-14: Servo Control Module

This module accepted serial inputs at 2400 or 9600 bps and provided 8 channels of servo-control signals (PWM). The module needed a 3-byte control package including one header byte, one channel selection byte and one byte for the control signal. A total of 6 channels were used to control the aircraft with an update frequency of 50 Hz.

Compact Flash Reader

The operating system and the flight control software were both installed on an 8 MB removable compact flash card. An IDE card reader, shown in Figure 3-15, was installed in each aircraft OBC.
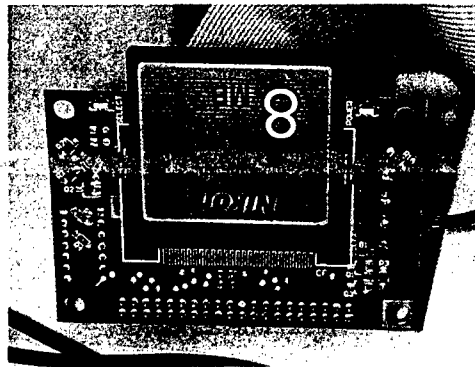
Figure 3-15: Compact Flash Card and Reader

The flash card performed both as a bootable system and a hard drive. This type of device was robust to high levels of vibration; poor robustness to high levels of vibration was the main drawback associated with the use of a standard hard drive setup. The use of a flash card also provided a high level of flexibility during the flight testing program; in fact, it allowed different sets of control laws to be stored in different compact flash cards for quick task reconfiguration on

the field. Furthermore, the use of a removable compact flash card greatly simplified the procedures for downloading data after each flight.

3.3.2 - On-Board Sensors

The suite of aircraft sensors included an air data probe, multiple pressure sensors, a temperature sensor, an Inertial Measurement Unit (IMU), a vertical gyro, a GPS receiver, and potentiometers on each of the primary control surfaces. A detailed description of each component is provided below.

Nose Probe – SpaceAge© Mini Air Data Boom

The nose air-data probe, shown in Figure 3-16, was manufactured by SpaceAge, Inc.
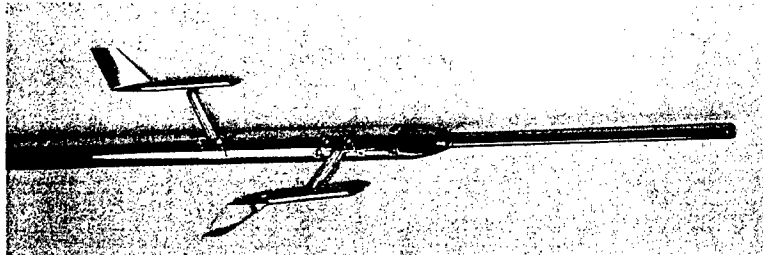
Figure 3-16: Air Data Probe

It is a lightweight component (approx. 6 oz) specially designed for light aircraft and UAV use. The total length of the probe is 30 inches and the nominal maximum calibrated speed is 340 knots. The probe features an angle-of-attack and sideslip vane for flow measurements, as well as static and dynamic pressure taps along the tip of the boom.

Pressure Sensors

For the measurements of dynamic and static pressure, two types of pressure sensors – similar to the one shown in Figure 3-17 - were used:
- Differential Pressure Sensor: SenSym ASCX01DN;
- Absolute Pressure Sensor: SenSym ASCX15AN.
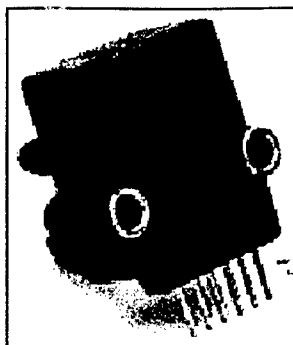
Figure 3-17: Pressure Sensor

The absolute pressure sensor measured the static pressure, which was then used to calculate the altitude of the UAV. The range of the SenSym ASCX15AN pressure sensor was 0-15 psi. The differential pressure sensor measured the difference between the static and dynamic pressure, which was then used to calculate the aircraft airspeed. The range of the SenSym ASCX01DN pressure sensor was 0-1 psi.

Inertial Measurement Unit (IMU) - IMU400

The selected IMU was the Crossbow IMU400, shown in Figure 3-18.
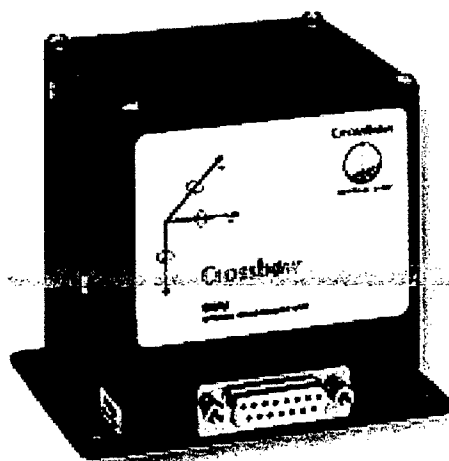
Figure 3-18: Inertial Measurement Unit (IMU)

This component was a solid-state 6-degree-of-freedom (6 DOF) inertial package intended for navigation and control, dynamic testing, and instrumentation applications. This system provided measurements of the angular rates and linear accelerations. Fully compensated angular rate and acceleration outputs were provided in both analog and digital (RS-232) formats. The range of measurement for the IMU400 unit was ±90 °/sec for angular rates and ±4 g for accelerations.

Vertical Gyro - VG34

The VG34 vertical gyro, shown in Figure 3-19, was selected for the measurement of the Euler angles. The unit was manufactured from Goodrich Sensor Systems. Although a fairly expensive component when compared to the IMU or air-data systems, this unit provided a significant reduction in size and weight. Furthermore, it provided very accurate measurements.
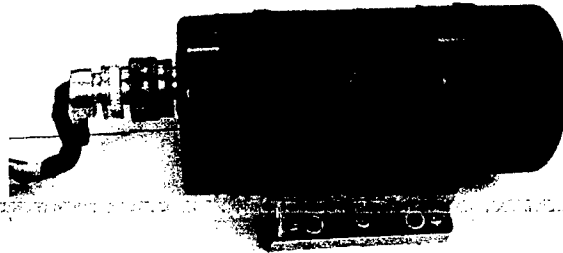
Figure 3-19: Vertical Gyro

The measurement range for the vertical gyro was ±90° for the roll angle, with an accuracy of ±1°, and ±60° for the pitch angle, also with an accuracy of ±1°.

Potentiometers

Potentiometers were installed on each hinge axis to measure the deflections of the primary control surfaces. An horizontal tail potentiometer is shown in Figure 3-20. Particularly, the stabilators, the ailerons and the rudders were each instrumented. Potentiometers were not installed on the flaps since they were only used for takeoff and landing.
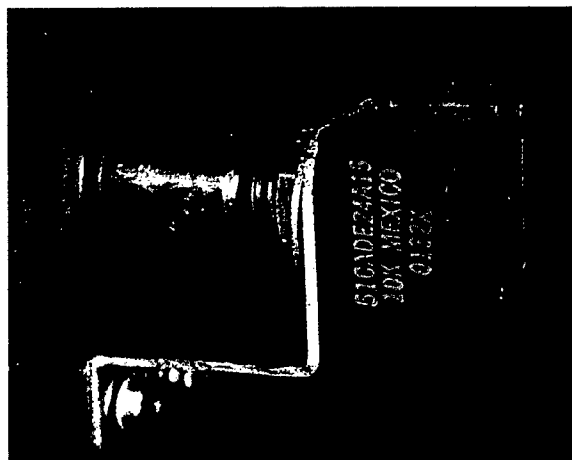
Figure 3-20: Potentiometer

Each potentiometer was selected to be 10 kΩ. This value provided a desirable trade-off between the Signal Noise ratio (S/N) and power consumption. A 12-volt supply was applied to each potentiometer; next, the reading output was collected and calibrated to provide the measurement of surface deflection in degrees.

GPS Receiver

The position and velocity information for each aircraft was required for formation flight purposes. The selected GPS receiver was the OEM4 unit manufactured by Novatel, Inc. A picture of the unit is shown in Figure 3-21.
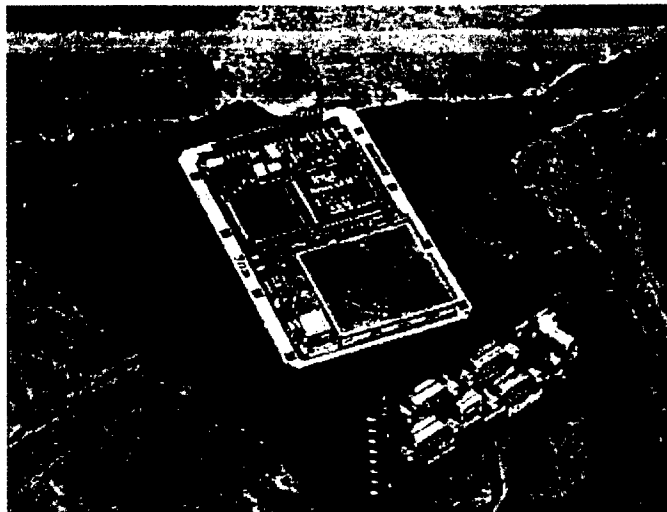
Figure 3-21: GPS Receiver

The GPS unit provides the 3-axis position and velocity information using a serial port. The selected GPS antenna was the GPS-511, also manufactured by Novatel, Inc., which offered desirable performance for airborne and high dynamic applications. The GPS antenna was mounted on the top section of the aircraft fuselage, as shown in Figure 3-22. The slotted sections to the right of the antenna are the airflow intakes as discussed in Section 2.2.
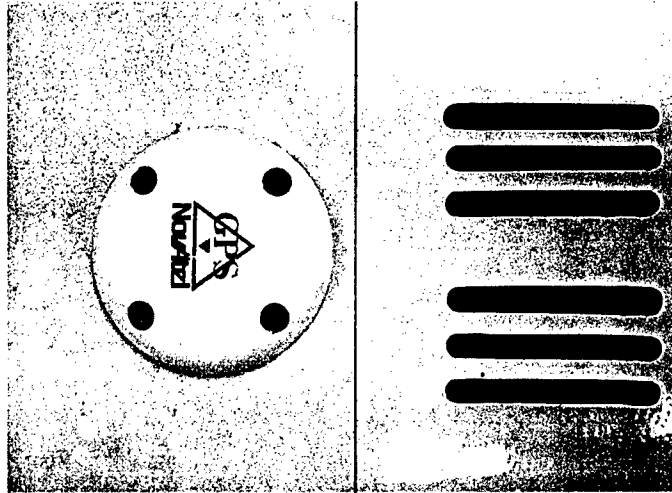
Figure 3-22: GPS Antenna

3.3.3 - Custom Designed Components

In addition to "off-the-shelf" components described above, several pieces of hardware had to be custom-designed and custom-built. Therefore, Printed Circuit Boards (PCBs) were designed and developed to meet the specified requirements. The design involved an interface board, a controller board, a nose sensor board, a power supply board, a sensor and servo hub boards.

Interface Board

The baseboard, shown in Figure 3-23, is a custom-made signal connection board designed to connect individual sensor outputs to each specified data acquisition channel. It provided power to each sensor (except the vertical gyro and the GPS, which are powered separately) and provided a reference voltage for the controller usage.
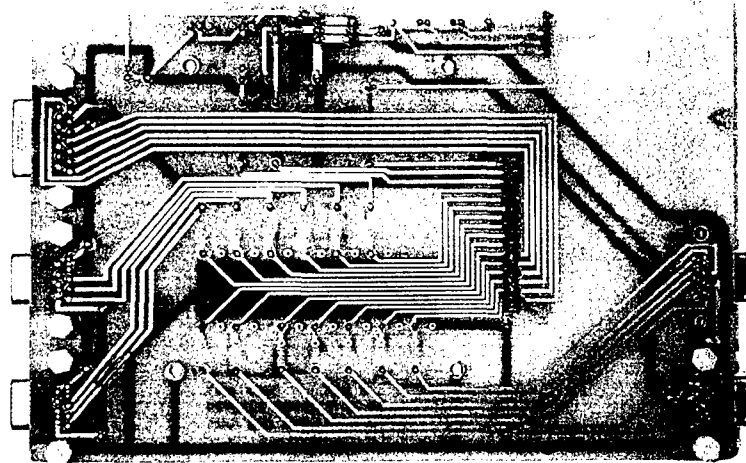
Figure 3-23 Interface Board (Baseboard)

Controller Board

The controller board, shown in Figure 3-24, is one of the most critical components. This board received control signals from both the pilot (R/C receiver) and the OBC.
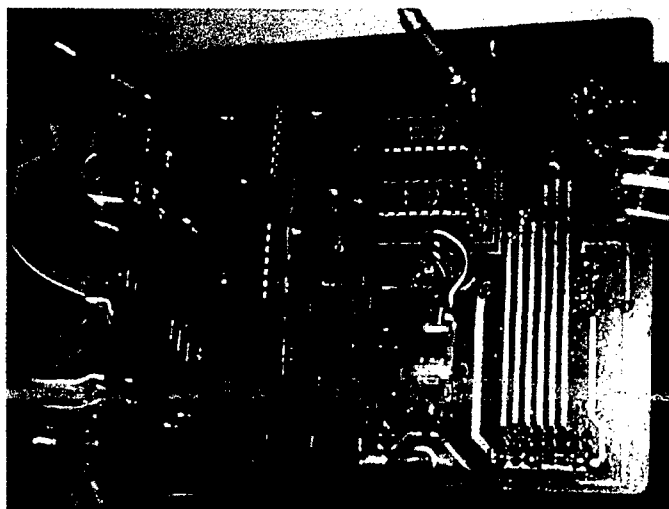
Figure 3-24: Controller Board

Two switching mechanisms were designed to guarantee the safety of the aircraft, that is 'Hardware Switching' and 'Software Switching'.

Hardware Switching: Hardware switching gives the pilot the ability to switch off the entire controller instantly at any circumstance even if the OBC power is lost. A R/C channel was allocated for this specific purpose. The PWM switch signal from the receiver is converted to High/Low switching signal according to the signal pulse width. This switching signal is then used to drive a set of AND gates to enable/disable the entire on-board controller.

Software Switching: Software Switching gives the OBC the capability to control all or any subset of the aircraft's control surfaces with pre-programmed selections. With this ability, the flight test can be configured to include different subtests and greatly enhances the flexibility and the safety of the experiment. The software switching is implemented through a synthesis of both hardware and software. The on-board software reads pre-determined channel selection information from a 'log' file at the initialization stage (see section 5.6.1 for more details). Once the controller switch is turned on, it sends out the channel selection signal through the Digital Input/Output (DIO) port of the data acquisition card. This signal is then passed to the multi-channel 74HC4053 analog multiplexer/demultiplexer on the controller board to select the pilot/on-board control. The design of the controller board is shown in Figure 3-25.
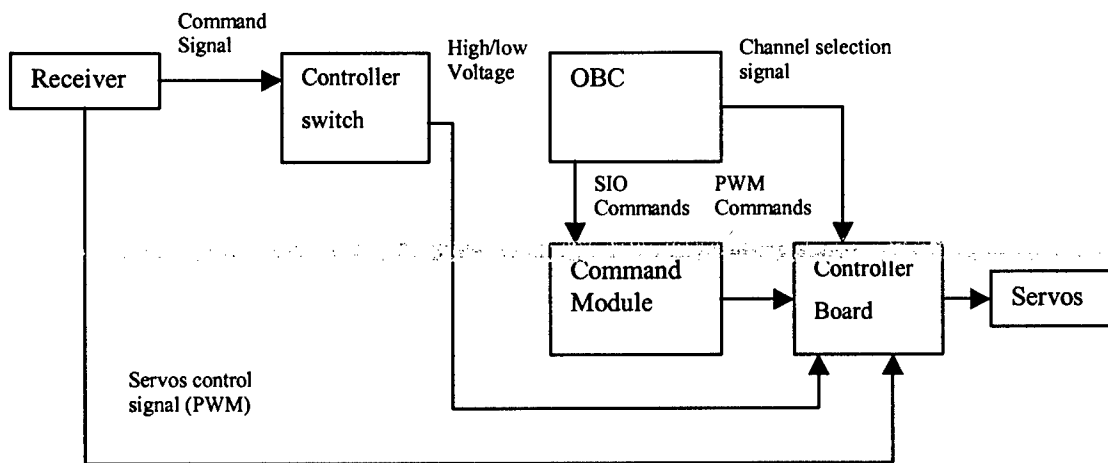
Figure 3-25: Controller Board Design

Nose Sensor Board

The nose sensor board, shown in Figure 3-26, was designed to interface with the dynamic pressure sensor, the static pressure sensor, and the temperature sensor.
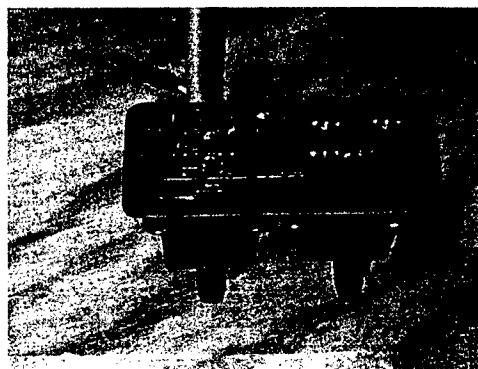
Figure 3-26: Nose Sensor Board

Additional connectors on the nose sensor board allowed for the air-data probe potentiometers to be added to the data acquisition system.

Power Supply

The voltage requirement of the vertical gyro is a 24-32V supply-range. The aircraft on-board battery pack only supplies 14.8V; therefore, a DC-DC converter was necessary to power the unit. A 24v DC converter was mounted on a custom-made power supply PC board, as shown in Figure 3-27.
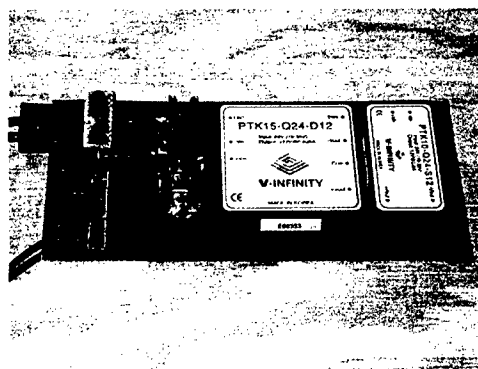
Figure 3-27: Power Supply

To minimize potential EMI problems several RF chokes were introduced; additionally, the package was enclosed in an aluminum case. The power for the GPS receiver and RF modem were also included within this custom-designed power supply board.

Sensor Hub

The sensor hub, shown in Figure 3-28, was designed to connect the OBC to the potentiometers mounted on the primary control surfaces.

Figure 3-28: Sensor Hub

A 12 V voltage was supplied to each of the potentiometer; the measured signal is forwarded back to the on-board data acquisition card. Two sensor hubs were used to provide connections on the left and right sides of the plane.

Servo Hub

The servo hub, shown in Figure 3-29, was designed to connect the controller hardware to the individual aircraft servos.
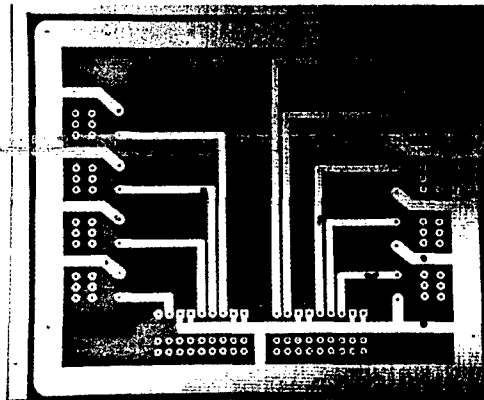
Figure 3-29: Servo Hub

In particular, the servo control commands were sent out to the servo hub and re-distributed to each individual servo including left/right stabilators, left/right rudders, left/right ailerons, left/right flaps, and the engine throttle signal.

Interface Panel

The interface panel was integrated on the computer casing. It is made of aluminum sheeting and featured power and mode switches while providing connection to instrumentation sensors, video monitor output, and keyboard. The interface panel features a front section, a rear section, and a top section, as shown in Figure 3-30.
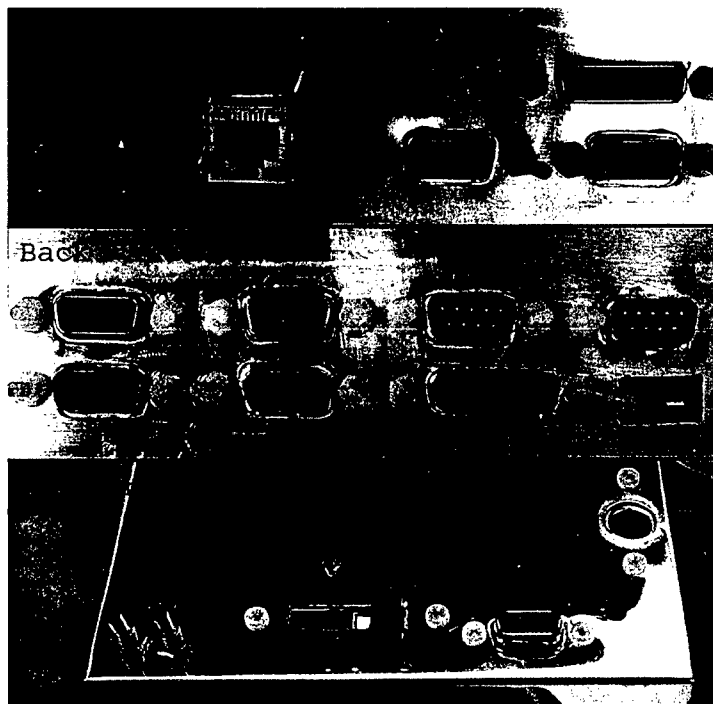
Figure 3-30: Interface Panels

The front panel connects the battery power, the R/C receiver, the vertical gyro, and the nose probe sensors. The rear panel connects to the IMU, the GPS receiver, the sensor and servo hubs. The top panel is for user interface and features a computer power switch, a vertical gyro power switch, a running mode switch, a power LED, a controller switch LED, and a slot for the compact flash card.

3.3.4 - Power Sources

Following a detailed power budget, a total of six battery packs were introduced in each UAV. In particular, four 4.8v 1600mAh NiMN battery packs were used for R/C system, including two for the receiver and two for the aircraft servos. This provided a dual-redundancy for the R/C power system, which was the most critical part for aircraft safety. A 7.2v 1250mAh NiCd battery pack was introduced to power the electronics for the propulsion system. Finally, the OBC and the instrumentation were powered by a single battery pack made of 4 Li-Poly battery cells. A single Li-Poly cell is shown in Figure 3-31.
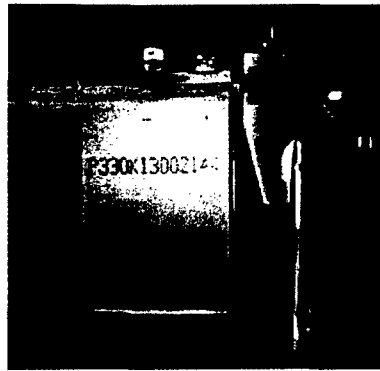
Figure 3-31: Battery Cell

This battery pack provided 14.8v (nominal) with a 3300mAh capacity. The on-board payload power consumption provided in Table 3-2 shows that, once fully charged, the selected Li-Poly battery pack lasted for more than 1 hour. Typical mission duration for the payload system operation was under 30 minutes, providing sufficient run time.

Device	Current (start)	Current (nominal)	Notes
Vertical Gyro	1.0	0.5	Requires a 3-minute stabilizaion phase
OBC	0.7	0.65	Without sensor power
GPS	0.2	0.2	
Miscellaneous	0.5	0.5	Estimates
Total Estimation	2.4	1.85	

Table 3-2: On-board Payload Power consumption

3.4 - Hardware Mounting

The installation of the hardware components required careful consideration of the following issues:

- length of the required cables;
- levels of vibration;
- EMI issues;
- weight/balance of the aircraft.

Most of the payload components (including the OBC, the vertical gyro, the IMU, the GPS, and the power supply) were mounted on two rails installed in the payload bay, shown in Figure 3-32.
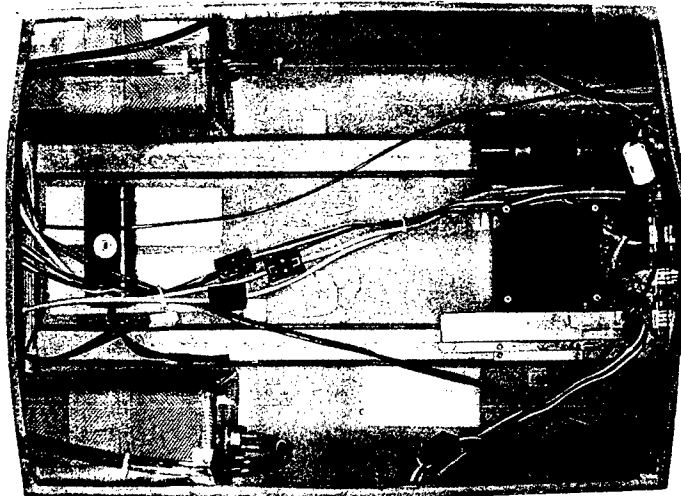
Figure 3-32: Payload Bay (Overhead View)

Since the jet engine was mounted in the rear of the aircraft, most of the payload components were installed toward the forward section of the aircraft for balance purposes. Special care was used for the installation of some of the components. In fact, the vertical gyro and the IMU had to be installed in parallel with the X-axis (body frame) while the air-data probe was mounted to be aligned with the X-axis.

Using the maximum length of the aircraft and attempting to avoid on-board EMI sources (discussed in Section 3.5), the R/C receiver was mounted in the nose bay of the aircraft - as shown in Figure 3-33 - with the antenna attached to the tip of the right vertical tail.
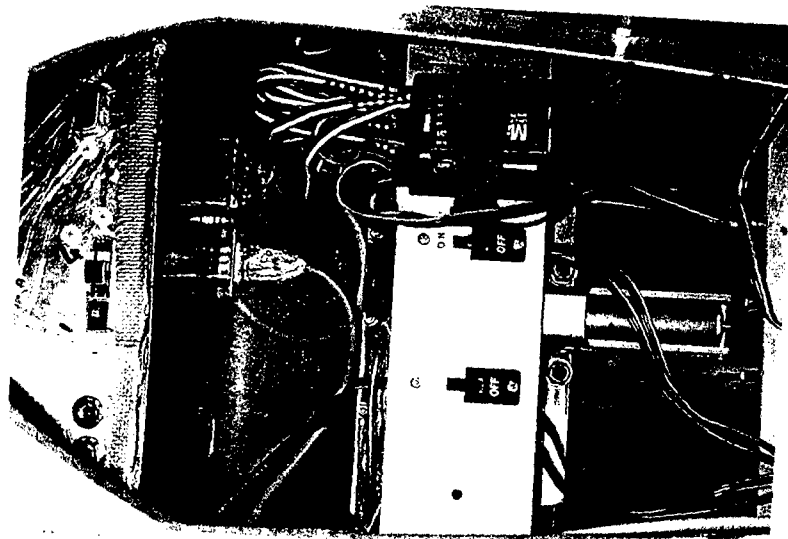
Figure 3-33: Nose Section (Overhead View from Canopy Hatch)

3.5 - EMI

Electro-magnetic Interference (EMI) effects could pose significant threats to the appropriate functioning of the on-board electronic systems. In fact, for such a small aircraft like the YF-22 model with a variety of electronic components confined in a relatively small space, there were several potential sources of interferences, such as:

- the OBC;
- the vertical gyro;
- the custom-built power supply.

Since prevention is one of the best strategies against the occurrence of EMI problems, special care was taken in the design, manufacturing, and installation of both the customized and 'off-the-shelf' components. Aluminum enclosures were designed and manufactured to shield most of the hardware components; additional ferrite RF chokes were also used on power and signal cables. Once the electronic payload was assembled, the next step was to test the payload with a spectrum analyzer. This analysis revealed that most of the EMI issues had been addressed and only a few additional RF chokes were necessary to eliminate residual EMI sources at the field. Nevertheless, although EMI results in the lab were completely satisfactory, for maximizing the safety of the flight operations, it became standard procedure to perform a radio range check on the R/C system before each flight session. During a range check, the OBC, aircraft sensors, and engine were powered and an approximate radio range of 91.44 m (300 ft) on the ground was

required with the transmitter antenna fully retracted before flight operations were allowed to proceed.

Chapter 4 - Design of the Formation Control Laws

4.1 - Formation Controller Architecture

The main objective of this effort was to design a formation controller for the two 'follower' aircraft so that they would be capable of tracking a 'leader' aircraft at a pre-defined forward, lateral, and vertical distance. One constraint for flight experiments was that the aircraft had to remain within visual range. Therefore, each UAV was required to perform tight maneuvers at high Euler angles and moderately high angular rates for many segments of the mission. An additional objective of the design phase was to limit the amount of information exchanged between the 'leader' and 'follower(s)' to maintain the pre-defined formation geometry.

The formation controller was designed to allow the 'follower' vehicle to position itself at a pre-defined forward, lateral, and vertical distance from the 'leader' once formation flight was engaged. From a geometric point of view, the control problem was divided into two independent problems: a level plane tracking problem (horizontal geometry) and a vertical plane-tracking problem (vertical geometry).

The formation control problem can be ultimately modeled as a non-linear minimization problem in which the controller acts on the throttle, stabilators, and ailerons/rudder commands to minimize the 'error' coefficients f, l, and h (f for forward, l for lateral, and h for height or vertical direction). Like other trajectory control problems, this problem exhibited a two-time-scale feature because the trajectory dynamics (relative position and velocity) was slower than the attitude dynamics (angular velocity and orientation) of the aircraft. Due to this specific characteristic, the controller design was divided into two phases, an outer loop and inner loop controller. A mathematical model of the aircraft was determined through a parameter identification study for use with the design, simulation, and flight testing of the formation controller. In this section, the identification of the aircraft mathematical model, design of the inner loop and outer loop controllers, and development of the formation flight simulation environment will be discussed.

4.2 - Linear Mathematical Model

A linear mathematical model for the aircraft was required for the design of the linear inner loop controller. Parameter Identification (PID) from flight data was the approach used for the determination of the mathematical model in lieu of evaluating the aerodynamic coefficients through a wind tunnel or a CFD analysis. Therefore, a series of flight tests were performed to collect flight data for PID purposes. Typical maneuvers - including stabilator doublets, aileron doublets, rudder doublets and a combination of lateral-directional aileron/rudder doublets - were performed to excite the aircraft longitudinal and lateral-directional dynamics. A Batch Least Squares (BLS) technique was then used for estimating these parameters and, thus, developing the linear mathematical model.

In general, the Least Square (LS) method assumes that the best-fit curve of a given type is the polynomial curve which provides the minimal sum of the deviations squared (*least square error*) from a given set of data. The BLS technique consists essentially in solving an over-determined linear system in a 'least square' sense. The reliability of this method comes from the property that a pseudo-inverse solution for a linear system with more equations than unknowns is optimal in the least squares sense. The general linear regression model is given by:

$$Y = X\beta + \varepsilon \qquad (4\text{-}1)$$

where

- Y is a $(n \times 1)$ vector of known responses of the system;

- X is a $(n \times p)$ matrix of known inputs to the system;

- β is the $(p \times 1)$ vector of parameters to be estimated;

- ε is a $(n \times 1)$ vector of independent normal random variables, with zero mean ($E\{\varepsilon\} = 0$) and unknown diagonal variance-covariance matrix.

This matrix was assumed to be a multiple of the $(n \times n)$ identity matrix: ($\sigma^2\{\varepsilon\} = \sigma^2 I$). Therefore, $E\{Y\} = X\beta$ and $\sigma^2\{Y\} = \sigma^2 I$. The problem is to evaluate the vector β such that $X\beta$ (which is the expected value of Y) is as close as possible (in the 'least square' sense) to Y, so that σ^2 is then minimized. Thus, the objective was to find a value of β which minimizes the following quadratic index:

$$Q = \varepsilon^T \varepsilon = (Y - X\beta)^T (Y - X\beta) \qquad (4\text{-}2)$$

The goal was to identify a linear system of the following form:

$$\begin{bmatrix} \dot{x}(t) \\ y(t) \end{bmatrix} = \begin{bmatrix} A & B \\ C & D \end{bmatrix} \begin{bmatrix} x(t) \\ u(t) \end{bmatrix}$$

(4-3)

By transposing Eqn. 4-3, one can define the following:

$$Y = \begin{bmatrix} \dot{x}^T(t) & y^T(t) \end{bmatrix};$$

$$X = \begin{bmatrix} x^T(t) & u^T(t) \end{bmatrix}$$

(4-4)

$$\beta = \begin{bmatrix} A & B \\ C & D \end{bmatrix}^T$$

At nominal conditions a linear aircraft model can be considered as the integration of decoupled longitudinal and lateral-directional sub-models. Both sub-models are normally considered to be linearized models obtained from a non-linear model which was trimmed at a steady-state condition of straight-level flight at nominal altitude with nominal airspeed. For the WVU YF-22 the nominal airspeed and nominal altitude were considered to be approx. 42 m/s and approx. 310 m respectively.

4.2.1 - Longitudinal Model Identification

The goal for the longitudinal model identification was to identify the 2nd order short-period model from the flight data:

$$\begin{bmatrix} \dot{\alpha} \\ \dot{q} \end{bmatrix} = A_{long} \begin{bmatrix} \alpha \\ q \end{bmatrix} + B_{long} i_H$$

(4-5)

Two sets of data, shown in Figure 4-1 and Figure 4-2, were selected from the recorded flight data – one for identification purposes and the second set used for validation purposes. The measured flight data was sampled at 100Hz. Since the small perturbation equations were used, the flight data was pre-processed (such that, the non-zero steady state value of α and i_H were subtracted. Both data sets were associated with a typical stabilator doublet maneuver designed to excite the short-period mode.

Selected Data For Identification
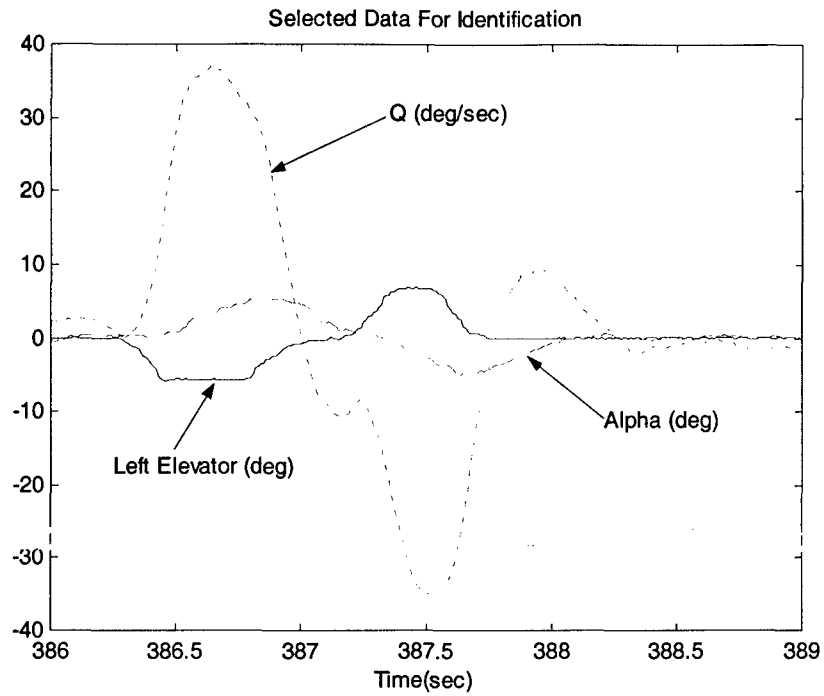
Figure 4-1: Flight Data for Longitudinal Model Identification

Selected Data For Validation
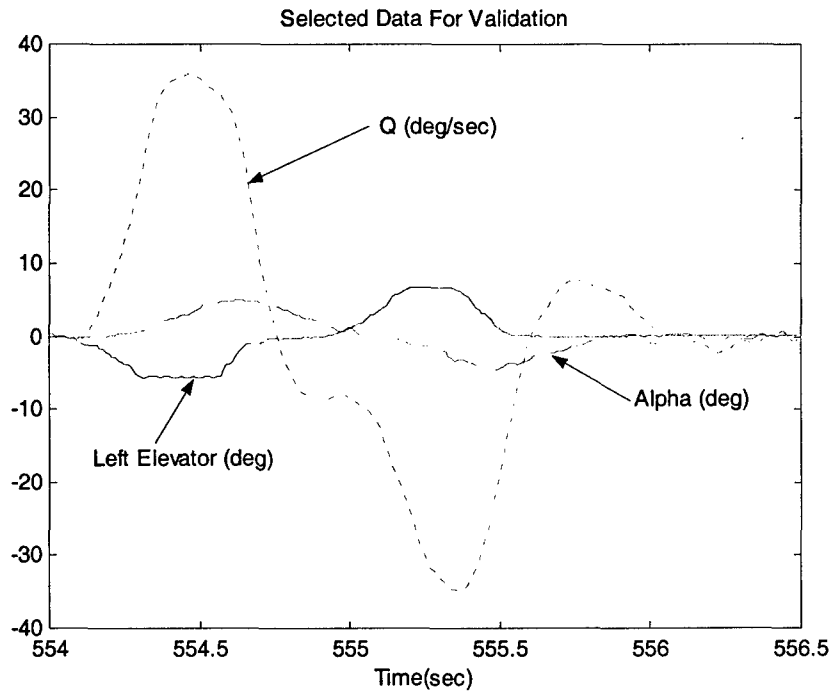
Figure 4-2: Flight Data for Longitudinal Model Validation

47

Using the BLS method, the identified discrete time state space longitudinal model was given by:

$$\begin{bmatrix} \alpha(n+1) \\ q(n+1) \end{bmatrix} = \begin{bmatrix} 0.9161 & 0.0144 \\ -0.6264 & 0.9261 \end{bmatrix} \begin{bmatrix} \alpha(n) \\ q(n) \end{bmatrix} + \begin{bmatrix} 0.0046 \\ -0.7566 \end{bmatrix} i_H(n) \qquad (4\text{-}6)$$

$$q(n) = \begin{bmatrix} 0 & 1 \end{bmatrix} \begin{bmatrix} \alpha(n) \\ q(n) \end{bmatrix} + \begin{bmatrix} 0 \end{bmatrix} i_H(n) \qquad (4\text{-}7)$$

This model was then converted into an equivalent continuous time model:

$$\begin{bmatrix} \dot{\alpha} \\ \dot{q} \end{bmatrix} = \begin{bmatrix} -4.1172 & 0.7781 \\ -33.8836 & -3.5729 \end{bmatrix} \begin{bmatrix} \alpha \\ q \end{bmatrix} + \begin{bmatrix} 0.5435 \\ -39.0847 \end{bmatrix} i_H \qquad (4\text{-}8)$$

$$q = \begin{bmatrix} 0 & 1 \end{bmatrix} \begin{bmatrix} \alpha \\ q \end{bmatrix} + \begin{bmatrix} 0 \end{bmatrix} i_H \qquad (4\text{-}9)$$

The sampling time for the discrete system was $T_s = 0.02 \sec$. The full continuous time longitudinal model with the additional velocity and pitch angle states was also tentatively identified as given by:

$$\begin{bmatrix} \dot{v} \\ \dot{\alpha} \\ \dot{q} \\ \dot{\theta} \end{bmatrix} = \begin{bmatrix} -0.2835 & -23.0959 & 0 & -0.1711 \\ 0 & -4.1172 & 0.7781 & 0 \\ 0 & -33.8836 & -3.5729 & 0 \\ 0 & 0 & 1 & 0 \end{bmatrix} \begin{bmatrix} v \\ \alpha \\ q \\ \theta \end{bmatrix} + \begin{bmatrix} 20.1681 \\ 0.5435 \\ -39.0847 \\ 0 \end{bmatrix} i_H \qquad (4\text{-}10)$$

As well known in aircraft PID, the determination of the 'drag' related coefficients was not deemed to be accurate. However, estimates of the 'lift' and 'pitch' related coefficients were fairly accurate, as shown in the enclosed figures. Particularly, Figures 4-3 and 4-4 show the measured and computed responses for the pitch rate and angle of attack respectively.
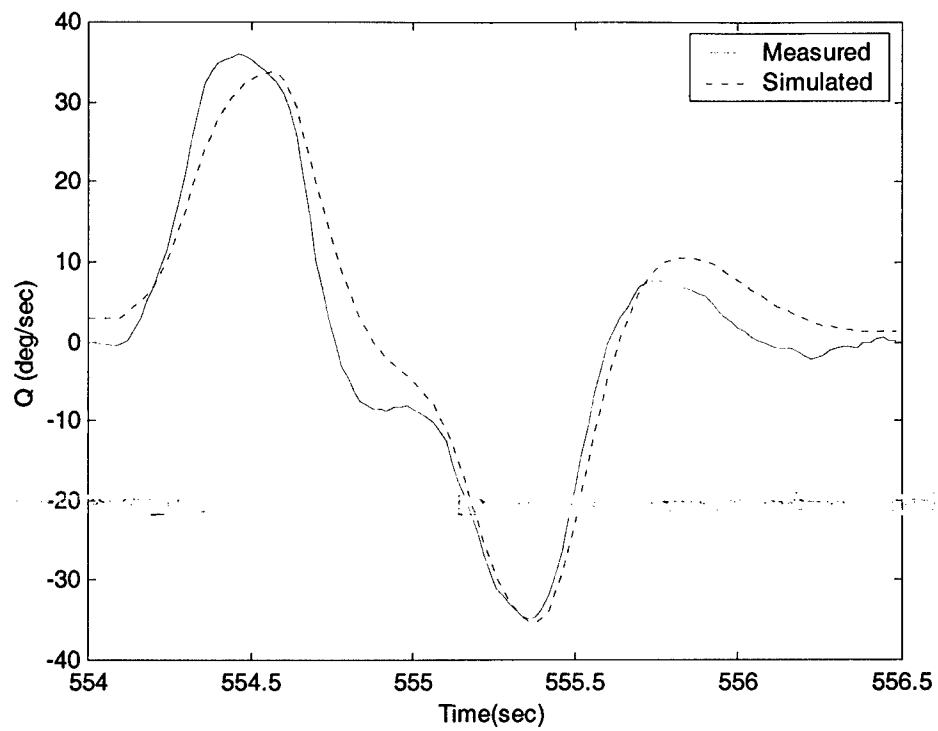
Figure 4-3: Model Validation - Measured and Simulated Pitch Rate
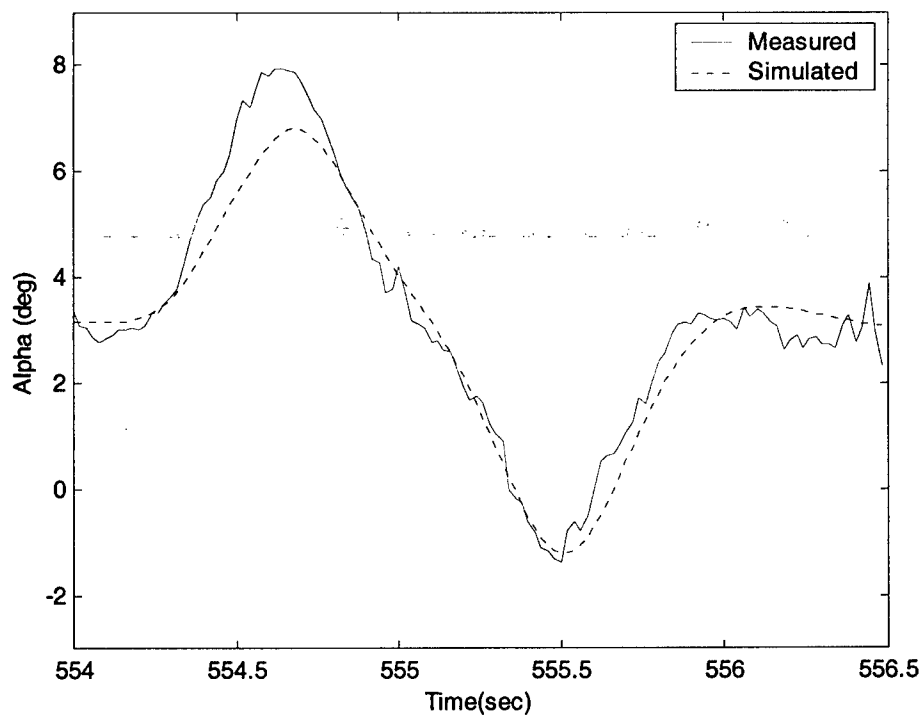
Figure 4-4: Model Validation - Measured and Simulated Angle-of-Attack

4.2.2 - Lateral-Directional Model Identification

The task of the lateral-directional model identification was to identify the following 3rd order linear model from the collected flight data:

$$\begin{bmatrix} \dot{\beta} \\ \dot{p} \\ \dot{r} \end{bmatrix} = A_{lat-dir} \begin{bmatrix} \beta \\ p \\ r \end{bmatrix} + B_{lat-dir} \begin{bmatrix} \delta_A \\ \delta_R \end{bmatrix} \qquad (4\text{-}11)$$

As performed for the longitudinal identification, two sets of data - shown in Figure 4-5 and Figure 4-6 - were selected from the available flight testing data - one set for identification purposes and a second set for validation purposes. As previously stated, the flight data was sampled at a rate of 100Hz. Unlike the case of the longitudinal dynamics, there was no need to perform data pre-processing since all the steady-state values of the sampled data were found to be approximately zero. Both data sets were representative of a typical aileron/rudder doublet combination, which included an aileron doublet immediately followed by a rudder doublet maneuver. This maneuver was found to provide a desirable excitation for both the dutch-roll and rolling dynamic modes.
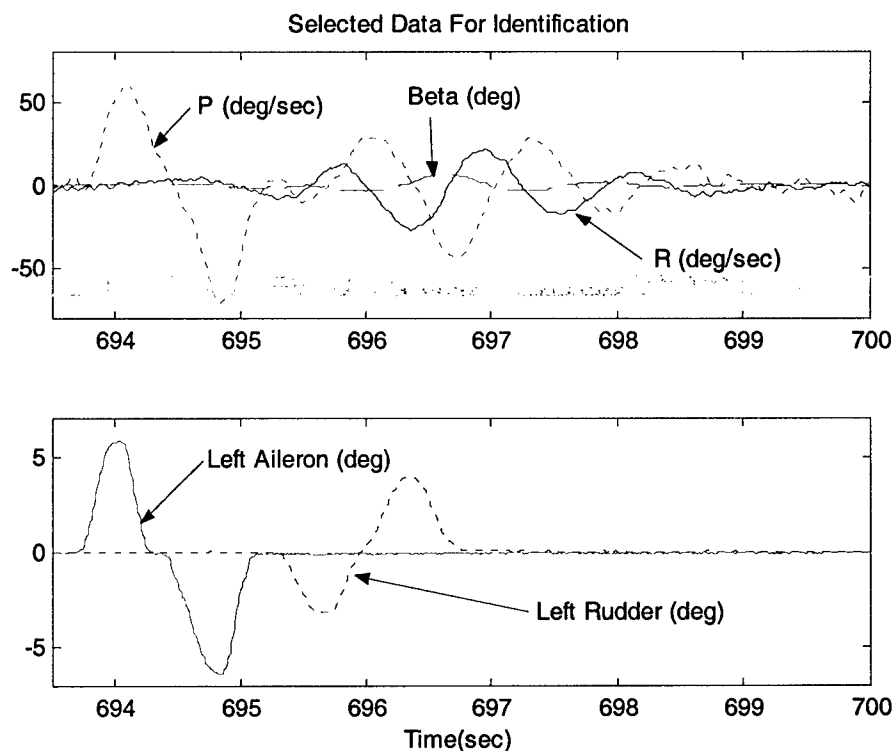
Figure 4-5: Flight Data for Lateral-Directional Model Identification

50
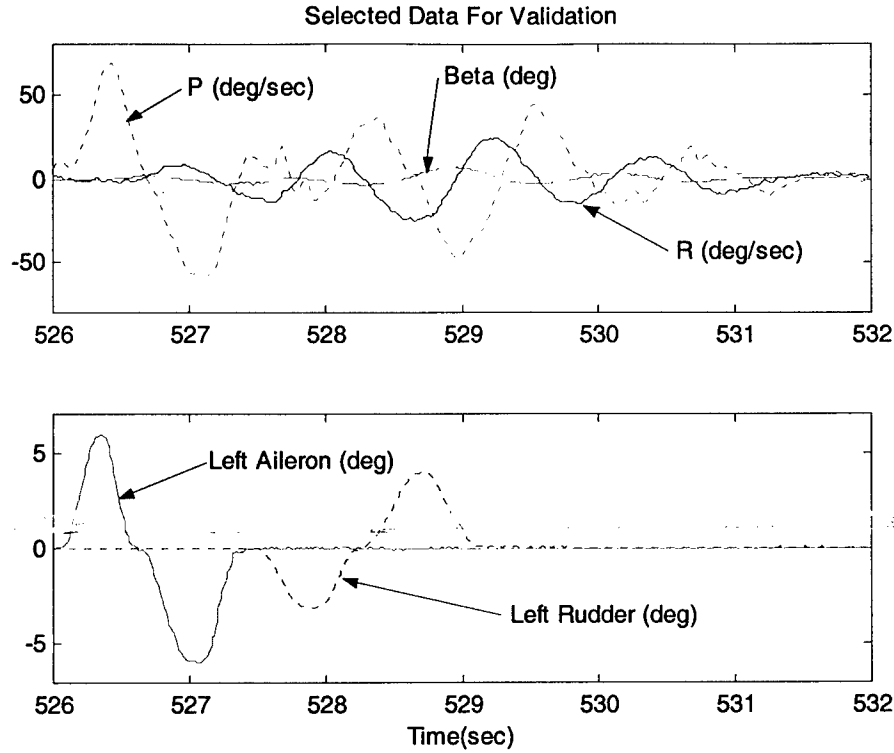
Figure 4-6: Flight Data for Lateral-Directional Model Validation

Using the BLS method, the discrete-time state-space lateral-directional model was identified as:

$$\begin{bmatrix} \beta(n+1) \\ p(n+1) \\ r(n+1) \end{bmatrix} = \begin{bmatrix} 1.0032 & 0.0019 & -0.0201 \\ -1.2262 & 0.8512 & 0.1150 \\ 0.4118 & -0.0115 & 0.9560 \end{bmatrix} \begin{bmatrix} \beta(n) \\ p(n) \\ r(n) \end{bmatrix}$$

$$+ \begin{bmatrix} 0.0048 & -0.0099 \\ -1.8926 & 0.6005 \\ -0.1092 & -0.4841 \end{bmatrix} \begin{bmatrix} \delta_a(n) \\ \delta_r(n) \end{bmatrix}$$

(4-12)

$$\begin{bmatrix} p(n) \\ r(n) \end{bmatrix} = \begin{bmatrix} 0 & 1 & 0 \\ 0 & 0 & 1 \end{bmatrix} \begin{bmatrix} \beta(n) \\ p(n) \\ r(n) \end{bmatrix} + \begin{bmatrix} 0 & 0 \\ 0 & 0 \end{bmatrix} \begin{bmatrix} \delta_a(n) \\ \delta_r(n) \end{bmatrix}$$

(4-13)

As with the longitudinal model, this model was also then converted into an equivalent continuous time model.

$$\begin{bmatrix} \dot{\beta} \\ \dot{p} \\ \dot{r} \end{bmatrix} = \begin{bmatrix} 0.4299 & 0.0938 & -1.0299 \\ -67.3341 & -7.9485 & 5.6402 \\ 20.5333 & -0.6553 & -1.9955 \end{bmatrix} \begin{bmatrix} \beta \\ p \\ r \end{bmatrix} + \begin{bmatrix} 0.2724 & -0.7713 \\ -101.8446 & 33.4738 \\ -6.2609 & -24.3627 \end{bmatrix} \begin{bmatrix} \delta_a \\ \delta_r \end{bmatrix}$$

(4-14)

51

$$\begin{bmatrix} p \\ r \end{bmatrix} = \begin{bmatrix} 0 & 1 & 0 \\ 0 & 0 & 1 \end{bmatrix} \begin{bmatrix} \beta \\ p \\ r \end{bmatrix} + \begin{bmatrix} 0 & 0 \\ 0 & 0 \end{bmatrix} \begin{bmatrix} \delta_a \\ \delta_r \end{bmatrix} \qquad (4\text{-}15)$$

An augmented lateral-directional model (including the roll angle) in continuous time was also introduced:

$$\begin{bmatrix} \dot{\beta} \\ \dot{p} \\ \dot{r} \\ \dot{\phi} \end{bmatrix} = \begin{bmatrix} 0.4299 & 0.0938 & -1.0300 & 0.2366 \\ -67.3341 & -7.9485 & 5.6402 & 0 \\ 20.5333 & -0.6553 & -1.9955 & 0 \\ 0 & 1 & 0 & 0 \end{bmatrix} \begin{bmatrix} \beta \\ p \\ r \\ \phi \end{bmatrix} + \begin{bmatrix} 0.2724 & -0.7713 \\ -101.8446 & 33.4738 \\ -6.2609 & -24.3627 \\ 0 & 0 \end{bmatrix} \begin{bmatrix} \delta_A \\ \delta_R \end{bmatrix} \quad (4\text{-}16)$$

Figures 4-7 through 4-9 show the validation of the identified linear lateral-directional model. The measured and computed responses for the sideslip angle, roll, and yaw rates are shown.
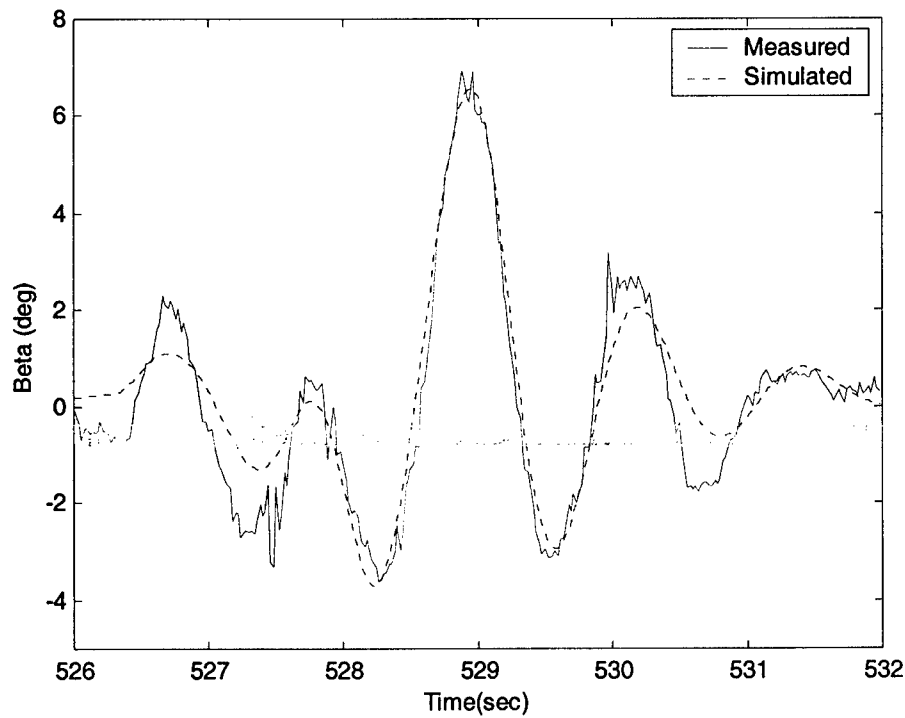
Figure 4-7: Model Validation - Measured and Simulated Sideslip Angle
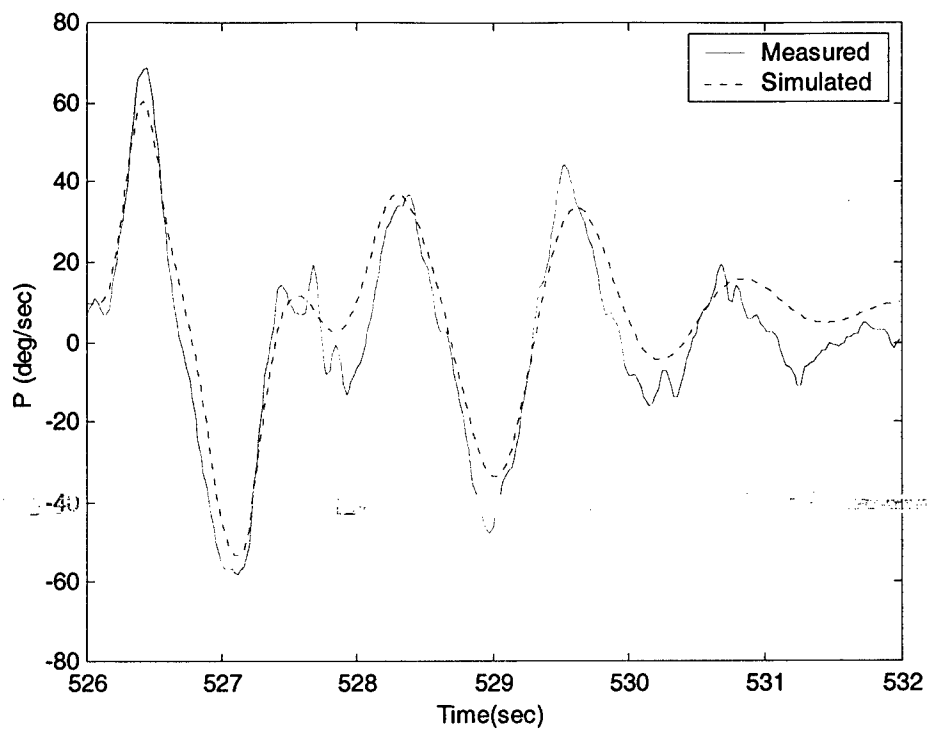
Figure 4-8: Model Validation - Measured and Simulated Roll Rate
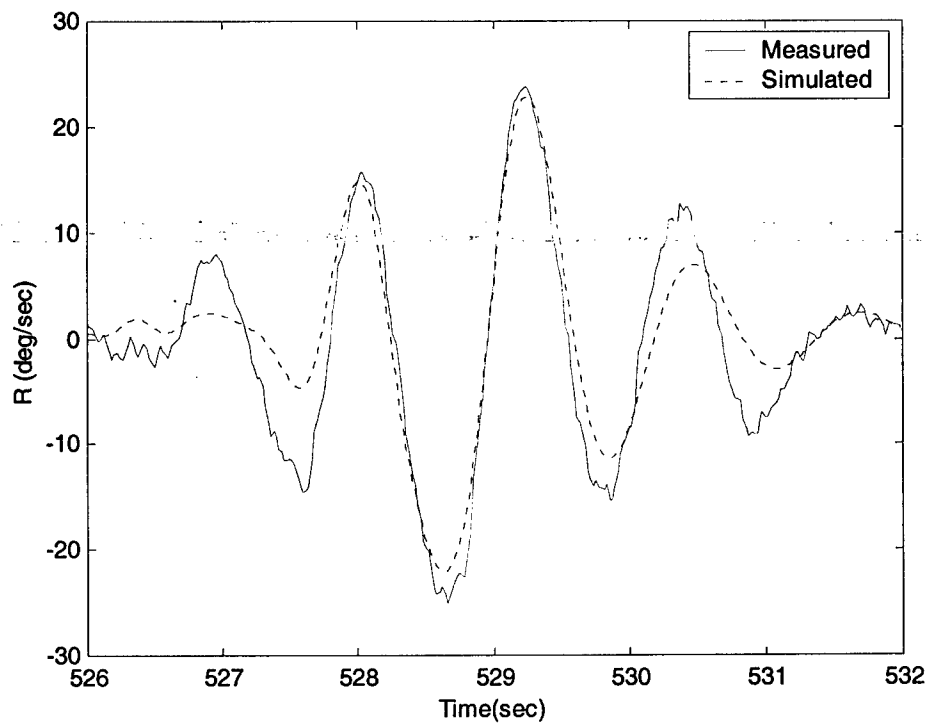
Figure 4-9: Model Validation - Measured and Simulated Yaw Rate

4.2.3 - Engine Model Identification

The task of the engine model identification was to derive a mathematical model describing the input/output relationship of the engine with respect to the throttle command (coming from the computer digital output) to the thrust. This model was later used for the purpose of designing the airspeed control laws.

Figure 4.10 below illustrates the experimental set-up used for the identification of the engine dynamic characteristics. The aircraft engine was mounted on a test bed where the motion was allowed to move only along the thrust force (X) direction. A spring attached to one end of the engine measured the thrust force by reading the displacement of the spring when thrust was acting on it. The displacement of the spring was then measured by a potentiometer with output values provided to a PC data acquisition system, which also provided the throttle commands used by engine ECU.
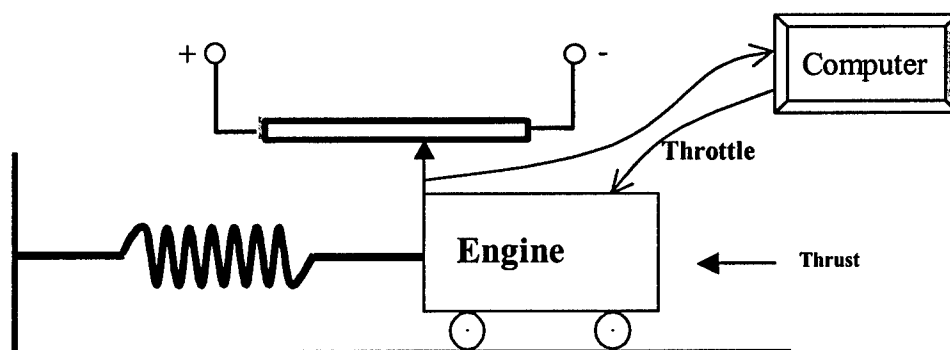
Figure 4-10: Engine Ground Test

Before conducting the engine test, a calibration experiment was performed by reading the spring displacement with a set of object with known weight acting on the spring as calibration force. Table 4.1 shows the data collected from the calibration tests. A standard least square (LS) method was then applied to find the coefficient of the linear equation which fit the measured engine data. The result is as follows:

$$T \ (lb) = 0.008136 \ T' - 136.58 \qquad (4\text{-}17)$$

where T' is the digital reading from the computer.

Weight (lbs)	0	5.44	10.44	15.44	20.44	25.44	30.44
Computer reading	16753	17372	18013	18592	19266	19883	20430

Table 4-1: Engine Ground Testing Stand Calibration

Figure 4.11 shows the data fitting with a linear polynomial.
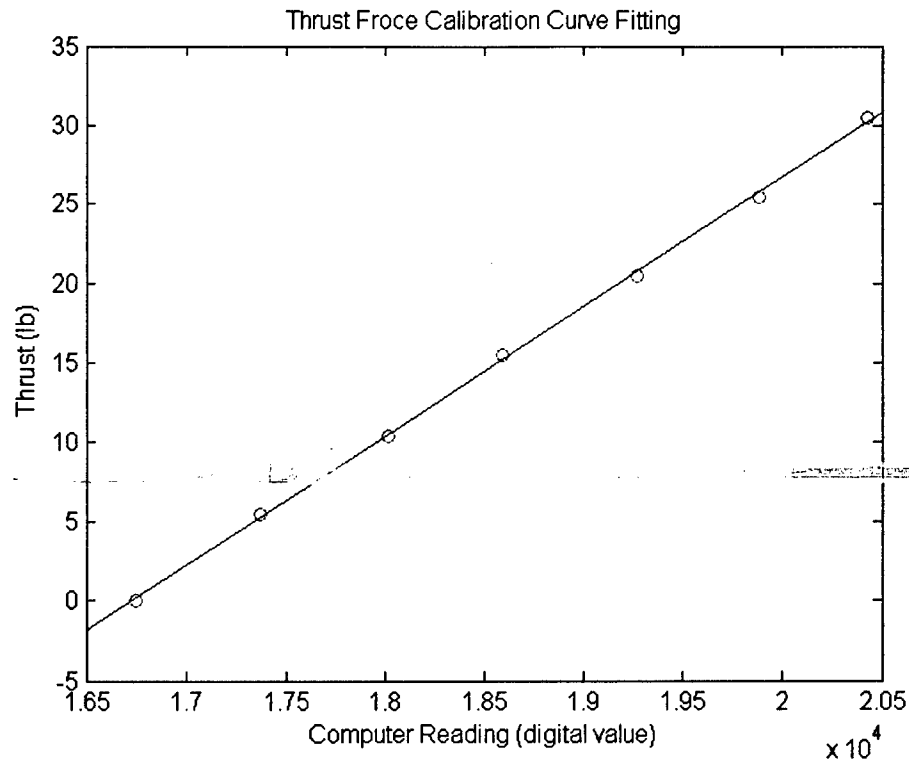
Figure 4-11: Thrust Calibration Using Line Curve Fitting

To test the engine thrust response compared with the input throttle commands, a sequence of designed throttle test signals were sent to the engine ECU through the computer while the engine thrust response was recorded by a PC. Figure 4.12 shows the throttle command along with the measured thrust response (converted from the computer reading to the thrust using the calibration equation outlined above).
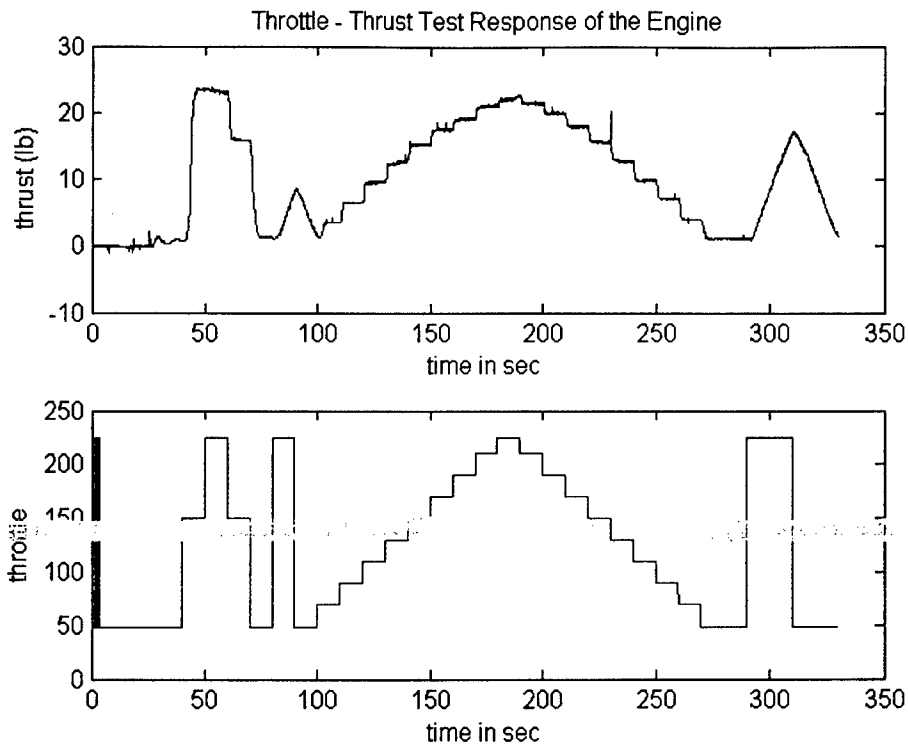
Figure 4-12: Throttle Thrust Response in Test Time Sequence

The throttle test signal consisted of a series of 'step-like' time sequences. The first step in engine model identification was to identify the static gain of the engine response from throttle to thrust. Table 4.2 shows the experiment results obtained with typical throttle input values along with the corresponding thrust values (averaged over a certain period of time).

Throttle	70	90	110	130	150	170	190	210
Thrust (lbs)	3.77	6.84	9.77	12.66	15.38	17.70	19.51	21.23

Table 4-2: Static Throttle - Thrust Response Data

Next, a Least Square-based curve-fitting procedure was applied - as shown in Figure 4-13. For simplicity purposes, a linear fitting was selected.
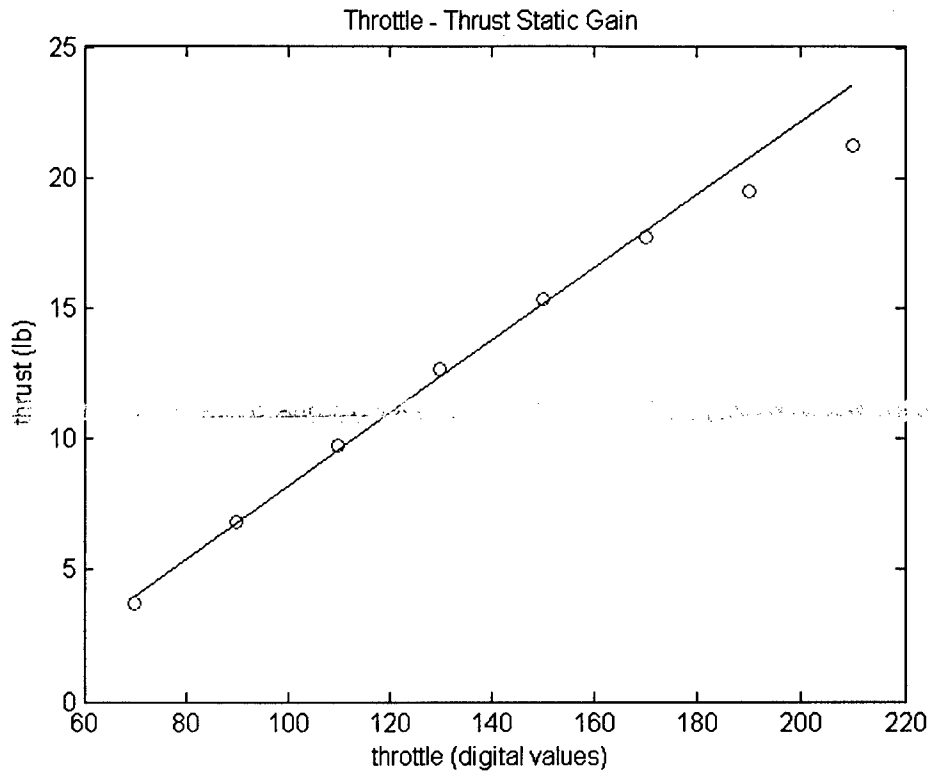
Figure 4-13: Static Throttle - Thrust Response

The resulting linear relationship was found to be:

$$T \ (lb) = 0.14\delta_T - 5.8 \qquad\qquad (4\text{-}18)$$

Next, using Newton's as the unit of the force, the above equation was then converted to:

$$T \ (N) = 0.624\delta_T - 25.86 \qquad\qquad (4\text{-}19)$$

A standard prediction error method - implemented through '*ident*'- a GUI utility within the Matlab® System Identification Toolbox - was applied to selected data segments (between 90 sec to 280 sec) where the throttle input consisted of a series of step-increase/decrease type signals, as shown in Figure 4-12. The identification results show that the engine dynamic response can be modeled by a 'piecewise' 1st order model with a time delay. Furthermore, the time delay can be considered to be a fairly constant value (0.26±0.02 sec) with the time constant in the 1st order model oscillating around 0.25 sec. Therefore, the identified mathematical model of the jet engine is given by:

57

$$G_T(s) = \frac{T(s) - T_0(s)}{\delta_T(s)} = \frac{K_T}{1 + \tau_T s} e^{-\tau_d s} \qquad (4\text{-}20)$$

where T, δ_T denote the thrust (N) and throttle respectively. The constant values are given by:

$$T_0 = -25.86 \text{ (N)}, \; K_T = 0.624, \; \tau_T = 0.25 \text{sec}, \; \tau_d = 0.26 \text{sec} \qquad (4\text{-}21)$$

Figure 4-14 shows the step response of the engine thrust - along with the simulated output - when the throttle input moves with small increments from 110 to 130.
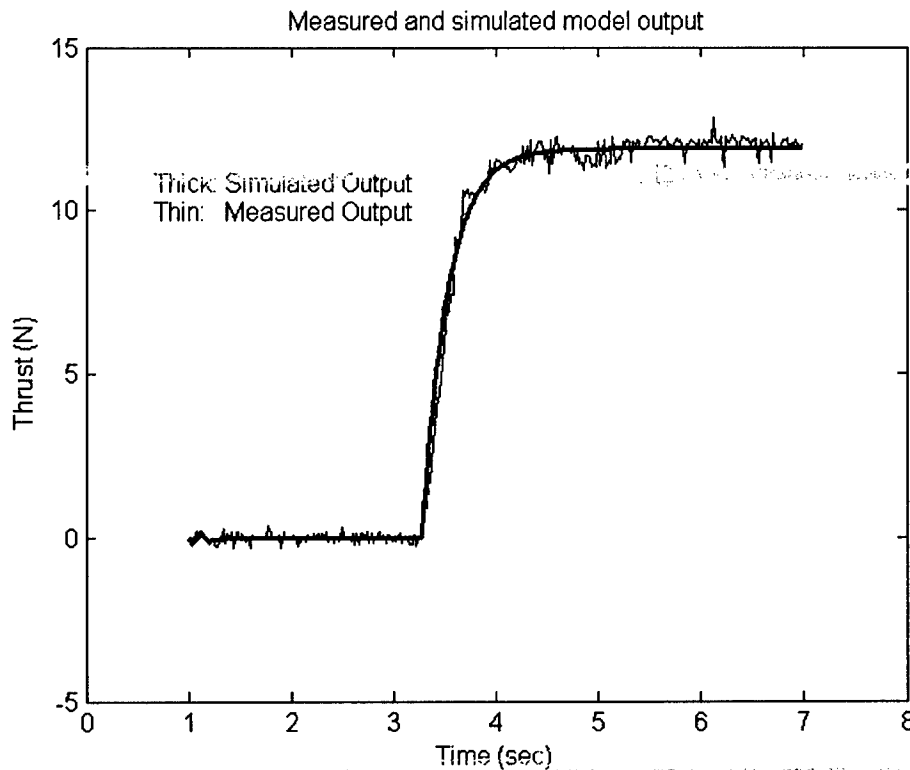
Figure 4-14: Engine Response - Measured and Simulated

After the completion of the ground engine-testing phase, flight experiments were performed to validate the engine mathematical model. The details of these flight tests are discussed in Section 6.5.

58

4.2.4 - Actuator Model Identification

The actuators installed in the aircraft control surfaces were digital servos manufactured by JR Corp. One of the digital servos is shown in Figure 4-15. A mathematical model of the actuator was needed for both controller design and simulation purposes.
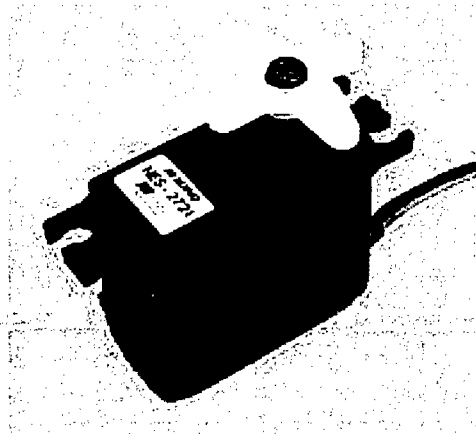
Figure 4-15: R/C Servo

The importance of a good actuator model is due to the fact that the bandwidth of the entire flight control system is mainly dominated by the actuator's bandwidth. Since the command to the actuator's position is elaborated by the OBC through the controller board, the actuator model was defined as the transfer function from the digital command from the computer to the actuator's actual position.

For the PID of the actuator dynamics, a step input was sent to the actuator - through a command supplied from the OBC - while the actuator response was recorded by the OBC. Both the command and data sampling rates were set at 50Hz. The procedure was repeated for all 6 actuators on each of the primary control surfaces (stabilators, ailerons, and rudders). Figure 4-16 represents a typical set of actuator data from the aircraft hardware.
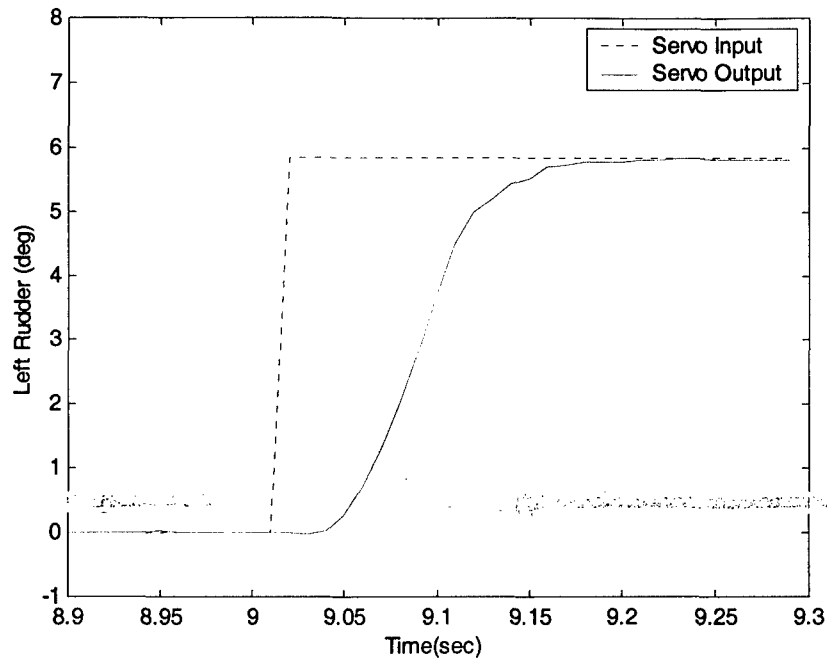
Figure 4-16: Data from Actuator Identification

Thus, from data analysis it was found that the actuator model was described by the following transfer function:

$$G_{Act}(s) = \frac{1}{1 + \tau_a s} e^{-\tau_d s} \qquad (4-22)$$

The time delay constant, τ_d, was measured to be 0.02 sec for all six actuators. τ_a represents the actuator time constant, which takes on different values for each actuator, as listed in Table 4-3.

Left stabilator	Right stabilator	Left rudder	Right rudder	Left aileron	Right aileron
0.0375	0.0294	0.0294	0.0313	0.0424	0.0391

Table 4-3: Actuator Time Constants

Figure 4-17 shows the measured and simulated step response of the identified actuator model.
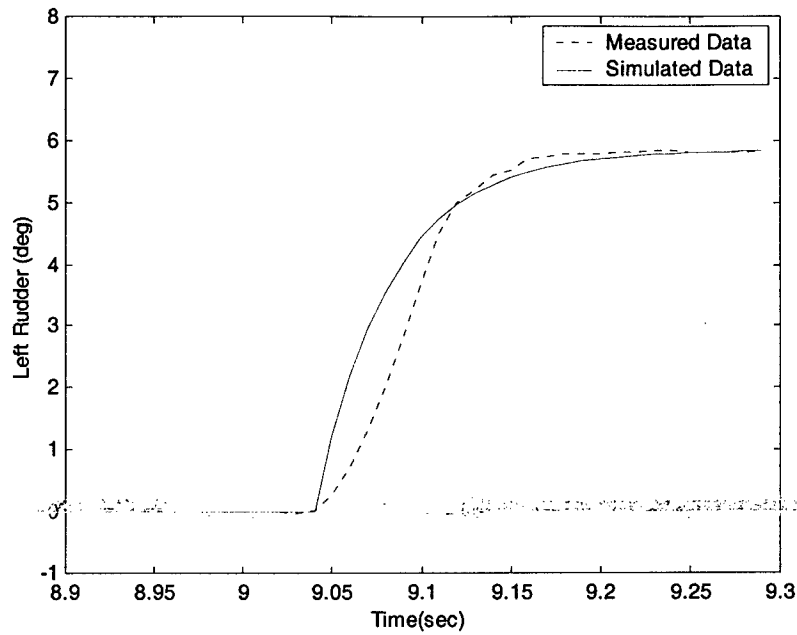
Figure 4-17: Measured and Simulated Actuator Step-Response

The final actuator model was validated using actual flight test data. Sample flight data - shown in Figure 4-18 - was collected during a flight test session conducted on Oct.16th, 2003. The flight data represents the input-output relationship of the left rudder actuator.
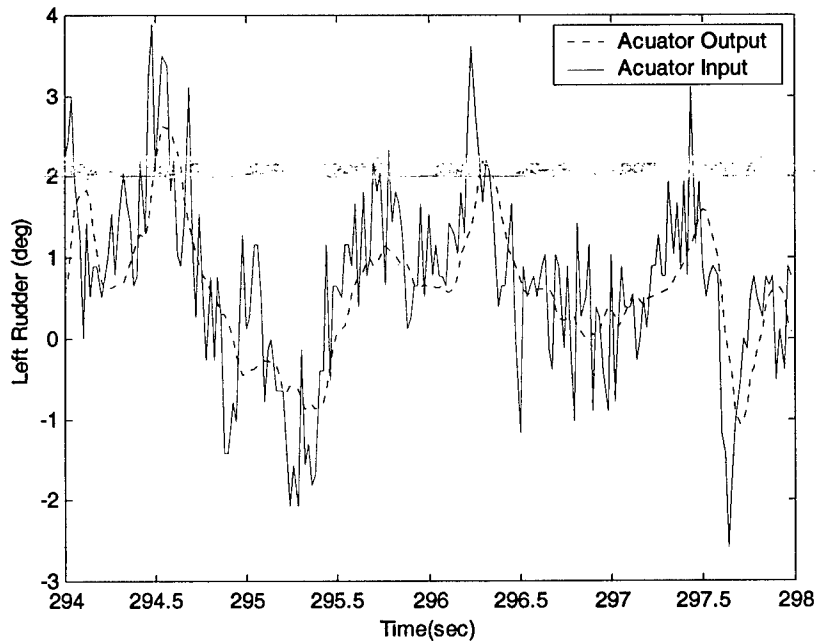
Figure 4-18: In-Flight Actuator's Response

61

As expected, it was clear that the bandwidth of the actuator limited the response of the flight-control system. In fact, the actuator worked as a low pass filter (with delay) and smoothed out the noisy control command caused by the rate-sensor feedback but, still, was able to maintain enough speed to control the aircraft. Simulation testing was performed to simulate the stabilator's actuator response using the estimated actuator model:

$$G_{Act}(s) = \frac{1}{1 + 0.0424s} e^{-0.02s} \qquad (4\text{-}23)$$

Figure 4-19 shows the comparison of the measured and computed actuator's response with the same controller command previously shown in Figure 4-18.
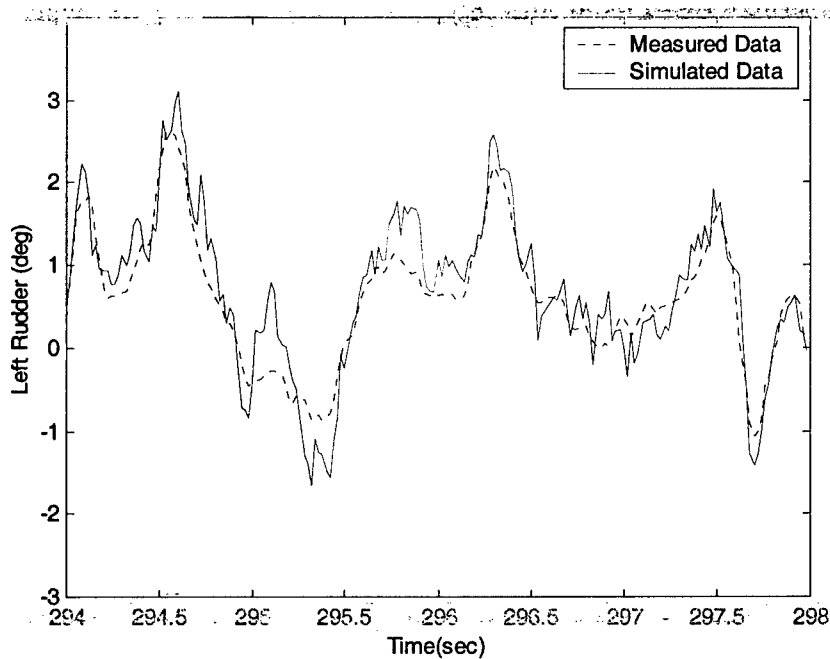
Figure 4-19: Model Validation - Measured and Simulated Actuator In-Flight Response

4.3 - Identification of a Non Linear Model for the WVU YF-22 Aircraft

Although the linear model described above was used for control design purposes, it was decided that the full non-linear mathematical model was required for formation simulation purposes. The PID process for a non-linear dynamic system was clearly more challenging. Most of the non-linear identification tools require a more detailed knowledge of the system dynamics[1] - with respect to simpler linear identification tools - along with the application of minimization algorithms[2]. In general the non-linear model of an aircraft system can be described as[3,4]:

$$
\begin{aligned}
\dot{x} &= f(x, \delta, G, F_A(x, \delta), M_A(x, \delta)); \\
y &= g(x, \delta, G, F_A(x, \delta), M_A(x, \delta));
\end{aligned}
\tag{4-24}
$$

where x is the state vector, y is the output vector, δ is the input vector (surface deflections), G is a vector of geometric parameters and inertia coefficients and F_A and M_A are aerodynamic forces and moments acting on the aircraft. The functions f and g are known as analytic functions modeling the dynamics of a rigid-body system. The aerodynamic forces and moments are expressed using the aerodynamic coefficients[3,4] C_D, C_Y, C_L, C_l, C_m, C_n:

$$
F_A = \overline{q}S \begin{bmatrix} C_D(x, \delta) \\ C_Y(x, \delta) \\ C_L(x, \delta) \end{bmatrix}, M_A = \overline{q}S \begin{bmatrix} bC_l(x, \delta) \\ \overline{c}C_m(x, \delta) \\ bC_n(x, \delta) \end{bmatrix}
\tag{4-25}
$$

The aerodynamic coefficients can be approximated by 'affine' functions of the vectors x and δ. For example, the 'lift coefficient' function can be described by:

$$
C_L(x, \delta) = C_{L0} + C_{La}\alpha + C_{Lq}q + C_{Li_H}i_H + \dots
\tag{4-26}
$$

where the individual coefficients are referred to as 'lift stability derivatives'.

An accurate estimate of the aircraft inertial data (vector G in Eqn. 4-24) was first required. Two methods are typically used for this purpose. The first method estimates values from design data[5] while the second method features a pendulum based experimental setup[6,7]. The first method required detailed information about the specific weight of each of the structural components. Since several layers of different composite materials were used for the construction of the models, it was difficult to estimate correctly the specific weights. Therefore, the pendulum-based method was used to determine the inertial characteristics of the WVU YF-22 aircraft. Table 4.4 provides the resulting values of the inertial parameters of the WVU YF-22 model. Note that the values were measured with a 60% fuel capacity.

Parameter	Value	Units
I_{xx}	1.61	$Kg\ m^2$
I_{yy}	7.51	$Kg\ m^2$
I_{zz}	7.18	$Kg\ m^2$
m	20.63845	Kg

Table 4-4: WVU YF-22 Inertial Data (Note: 60% Fuel Loading)

Note that the product of inertia I_{xz} could not be evaluated using the pendulum-based experimental method. The determination of I_{xz} will be described next.

The next critical issue was to evaluate the aerodynamic derivatives for the UAV. The relationships for deriving the coefficients of the matrices in the linear models - as described by Eqns. 4-10 through 4-16 - from the values of the aerodynamic derivatives and geometric-inertial parameters are well known[8]. By inverting these relationships and using the experimental values of the geometric and inertial parameters it was possible to calculate the initial values for each of the aerodynamic stability derivatives from the matrices in Eqns. 4-10 and 4-16. Next, a parameter optimization scheme based on routines available from the Matlab® Optimization Toolbox was introduced. Specifically, a Matlab® code was developed to find the *RMS* of the difference between the 'actual' and 'simulated' aircraft outputs. The *"fmincon"* function, which features a constrained optimization of a multivariable function using a Sequential Quadratic Programming (SQP) technique[9], was then used to find the set of aerodynamic derivatives – along with the product of inertia I_{xz} - providing the best fit with the flight data starting from the initial set of aerodynamics derivatives calculated from the linear models. It should be emphasized that the selection of the cost function has to be performed carefully to avoid local minima problems. Particularly, the selected cost function contained three components, that is a term modeling the *RMS* of the deviation between the real and predicted output, a frequency based term expressing the lowest spectral components of the deviation, and a term expressing the difference between the current linearized model (obtained by performing a numerical linearization algorithm on the current non-linear model) and the 'baseline' linear model in Eqns. 4-10 and 4-16. A final validation of the non-linear model was then conducted using the validation flight data set, as it was performed for the linear mathematical model. Figure 4-20 shows a substantial agreement between the measured and computed data.
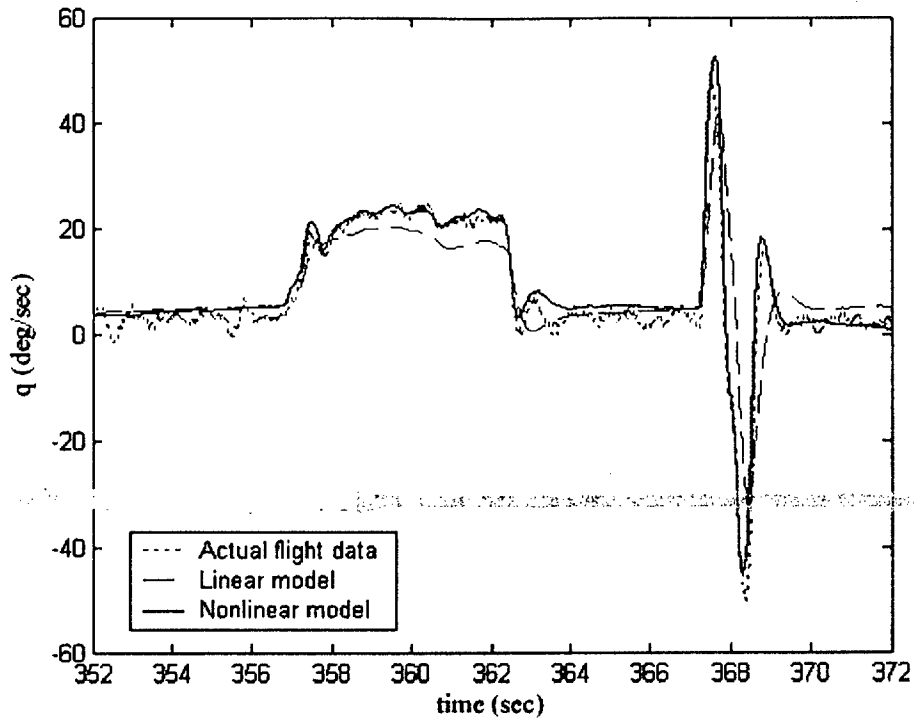
Figure 4-20: Linear and Non-linear Models Compared to Actual Flight Data

The resulting non-linear mathematical model is given by:

Geometric and Inertial Data (with a 60% fuel capacity)

$c = 0.76$ m, $b = 1.96$ m, $S = 1.37$ m^2

$Ixx = 1.6073$ Kg m^2, $Iyy = 7.51$ Kg m^2, $Izz = 7.18$ Kg m^2, $Ixz = -0.24$ Kg m^2

$m = 20.64$ Kg, $T = 54.62$ N

Longitudinal Aerodynamic Derivatives

$C_{D0} = 0.008$, $C_{D\alpha} = 0.507$, $C_{Dq} = 0$, $C_{DiH} = -0.033$

$C_{L0} = -0.049$, $C_{L\alpha} = 3.258$, $C_{Lq} = 0$, $C_{LiH} = 0.189$

$C_{m0} = 0.022$, $C_{m\alpha} = -0.473$, $C_{mq} = -3.449$, $C_{miH} = -0.364$

Lateral-directional Aerodynamic Derivatives

$C_{Y0} = 0.016$, $C_{Y\beta} = 0.272$, $C_{Yp} = 1.215$, $C_{Yr} = -1.161$, $C_{Y\delta A} = 0.183$, $C_{Y\delta R} = -0.459$

$C_{l0} = -0.001$, $C_{l\beta} = -0.038$, $C_{lp} = -0.213$, $C_{lr} = 0.114$, $C_{l\delta A} = -0.056$, $C_{l\delta R} = 0.014$

$C_{n0} = 0$, $C_{n\beta} = 0.036$, $C_{np} = -0.151$, $C_{nr} = -0.195$, $C_{n\delta A} = -0.035$, $C_{n\delta R} = -0.055$

4.4 - Formation Geometry

As described above, the formation flight control problem can be decomposed into two decoupled problems, that is horizontal tracking (level plane) and vertical tracking, as shown in Figure 4-21.
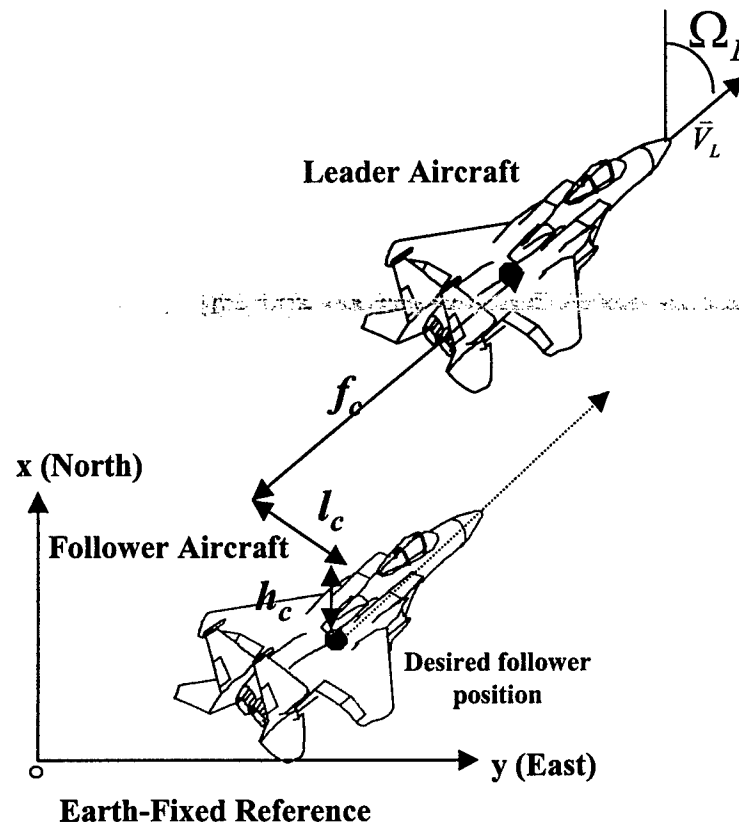
Figure 4-21: 3D Formation Geometry

For navigation purposes, the position and velocity of both 'leader' and 'follower' were expressed with respect to a pre-defined earth-fixed inertial reference frame and are measured by the on-board GPS receivers.

4.4.1 - Horizontal Geometry (Level Plane)

The pre-defined formation geometric parameters were the forward clearance, f_c, and lateral clearance, l_c, as defined in Figure 4.21. The forward distance error, f, and lateral distance error, l, could be calculated from position and velocity data using the following relationship:

$$\begin{bmatrix} l \\ f \end{bmatrix} = \begin{bmatrix} \sin(\chi_L) & -\cos(\chi_L) \\ \cos(\chi_L) & \sin(\chi_L) \end{bmatrix} \begin{bmatrix} x_L - x \\ y_L - y \end{bmatrix} - \begin{bmatrix} l_c \\ f_c \end{bmatrix} \qquad (4\text{-}27)$$

where χ_L is the azimuth angle for the 'leader'. The trigonometric expressions for the azimuth angle was given as:

$$\cos(\chi_L) = \frac{V_{Lx}}{\sqrt{V_{Lx}^2 + V_{Ly}^2}} \qquad \sin(\chi_L) = \frac{V_{Ly}}{\sqrt{V_{Lx}^2 + V_{Ly}^2}} \qquad (4\text{-}28)$$

Note that the (2 x 2) matrix in Eqn. 4-27 above is a rotation matrix allowing for a transformation of the axis from an earth fixed inertial reference frame to a reference frame oriented with the velocity of the 'leader'. V_{Lx}, and V_{Ly} represent the projections of the 'leader' velocity along the x and y axes of the earth fixed reference frame.

4.4.2 - Vertical Geometry

The vertical distance error, h, could be simply obtained as:

$$h = z_L - z - h_c \qquad (4\text{-}29)$$

where the vertical distance clearance, h_c, is also shown in Figure 4.21.

4.5 - Design of the Formation Control Laws

The formation control problem could be modeled as a non-linear control problem in which the controller acted on the throttle, stabilators, and ailerons/rudder commands to minimize the distance errors l, f, and h. Both the lateral-directional and vertical controllers were based on an inner loop controller (used for pitch and roll angle tracking) and an outer loop controller (used for lateral-directional and height tracking). The design of the outer and inner loop control laws for the 'follower' aircraft systems will be described next.

4.5.1 - Design of Outer Loop Controller

The outer loop controller consisted of two components, that is the 'vertical' controller and the 'horizontal' controller.

The 'vertical' controller was a simple linear altitude control. Its inputs were the vertical distance and its rate of change. The output was given by the desired pitch angle:

$$\theta_d = K_z h + K_{zs} \dot{h} \qquad (4\text{-}30)$$

This desired pitch angle was then taken as a reference signal by the longitudinal inner loop controller.

The 'horizontal' controller was a NLDI based controller. Its inputs were the lateral and the forward errors along with their time derivatives. The outputs were given by the throttle and desired roll angle (ϕ).

$$\begin{bmatrix} \delta_T \\ \phi_d \end{bmatrix} = f(\chi - \chi_L, \begin{bmatrix} f \\ l \end{bmatrix}, \begin{bmatrix} \dot{f} \\ \dot{l} \end{bmatrix}) \qquad (4\text{-}31)$$

The desired roll angle was then used as a reference signal by the lateral inner loop controller while the throttle value was used directly as a control command. In other words, the task of the inner loop control was to 'track' the desired pitch and roll angles - which were then calculated by the outer loop controller. The use of an NLDI-based control was deemed necessary to cope with the non-linear kinematics associated with the high bank angles flight conditions.

The NLDI control approach aimed at canceling the non-linearities in the system dynamics by using (output) feedback linearization[10-11]. Under some assumptions[10], this control method reduced the nonlinear system to a series of integrators, which could then be controlled using a set of simple linear techniques. For this specific guidance problem, the non-linear system featured the forward and lateral distance errors f and l as outputs. The desired bank angle, ϕ_d, and throttle command, δ_T, were the inputs. According to the output feedback linearization technique[10], the outputs should be derived until the inputs explicitly appear in the expression. The relationship among inputs and derivatives of the outputs was then inverted. For this problem, the first and second derivatives of the outputs were defined as:

68

$$\begin{bmatrix} \dot{\ell} \\ \dot{f} \end{bmatrix} = \begin{bmatrix} V_{xy}\sin(\chi-\chi_L) \\ V_{Lxy} - V_{xy}\cos(\chi-\chi_L) \end{bmatrix} + \Omega_L \begin{bmatrix} f \\ -\ell \end{bmatrix}$$

$$\begin{bmatrix} \ddot{\ell} \\ \ddot{f} \end{bmatrix} = \begin{bmatrix} V_{xy}\cos(\chi-\chi_L) & \dfrac{V_{xy}}{V}\omega_1\sin(\chi-\chi_L) \\[2mm] V_{xy}\sin(\chi-\chi_L) & -\dfrac{V_{xy}}{V}\omega_1\cos(\chi-\chi_L) \end{bmatrix} \begin{bmatrix} \dfrac{g}{V}\tan(\phi_d) \\[2mm] T_b + K_T\delta_T \end{bmatrix} \qquad (4\text{-}32)$$

$$+ \frac{V_{xy}}{V}\omega_2 \begin{bmatrix} -\sin(\chi-\chi_L) \\ \cos(\chi-\chi_L) \end{bmatrix} - \Omega_L V_{xy}\begin{bmatrix} \cos(\chi-\chi_L) \\ \sin(\chi-\chi_L) \end{bmatrix} + \dot{\Omega}_L \begin{bmatrix} f \\ -\ell \end{bmatrix} + \Omega_L\begin{bmatrix} \dot{f} \\ -\dot{\ell} \end{bmatrix}$$

where: $\omega_1 = \dfrac{1}{m}\cos\alpha\cos\beta$, and $\omega_2 = \dfrac{\bar{q}S}{m}\left(c_D\cos\beta - c_Y\sin\beta\right) + g\sin\gamma$

Note, that a coordinated turn condition was assumed for both the 'leader' and 'follower' aircraft. This condition could be described by the following relationship:

$$\Omega = \dot{\chi} \cong \dot{\psi} \cong \frac{g}{V}\tan\phi \qquad (4\text{-}33)$$

Also note that both ϕ_d and δ_T appear as inputs in Eqn. 4-32, and that the (2 x 2) matrix relating the inputs and the 2nd order derivatives of the output is invertible. Therefore, by inverting Eqn. 4-32 and replacing $\ddot{f}$ and $\ddot{\ell}$ respectively with $\ddot{f}_d$ and $\ddot{\ell}_d$ - which were the desired values for the double derivatives of f and l - the following was derived:

$$\begin{bmatrix} \dfrac{g}{V}\tan(\phi_d) \\[2mm] T_b + K_T\delta_T \end{bmatrix} = \frac{1}{V_{xy}}\begin{bmatrix} \cos(\chi-\chi_L) & \sin(\chi-\chi_L) \\[2mm] \dfrac{V}{\omega_1}\sin(\chi-\chi_L) & -\dfrac{V}{\omega_1}\cos(\chi-\chi_L) \end{bmatrix}\begin{bmatrix} \ddot{\ell}_d \\[2mm] \ddot{f}_d \end{bmatrix}$$

$$+ \begin{bmatrix} \Omega_L \\[1mm] \dfrac{\omega_2}{\omega_1} \end{bmatrix} + \begin{bmatrix} \ell\sin(\chi-\chi_L) - f\cos(\chi-\chi_L) \\[2mm] -\dfrac{V}{\omega_1}\dot{\ell}\cos(\chi-\chi_L) - \dfrac{V}{\omega_1}\dot{f}\sin(\chi-\chi_L) \end{bmatrix}\dfrac{\Omega_L}{V_{xy}} \qquad (4\text{-}34)$$

$$+ \begin{bmatrix} \ell\sin(\chi-\chi_L) - f\cos(\chi-\chi_L) \\[2mm] -\dfrac{V}{\omega_1}\ell\cos(\chi-\chi_L) - \dfrac{V}{\omega_1}f\sin(\chi-\chi_L) \end{bmatrix}\dfrac{\dot{\Omega}_L}{V_{xy}}$$

By imposing $\alpha = \alpha_0$, $\beta = 0$, $\Omega_L = $ constant, the lateral NLDI control law was found to be:

$$\phi_d = \arctan\left\{ \frac{1}{g\cos\gamma}\left[\ddot{\ell}_d\cos(\chi-\chi_L) + \ddot{f}_d\sin(\chi-\chi_L)\right] \right.$$

$$\left. + \frac{V}{g}\Omega_L + \left[\ell\sin(\chi-\chi_L) - f\cos(\chi-\chi_L)\right]\frac{\Omega_L}{g\cos\gamma} \right\} \qquad (4\text{-}35)$$

69

The NLDI control law on the forward channel was found to be:

$$\delta_T = \frac{m}{K_T \cos\gamma}\left[\ddot{\ell}_d \sin(\chi - \chi_L) - \ddot{f}_d \cos(\chi - \chi_L)\right]$$

$$+\frac{1}{K_T}\left(\frac{1}{2}\rho_0 V^2 S\left(C_{D0} + C_{D\alpha}\alpha_0\right) + m\sin\gamma - T_b\right) \qquad (4\text{-}36)$$

$$-\frac{m}{K_T \cos\gamma}\Omega_L\left[\dot{\ell}\cos(\chi - \chi_L) + \dot{f}\sin(\chi - \chi_L)\right]$$

The application of the inputs $[\delta_T, \phi_d]$ in Eqns. 4-35 and 4-36 to the system described by Eqn. 4-32 ultimately canceled the non-linearities (assuming no uncertainties) leading to:

$$\begin{bmatrix}\ddot{\ell}\\ \ddot{f}\end{bmatrix} = \begin{bmatrix}\ddot{\ell}_d\\ \ddot{f}_d\end{bmatrix} \qquad (4\text{-}37)$$

The above system was essentially a linear system consisting of two channels, each featuring two integrators in series. This system could then be controlled using a conventional linear control law:

$$\ddot{\ell}_d = -\tilde{K}_{\ell s}\dot{\ell} - \tilde{K}_\ell \ell$$
$$\ddot{f}_d = -\tilde{K}_{fs}\dot{f} - \tilde{K}_f f \qquad (4\text{-}38)$$

The values for the above gains were selected so that the controller could be locally equivalent to a previously designed linear controller[11]. The resulting values were found to be:

$$\tilde{K}_\ell = 0.2027, \quad \tilde{K}_{\ell s} = 0.8894$$
$$\tilde{K}_f = 0.2419, \quad \tilde{K}_{fs} = 2.0560 \qquad (4\text{-}39)$$
$$K_z = 3.2254, \quad K_{zs} = 1.7593$$

4.5.2 - Design of the Lateral Inner Loop Controller

The lateral inner loop controller acted as a linear controller tracking a desired bank angle (provided from the outer loop controller) and augmented the lateral-directional stability of the aircraft using the relationships:

$$\delta_A = K_p p + K_\phi (\phi - \phi_d) \tag{4-40}$$

$$\delta_R(s) = K_r \frac{s}{s + \omega_0} r(s) \tag{4-41}$$

Yaw rate feedback gain and washout filter constant

The uncompensated 'open-loop' dutch-roll damping ratio was found to be 0.192. The design objective was to increase the 'closed-loop' dutch-roll damping ratio through an appropriate selection of both the yaw rate feedback gain K_r and the washout filter constant ω_0. A root-locus analysis – shown in Figure 4-22 - provided the following values for the gains:

$$\omega_0 = 0.18, \quad K_r = 0.16 \tag{4-42}$$

The resulting 'compensated' dutch-roll damping ratio was 0.7 with a natural frequency of 7.47.
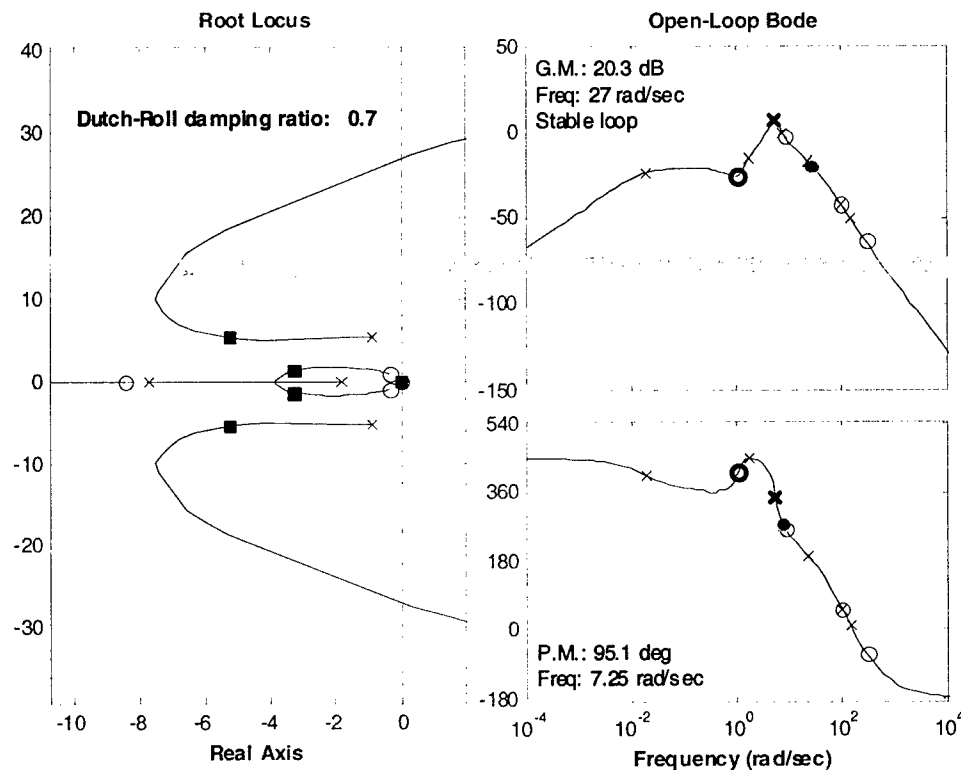
Figure 4-22: Yaw Rate Feedback Gain/Washout Filter Constant Design

Roll angle/rate feedback gains

The objective for the roll rate/angle feedback gains was to make the roll angle feedback gain as large as possible with the goal of achieving desirable disturbance attenuation along with desirable roll tracking capability while maintaining a reasonable stability margin and damping ratio. This was achieved by tuning the roll rate/angle feedback gains. In this design, the yaw rate feedback loop was closed. The roll rate/angle feedback gains were selected to be:

$$K_p = 0.04, \quad K_\phi = 0.35 \qquad (4\text{-}43)$$

Figure 4-23 shows the root locus and Bode diagram, the damping ratio, and the stability gain/phase margins (denoted as G.M and P.M respectively).
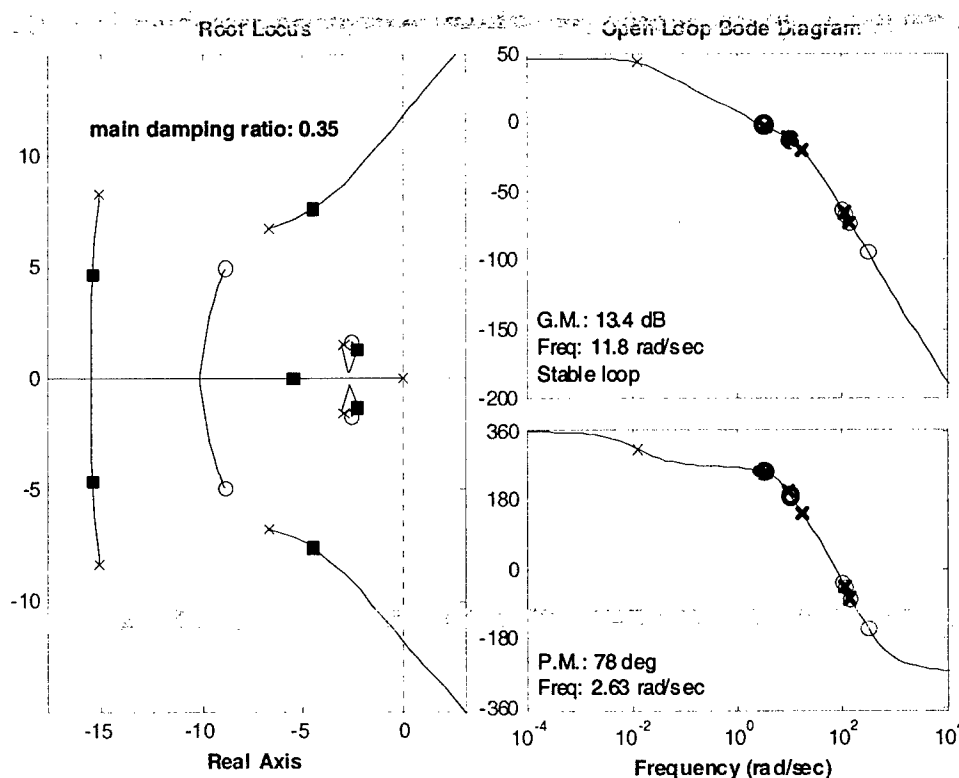
Figure 4-23: Roll Rate/Angle Feedback Gains Design

Note that the selected gains provided a 'closed-loop' damping coefficient around 0.7.

4.5.3 - Longitudinal Control Design

The longitudinal inner loop controller acted as a linear controller tracking a desired pitch angle (provided from the outer loop controller) using the following relationship:

$$\delta_{i_H} = K_q q + K_\theta (\theta - \theta_d) \tag{4-44}$$

To achieve desirable disturbance attenuation along with desirable pitch angle tracking, the design objective for the pitch rate/angle feedback gains was to make the pitch angle feedback gain as large as possible while maintaining a reasonable stability margin and damping ratio. This was achieved by coordinately adjusting the pitch rate/angle feedback gain pair. The final pitch rate/angle feedback gains were:

$$K_q = 0.12, \quad K_\theta = 0.50 \tag{4-45}$$

The relative root locus, Bode diagram, short-period damping ratio, and stability margins are shown in Figure 4-24.
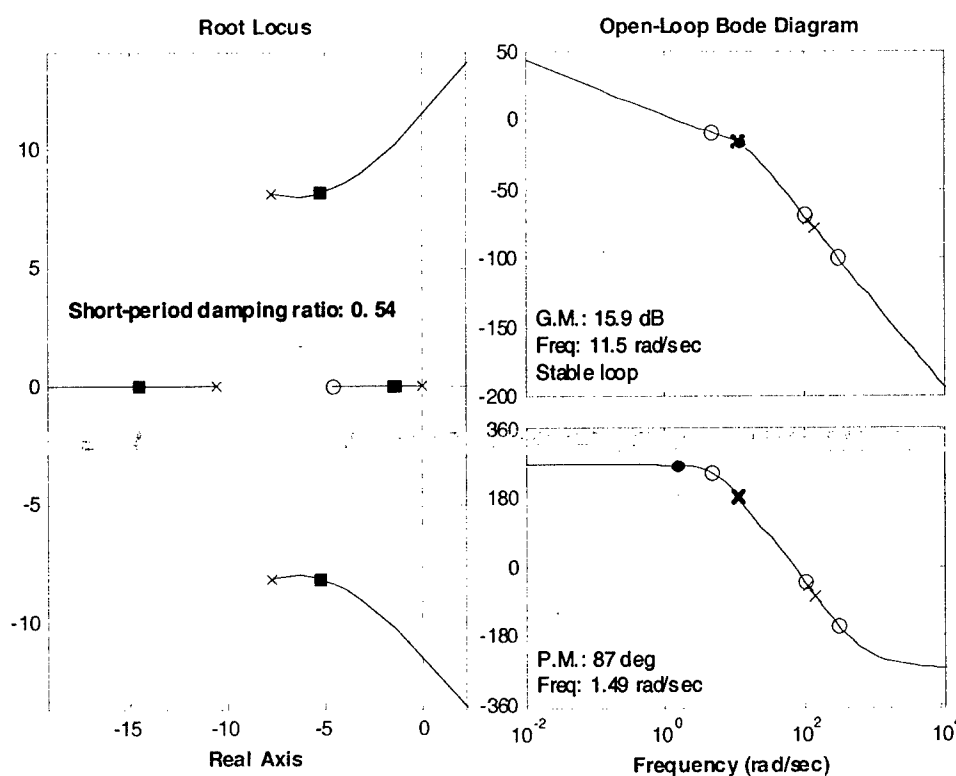
Figure 4-24: Pitch Rate/Angle Feedback Gains Design

4.6 - Controller Validation Through Flight Testing (Inner Loop)

A series of flight tests was performed to test the longitudinal and lateral inner loop control law design. An example of the inner-loop controller test was to have the aircraft manually operated initially. Then, a pilot induced input was executed to excite the aircraft dynamics. Next, the controller was activated and the computer system 'intentionally' brought the aircraft back a pre-defined (straight-level flight) flight condition. Through the pitch and roll angle flight data, the controller performance was evaluated by comparing the measured and simulated responses.

Figures 4-25 and 4-26 show the aircraft attitude (pitch and roll angle) responses starting from the initial condition at the moment the controller is switched on. From the figures it can be seen that the measured and simulated responses matched fairly well.
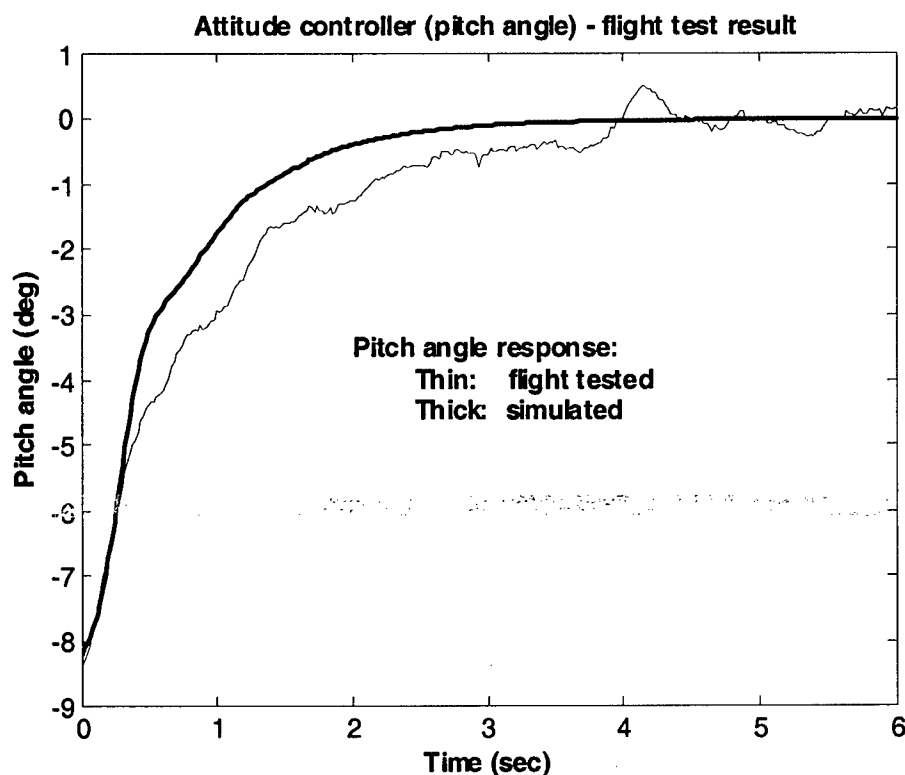
Figure 4-25: Controller Validation Through Flight - Inner Loop (Pitch Attitude)
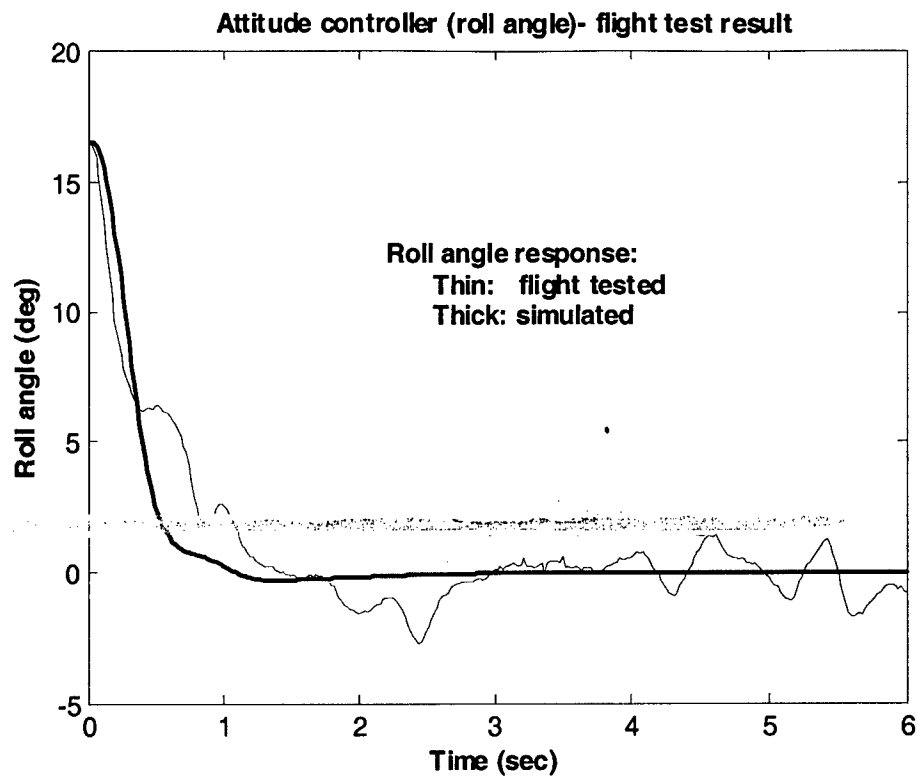
Figure 4-26: Controller Validation Through Flight - Inner Loop (Roll Attitude)

4.7 - Development of a Formation Flight Simulation Environment

A Simulink® simulation environment using the mathematical model obtained from flight data for the WVU YF-22 aircraft along with the formation control laws - as described in the previous sections - was developed. The general Simulink architecture is shown in Figure 4-27. The simulation environment provided a platform for development and initial testing of each control law, prior to performing individual flight tests.
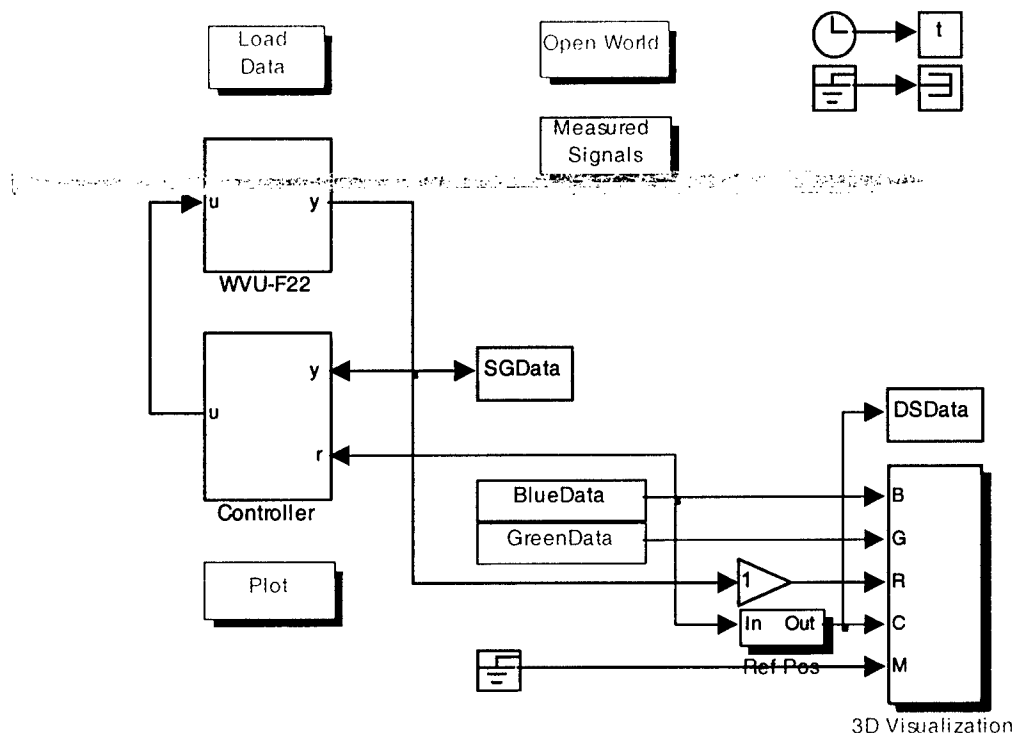
Figure 4-27: Simulink Simulation Environment

The overall schemes were interfaced with the Matlab® Virtual Reality Toolbox (VRT). Essentially, the VRT allowed for objects and events of a virtual world (coded in VRML 2.0 or higher[12]) to be driven by signals from a Matlab®/Simulink® simulation scheme. A sample image from the VRT-based simulator, shown in Figure 4-28, displays a view of 'follower' aircraft following the 'leader'.
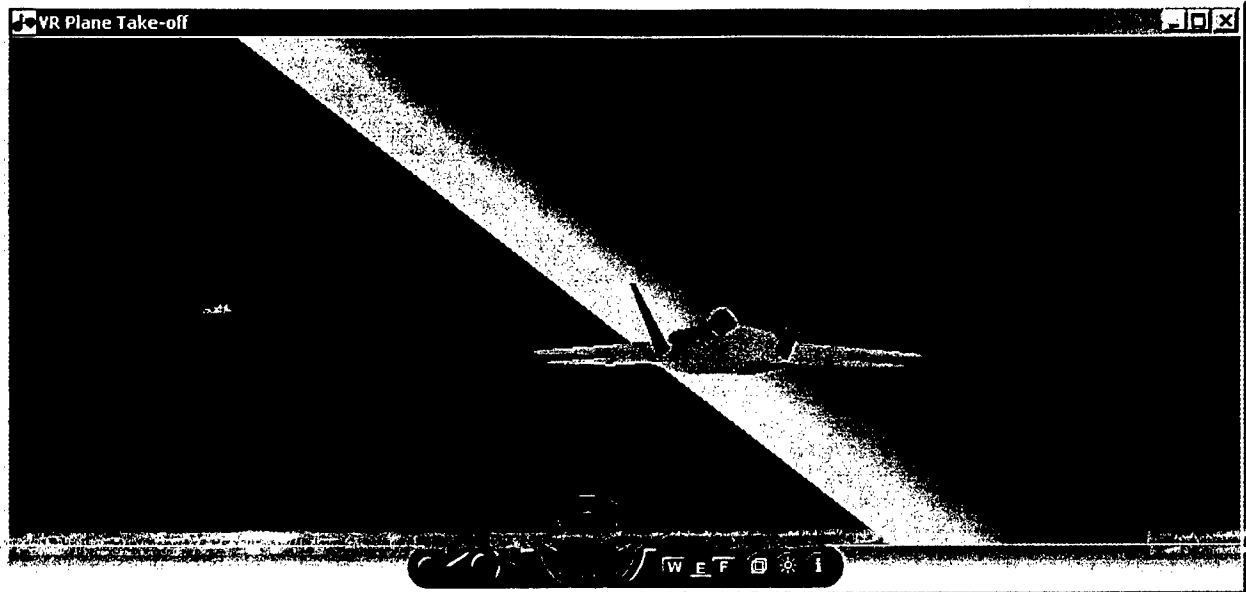
Figure 4-28: Image from the 'Formation Flight' Simulator (View Behind 'Follower')

Several simulation studies were conducted for evaluating, testing, modifying and optimizing the formation flight controller and assessing the sensitivity to various configuration parameters. Once fully simulated, the formation control modules were then compiled using Matlab® Real Time Workshop (RTW) to generate real-time executable software. This software was then uploaded to the OBC for flight test evaluation.

Chapter 5 - On-board Software

5.1 - Flight Control Software Architecture

With the formation controller design completed and the on-board hardware installed, focus was directed toward the on-board software required for implementing the control laws. The on-board software had to provide an interface between the actual hardware controller and additional on-board systems. As with any flight control software, it must be suitable for real time implementation. Matlab® Real-Time Workshop (RTW) was selected to generate the real-time target used for the UAV fleet. Simulink®, which provided the simulation environment, also provided the development environment and interface. Specifically, the on board software was implemented as several Simulink blocks with all the hardware drivers written in C as Matlab® 'S-functions'.

Once simulation testing was completed for a particular test, an executable program was compiled (via RTW) as a real-time DOS target for flight test evaluation onboard the aircraft hardware. The DOS operating system was selected for use with the flight computer due to its simplicity. Both the operating system and on-board software were stored in the 8 MB compact flash card – shown in Figure 3-15 - which also acted as a self-supporting bootable device. All software components were developed as individual modules and easily configured for various flight-testing activities.

The UAV software was designed to perform data acquisition, communication, execution of control laws, and implementation of the OBC-generated control commands. The following 10 requirements were used to define the overall software architecture:

1. Reliability;
2. 'Real time' performance;
3. System sampling rate no slower than 25Hz;
4. Data acquisition from all sensors and conversion into engineering units;
5. Data communication with other aircrafts;
6. Execute control laws on-board;
7. Provide control command and control channel selection signals;
8. Store data for post flight analysis;

9. Ability to be reconfigured for different flight task at the flight testing facility (without recompiling);

10. Automatically update calibration data at the field (without recompiling).

5.2 - Selected Architecture

With the system requirements defined from Section 5.1, the on-board software was designed to have three major subsystems:

1. Data acquisition (DAQ);

2. Data communication;

3. Formation flight control;

The data acquisition software acquired sensor signals from analog I/O module, which then converted the analog voltage signals into 16-bit digital signals. This raw voltage measurement was then calibrated to generate meaningful engineering values used by the controller software.

The data communication software performed the information transfer between each aircraft. The GPS information of the 'leader' provided to each 'follower' aircraft, which, in turn, was used by the formation flight controller.

The formation flight control software received - as inputs – the flight data acquired through both the DAQ software and relayed 'leader' GPS information. The formation controllers described in Chapter 4 were executed in real-time for flight test evaluation. The control commands generated by the formation control laws were calibrated and sent to the servo control hardware. A block diagram of the on-board software, shown in Figure 5-1, provides a layout of the various software modules.
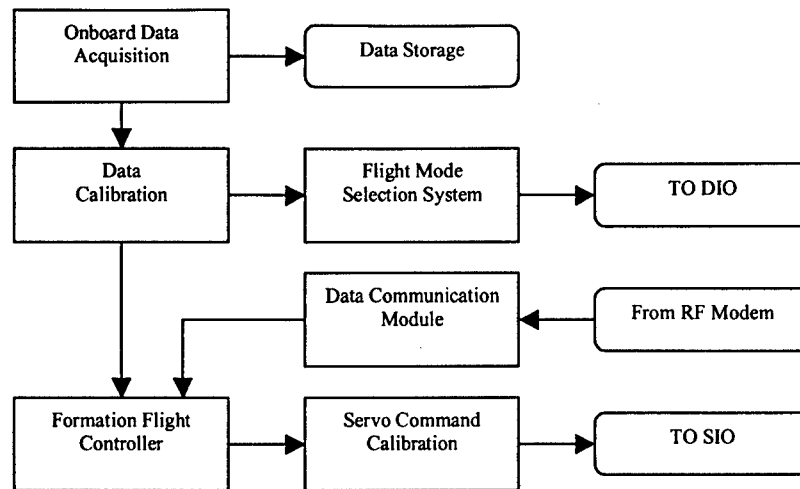
Figure 5-1: On-Board Software

A detailed description of each software component is provided in Sections 5.3 through 5.7.

5.3 - Data Acquisition Software

The main purpose of the DAQ software was to collect, convert, send, and store sensor readings from the electronic payload. Development of this software was based upon using the Diamond-MM-32 PC/104 format 16-bit analog I/O module.

Analog Input Channels

The DAQ Diamond board was capable of 32 analog I/O channels. Only 22 analog I/O channels were actually used with the on-board aircraft system. Table 5-1 provides a list of the data acquisition channels.

Number	Channel Name	Sensor/Notes
1	Static Pressure	Nose Probe
2	Dynamic Pressure	Nose Probe
3	Alpha	Nose Probe
4	Beta	Nose Probe
5	Temperature	Temperature Sensor
6	Roll Angle	Vertical Gyro
7	Pitch Angle	Vertical Gyro
8	Left Aileron	Potentiometer
9	Left Rudder	Potentiometer
10	Left Stabilator	Potentiometer
11	Right Aileron	Potentiometer
12	Right Rudder	Potentiometer
13	Right Stabilator	Potentiometer
14	Control Switch	Manual/Automatic Control
15	Throttle Reading	Receiver
16	Command Switch	Voltage Reference
17	Acceleration X	IMU
18	Acceleration Y	IMU
19	Acceleration Z	IMU
20	P	IMU
21	Q	IMU
22	R	IMU

Table 5-1: Data Acquisition Channels

Input Ranges and Resolution

All sensors had an output range within ±10V. Therefore all analog I/O channels were configured to accept ±10V bipolar inputs. With the 16-bit A/D conversion, the resolution of the data acquisition is 305 µV, which was deemed to be accurate for data analysis and control purposes.

A/D Conversion Formulas

The 16-bit value returned by the A/D converter was an integer ranging from -32768 to 32767, regardless of the input range. The input signal was magnified and shifted to match this range before it reached the A/D conversion. The calculation of the bipolar input range used the following format:

FS = full-scale voltage (e.g. 10 for ±10V range)

Input voltage = (A/D code / 32768) x FS

A/D Conversion

There were a total of 7 steps involved in performing the A/D conversion:

Step #1: Selection of the input channel or input channel range;

Step #2: Selection of the analog input range (range, polarity, and gain codes);

Step #3: Wait for analog input circuit to settle;

Step #4: Start an A/D conversion on the current channel;

Step #5: Wait for the conversion to finish;

Step #6: Read the A/D data;

Step #7: Convert the numerical data to meaningful engineering unit.

A block diagram of the on-board data acquisition software is shown in Figure 5-2.
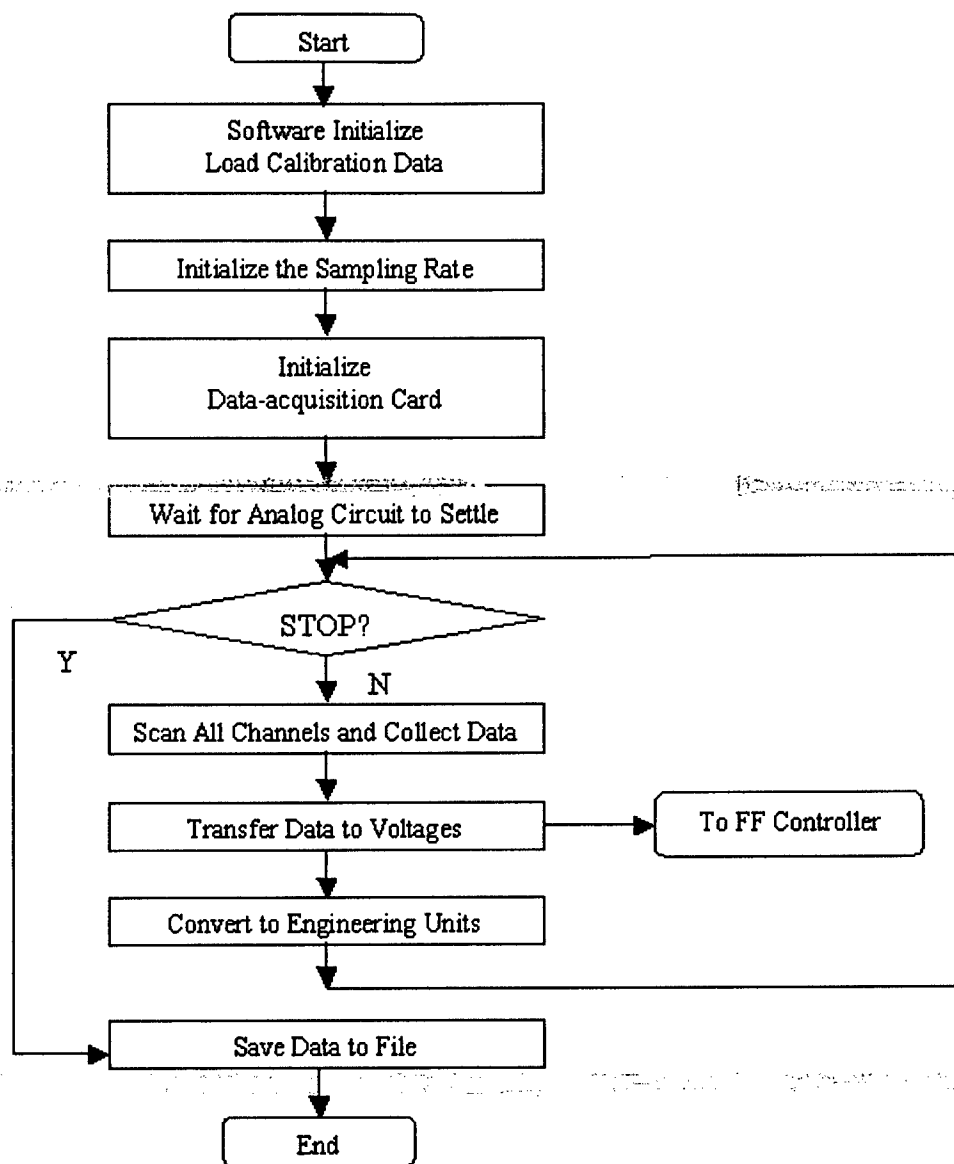
Figure 5-2: Data Acquisition Software

Digital Input Channels

The 3-axis position and velocity information of the aircraft GPS were acquired through a serial port. A total of 6 channels were acquired and are listed in Table 5-2.

Number	Channel Name
1	Position - x
2	Position - y
3	Position - z
4	Velocity - x
5	Velocity - y
6	Velocity - z

Table 5-2: GPS Channels

The controller commands generated by the formation controller were also recorded for post-flight analysis. A list of controller command channels is shown in Table 5-3.

Number	Controller Command
1	Left Stabilator
2	Right Stabilator
3	Left Aileron
4	Right Aileron
5	Left/Right Rudders
6	Engine Throttle

Table 5-3: Control Command Channels

Sampling Rates

For the PID flight-testing phase the sampling rate was set at 100 Hz. For all other flight-testing phases the sampling rate was reduced to 50 Hz due to computational limits of the OBC. The GPS unit was sampled at 20 Hz, which was the maximum allowed value.

Data Outputs

The flight data acquired from the DAQ could be used for the following purposes:

1. To provide information to the on-board formation control software simultaneously for controller use.

2. To send out selected sensor readings (at a reduced sampling rate) through the serial port simultaneously. Ex.: during flight tests, a ground station through RF-Modems could then receive this signal.

3. To save the flight data file for post flight analysis.

5.4 - Communication Software

The data communication software performed the information transfer between the UAVs. This involved the following software modules:

1. Data-sending module (used on 'leader' aircraft);

2. Data-receiving module (used on 'follower' aircraft).

GPS information and Euler angle measurements of the 'leader' aircraft were sent to the 'follower' using these communication modules. The exchanged flight information was integrated into a data package before transferring via the RF modems. The structure of the data package is listed in Table 5-4.

Byte	1,3	4,5	6,7	8,9	10,11	12,13	14,15	16,17	18,19
Content	120-122	Binary	Binary	Binary	Binary	Binary	Binary	Binary	Binary
Signal	Header	GPS-X	GPS-Y	GPS-Z	GPS-Vx	GPS-Vy	GPS-Vz	theta	phi

Table 5-4: Communication Package Structure

5.5 - 'Leader' On-Board Software

The 'leader' on-board software could be considered as the integration of the data acquisition and communication software modules. A general Simulink® diagram of the 'leader' software is shown in Figure 5-3.
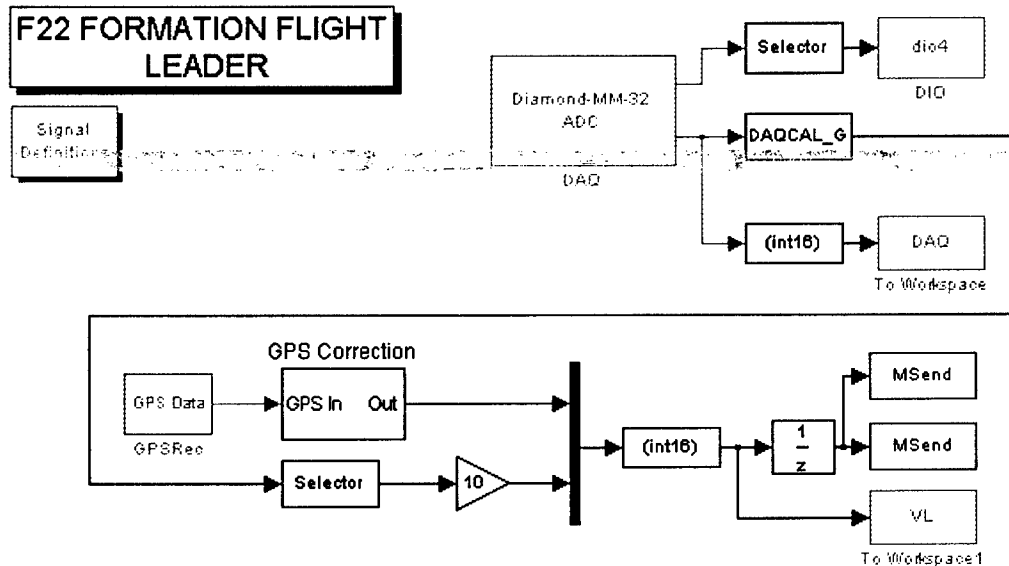
Figure 5-3: Simulink Diagram of the 'Leader' Aircraft Software

This scheme performed data acquisition from both on-board sensors and GPS while sending a data package through the RF modem. This package was then received by the 'follower' aircraft RF modems and/or the ground station modem.

5.6 - Formation Flight Control Software

The formation flight control software gave the OBC the capability to engage and maintain the formation configuration. In addition to the DAQ and communication software, several additional components were necessary for achieving this goal:

- Digital channel selections;
- Formation controller;
- On-board servo calibration;
- Servo control.

A Simulink® diagram for the formation flight control software of the 'follower' aircraft is shown in Figure 5-4.
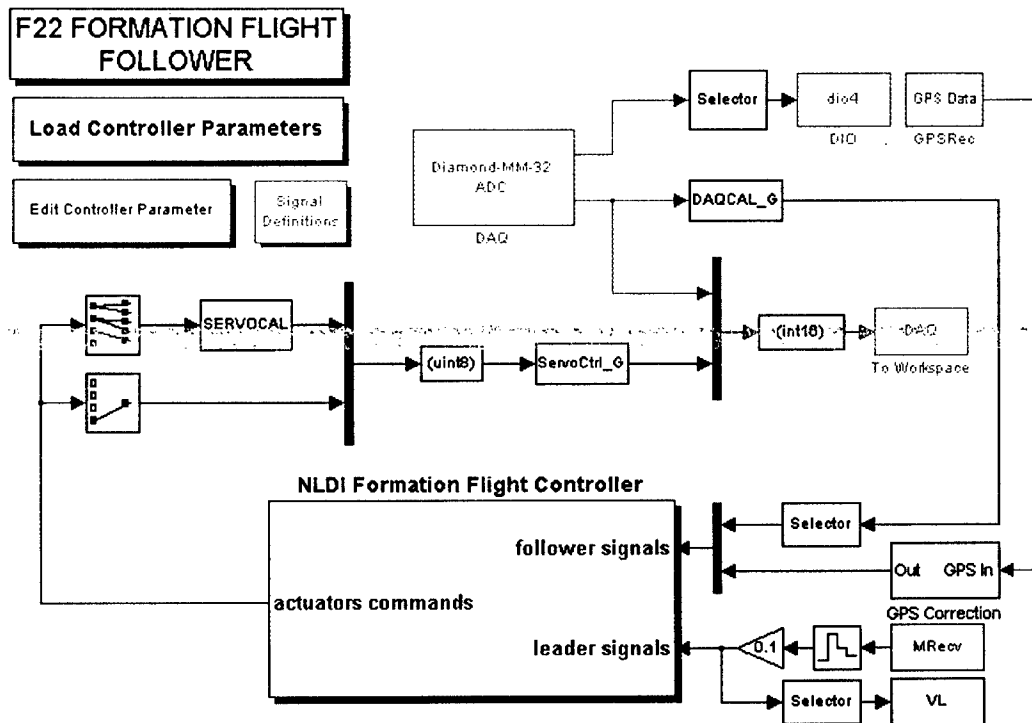
Figure 5-4: Simulink Diagram of the 'Follower' Aircraft Software

A description of the individual modules of the 'follower' software is provided in Sections 5.6.1 through 5.6.4.

5.6.1 - Digital Channel Selection

The on-board software had the ability to be configured for various flight experiments at the airfield. The hardware was giving the ability to use a subset of control surfaces - as discussed in Section 3.2.3 - to simplify the problem of evaluating individual control laws. Therefore, a digital channel selection module was created to perform the selection of individual servo channels. A small data file, called "Judgenum.dat", was stored on each compact flash card. This file provided a 6 digit binary number associated with a specific number of active servo channels. A list of values for the binary numbers associated with the active servo channels is shown in Table 5.5.

Binary Number	Decimal Number	Control Activity
000000	00	No Control
000001	01	Left Stabilator
000010	02	Right Stabilator
000011	03	All Longitudinal Surfaces
000100	04	Left Aileron
001000	08	Right Aileron
001100	12	Both Ailerons
010000	16	Rudders
011100	28	All Lateral-Directional Surfaces
011111	31	All Control Surfaces
100000	32	Engine Throttle
111111	63	All Control Channels

Table 5-5: Control Channel Selections

The digital channel selection software read this binary number at the initialization stage of execution and stored the value into memory. During each flight test, the digital channel selection software read the control switch signal (channel 14) from the DAQ software. Once channel 14 had a value of 5V - implying that the pilot activated the controller switch - the digital channel selector would then send the channel selection signal through the Digital Input/Output (DIO) port of the data acquisition card to the on-board controller. In this case, any pre-assigned channel would be activated and controlled by the OBC while the R/C pilot retained control of the remaining channels. This capability allowed for the testing of individual control channel (for example: engine throttle testing) without engaging all servo channels at one time.

5.6.2 - Formation Controller

The formation controller software module used information collected by both the on-board DAQ and the RF modem communication link. Next, the formation controller block executed the formation control laws and determined the controller commands to be sent out to the individual aircraft servos.

5.6.3 - On-Board Servo Calibration

The control command generated by the formation controller was calculated in degrees. However, the servo control module (discussed in the next section) required an 8-bit digital signal between 0-255 as an input. Thus, the control commands had to be calibrated into a digital signal before it could be fed back into the servo control module. The on-board servo calibration software provided the calibration information – as acquired during a ground servo calibration - at the initialization stage of the execution and stored that information into memory. During the flight, the control commands were then converted and sent to the servo control software.

5.6.4 - Servo Control

The servo control module was the final step of the flight control software. This module sent the calibrated control commands directly to the serial port. The servo control module on the controller board then converted these signals into multi-channel Pulse Width Modulation (PWM) signals, which were used by the aircraft servos.

5.7 - Ground Calibration Software

Auxiliary software – such as the 'Ground Calibration' software - was developed for flight test operations in addition to the real-time flight control software. The 'Ground Calibration' software was critical for the accuracy and the overall safety of the flight control system operations. The 'Ground Calibration' included control surface calibration, individual servo calibration, and trim position detection software. Each of these schemes will be discussed below.

5.7.1 - Control Surface Calibration

The surface calibration software measured the relationship between the aircraft primary control surfaces and the potentiometers directly linked to them. In addition, the two potentiometers in the nose probe were also calibrated for the air-data information. This calibrated value was then used to measure the actual deflection of each control surface as well as the aerodynamic flow angles from each of the potentiometers.

During a surface calibration procedure, the operator moved each surface to a maximum positive deflection, zero deflection, and maximum negative deflection sequentially. The calibration software then measured the output voltage for each potentiometer via the DAQ card. These voltages were then recorded and used to calculate the gain/offset information with a linear fitting method.

5.7.2 - Servo Calibration

The 'Servo Calibration' software provided the information for the on-board controller to convert control commands into the actual surface deflections. This fully automated procedure was performed after the surface calibration phase. Essentially the 'Servo Calibration' software sent out individual servo control signals and scanned the entire range of the control surface range. Next, the DAQ software measured the control surface deflection and stored the associated servo command. The calibration results for each servo were then stored onto the compact flash card and later used by the formation control software.

5.7.3 - Trim Position Detection

The trim positions for each of the 'follower' aircraft could slightly change with the various load configurations during each flight test. A trim position technique was designed to identify the trim position of each primary control surface and to provide that information to the controller. In fact, through the 'Trim Position Detection' procedure, the operator turned on the R/C system and kept all the control surfaces at the trim position from the previous flight. The calibration software would then read all control surface deflections and store the values into memory. Next, a servo control command was sent to each servo to sweep the control surfaces throughout the entire deflection range. Once the trim position reached the servo command relative to the trim position, a value was stored onto the file.

Chapter 6 - Flight Testing of the Formation Control Laws

6.1 - Flight Testing Phases

As stated before, the configuration of the formation flight test experiment was a 'leader/follower' configuration with all aircraft under manual control during the takeoff and landing phases. Once airborne, the R/C aircraft pilots were tasked to position their vehicle at a 'nominal' flight condition within a pre-selected 'rendezvous' area. Once at the rendezvous area, pilots of the 'follower' aircraft were tasked to engage their formation controllers. After the formation mode was engaged, the 'follower(s)' aircraft was/were controlled with the designed formation controller, while the R/C pilot remained on standby mode in the event of an emergency. Essentially, once formation was engaged, the 'leader' R/C pilot manually controlled and directed the 'leader/follower(s)' group. After the disengagement of formation mode, each aircraft landed under manual control.

Safety in the flight operations was a critical factor throughout the entire flight-testing program. To maximize safety, an 'incremental small step' approach was used. Thus, the flight testing program was divided into the following 11 phases:

Phase #1   Flights for assessment of handling qualities;

Phase #2   GPS communication flights;

Phase #3   Data acquisition flights (for PID analysis);

Phase #4   Engine PID flights;

Phase #5   Inner-loop controller flights;

Phase #6   Outer-loop controller flights (along the forward, lateral and vertical channels).

Phase #7   'Virtual leader' flights;

Phase #8   Pilot training flights;

Phase #9   Communication tests;

Phase #10   2-aircraft formation flights;

Phase #11   3-aircraft formation flight.

A description of each flight-testing phase and a detailed analysis of the relative experimental results are presented in Sections 6.2 through 6.12.

6.2 - Flight for Assessment of Handling Qualities

The first flight phase included a set of 'R/C only' flights, without any payload on the aircraft. The objective was to evaluate the handling qualities and the dynamic characteristics of the test-bed, as well as the trim characteristics and the performance of the propulsion system. After a few satisfactory test flights, a 'dummy' payload system was installed to provide the R/C pilots a feeling of the handling qualities at the final aircraft weight (with the full electronic payload). At the end of this set of test flights the pilot ranked the different handling qualities at the different 'dummy' payload configurations to be desirable or very desirable (equivalent to the 'conventional' ranking of Level 1 Handling Qualities using the Cooper-Harper pilot rating scale for manned aircraft).

6.3 - GPS Communication Flights

The second set of test flights involved the evaluation of the GPS and RF modem hardware. This hardware was installed without the OBC so that the GPS information could be directly transmitted to a ground station. This phase provided the aircraft trajectory information to be later used for the design of the formation control laws. Figures 6-1 and 6-2 show a sample set of collected raw GPS flight data from a session conducted on July 16th, 2003 ('red' WVU YF-22 aircraft).
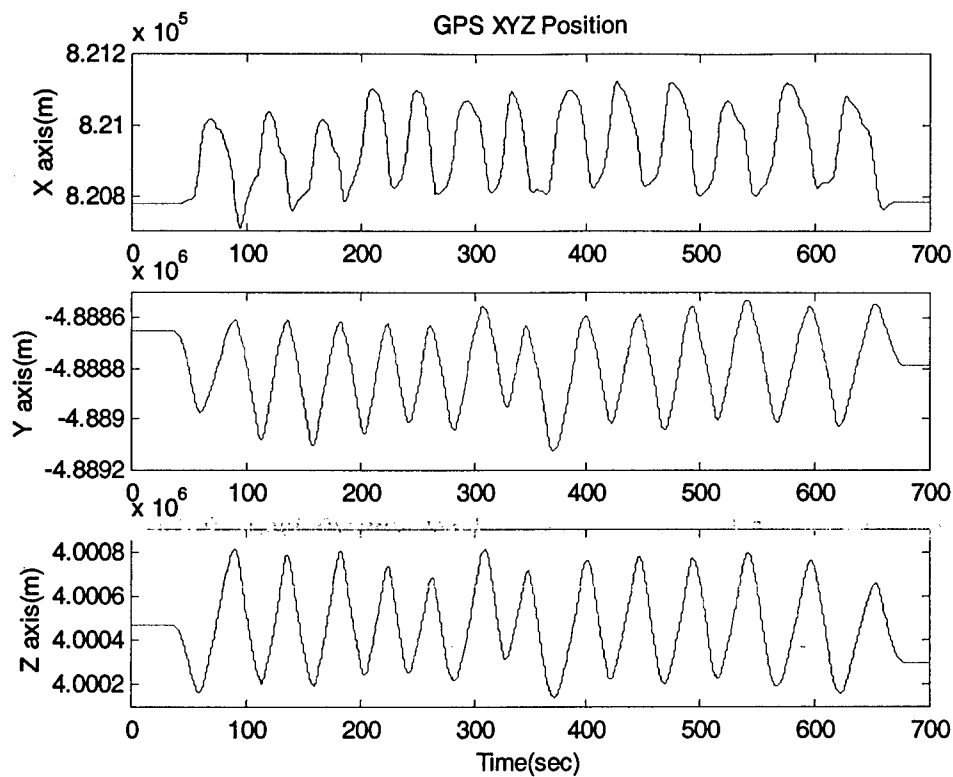
Figure 6-1: GPS Position Flight Data
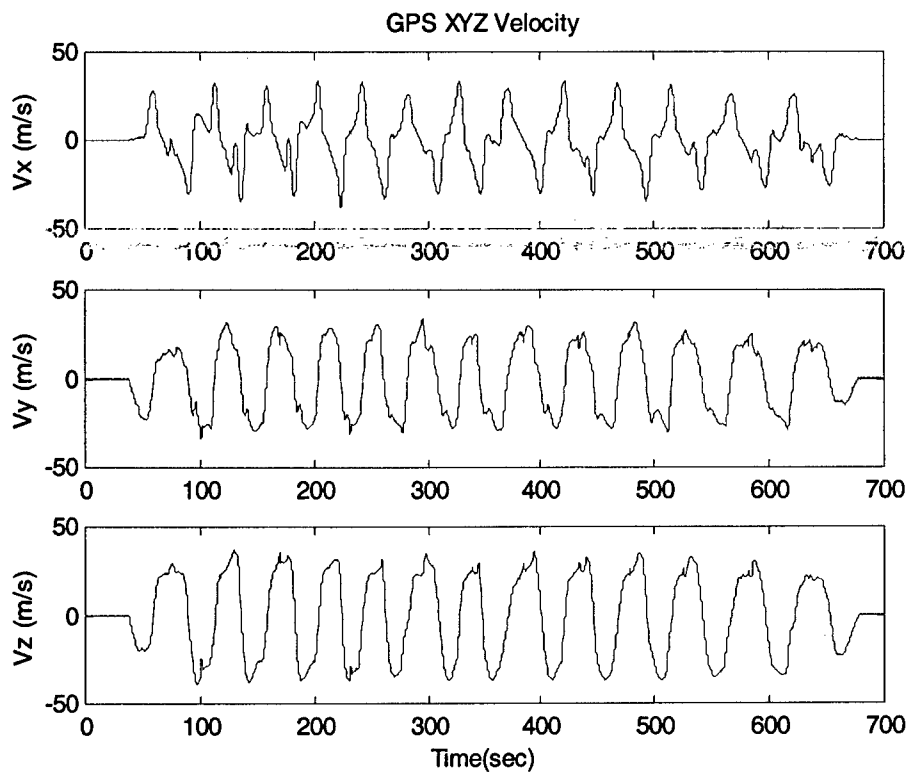
Figure 6-2: GPS Velocity Flight Data

93

6.4 - Data Acquisition Flights

During this phase the OBC collected flight data from all of the aircraft sensors and stored that information directly into a compact flash card for post-flight analysis. The purpose of this phase was to acquire flight data for the parameter identification (PID) analysis and, more in general, to check the functional status of the following aircraft subsystems:

- sensors;
- OBC;
- data acquisition hardware/software;
- power systems;
- Electro Magnetic Interference (EMI).

For PID purposes a set of dedicated PID maneuvers was performed throughout multiple flights. The list of maneuvers included:

- stabilator doublets;
- aileron doublets;
- rudder doublets;
- combined aileron-rudder doublets.

As discussed previously in Section 4.2, the linearized mathematical model of the aircraft used for the controller design was then estimated from flight data. Sample data from a flight session conducted on July 17th, 2003 ('red' WVU YF-22 aircraft) - involving an aileron-rudder combination and a stabilator doublet - are shown in Figures 6-3 and 6-4. Figure 6-3 shows a typical aileron-rudder doublet combo maneuver used to estimate the lateral-directional portion of the aircraft mathematic model.

94
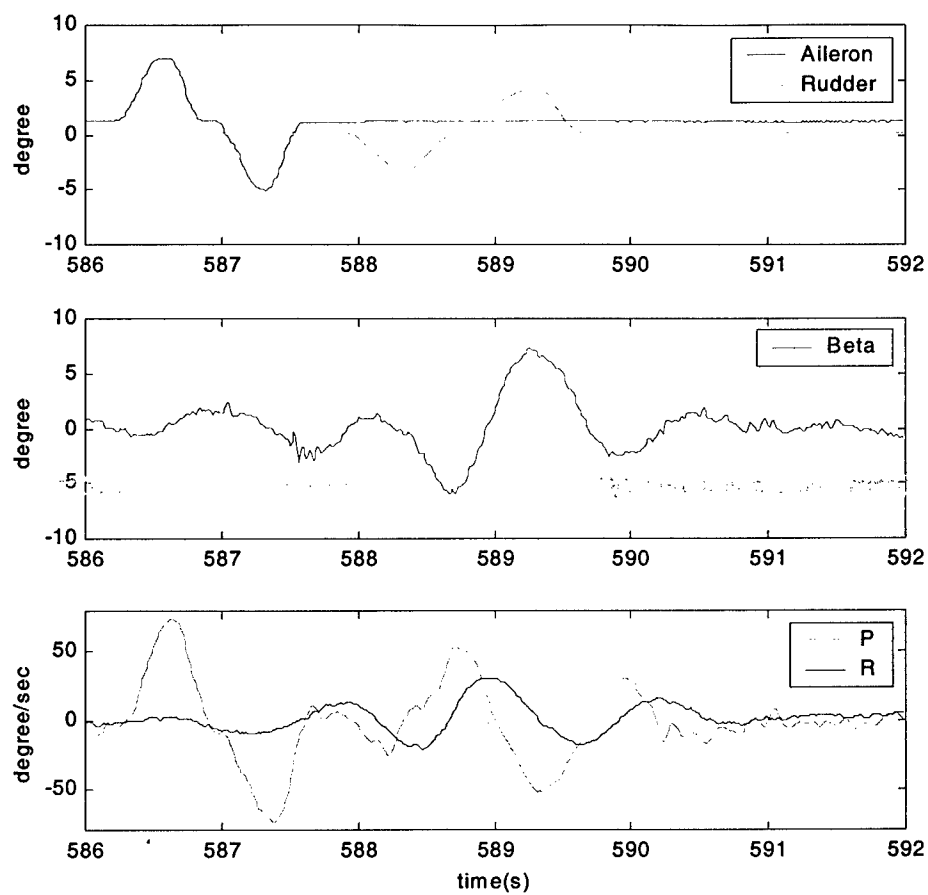
Figure 6-3: Flight Data - Aileron/Rudder Doublet Combination

Figure 6-4 shows a typical stabilator doublet used for estimating the longitudinal portion of the aircraft mathematical model. The PID phase included a total of 3 flights with approx. 30 PID maneuvers.
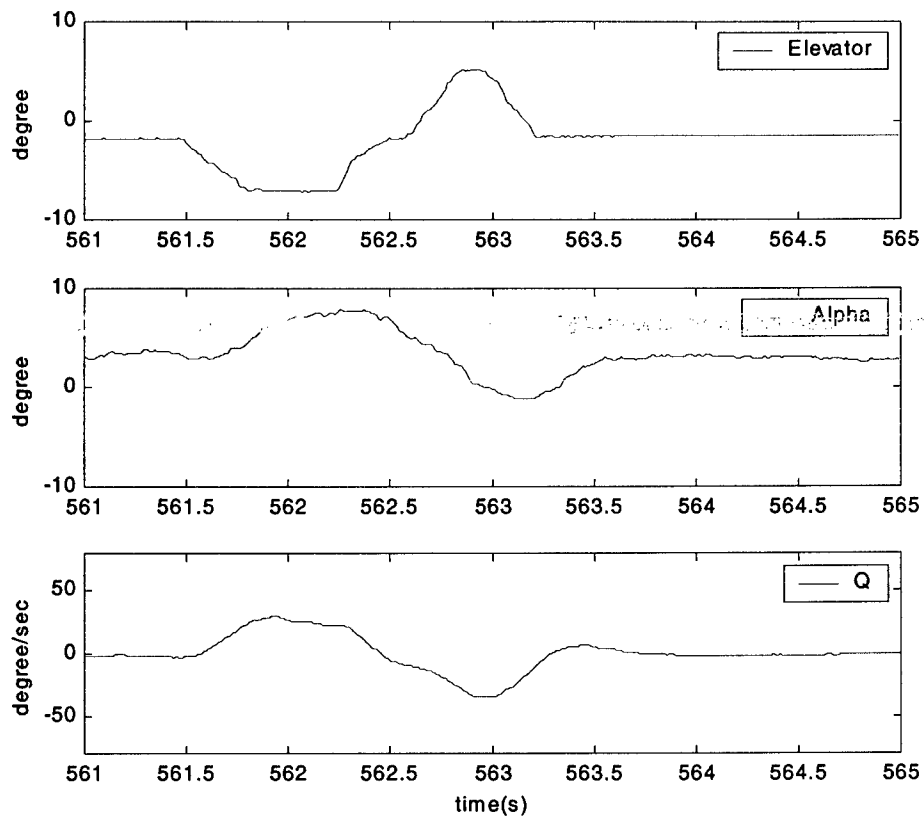
Figure 6-4: Flight Data - Stabilator Doublet

6.5 - Engine PID Flights

Within this phase flight data was collected to validate results obtained from the engine PID ground analysis. During these flight sessions, the engine throttle was set to a number of specific settings including idle, ¼ throttle, ½ throttle and full throttle. Throttle values and aircraft parameters were then recorded for post-flight analysis. Figure 6-5 shows a sample of the engine PID flight data collected on a flight testing session on August 12th, 2003 ('green' WVU YF-22 aircraft).
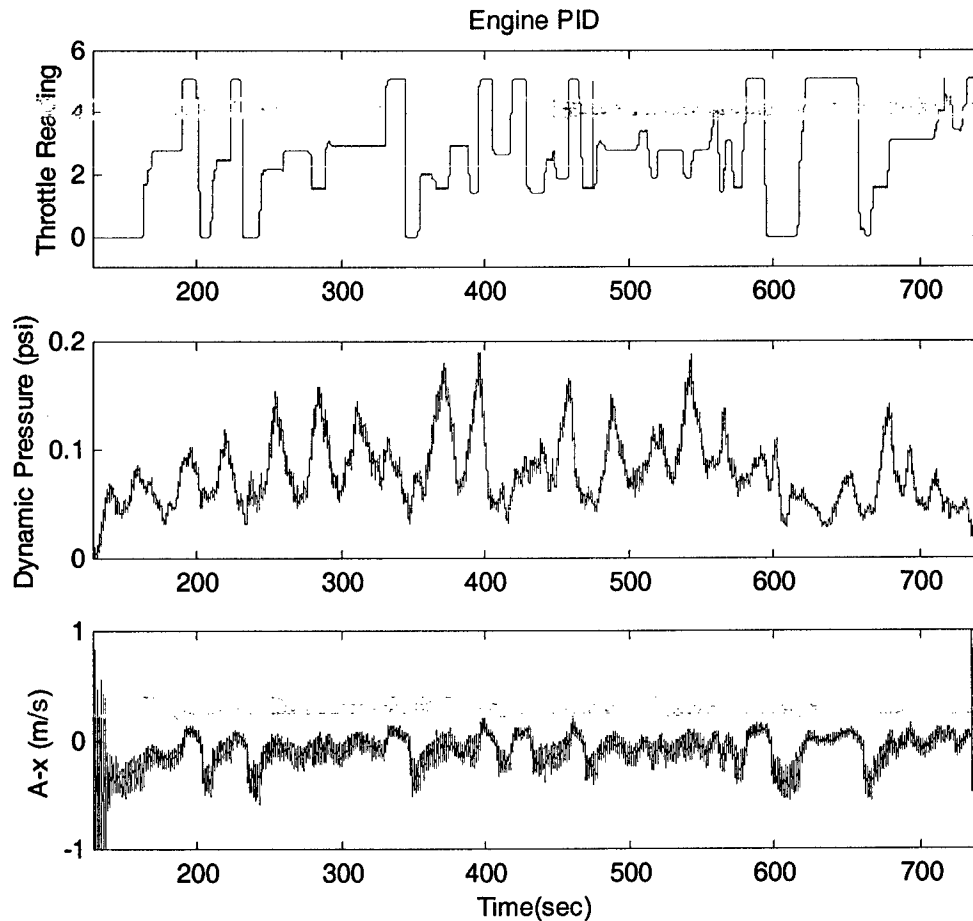
Figure 6-5: Engine PID Flight Data

6.6 - Inner Loop Controller Flights

A linear controller was designed using the mathematical model derived from the PID study - as described in Chapter 4. The linear controller software was then implemented on the OBC system for flight-testing evaluation. This was the first set of flights where the pilot had only partial control of the aircraft systems; in fact, he was only able to control the engine throttle level while the primary control surfaces were deflected by the OBC-generated commands. The goal of this phase was to evaluate the accuracy of the mathematical model and validate the linear controller design. Sample data collected from linear controller validation flights are shown in Figures 6-6 and 6-7.
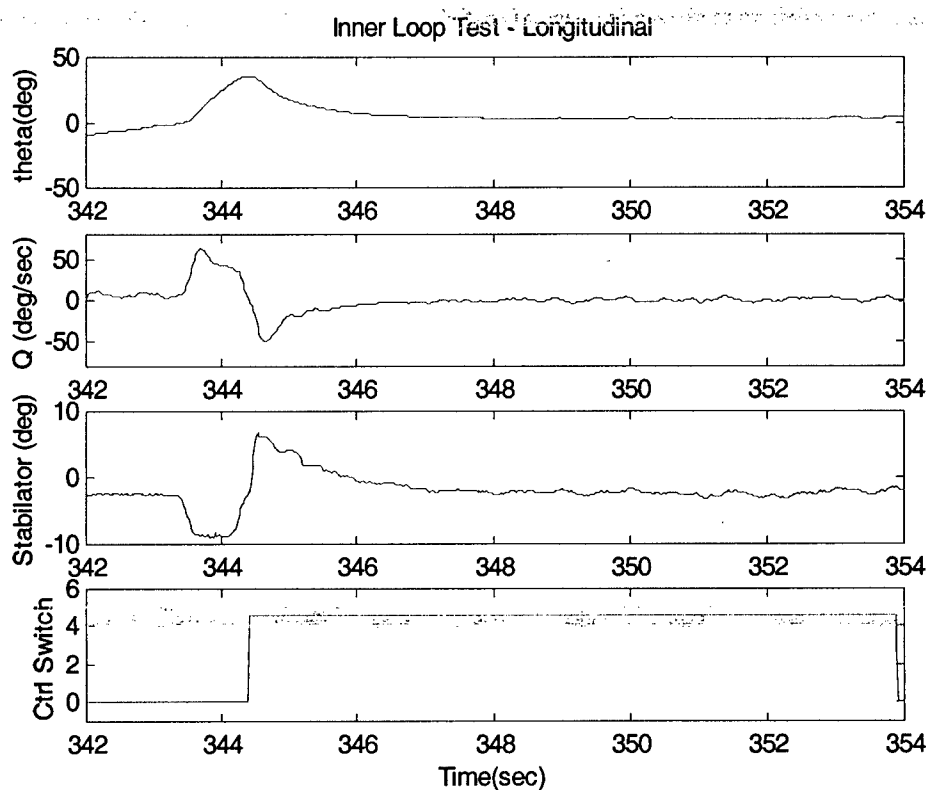
Figure 6-6: Inner Loop Control: Longitudinal Flight Data

98
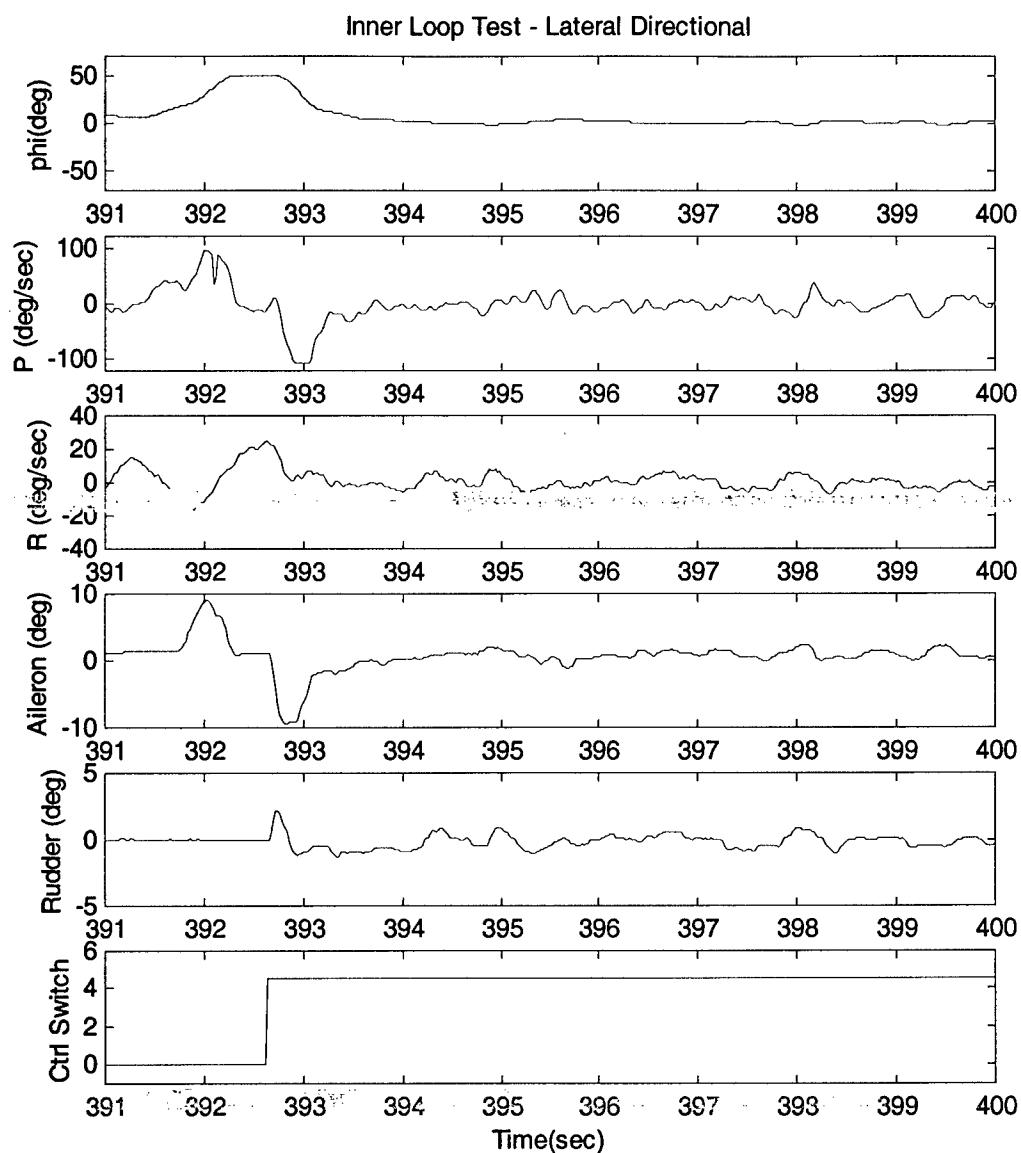
Figure 6-7: Inner Loop Control: Lateral-Directional Flight Data

The flight data shown above are from a flight-testing session conducted on October 16th, 2003 ("green" WVU YF-22 aircraft). This phase included a total of 4 flights. A detailed analysis of the flight data demonstrated the effectiveness of the design of the inner loop control laws.

6.7 - Outer Loop Controller Components (Height, Heading, and Velocity)

During this flight-testing phase individual components of the outer loop controller were tested. As discussed above, there were 3 control channels for forward control, lateral-directional control, and vertical control. The combined performance of these controllers was critical for the overall performance of the formation control laws.

The height/heading controller was tested in a flight-testing session on March 28th, 2004 ('red' WVU YF-22 aircraft). Sample flight data are shown in Figures 6-8 through 6-10. Figure 6-8 represents the results from the height controller flight experiments. In that particular flight segment the UAV was commanded to fly at an altitude of 150 m. As shown in the plot, the aircraft altitude, starting from approximately 167 meters, was stabilized at around 150 meters within approx. 7 sec from the activation of the controller.
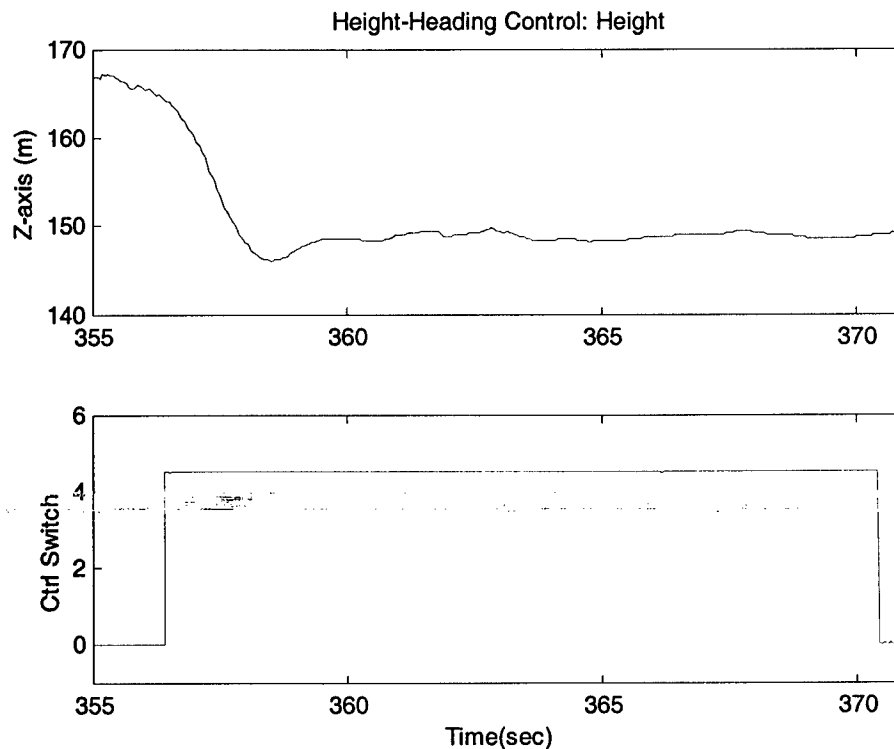
Figure 6-8: Height-Heading Control: Height

Figure 6-9 represents the test results of the heading controller. Once the controller was activated, the aircraft was designed to track the runway direction with a 186° heading.
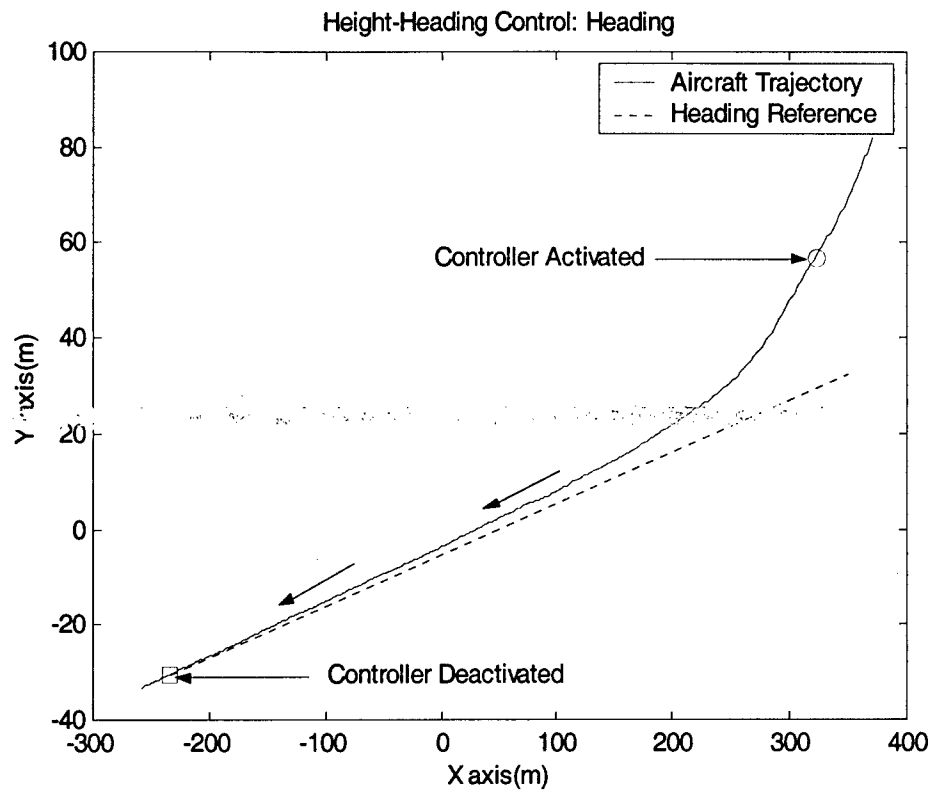
Figure 6-9: Height-Heading Control: Heading

Figure 6-10 shows the corresponding control surface deflections from each aircraft during the test. The pilot activated the controller switch for approx. 14 sec.
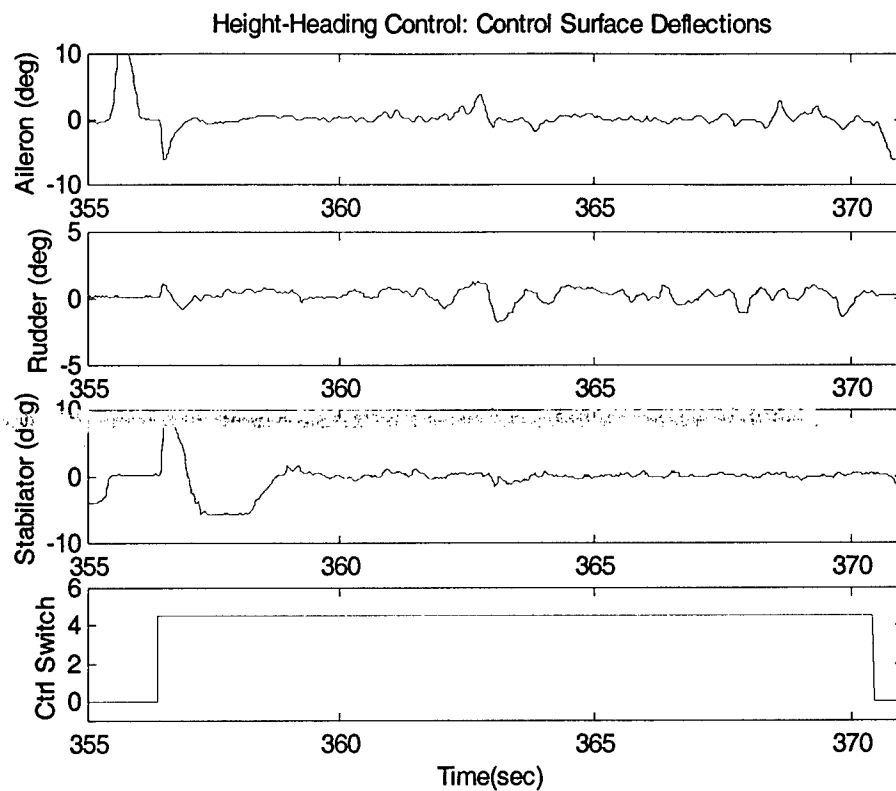
Figure 6-10: Height-Heading Control: Control Surface Deflections

Finally, Figure 6-11 shows the flight data relative to a 'velocity-hold' flight experiment conducted on May 8th, 2003 ('green' WVU YF-22 aircraft).
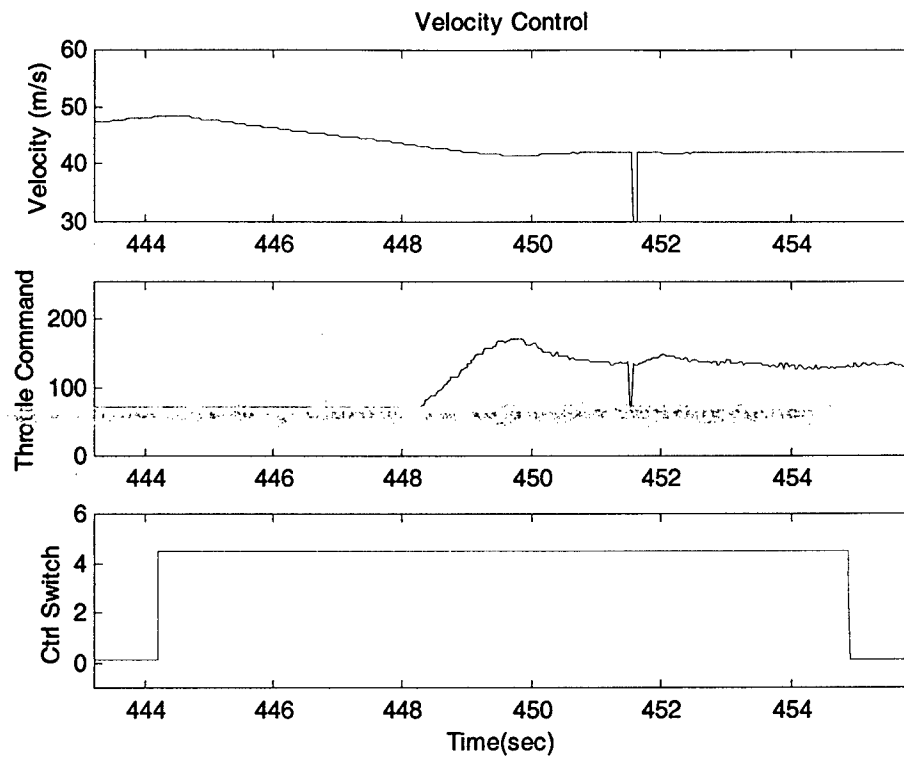
Figure 6-11: Velocity Control

Once the controller was activated, the velocity converged toward the commanded value of 42 m/s. A data spike, clearly visible around 451.5 seconds, illustrates a typical GPS dropout. Throughout the flight test program GPS dropouts would usually occur once or twice during a flight without a significant degradation of the controller performance.

6.8 - 'Virtual Leader' Flights

A 'Virtual Leader' (VL) approach was implemented for a detailed analysis of the formation control laws prior to an actual 2-aircraft formation demonstration. The use of the VL concept allowed a detailed testing of the formation control laws without the risks associated with the flight-testing of multiple aircraft. This experiment consisted of a single aircraft tracking the trajectories of a VL, which was essentially a flight path previously recorded by one of the aircraft. A 2-part implementation strategy was adopted for the VL flights. First the flight data - to be tracked - were pre-loaded on the aircraft OBC and fed to the formation control software. After this strategy proved successful, an additional step of beaming the VL flight data to the RF modem was performed. A sample of the VL flight data showing the aircraft altitude and GPS XY trajectories is shown in Figures 6-12 and 6-13. This particular flight experiment was performed during the June 23rd, 2004 flight session ('green' WVU YF-22 aircraft).
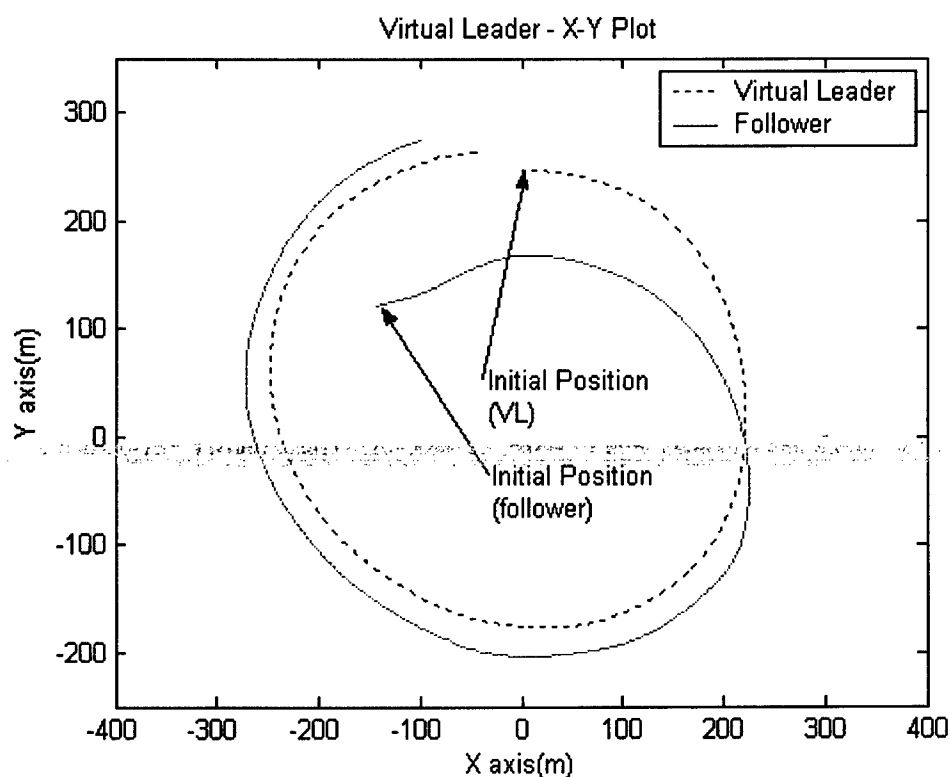
Figure 6-12: 'Virtual leader' Test - Flight Data and Simulation (X-Y Plane)

The parameters of the formation controller were set at:

$$l_c = 30m, \quad f_c = 30m, \quad h_c = -20m$$

which implied that the 'follower' aircraft tracked the VL data from 30 meters behind, 30 meters to the right and 20 meters above. In Figure 6-13, the 'follower' height measurement had a mean error of 1.25 meters for this particular flight test.
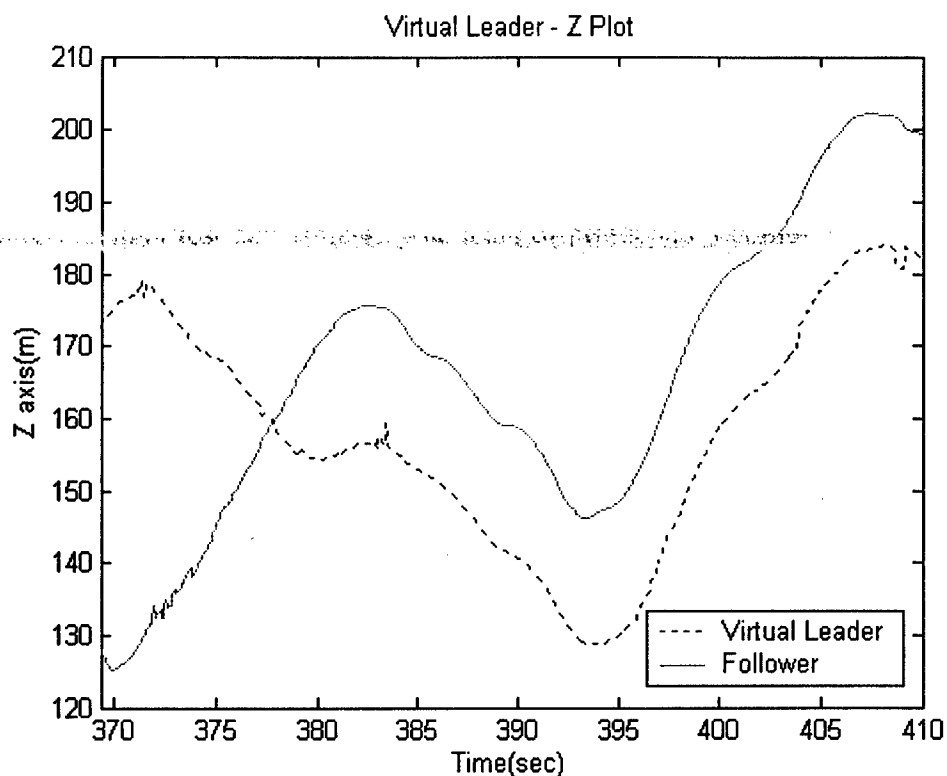
Figure 6-13: 'Virtual leader' Test June 23rd 2004 - Flight Data and Simulation (Z-plot)

The 'Virtual Leader' flights were critical for testing the formation control laws. A total of 12 VL flights were performed with various configurations. Results from the VL configuration confirmed a desirable performance of the formation control laws.

6.9 - Pilot Training Flights

Detailed training of 3 pilots capable of individual takeoff and landing, as well as formation engagement and disengagement was considered to be a critical factor for the success of this project - assuming that the formation control laws had been designed correctly. It should be emphasized that the skills required for these missions were much higher than the piloting skills of normal R/C recreational aircraft pilots. The selected individuals had extensive experience in flying RC models of various size and configurations, including jet propulsion. The 'primary' aircraft pilot was a WVU Aerospace Engineering undergraduate student with 18 years of R/C pilot experience. Two additional pilots were trained to fly the 'followers' in preparation for the 2-aircraft flight test experiment. The team of pilots had a combined 80 years experience with R/C models. The training flights consisted of flights with empty aircraft (without 'dummy' or electronic payload installed), with dummy payload, with actual electronic payload without data acquisition (to avoid possible EMI issues during training), flights with the OBC, with controller turned on and off, and VL flights.

6.10 - Communication Tests

Communication tests were performed before actual formation flight with multiple aircraft for evaluating the performance of the data communication system. Different configurations were tested with and without a ground station setup (as discussed in Section 3.2.3). Figure 6-14 shows the results of the final communication test performed on November 16th, 2004.
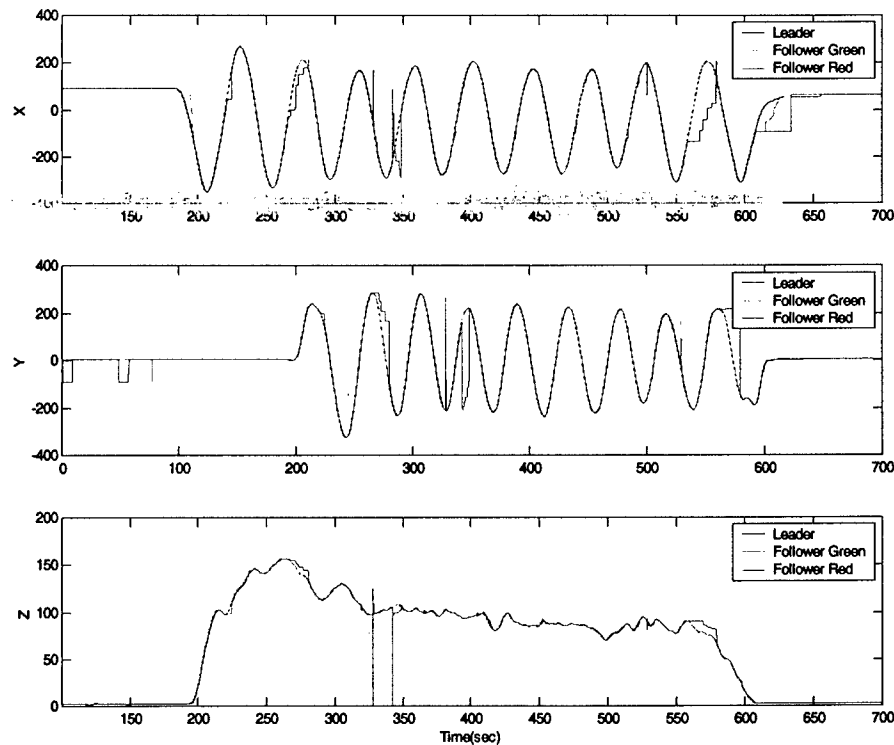
Figure 6-14: Communication Test - Position

In this particular test, the 'red' and 'green' aircraft were placed on stationary table platforms while the 'blue' aircraft was in flight. The purpose of this particular test was to ensure that the GPS information was correctly sent from the 'blue' aircraft to both 'follower' aircraft on the ground using the RF modems. Since both 'follower' aircraft were on the ground, this condition was deemed to be a worst-case scenario than an actual formation flight. In fact, once airborne, the 'followers' would be in close proximity to the 'leader'; therefore, the communication was expected to be more reliable. The flight test data, in Figure 6-14, showed a satisfactory performance with occasional data dropouts only when the 'leader' was flying very low or far away from the actual 'follower' positions.

6.11 - 2-Aircraft Formation Flights

After the training of the pilots was completed and desirable performance of the formation control laws were demonstrated through the VL flights, the flight-testing of a 2-aircraft formation began in early Summer 2004. The maiden flight for the 2-aircraft formation took place on June 29th 2004. As with the VL testing, the objective was to track the 'leader' trajectory with a pre-selected distance for the forward, lateral and vertical clearances set on the 'follower' vehicle. Figure 6-15 shows a collection of captured video images from a ground camera, along with images from a miniature DV camera installed in the nose canopy. For multiple aircraft flights, a customized canopy - housing the DV camera - replaced the standard canopy.
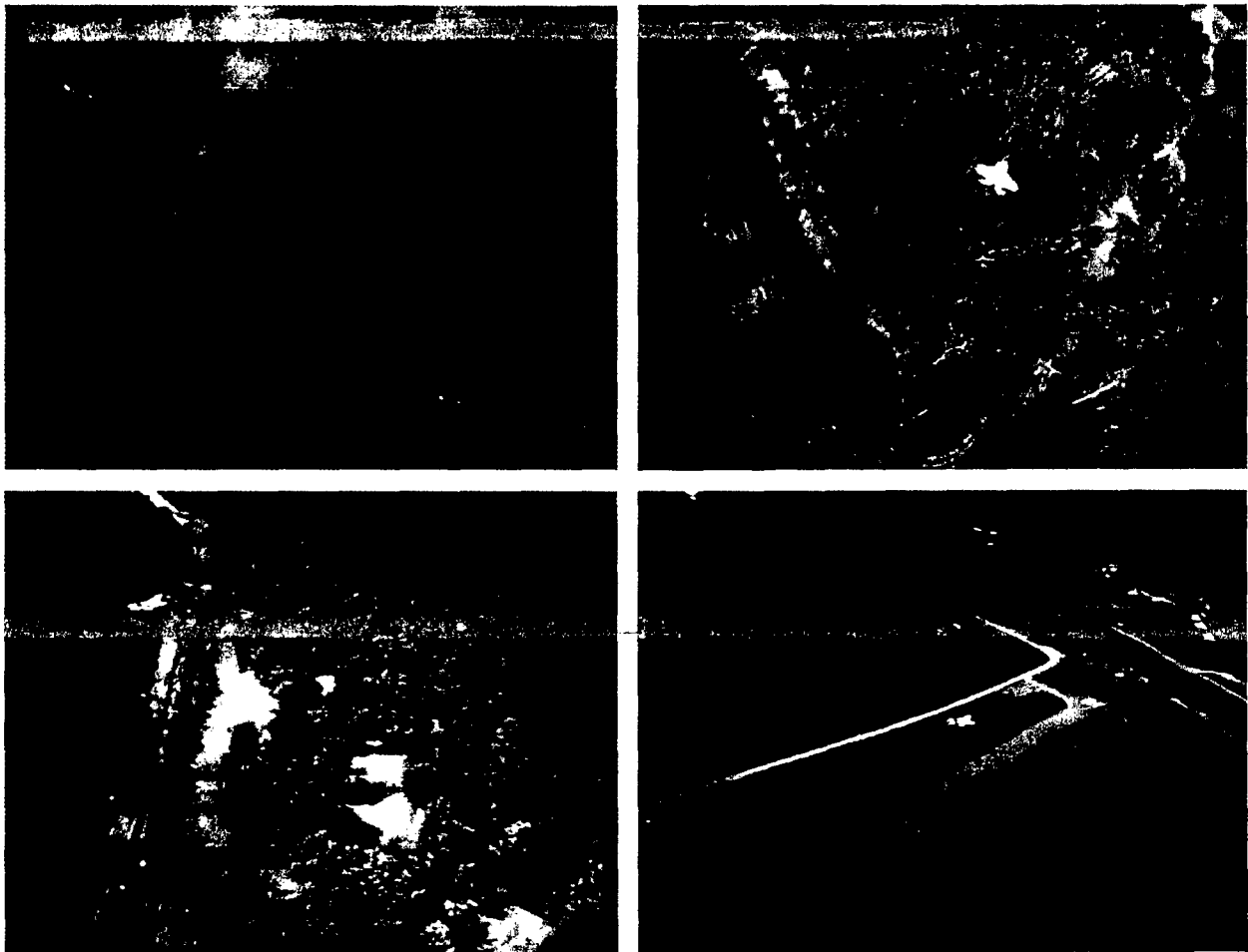
Figure 6-15: Formation Flight Images (1-Ground Camera; 2,3,4-On-board Camera)

108

A total of 4 2-aircraft formation flight experiments were performed using various geometries for the formation (from larger to lower distances between the 'leader' and 'follower' aircraft). These flight experiments were performed on the following dates:

- June 29th 2004;

- September 2nd 2004;

- October 1st 2004;

- October 6th 2004.

Detailed results relative to each of these flight test sessions are provided in the sections below.

6.11.1 - June 29th 2004 Flight Testing

For the 1st 2-aircraft formation flight the pre-selected distance between the 'leader' and the 'follower' was the same as in the VL flights. The formation parameters were set at:

$$l_c = 30m, \quad f_c = 30m, \quad h_c = -20m \tag{6-1}$$

Formation control with 2-aircraft was engaged for approximately 3 laps (approx. 108 seconds) with the 'leader' pilot flying in a circular pattern. The sequence of the activities during the flight is shown in Table 6-1.

	Blue Aircraft	Green Aircraft
Computer Clock Offset (sec)	0	-36.08
Take Off Time (sec)	184.96	220.74
Landing Time (sec)	543.5	645.78
Flight Duration (sec)	358.54	425.04
Controller Activation (sec)	-	291.74
Controller Deactivation (sec)	-	399.76
Formation Duration (sec)	108.02	

Table 6-1: 2-Aircraft Formation Flight Test June 29th 2004 - Flight Activities

Figure 6-16 shows a 3D plot of the flight data. Only the first formation lap is shown for clarity purposes. In terms of flight time, the data started at 291.74 s. and ended at 323.74 s. Figure 6-16 also illustrates a comparison of the 'follower' data (green) and 'simulated follower' data (red). The 'simulated follower' data was obtained by feeding the flight data to the formation simulator using the same initial conditions at formation engagement.

Formation Flight - 3D Plot

Initial Position
(follower & simulator)

Initial Position
(Leader)

t=323.74sec

t=291.74sec

Z axis(m)

Y axis(m)

X axis(m)
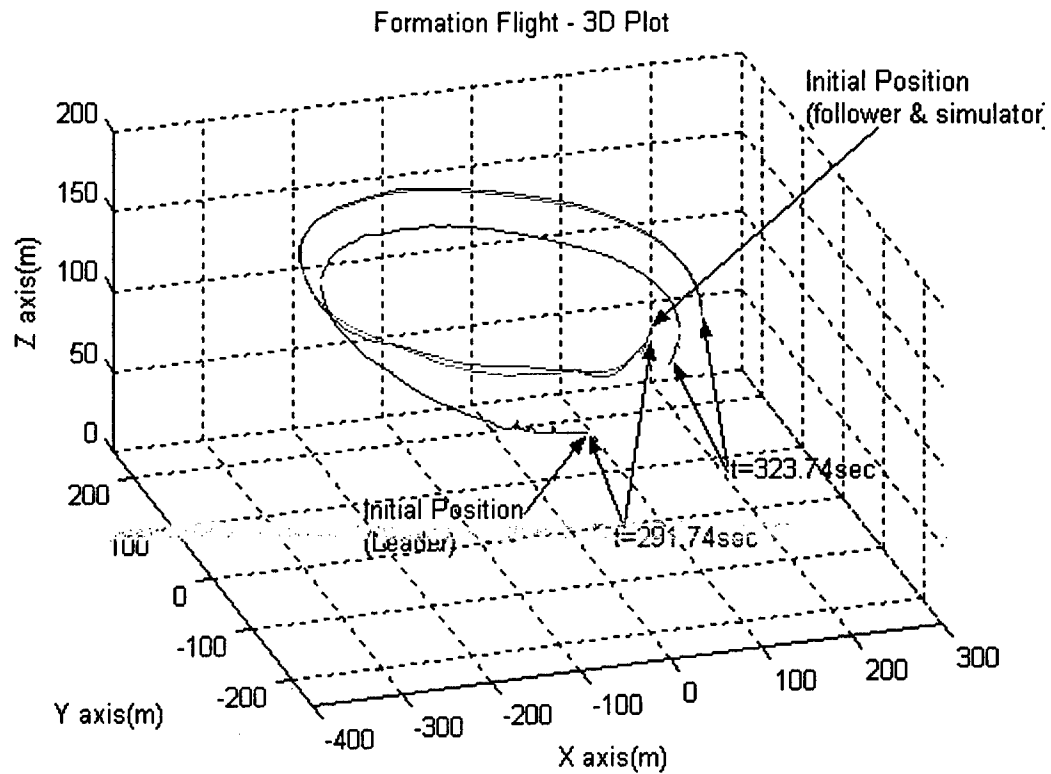
*Figure 6-16: 2-Aircraft Formation Flight Test June 29th 2004 - Flight Data and Simulation (3D Plot)
(Blue=Leader, Green=Follower, Magenta=Simulation)*

Figure 6-17 shows the aircraft trajectories in the X-Y (horizontal) plane. The data shows a desirable agreement between the 'follower' and 'simulated follower' flight data. Figure 6-18 shows the altitude for both aircraft ('leader' in blue, and 'follower' in green), as well as the altitude for the 'simulated follower' ('red'). The Euler angles for both 'leader' and 'follower' are shown in Figure 6-19.

Figure 6-17: 2-Aircraft Formation Flight Test June 29th 2004 - Flight Data and Simulation (X-Y Plane)

Figure 6-18: 2-Aircraft Formation Flight Test June 29th 2004 - Flight Data and Simulation (Z-Plot)

Figure 6-19: 2-Aircraft Formation Flight Test June 29th 2004 - Euler Angles

112

The performance of the formation control laws was evaluated in terms of 'tracking error' between the actual distance and the pre-selected clearance. The tracking errors were previously defined in Eqns. (4.27)-(4.29):

$$\begin{bmatrix} l \\ f \end{bmatrix} = \begin{bmatrix} \sin(\chi_L) & -\cos(\chi_L) \\ \cos(\chi_L) & \sin(\chi_L) \end{bmatrix} \begin{bmatrix} x_L - x \\ y_L - y \end{bmatrix} - \begin{bmatrix} l_c \\ f_c \end{bmatrix}$$

$$h = z_L - z - h_c$$

$$\text{with } \cos(\chi_L) = \frac{V_{Lx}}{\sqrt{V_{Lx}^2 + V_{Ly}^2}} \quad , \quad \sin(\chi_L) = \frac{V_{Ly}}{\sqrt{V_{Lx}^2 + V_{Ly}^2}}$$

where χ_L is the 'leader' azimuth angle. For clarity purposes, the parameters 'l', 'f', and 'z' are now referred to as the vertical distance (VD), lateral distance (LD), and forward distance (FD). The formation tracking errors are shown in Figure 6-20 in terms of the VD, LD, and FD.
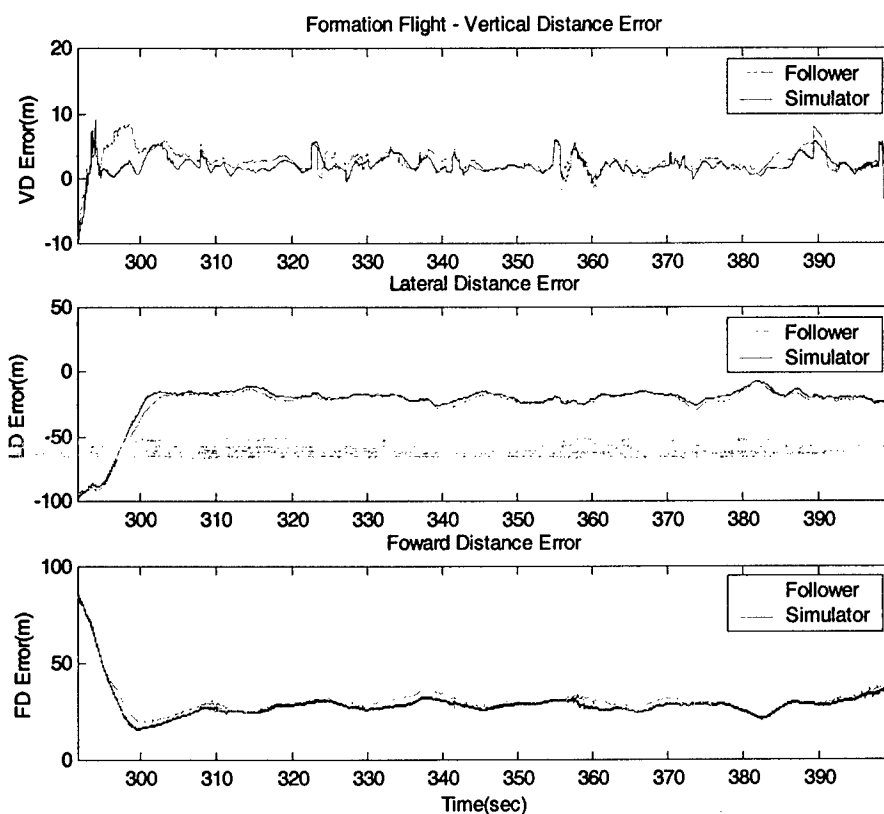
Figure 6-20: 2- Aircraft Formation Flight Test June 29th 2004 - Flight Data and Simulation (Tracking Errors)

It was observed in earlier simulation studies and early flight experiments that the use of higher gains for both the inner and outer loop controllers could reduce the formation tracking errors in

terms of VD, FD, and LD. However, as expected, there were drawbacks. Particularly, simulation studies and VL flights with higher controller gains showed the following adverse effects:

- deteriorated robustness to uncertainties;

- decreased smoothness in the trajectory;

- decreases rendezvous capability when the follower starts from an initial position farther away from the 'leader';

- substantially increased throttle activity;

- sensitivity to 'overshooting' during tracking of the 'leader's trajectory.

Furthermore, built-in delays with the aircraft actuators and propulsion subsystems imposed an upper limit on the controller gains so that closed-loop stability could be preserved. Therefore, it was decided to converge toward a set of relatively conservative gains even if those values implied an overall slower system and/or larger formation errors.

6.11.2 - September 2nd 2004 Flight Testing

After the 1st 2-aircraft formation flight the pre-selected clearance between the 'leader' and the 'follower' was decreased for a closer formation for the remaining flights. For the 2nd 2-aircraft formation flight, the pre-selected clearances were set at:

$$l_c = 20m, \quad f_c = 20m, \quad h_c = -20m \tag{6-2}$$

The sequence of the activities during this flight is shown in Table 6-2.

	Blue Aircraft	Green Aircraft
Computer Clock Offset (sec)	0	12.56
Take Off Time (sec)	162.6	194.64
Landing Time (sec)	631.2	705.04
Flight Duration (sec)	468.6	510.4
Controller Activation (sec)	-	255.54
Controller Deactivation (sec)	-	549.62
Formation Duration (sec)	294.08	

Table 6-2: 2-Aircraft Formation Flight Test Sept. 2nd 2004 - Flight Activities

Figures 6-21 through 6-25 show sample flight data obtain from the September 2nd, 2004 experiment. Again, for clarity purposes, only the flight data for the first formation lap are shown. As with the previous flight test, the plot comparisons for the September 2nd, 2004 flight showed a satisfactory agreement between the flight and simulated data, even with the tighter formation settings. Note for this particular formation engagement, the controller was intentionally activated when the 'follower' aircraft was actually further away than the previous June 29th, 2004 test. This condition lead to a longer transient but also proved that the designed formation control laws could handle a large range of initial conditions. This can be deduced in both Figures 6-21 and 6-22 (the 3D and X-Y plot from the September 2nd, 2004 flight).

115
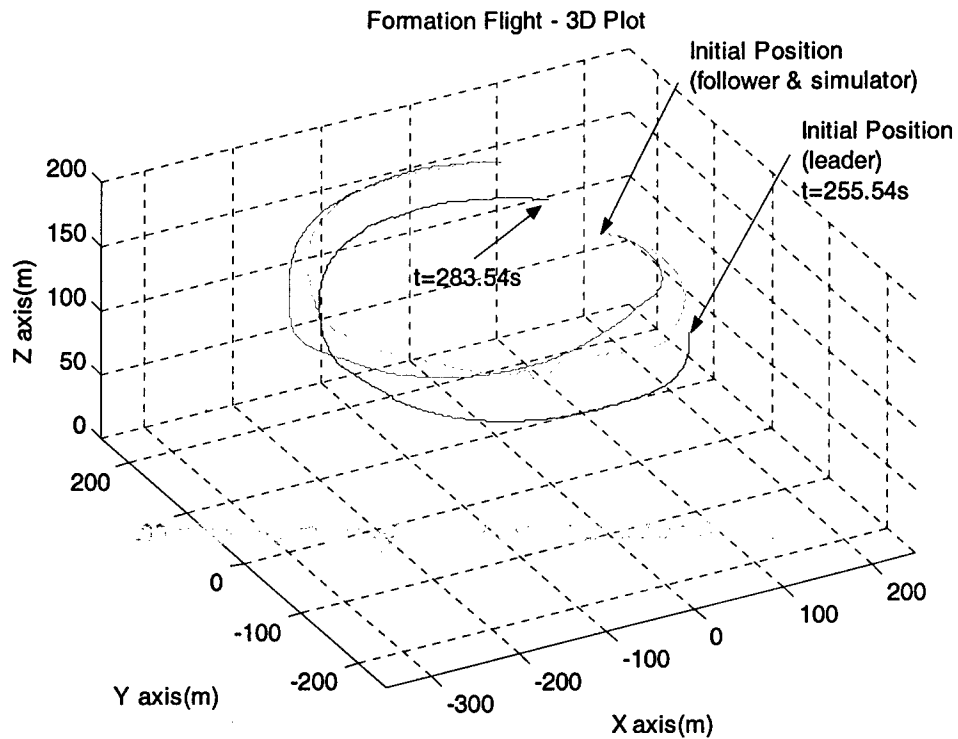
Figure 6-21: 2-Aircraft Formation Flight Test Sept. 2nd 2004 - Flight Data and Simulation (3D Plot) (Blue=Leader, Green=Follower, Magenta=Simulation)
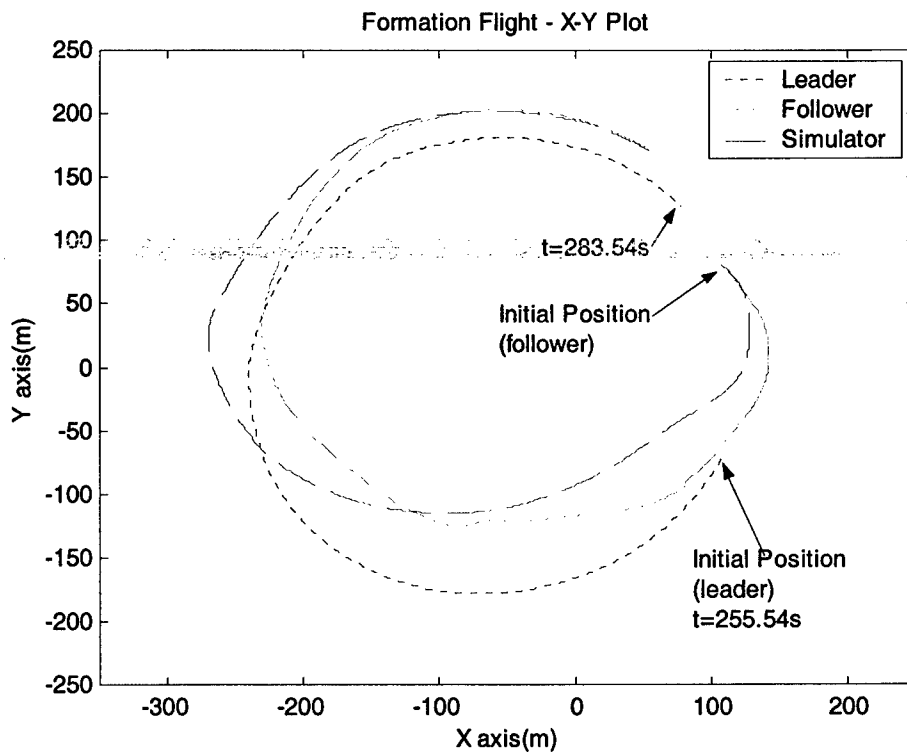
Figure 6-22: 2- Aircraft Formation Flight Test Sept. 2nd 2004 - Flight Data and Simulation (X-Y Plane)

Formation Flight - Z Plot
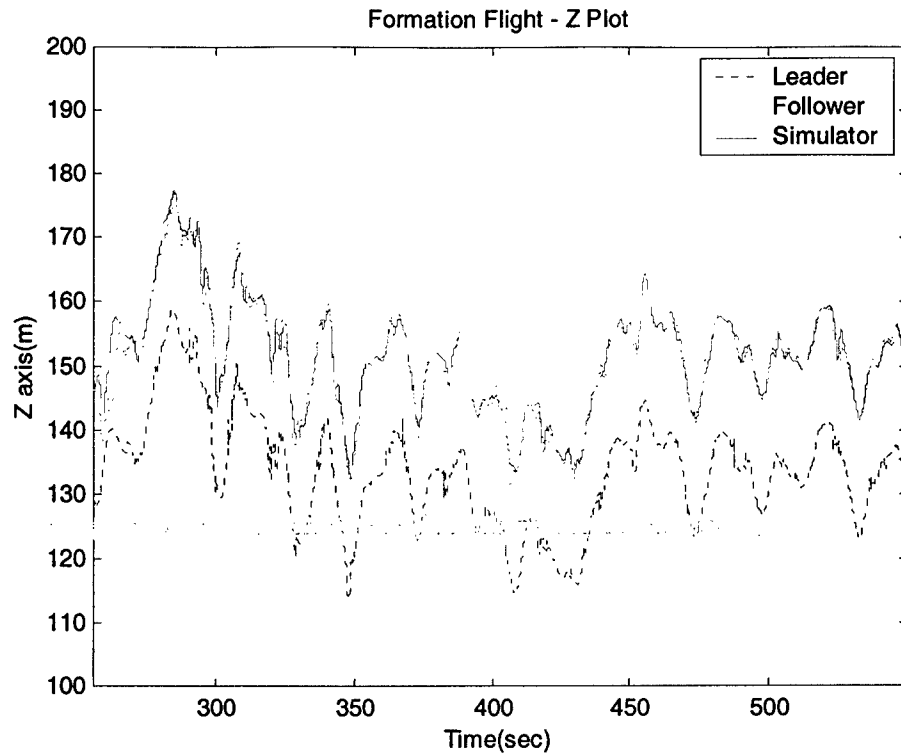
Figure 6-23: 2- Aircraft Formation Flight Test Sept. 2nd 2004 - Flight Data and Simulation (Z-Plot)

Formation Flight - theta

phi
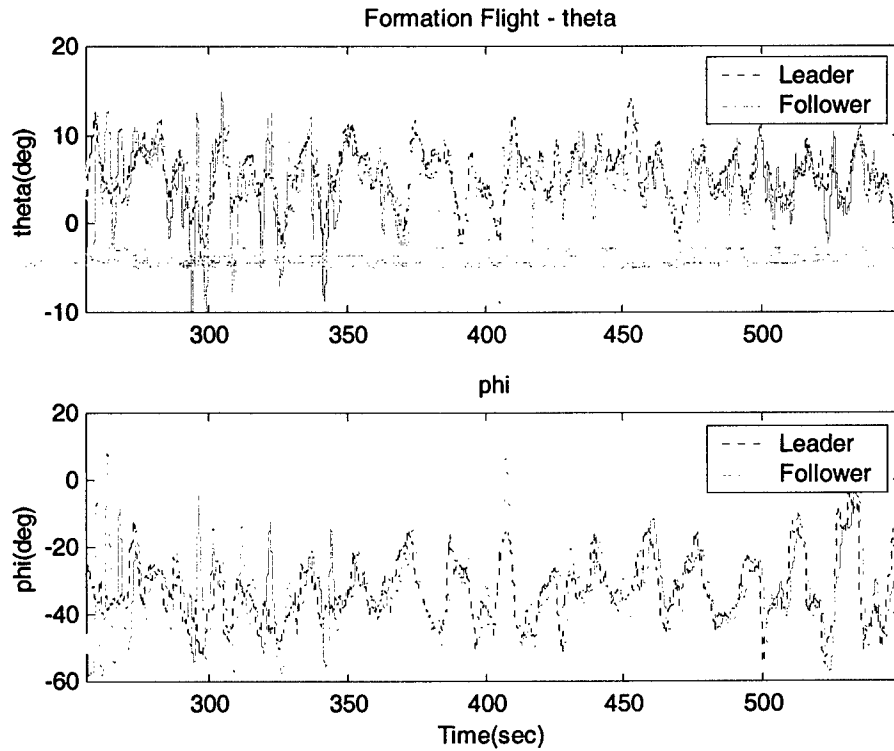
Figure 6-24: 2-Aircraft Formation Flight Test Sept. 2nd 2004 - Euler Angles
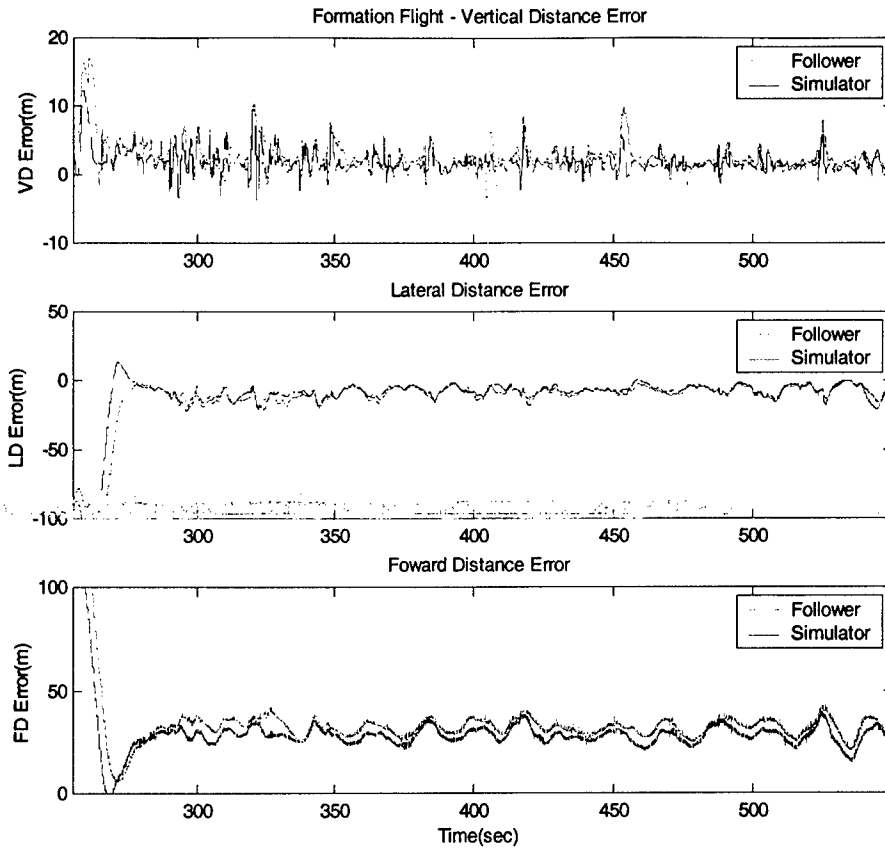
Figure 6-25: 2-Aircraft Formation Flight Test Sept. 2nd 2004 - Flight Data and Simulation (Tracking Errors)

6.11.3 - October 1st 2004 Flight Testing

The first two 2-aircaft formation flight tests were performed with the follower at the right side (or outside track) of the 'leader' aircraft. To test the performance of the 'follower' on the inside track (that is, on the left side of the 'leader'), the formation parameters for the 3rd 2-aircraft formation flight were set as:

$$l_c = -20m, \quad f_c = 20m, \quad h_c = 20m \tag{6-3}$$

implying that the 'follower' tracks the 'leader' from 20 meters behind, 20 meters to the left, and 20 meters below. The sequence of the activities during the flight is shown in Table 6-3.

	Blue Aircraft	Green Aircraft
Computer Clock Offset (sec)	0	4.90
Take Off Time (sec)	163.8	191.24
Landing Time (sec)	645.54	732.6
Flight Duration (sec)	481.74	541.36
Controller Activation (sec)	-	256.56
Controller Deactivation (sec)	-	592.2
Formation Duration (sec)	335.64	

Table 6-3: 2-Aircraft Formation Flight Test Oct. 1st 2004 - Flight Activities

A 3D plot of the measured and simulation results test of the inside track configuration can be seen in Figure 6-26. Again, only the 1st formation lap was shown for clarity purposes. Figure 6-27 - which shows the X-Y plot of the trajectory - indicated that the 'follower' response was actually slightly better than the response in the simulation due to some modeling errors for the determination of the nonlinear mathematical model. Figure 6-28 shows the altitude for both aircraft, while the Euler angle time histories for both the 'leader' and 'follower' aircraft are shown in Figure 6-29.

Formation Flight - 3D Plot

Initial Position
(leader)
t=256.56s

Initial Position
(follower & simulator)

200

Z axis(m)

100

0

200

100

0

-100

-200

-400

-300

-200

-100

0

100

200

300

t=292.56

Y axis(m)

X axis(m)
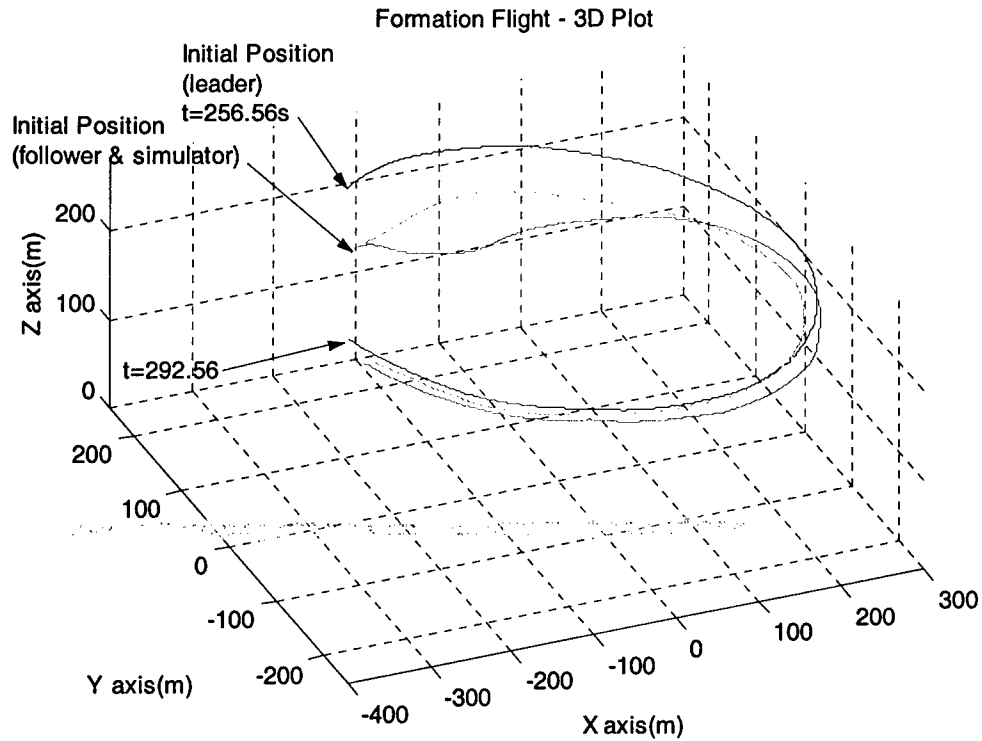
Figure 6-26: 2-Aircraft Formation Flight Test Oct. 1ˢᵗ 2004 - Flight Data and Simulation (3D Plot)
(Blue=Leader, Green=Follower, Magenta=Simulation)

Formation Flight - X-Y Plot

	Leader
	Follower
	Simulator

300

250

200

150

100

50

0

-50

-100

-150

-200

-250

Initial Position
(leader) t=256.56s

Initial Position
(follower & simulator)

t=292.56s

Y axis(m)

-400   -300   -200   -100   0   100   200   300

X axis(m)
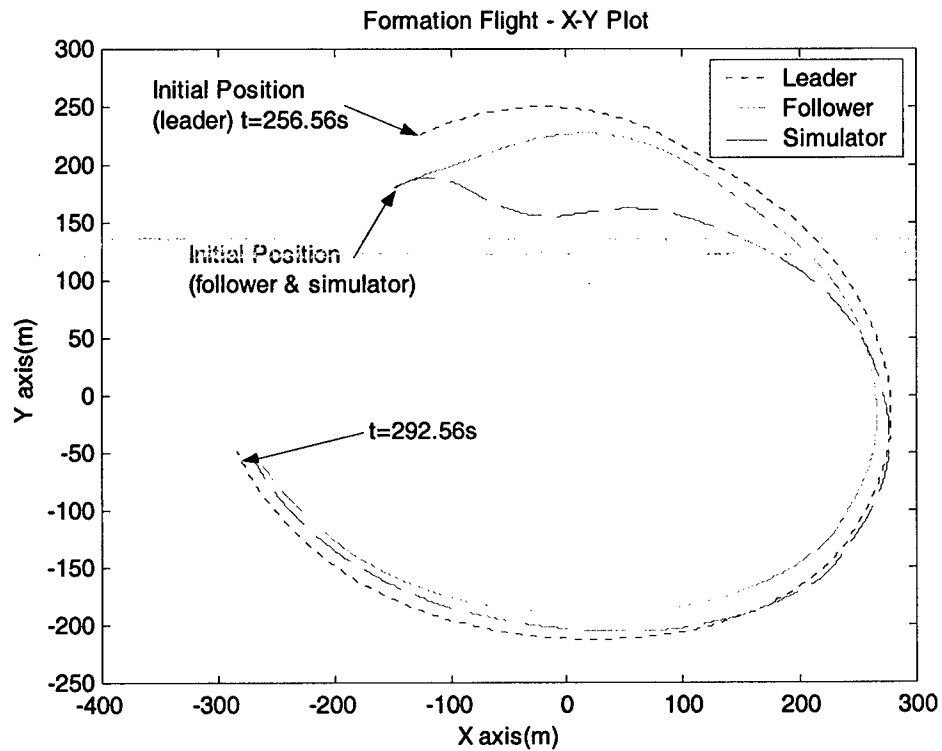
Figure 6-27: 2-Aircraft Formation Flight Test Oct. 1ˢᵗ 2004 - Flight Data and Simulation (X-Y Plane)
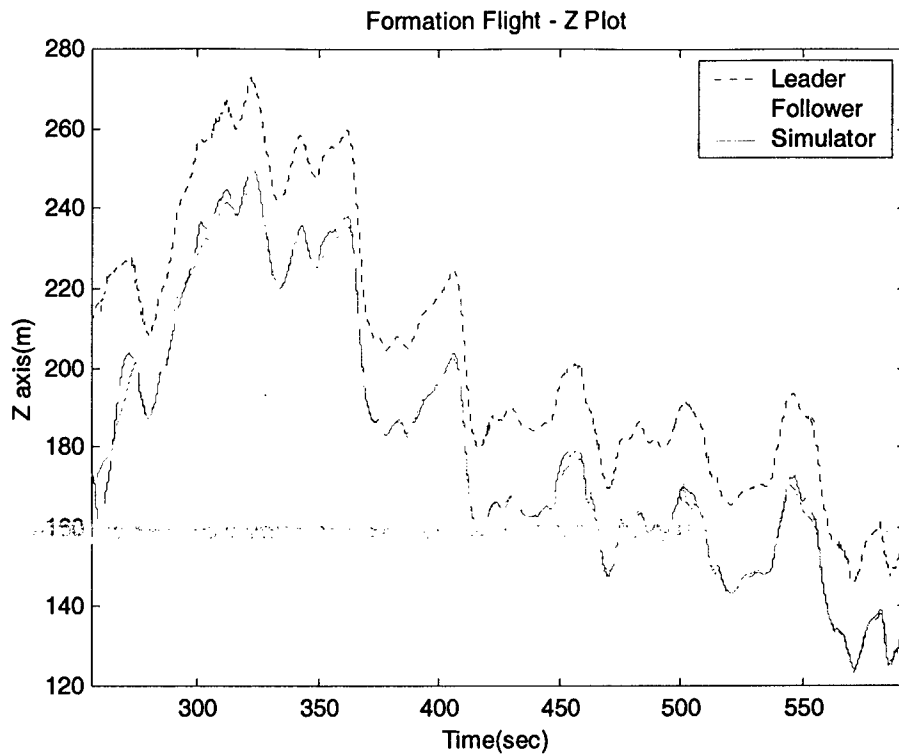
Figure 6-28: 2-Aircraft Formation Flight Test Oct. 1ˢᵗ 2004 - Flight Data and Simulation (Z-Plot)
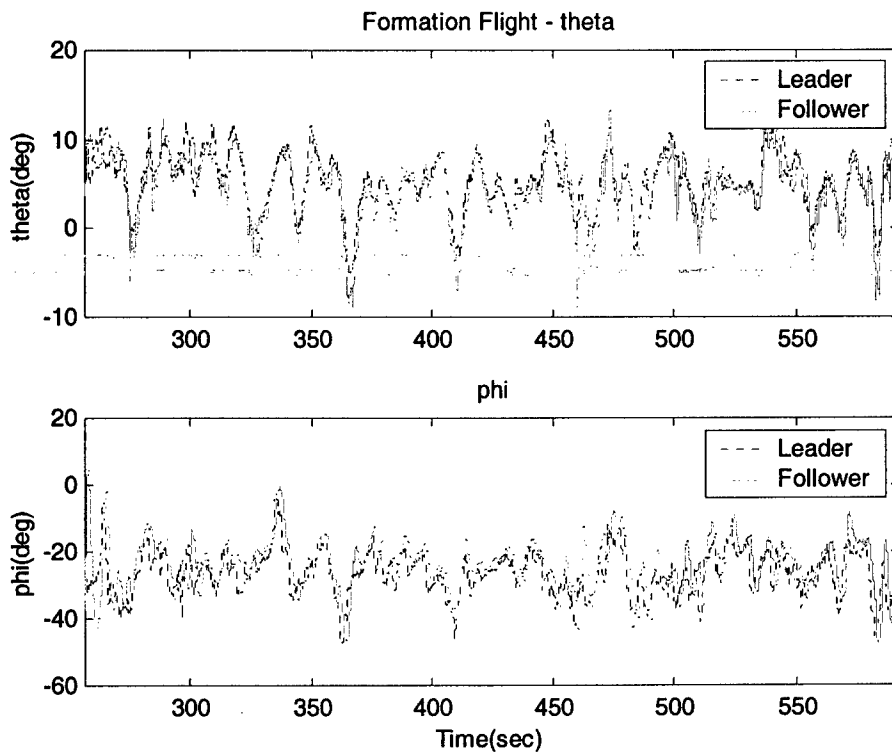
Figure 6-29: 2-Aircraft Formation Flight Test Oct. 1ˢᵗ 2004 - Euler Angles

The tracking errors are shown in Figure 6-30 in terms of VD, LD, and FD. Again, in this flight experiment the 'follower' was set to track an inside trajectory with respect to the 'leader' aircraft.
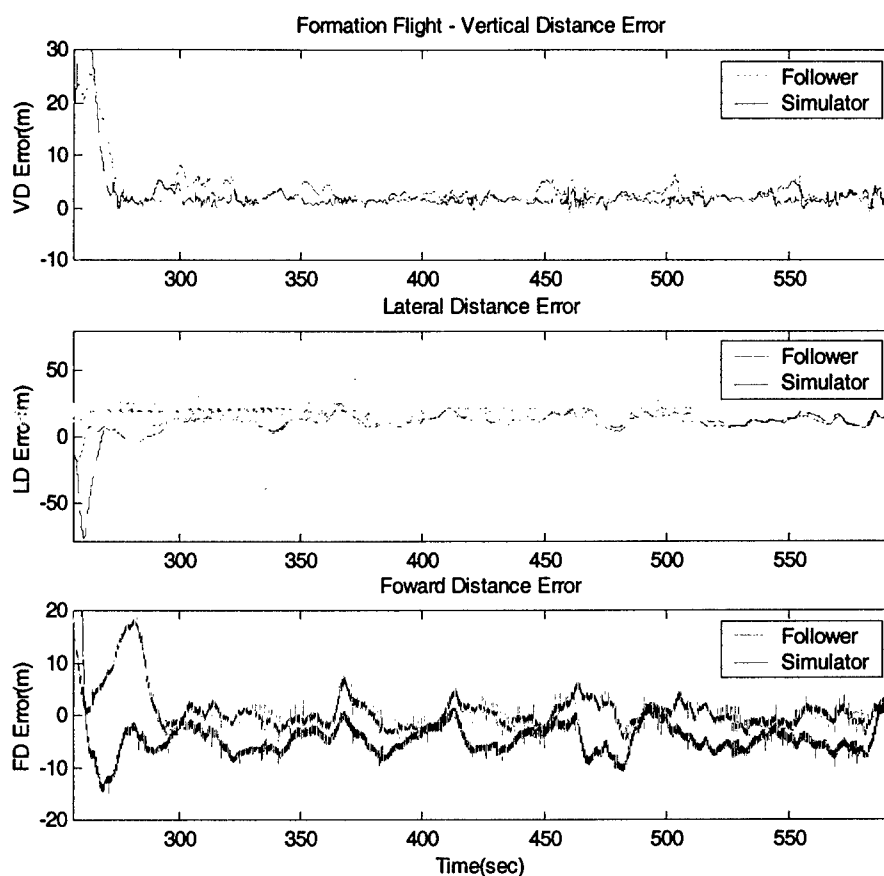
Figure 6-30: 2-Aircraft Formation Flight Test Oct. 1ˢᵗ 2004 - Flight Data and Simulation (Tracking Errors)

From a detailed analysis of the flight data, the formation tracking errors were substantially different with respect to the first two formation flights. Specifically, the 'follower' aircraft performance improved with respect to the forward distance tracking; however, a slightly increased lateral distance error was also noticed.

6.11.4 - October 6th 2004 Flight Testing

The October 6th, 2004 flight was essentially a repetition of the flight experiment performed on October 1st, 2004 with one important modification. In fact, formation flight was engaged and disengaged multiple times during the flight. The sequence of the flight activities is shown in Table 6-4.

	Blue Aircraft	Green Aircraft
Computer Clock Offset (sec)	0	8.50
Take Off Time (sec)	182.8	212.6
Landing Time (sec)	681.44	758.54
Flight Duration (sec)	498.64	545.94
Controller Activation 1 (sec)	-	252.18
Controller Deactivation 1 (sec)	-	327.3
Controller Activation 2 (sec)	-	389.44
Controller Deactivation 2 (sec)	-	600.12
Formation Duration 1 (sec)	137.26	
Formation Duration 2 (sec)	272.82	

Table 6-4: 2-Aircraft Formation Flight Test Oct. 6th 2004 - Flight Activities

For clarity purposes again, only the flight-testing results for the 1st lap of the 2nd formation engagement - starting at t=389.44 s - are shown in Figures 6-31 through 6-35. Figure 6-31 shows the 3D plot of both the measured and simulation flight data while Figure 6-32 displays the X-Y plot of the aircraft trajectories. Figure 6-33 provides the altitude flight data for the height comparison between the aircraft. The Euler angle response of both the 'leader' and 'follower' aircraft during the formation engagement are shown in Figure 6-34. Finally, the formation tracking errors are shown in Figure 6-35.

Formation Flight - 3D Plot

t=425.44sec

t=389.44sec

Initial Position
(follower & simulator)

Initial Position
(Leader)

Z axis(m)

200

150

100

50

0

200

100

0

-100

-200

Y axis(m)

-400   -300   -200   -100   0   100   200   300

X axis(m)
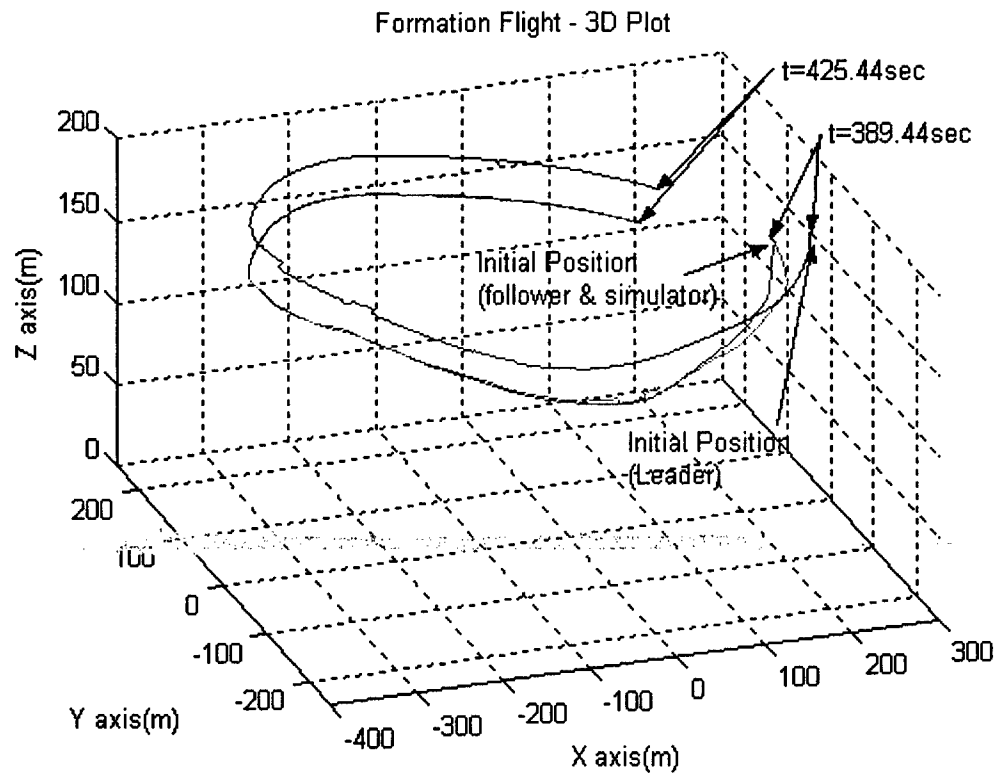
*Figure 6-31: 2-Aircraft Formation Flight Test Oct. 6th 2004 - Flight Data and Simulation (3D Plot)
(Blue=Leader, Green=Follower, Magenta=Simulation)*

Formation Flight - X-Y Plot

- - - - Leader
———— Follower
——— Simulator

t=425.44sec

t=389.44sec

Initial Position
(follower)

Initial Position
(Leader)

Y axis(m)

300

250

200

150

100

50

0

-50

-100

-150

-200

-250

-400   -300   -200   -100   0   100   200   300

X axis(m)
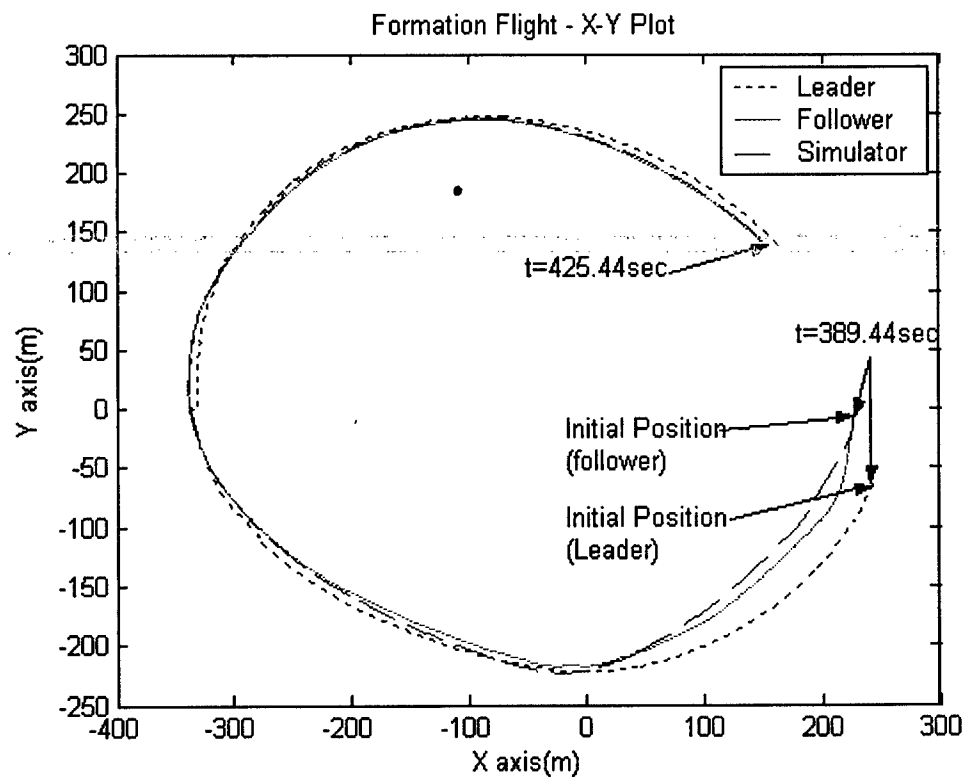
Figure 6-32: 2-Aircraft Formation Flight Test Oct. 6th 2004 - Flight Data and Simulation (X-Y Plane)
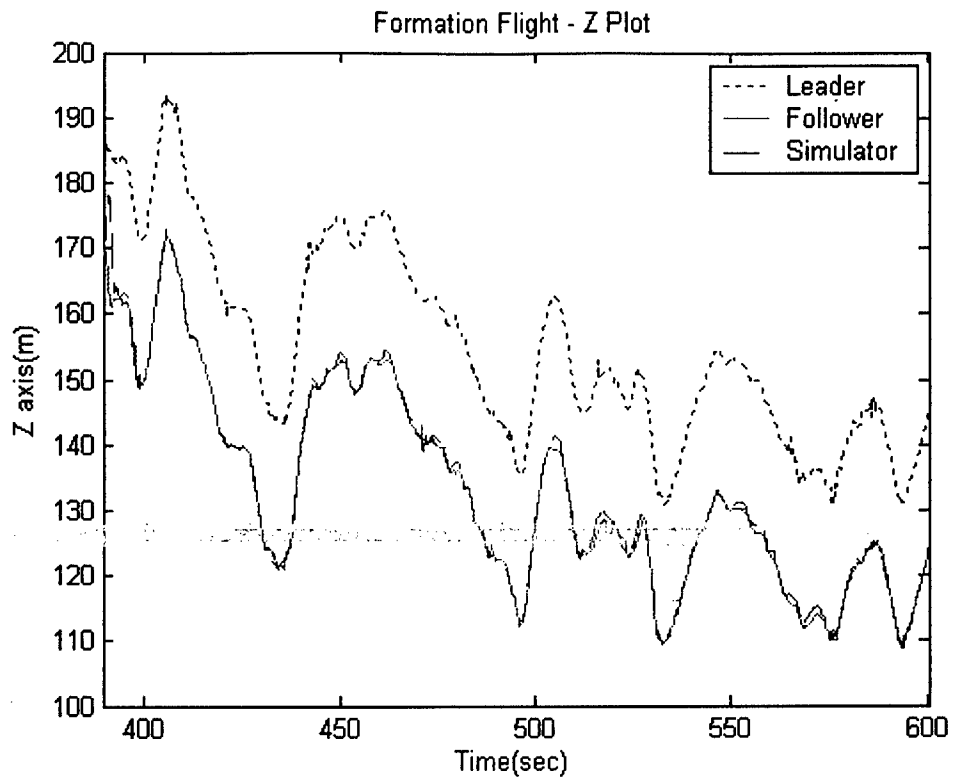
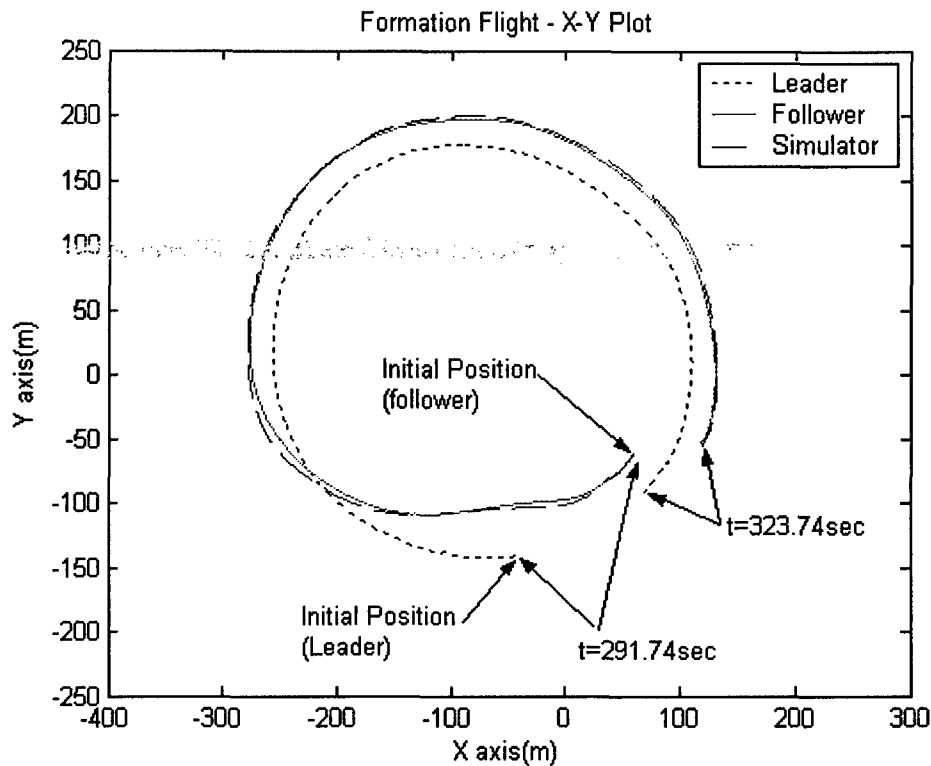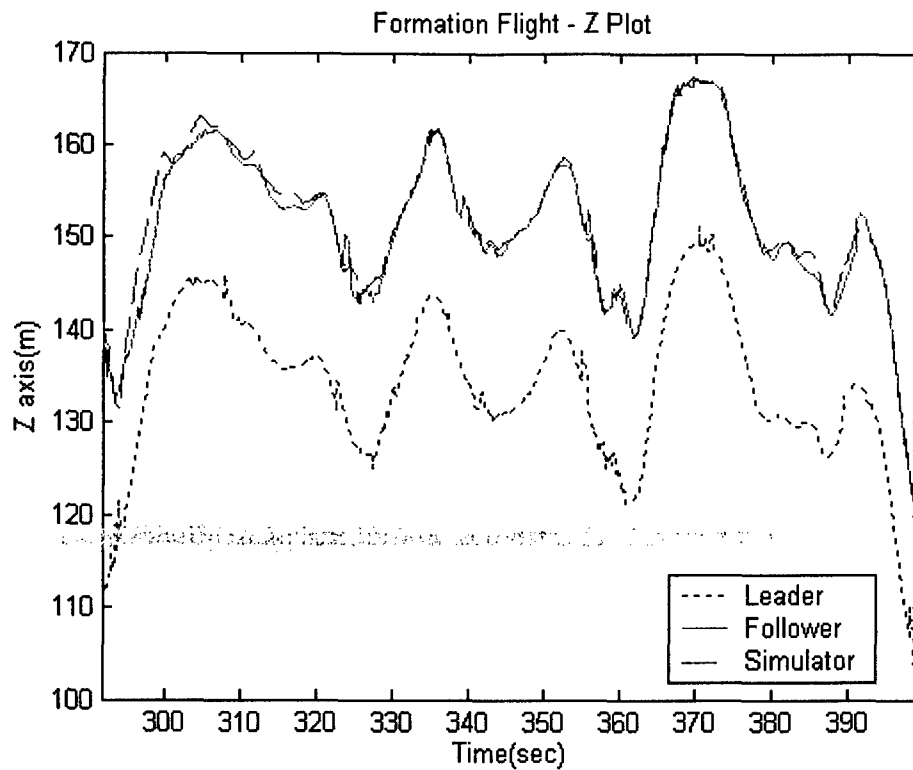*Figure 6-33: 2-Aircraft Formation Flight Test Oct. 6th 2004 - Flight Data and Simulation (Z-Plot)*
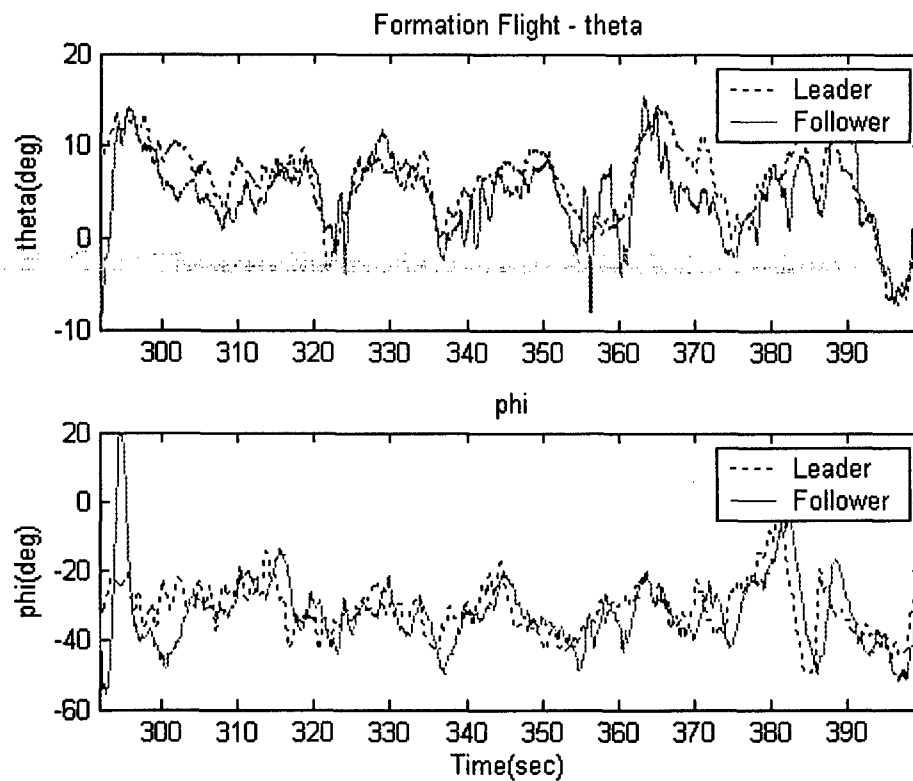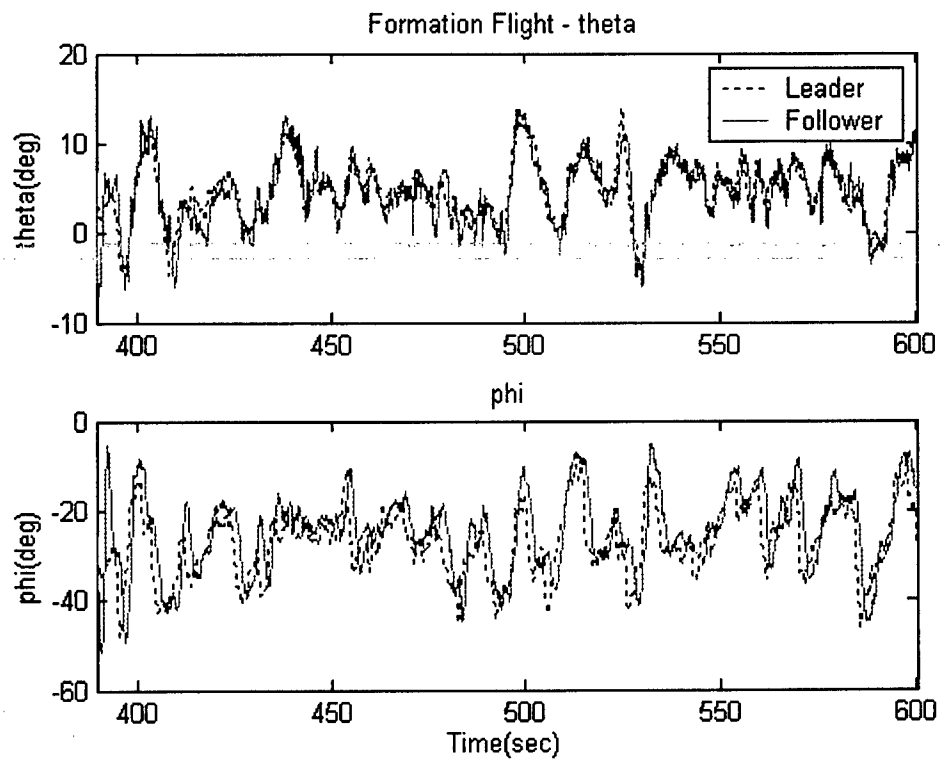

Figure 6-34: 2-Aircraft Formation Flight Test Oct. 6th 2004 - Euler Angles
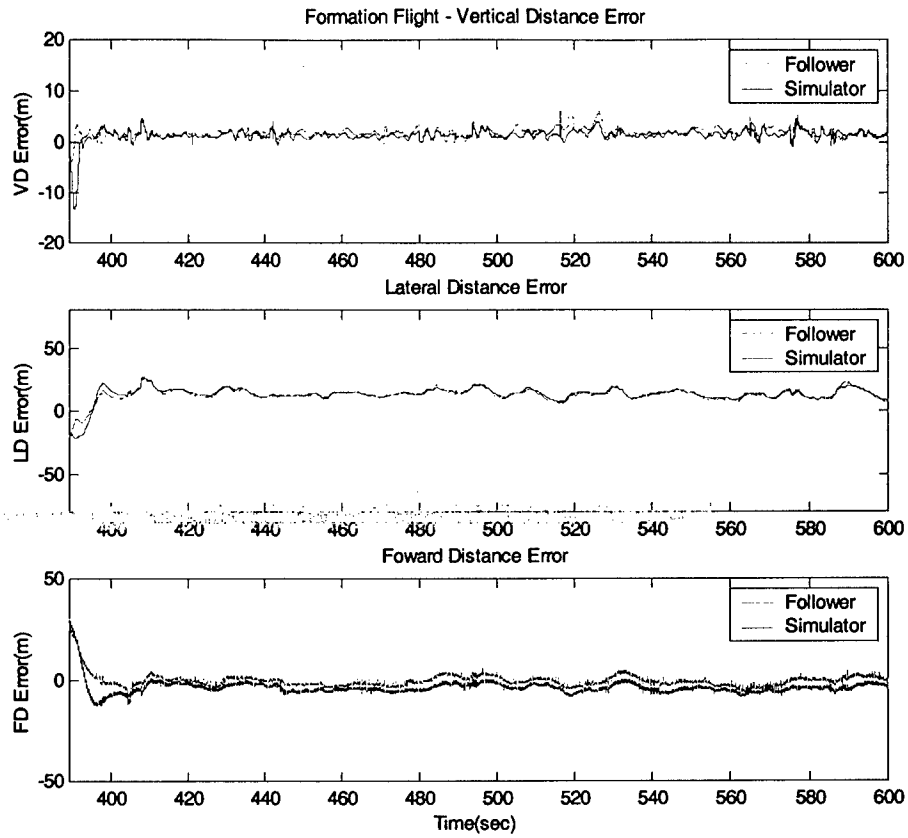
Figure 6-35: 2-Aircraft Formation Flight Test Oct. 6th 2004 - Flight Data and Simulation (Tracking Errors)

6.11.5 - 2-Aircraft Formation Tracking Errors

A detailed statistical analysis was performed using the flight data from all four 2-aircraft formation flights, including comparable results from a VL flight test. The statistical properties of the tracking errors - calculated with the flight data from 30 seconds after the formation control activation to the controller disengagement - are summarized in Table 6-5 below for both flight data and simulation data. The results showed satisfactory tracking performance under tight maneuvers at high Euler angles and high angular rates during the engagement of the formation controller. For a fair assessment of the performance of the formation control laws it should be recalled that these controllers were never evaluated at 'classic' steady state conditions - since the aircraft were never flown at steady rectilinear flight conditions – due to the need of maintaining the aircraft always within visible range. In other words, the statistical analysis was performed over a series of transients, each of them associated with a turn at high bank angles and substantial roll rates.

Flight Test		f_c (m)	l_c (m)	h_c (m)	Forward Distance Error (m)		Lateral Distance Error (m)		Vertical Distance Error (m)	
					Mean	STD	Mean	STD	Mean	STD
June 23rd 2004	Flight Data	30	30	-20	21.0183	5.2317	-12.397	5.1434	1.2534	1.0633
'virtual leader' Test	Simulation	30	30	-20	27.6886	4.1371	-11.047	3.8218	1.4737	0.8493
June 29th 2004	Flight Data	30	30	-20	29.6433	2.8142	-20.268	3.6034	2.4382	1.4308
2- Aircraft Formation	Simulation	30	30	-20	28.0582	2.5219	-18.547	3.6050	2.1194	1.1172
September 2nd 2004	Flight Data	20	20	-20	31.8633	3.7438	-8.6683	4.0247	2.0957	1.6019
2- Aircraft Formation	Simulation	20	20	-20	28.2605	3.8299	-7.1349	4.0184	1.7336	1.3297
October 1st 2004	Flight Data	20	-20	20	-0.3186	2.1447	11.8658	3.7101	2.2789	1.1841
2- Aircraft Formation	Simulation	20	-20	20	-4.8260	2.5440	14.0109	3.6275	1.6780	0.7756
October 6th 2004	Flight Data	20	-20	20	-0.9604	2.1480	13.3853	3.1714	1.9246	0.8705
2- Aircraft Formation	Simulation	20	-20	20	-4.1937	1.8422	13.8492	2.8407	1.5188	0.6932

Table 6-5: Flight Testing Data Analysis for 2-Aircraft Formation

6.12 - 3-Aircraft Formation Flight

After 4 successful 2-aircraft formation flights and successful communication flight experiments, the final phase involved the flight-testing of 3-aircraft formation.

The designed sequence for the 3-aircraft formation experiment was the following. The jet engines for all aircraft were started at approx. the same time running with auxiliary fuel tanks. The 'blue' aircraft - acting as the 'leader' - took off first while the 'red' aircraft ('follower #1') took off approximately 35 seconds later. Next, after both aircraft reached a pre-selected 'rendezvous' area, a 2-aircraft formation was first engaged with the 'follower #1' aircraft taking on an 'outside' tracking pattern. Once the 2-aircraft formation was engaged and stabilized for approx. one lap, the 'follower #2' aircraft was instructed to launch and join the other aircraft already engaged in formation. After the 'green' ('follower #2') aircraft reached a 'rendezvous' position (under manual control) behind the 2-aircraft formation, the R/C pilot for the 'follower #2' aircraft engaged the 'green' formation controller taking on an 'inside' track. Finally, the 3-aircraft formation was solely controlled by the 'leader' R/C pilot with the two 'follower' OBC systems executing fully autonomous GPS-based formation control. The total engagement of the 3-aircraft formation lasted for approx. 275 seconds. The entire flight experiment lasted approx. 900 seconds. A detailed sequence of the flight activities is shown in Table 6-6.

	Blue Aircraft	Red Aircraft	Green Aircraft
Computer Clock Offset (sec)	0	6.72	22.50
Take Off Time (sec)	179.18	207.54	350.3
Landing Time (sec)	719.64	794.43	842.1
Flight Duration (sec)	540.46	586.89	491.8
Controller Activation (sec)	-	297.12	401.92
Controller Deactivation (sec)	-	677.34	677.6
Formation Duration (sec)	-	380.22	275.68
3-Aircraft Formation Duration (sec)	275.42		

Table 6-6: 3-Aircraft Formation - Flight Activity

Figure 6-36 shows a ground photograph of the 3-aircraft formation on November 23rd, 2004 taken after the rendezvous of the 3rd aircraft ('follower #2').

Figure 6-36 shows a ground photograph of the 3-aircraft formation on November 23rd, 2004 taken after the rendezvous of the 3rd aircraft ('follower #2').
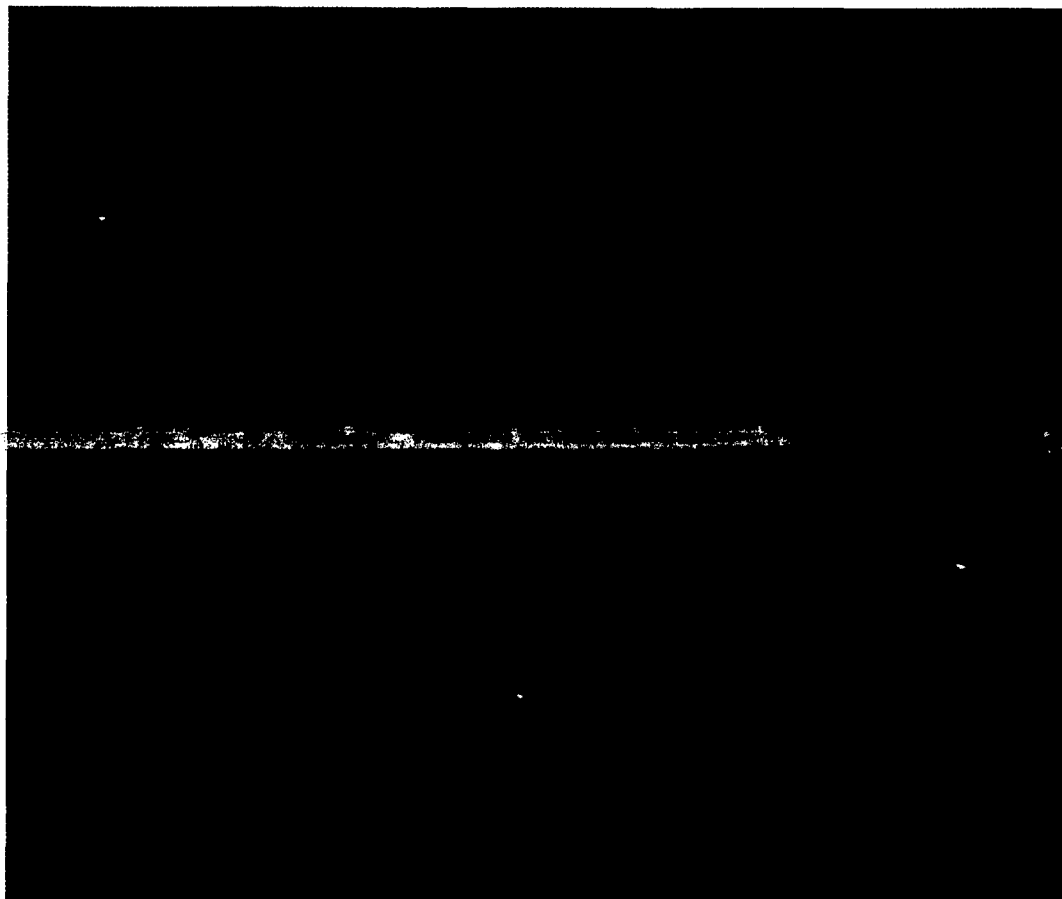
Figure 6-36: 3-Aircraft Formation Flight Test November 23rd 2004

Figure 6-37 shows a collection of images obtained from the on-board DV camera installed on the 'red' aircraft ('follower #1') during the 3-aircraft formation engagement.
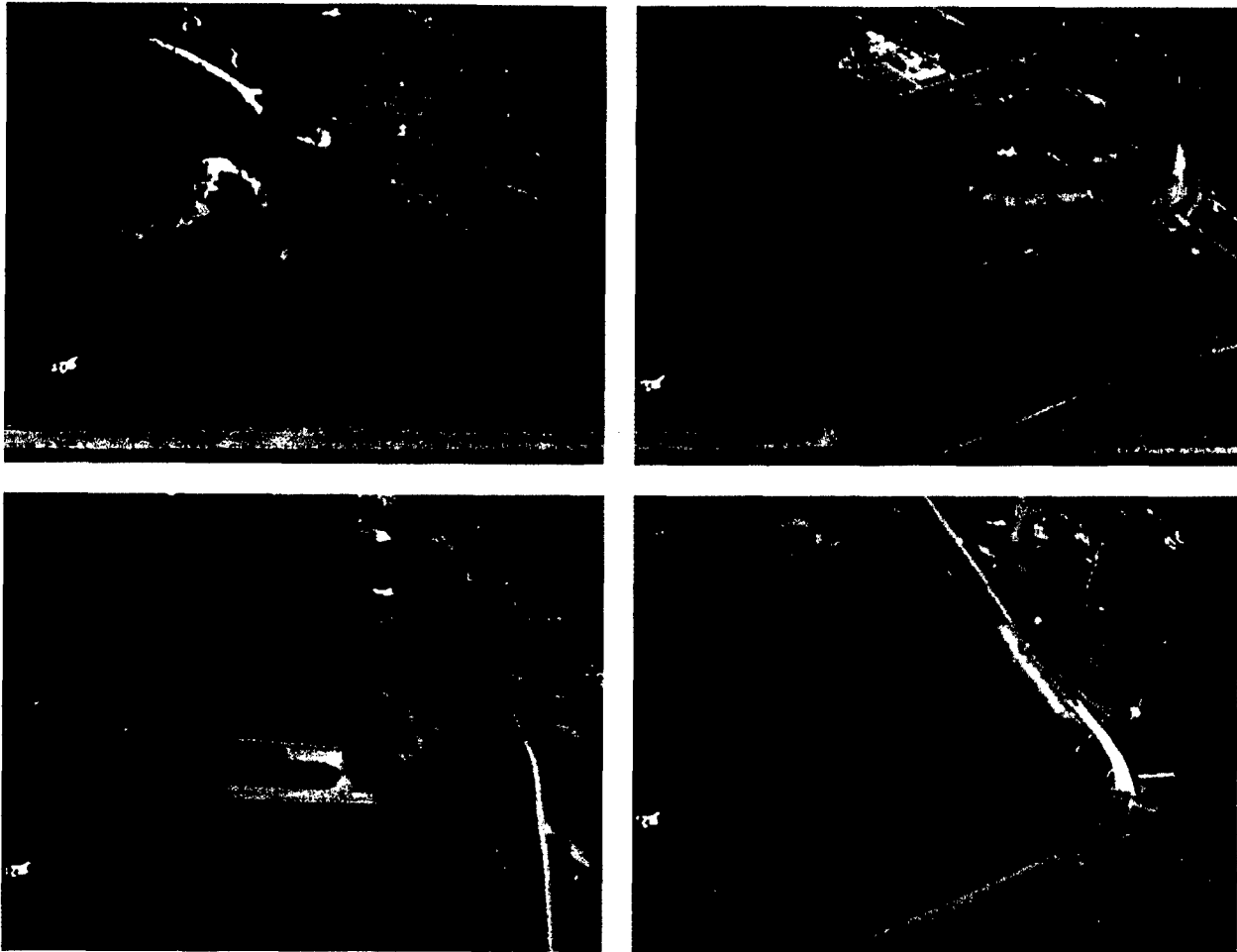
Figure 6-37: 3-Aircraft Formation Flight On-Board Camera Views

The following formation parameters were set for this experiment:

'follower #1', 'red' aircraft: $l_c = -20m$, $f_c = 20m$, $h_c = 20m$

'follower #2', 'green' aircraft: $l_c = 20m$, $f_c = 20m$, $h_c = -20m$

Figures 6-38 through 6-48 shows samples of the flight data collected from the 3-aircraft formation. Figure 6-38 represents a 3D plot while Figure 6-39 shows the X-Y plot for the final lap of the formation engagement. The color legend in the figures below is consistent with the actual paint schemes for each aircraft, where the 'leader', the 'follower #1' and 'follower #2' are indicated by blue, red, and green lines respectively.

130

3-Plane Formation Flight - 3D Plot

Initial Position
t=401.92s

t=437.92s
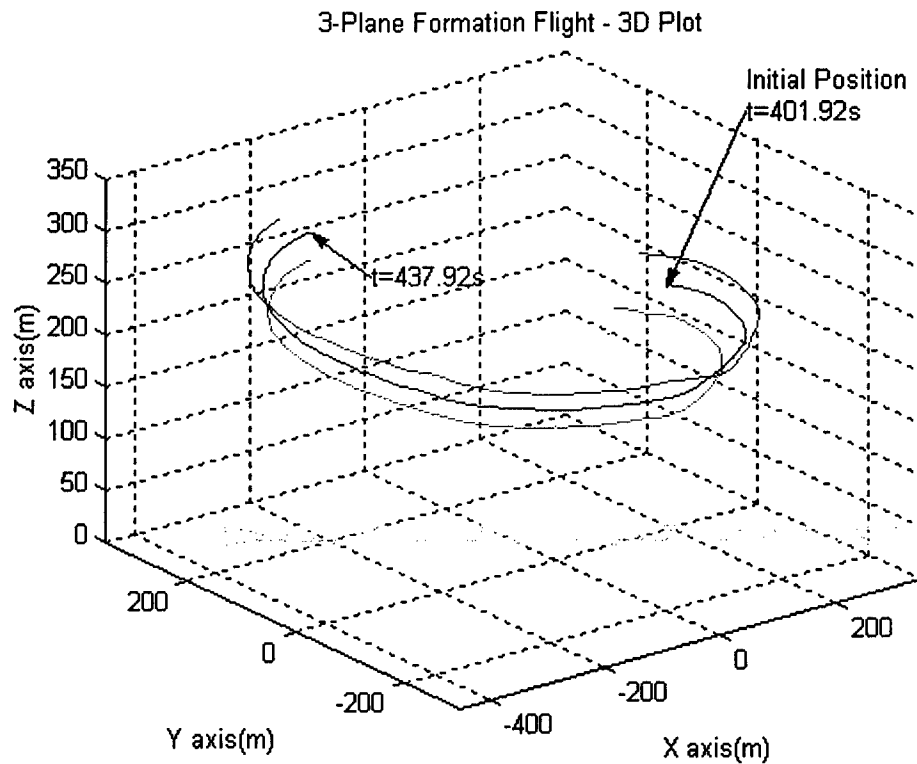
*Figure 6-38: 3- Aircraft Formation Test Nov. 23rd 2004 - Flight Data (3D Plot)
(Blue=Leader, Red=Outside Follower, Green=Inside Follower)*

3-Plane Formation Flight - X-Y Plot

Leader
Follower Green
Follower Red

t=437.92s

Initial Position
t=401.92s
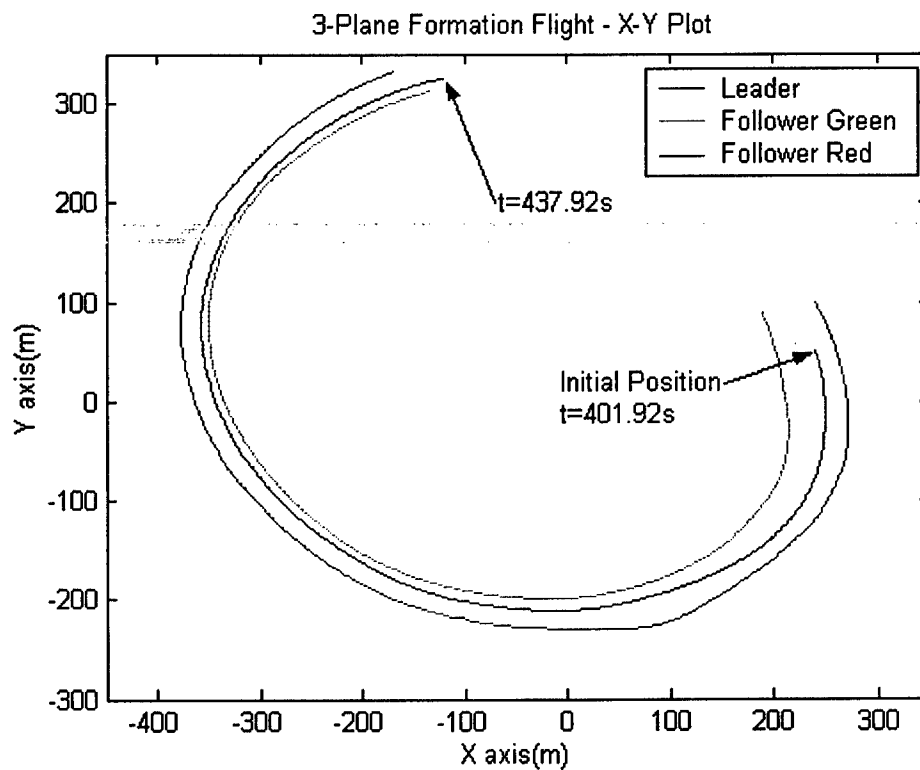
Figure 6-39: 3-Aircraft Formation Test Nov. 23rd 2004 - Flight Data (X-Y Plane)

131

Figure 6-40 shows the altitude flight data.
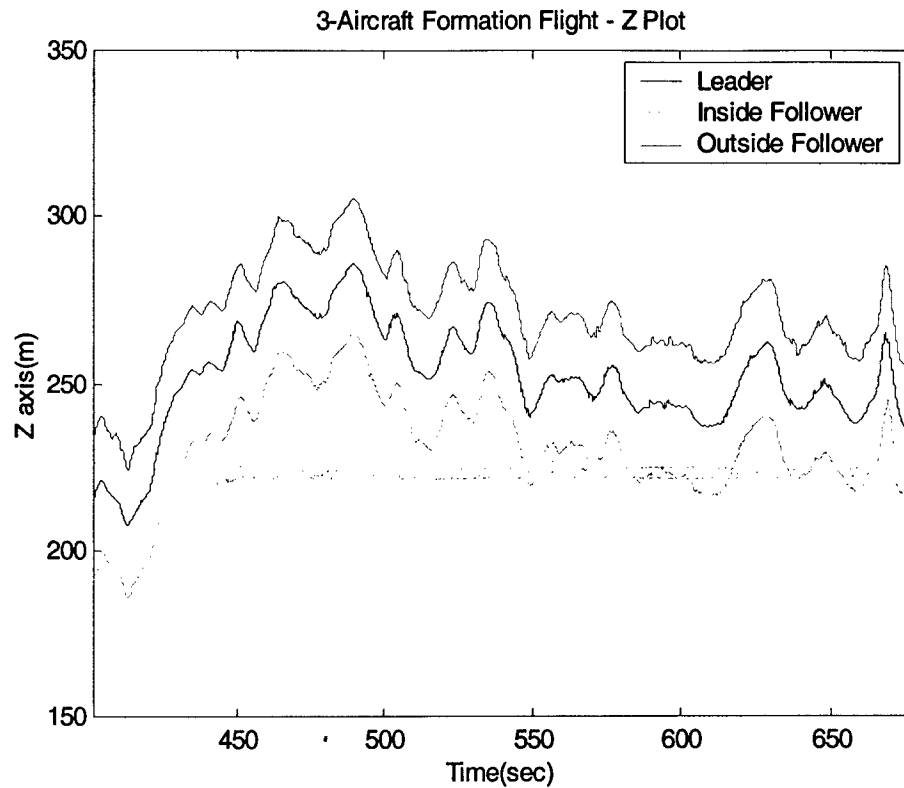
Figure 6-40: 3-Aircraft Formation Test Nov. 23rd 2004 - Flight Data (Z-Plot)

Figures 6-41 through 6-43 show the Euler angles, the angular rates, and the linear acceleration from the OBCs for each of the aircraft.
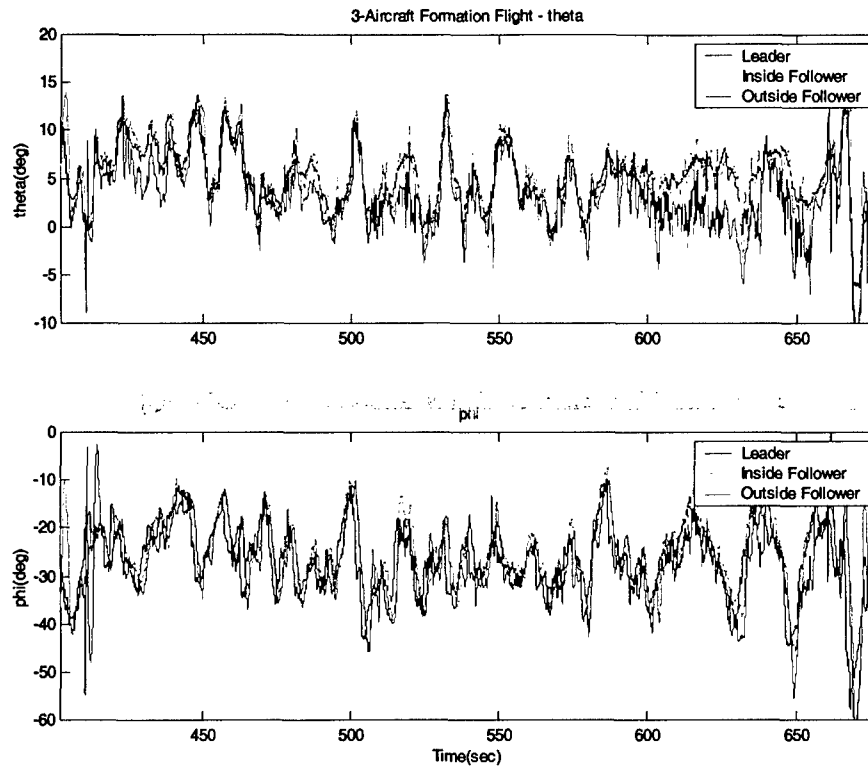
Figure 6-41: 3-Aircraft Formation Test Nov. 23rd 2004 - Euler Angles
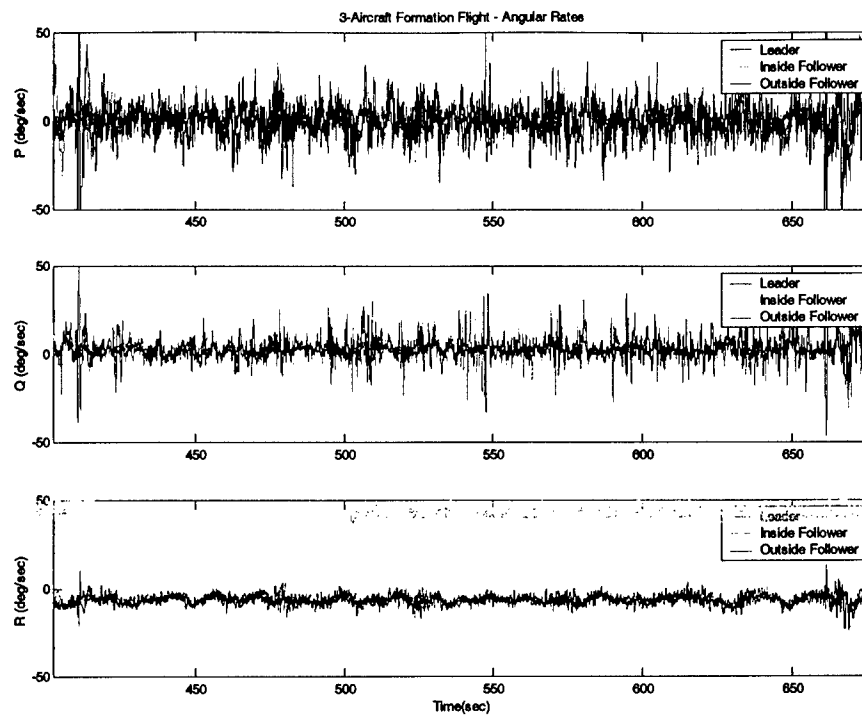
Figure 6-42: 3-Aircraft Formation Test Nov. 23rd 2004 - 3-Axis Angular Rates
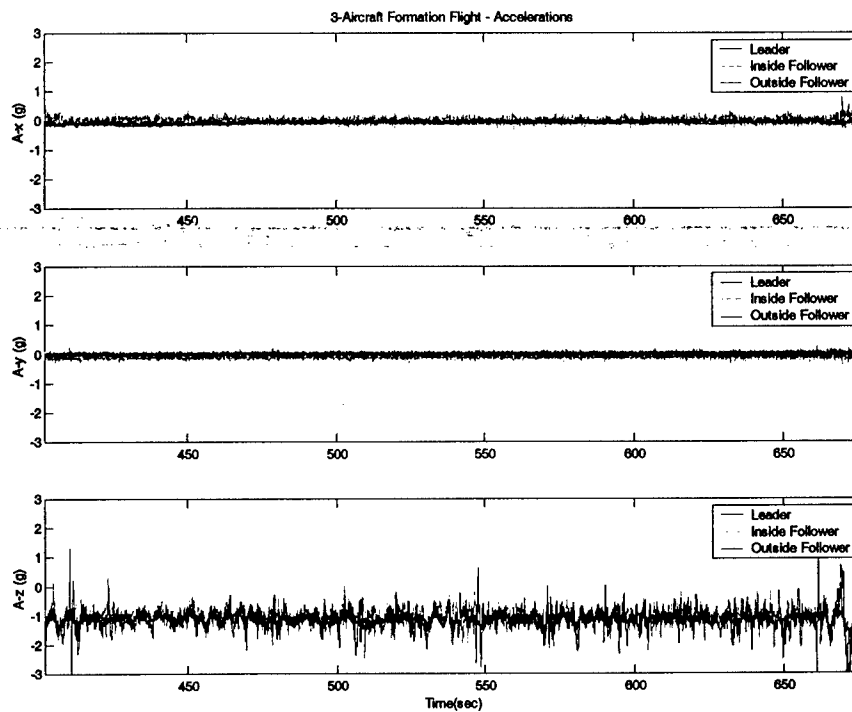
Figure 6-43: 3-Aircraft Formation Test Nov. 23rd 2004 - 3-Axis Accelerations

134

Figure 6-44 shows the deflections of the primary control surfaces for the 3 aircraft while formation control was engaged.
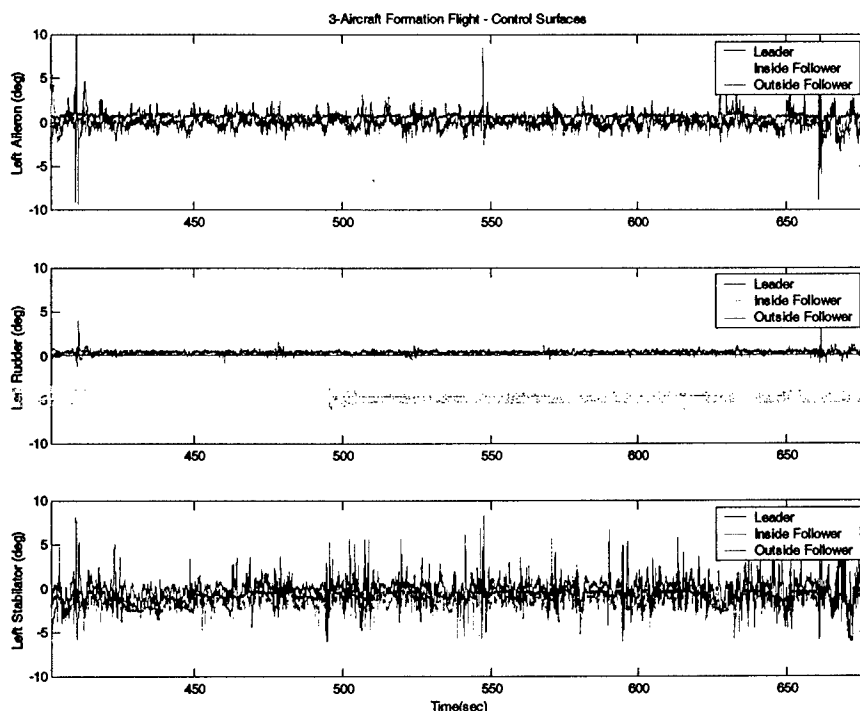
Figure 6-44: 3-Aircraft Formation Test Nov. 23rd 2004 - Control Surfaces Deflections

Figures 6-45 and 6-46 show the control commands generated by the formation control laws executed by the OBCs. Particularly, Figure 6-45 shows the inner-loop controller commands sent to each control surface while Figure 6-46 illustrates the outer-loop commands generated by the NLDI controller. As observed in the 2-aircraft formation, the pure delay associated with the engine model limited the bandwidth of the control system. Furthermore, the analysis of the throttle command, in Figure 6-45, provides another reason for the better performance on the forward channel of the 'inside' tracking formation with respect to the 'outside' tracking formation. In fact, during the 3-aircraft formation test, the 'inside follower' was required to fly at a lower airspeed with respect to the 'leader' while the 'outside follower' required a higher airspeed. This, in turn, required a higher power output from the 'outside follower' propulsion system to maintain the desired formation. However, as shown in Figure 6-45, higher output values were limited by the on-board software, which prevented the aircraft in reaching excessively high airspeed values.

135
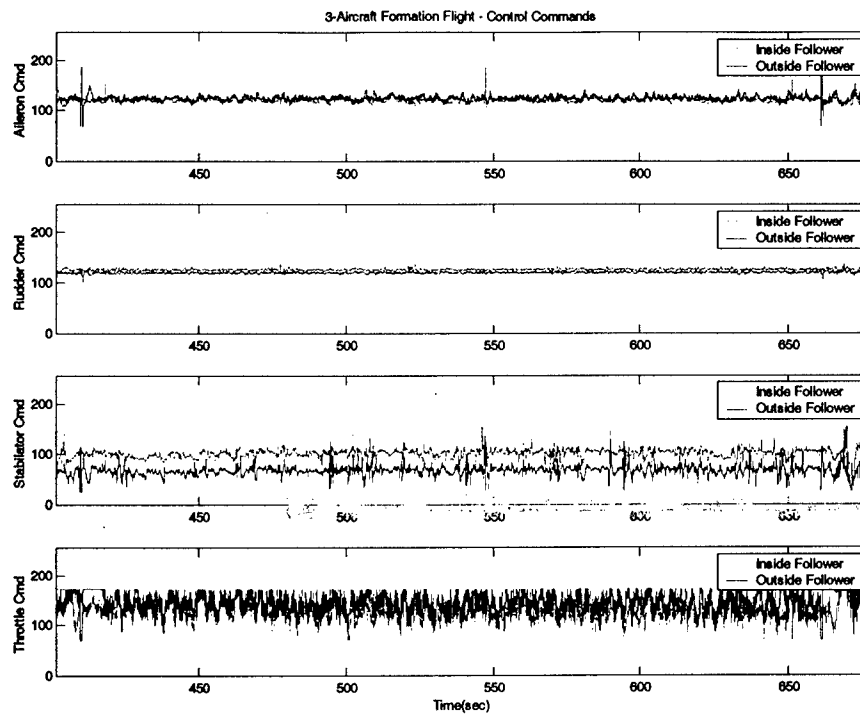
Figure 6-45: 3-Aircraft Formation Test Nov. 23rd 2004 - Control Commands
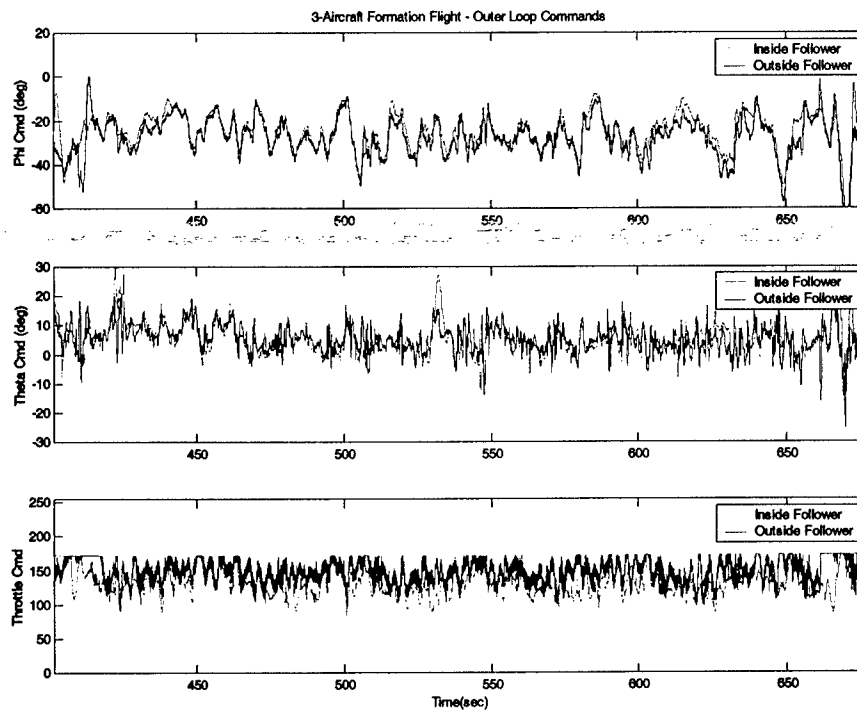
Figure 6-46: 3-Aircraft Formation Test Nov. 23rd 2004 - Outer Loop Commands

136

Finally Figure 6-47 displays the tracking errors along all three channels.
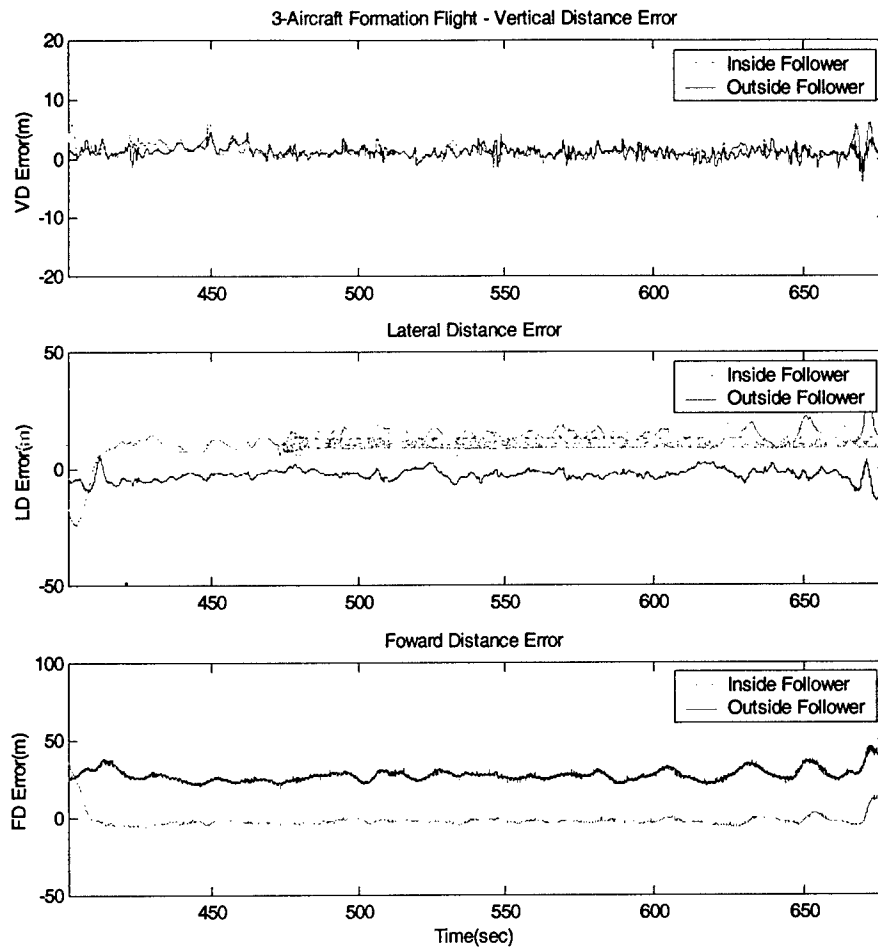
Figure 6-47: 3-Aircraft Formation Test Nov. 23rd 2004 - Flight Data (Tracking Errors)

The statistical analysis of the steady state tracking error for the 3-aircraft formation flight test is shown in Table 6-7. This analysis also included data from the 'formation simulator'.

Nov.23rd 2004 3-aircraft formation		f_c (m)	l_c (m)	h_c (m)	Forward Distance Error (m)		Lateral Distance Error (m)		Vertical Distance Error (m)	
					Mean	STD	Mean	STD	Mean	STD
Green Aircraft	Flight Data	20	-20	20	-2.4859	2.4616	13.2382	3.4461	1.1461	1.0444
	Simulation	20	-20	20	-3.5912	2.4980	14.3095	3.3037	1.3390	0.7112
Red Aircraft	Flight Data	20	20	-20	27.2798	3.7323	-2.5899	2.2851	1.1527	0.9462
	Simulation	20	20	-20	25.2998	3.8182	-0.4550	1.9831	1.1908	0.6646

Table 6-7: 3-Aircraft Formation Test Nov. 23rd 2004 - Flight Data Analysis

The 3-aircraft formation results mostly confirmed the performance of the formation control laws from the previous 2-aircraft formation flight phase. The 'outside' aircraft - 'follower #2' - achieved desirable lateral tracking performance but with a larger forward distance tracking error. On the opposite, the 'inside' aircraft had desirable forward tracking and a slightly degraded lateral distance performance. Overall, the vertical channel provided excellent tracking performance for both 'follower' aircraft. Because of the visual range flight restrictions the 'leader' aircraft was required to fly a circular pattern with even tighter rolling and yawing maneuvers with respect to the 2-aircraft formation case. Therefore, the tracking errors were slightly larger than in the case of 2-aircraft formation.

Once again, for a fair assessment of the performance of the formation control laws, it should be emphasized that these controllers were never evaluated at a 'classic' steady state condition and that the statistical analysis was performed over a series of transients - associated with the tight turns of the formation.

Conclusions

This report summarizes the effort of a research project focused on demonstrating closed-loop formation flight using flying aircraft models. The flight-testing program was conducted over three flight seasons (2002 thru 2004) and validated the overall design of the formation (linear inner and NLDI outer loop) control laws. The flight-testing phases started with a detailed evaluation of the aircraft handling qualities and dynamic characteristics and then moved on assessing the performance of the electronic payload, specifically the data acquiring capabilities and the real time execution of control laws. The application of a 'virtual leader' technique proved very useful in initially testing the formation control laws and provided a safe and simple testing stage. During the final flight season, a total of five-formation flight experiments were successfully performed, specifically four 2-aircraft formations and one 3-aircraft formation.

The research effort lasted a total of approx. 40 months and was a remarkable professional experience for all those involved, from the PI to the undergraduate students and the pilots. As typical for large and complex research efforts such as this, many important lessons were learned. Overall, it was felt that the project was very successful and provided a very real demonstration of the challenges associated with GPS-based formation flight. Considering all the different phases, a total of approx. 100 flight experiments were conducted without any catastrophic failure. According to available information, to the best of the PI's knowledge, the WVU team has been the first research team in the world ever to achieve 3-aircraft GPS-based formation control with 3 high performance jet-powered aircraft.

References

1. Ljung, L.,: System Identification: Theory for the User, 2nd Ed., PTR Prentice Hall, Upper Saddle River, Englewood Cliffs, NJ, 1999

2. Maine, R.E., Iliff, K.W., "Identification of Dynamic Systems: Theory and Formulation", NASA RF 1168, June 1986

3. Stevens, B. and Lewis, F. "Aircraft Control and Simulation," John Wiley & Sons, NY, 1992

4. Rauw, M.O.: "FDC 1.2 - A Simulink Toolbox for Flight Dynamics and Control Analysis". Zeist, The Netherlands, 1997. ISBN: 90-807177-1-1, http://www.dutchroll.com/

5. Kirschbaum, H.W., "Estimation of Moments of Inertia of Airplanes from Design Data", NACA TN-575, 1936

6. Miller, M.P., "An Accurate Method of Measuring the Moments of Inertia of Airplanes:, NACA TN-351, 1930

7. Soule, H.A., Miller, M.P., "The Experimental Determination of the Moments of Inertia of Airplanes", NACA Report No. 467, 1933

8. Stengel, R.F., "Optimal control and estimation", Dover Publication Inc. New York, 1994

9. Hock, W. and K. Schittowski, "A Comparative Performance Evaluation of 27 Nonlinear Programming Codes," Computing, Vol. 30, p. 335, 1983

10. Isidori, A., "Nonlinear Control Systems", Springer-Verlag, London, Third edition, 1995

11. Campa, G., Wan, S., Napolitano, M.R., Seanor, B., Fravolini, M.L., "Design of Formation Control Laws for Maneuvered Flight", The Aeronautical Journal, pg 125-134, March 2004

12. The VRML Web Repository (Dec. 2002): http://www.web3d.org/x3d/vrml/

Appendix A

List of technical publications already published*

ARCHIVAL JOURNALS

Campa, G., Wan, S., Napolitano, M.R., Seanor, B., Fravolini, M.L., **"Design of Formation Control Laws for Maneuvered Flight"**, *The Aeronautical Journal*, pg 125-134, March 2004

CONFERENCE PROCEEDINGS

Pollini, L., Mati, R., Innocenti, M., Campa, G., Napolitano, M., **"A Synthetic Environment for Simulation of Vision-Based Formation Flight"** *AIAA Modeling and Simulation Technologies Conference 2003*, AIAA 2003-5376, August 11-14, 2003, Austin, TX

Wan, S., Campa, G., Napolitano, M.R., Seanor, B., Gu, Y., **" Design of Formation Control Laws for Research Aircraft Models"**, *AIAA Guidance Navigation and Control Conference 2003*, AIAA 2003-5730,August 11-14, 2003, Austin, TX

Campa, G., Napolitano, M.R., Seanor, B., Perhinschi, M.G., **"Design of Control Laws For Maneuvered Formation Flight"** *American Control Conference 2004*, June30-July2, 2004, Boston, MA

Seanor, B., Campa, G., Gu, Y., Napolitano, M.R., Rowe, L., Perhinschi, M.G., **"Formation Flight Test Results for UAV Research Aircraft Models"**, *AIAA 1ˢᵗ Intelligent Systems Technical Conference,* AIAA 2004-6251, September 20-22, 2004, Chicago, IL

Campa, G., Seanor, B., Gu, Y., Napolitano, M.R., **"NLDI Guidance Control Laws For Close Formation Flight"** *American Control Conference 2005*, June 6-10, 2005, Portland, OR

DESIGN OF FORMATION CONTROL LAWS
FOR MANEUVERED FLIGHT

Giampiero Campa[*], Sheng Wan[*], Marcello R. Napolitano[*], Brad Seanor[*], Mario Fravolini[+]
[*]Department of Mechanical and Aerospace Engineering
West Virginia University, Morgantown, WV 26506/6106
[+] Department of Electronic and Information Engineering
University of Perugia, 06100 Perugia, Italy

Abstract

This paper presents identification, control synthesis and simulation results for an YF-22 aircraft model designed, built, and instrumented at West Virginia University. The ultimate goal of the project is the experimental demonstration of formation flight for a set of 3 of the above models. In the planned flight configuration, a pilot on the ground maintains controls of the 'leader' aircraft while a wingman aircraft is required to maintain a pre-defined position and orientation with respect to the 'leader'. The identification of both a linear model and a nonlinear model of the aircraft from flight data is discussed first. Then, the design of the control scheme is presented and discussed with an emphasis on the amount of information, relative to the 'leader' aircraft, needed by the wingman to maintain formation. Using the developed nonlinear model, the control laws for a maneuvered flight of the formation are then simulated with Simulink[®] and displayed with the Virtual Reality Toolbox[®]. Simulation studies have been performed to evaluate the effects of specific parameters and the system robustness to atmospheric turbulence. The conclusions from this analysis have allowed the formulation of specific guidelines for the design of the electronic payload for formation flight.

A SYNTHETIC ENVIRONMENT FOR SIMULATION
OF VISION-BASED FORMATION FLIGHT

Lorenzo Pollini[+], Roberto Mati[+], Mario Innocenti[+],
Giampiero Campa[*], Marcello Napolitano[*]
[+] Department of Electrical Systems and Automation
University of Pisa, 56126 Pisa, Italy
[*]Department of Mechanical and Aerospace Engineering
West Virginia University, Morgantown, WV 26506/6106

Abstract

This paper describes the design of autopilots and formation control laws and then the simulation setup and the first results of a novel architecture for close formation flight based on computer vision. The reference aircraft model is the West Virginia University YF-22 model aircraft. The simulation setup includes aircraft dynamics, autopilots and formation keeping controller and a module that creates a synthetic environment for the simulation of the vision equipment based on a commercial software called Dyna-WORLDS. DynaWORLDS is capable of generating synthetic images as if were captured by the camera onboard the wingman. Uniquely identifiable infrared light markers (light emitters each with different wavelength) are applied to the 'leader' aircraft and a recent iterative, globally convergent, pose estimation algorithm (LHM) is adopted to reconstruct the 'leader' position and attitude. The formation control laws, designed with GPS measurements in mind, have been applied successfully with the 'leader' position, velocity and Heading estimates obtained from the vision system alone. A more feasible and less expensive solution using light markers with unique wavelength is then introduced and evaluated yielding the same performance of the previous case.

144

DESIGN OF FORMATION CONTROL LAWS
FOR RESEARCH AIRCRAFT MODELS

Sheng Wan, Giampiero Campa, Marcello R. Napolitano, Brad Seanor, Yu Gu
Department of Mechanical and Aerospace Engineering
West Virginia University, Morgantown, WV 26506/6106

Abstract

This paper presents the design approach and simulation results of the preliminary design of the formation control laws for YF-22 aircraft models designed and built at WVU. In the planned configuration, a pilot on the ground controls the 'leader' aircraft while the wingman is required to maintain a pre-defined position and orientation with respect to the 'leader' during flight. The modeling and the design of the control scheme are presented and discussed, with emphasis on the amount of information relative to the 'leader' needed by the wingman to maintain formation. For this purpose, a critical issue is the availability of Euler angle measurements from the 'leader' aircraft. The necessity of identifying a non-linear mathematical model of the aircraft is also discussed. Using the developed nonlinear model, he control of the formation has been simulated within Simulink® and displayed with the Virtual Reality Toolbox®.

DESIGN OF CONTROL LAWS FOR MANEUVERED FORMATION FLIGHT

Giampiero Campa, Marcello R. Napolitano, Brad Seanor, Mario G. Perhinschi
Department of Mechanical and Aerospace Engineering
West Virginia University, Morgantown, WV 26506/6106

Abstract

This paper presents identification, control synthesis and simulation results for an YF-22 aircraft model designed, built, and instrumented at West Virginia University. The goal of the project is the experimental demonstration of formation flight for a set of 3 of the above models. In the planned flight configuration, a pilot on the ground maintains controls of the 'leader' aircraft while a wingman aircraft is required to maintain a pre-defined position and orientation with respect to the 'leader'. The identification of both a linear model and a nonlinear model of the aircraft from flight data is discussed first. Then, the design of the control scheme is presented and discussed. Using the developed nonlinear model, the control laws for a maneuvered flight of the formation are then simulated with Simulink® and displayed with the Virtual Reality Toolbox®. Simulation studies have been performed to evaluate the effects of specific parameters and the system robustness to atmospheric turbulence. The results of this analysis have allowed the formulation of specific guidelines for the design of the electronic payload for formation flight.

FORMATION FLIGHT TEST RESULTS FOR UAV RESEARCH AIRCRAFT

Brad Seanor, Giampiero Campa, Yu Gu, Marcello Napolitano,
Larry Rowe, Mario Perhinschi
Department of Mechanical and Aerospace Engineering
West Virginia University, Morgantown, WV 26506/6106

Abstract

This paper presents experimental results for a research program using research UAVs built and developed at West Virginia University. The main objective of this effort was to provide a flight demonstration of a formation control scheme using three YF-22 research aircraft models. For several years formation flight research has been an important topic for the aerospace community. The benefits of formation flight and development of formation control problems have been investigated and well documented. A detailed mathematical model was obtained using parameter identification techniques from previously recorded flight data of the WVU YF-22 aircraft. From this data, a Simulink® based simulation environment was developed and used to test the formation control laws. Simulation results used this mathematical model to design and refine a set of control laws to maintain desired formation geometry during maneuvered flight. The formation control law consists of a set of inner and outer loop control schemes executed by an on-board computer system on the "Follower" aircraft. Performance of the "Follower" inner-loop control laws has been assessed through a series of flight tests. Flight-testing activities focusing on the formation control laws initially used a 'virtual leader' scenario. Results of the 'virtual leader' testing validated the overall design of the formation controller and confirmed the performance of the on-board computer system. Formation flight with two aircraft was then performed during the 2004 flight season. This paper will first describe the UAV models along with their customized electronic computer systems. Next, the aircraft mathematical model as well as the formation control schemes will be presented. The overall control design process, with emphasis on the controller implementation on the on-board computer, will also be described. Finally, the flight-testing operations and experimental results obtained to date will be presented and discussed.

NLDI GUIDANCE CONTROL LAWS
FOR CLOSE FORMATION FLIGHT

Giampiero Campa, Brad Seanor, Yu Gu, Marcello R. Napolitano
Department of Mechanical and Aerospace Engineering
West Virginia University, Morgantown, WV 26506/6106

Abstract

This paper presents identification, control synthesis and simulation results for an YF-22 aircraft model designed, built, and instrumented at West Virginia University. The goal of the project was the experimental demonstration of formation flight for a set of 3 of the above models. In the planned flight configuration, a pilot on the ground maintained controls of the 'leader' aircraft while a follower aircraft was required to maintain a pre-defined position and orientation with respect to the 'leader'. In this paper, the identification of both a linear model and a nonlinear model of the aircraft from flight data is shown first. Then, the control laws, that feature a linear inner loop controller and a NLDI (nonlinear dynamic inversion) based outer loop guidance controller, are discussed in detail. Finally, both simulation and flight test results are presented.

Appendix B

List of technical publications currently
under preparation for submission

ARCHIVAL JOURNALS

Gu, Y., Seanor B., Campa G., Napolitano M.R., Rowe, L., Gururajan, S., Perhinschi, M.G., Wan, S., **"Design and Flight Testing Evaluation of Formation Control Laws"**, *submission to the IEEE Transactions on Control Systems Technology,* March 2005

Seanor B., Gu, Y., Campa G., Napolitano M.R., Rowe, L., Gururajan, S., Perhinschi, M., **"Flight Test Evaluation Of 3-Aircraft Formation Control"**, *submission to the AIAA Guidance, Navigation and Control Journal,* April 2005

Campa G., Gu. Y., Seanor B., Napolitano M.R., Rowe, L., Gururajan, S., Pollini. L., Perhinschi M., Fravolini, M., **"Design And Flight Testing Of Nonlinear Formation Control Laws"**, *submission to the Journal of Aerospace Science and Technology, Elsevier Journals,* April 2005

DESIGN AND FLIGHT TESTING EVALUATION OF FORMATION CONTROL LAWS

Yu Gu, Brad Seanor, Giampiero Campa, Marcello R. Napolitano,
Larry Rowe, Srikanth Gururajan, Mario Perhinschi, Sheng Wan
Department of Mechanical and Aerospace Engineering
West Virginia University, Morgantown, WV 26506/6106

Abstract

This paper will present the resulting effort of designing and flight testing formation control laws using 3 YF-22 research UAVs designed, built, and instrumented at West Virginia University. In the planned flight configuration, a radio control (R/C) pilot maintains ground control of the 'leader' aircraft while the follower aircraft are required to maintain a pre-defined position and orientation with respect to the 'leader' aircraft. In this paper, a brief introduction of the test-bed aircraft and on-board payload is provided first. The following sections will then describe the mathematical model obtained from flight data to develop a linear & non-linear aircraft model. Additional sections will discuss the design and development of the formation control laws featuring a inner loop controller and outer loop guidance controller based upon a NLDI (nonlinear dynamic inversion) in detail. The remaining sections will discuss simulation, virtual 'leader' flight test, and actual 2-aircraft formation flight tests.

FLIGHT TEST EVALUATION OF
3-AIRCRAFT FORMATION CONTROL

Brad Seanor[+], Yu Gu[+], Giampiero Campa[+], Marcello R. Napolitano[+],
Larry Rowe[+], Srikanth Gururajan[+], Mario Perhinschi[+]
[+]Department of Mechanical and Aerospace Engineering
West Virginia University, Morgantown, WV 26506/6106

Abstract

This paper will present the resulting effort for the flight testing of formation control laws using three YF-22 research UAVs designed, built, and instrumented at West Virginia University (WVU). In the selected 3-aircraft formation configuration, a radio control (R/C) pilot maintains ground control of the 'leader' aircraft while two autonomous 'follower' aircraft are required to maintain a pre-defined position and orientation with respect to the 'leader' aircraft. Each 'follower' aircraft essentially acted as an autonomous vehicle once engaged into the formation flight mode. The overall flight-testing program validated the design of the formation control laws, which implemented a linear inner loop and an NLDI (nonlinear dynamic inversion) outer loop scheme. During the final flight testing phases, a total of five-formation flight experiments were successfully performed, specifically four 2-aircraft formations and one 3-aircraft formation. The flight test results from the 3-aircraft formation flight will be presented and discussed in detail. This paper will also provide a brief introduction of the test-bed aircraft and on-board payload used for the period of the experiment. Additional sections will discuss design and development issues about the formation control laws, simulation testing and the flight test results obtained for the 3-aircraft formation flight experiment.

DESIGN AND FLIGHT TESTING OF
NONLINEAR FORMATION CONTROL LAWS

Giampiero Campa[+], Yu Gu[+], Brad Seanor[+], Marcello R. Napolitano[+],
Larry Rowe[+], Srikanth Gururajan[+], Lorenzo Pollini[^], Mario Perhinschi[+], Mario Fravolini[~]
[+]Department of Mechanical and Aerospace Engineering
West Virginia University, Morgantown, WV 26506/6106
[^]Department of Electrical Systems and Automation
Pisa University, 56126 Pisa, Italy
[~]Department of Electronic and Information Engineering
Perugia University, 06100 PG, Italy

Abstract

This paper will present the results of a research effort focused on the modeling, identification, control design, simulation, and closed loop flight-testing for a fleet of YF-22 research aircraft models. These models were designed, manufactured, and instrumented at West Virginia University (WVU). The guidance laws have been designed using nonlinear dynamic inversion of the kinematic equations. In the planned flight configuration, the 'follower' aircraft is required to maintain a pre-defined position with respect to a "Virtual Leader" (VL) aircraft, which is essentially a flight path from previously recorded flight data. The resulting controller has an inner-outer loop structure in which the horizontal outer loop guidance laws rely on feedback linearization. The inner loop controllers are instead of linear nature, and were designed using classical root locus methods. The flight-testing results confirmed the validity of both identification and control design efforts.

Design of formation control laws for manoeuvred flight

G. Campa, S. Wan, M. R. Napolitano and B. Seanor
Department of Mechanical and Aerospace Engineering
West Virginia University, Morgantown, USA
M. L. Fravolini
Department of Electronic and Information Engineering
Perugia University, Perugia, Italy

ABSTRACT

This paper presents identification, control synthesis and simulation results for an YF-22 aircraft model designed, built, and instrumented at West Virginia University. The ultimate goal of the project is the experimental demonstration of formation flight for a set of 3 of the above models. In the planned flight configuration, a pilot on the ground maintains controls of the leader aircraft while a wingman aircraft is required to maintain a pre-defined position and orientation with respect to the leader. The identification of both a linear model and a nonlinear model of the aircraft from flight data is discussed first. Then, the design of the control scheme is presented and discussed with an emphasis on the amount of information, relative to the leader aircraft, needed by the wingman to maintain formation. Using the developed nonlinear model, the control laws for a maneuvered flight of the formation are then simulated with Simulink® and displayed with the Virtual Reality Toolbox®. Simulation studies have been performed to evaluate the effects of specific parameters and the system robustness to atmospheric turbulence. The conclusions from this analysis have allowed the formulation of specific guidelines for the design of the electronic payload for formation flight.

NOMENCLATURE

BLS	batch least squares
DI	dynamic inversion
SQP	sequential quadratic programming
UAV	unmanned aerial vehicle
UCLA	University of California Los Angeles
WVU	West Virginia University
A_x	forward acceleration in body axis (g)
A_y	lateral acceleration in body axis (g)
A_z	normal acceleration in body axis (g)
b	wingspan (m)
c	mean Aerodynamic cord (m)
C_D	aerodynamic drag force coefficient
C_L	aerodynamic lift force coefficient
C_Y	aerodynamic lateral force coefficient
C_m	aerodynamic pitching moment coefficient
C_l	aerodynamic rolling moment coefficient
C_n	aerodynamic yawing moment coefficient
f	state evolution function of a dynamic system
f	forward clearance error between leader and wingman's aircraft
f_c	predefined forward clearance between leader and wingman's aircraft
F_A	aerodynamic forces acting on the aircraft (N)
g	output function of a dynamic system
g	gravitational acceleration (g)
G	vector of geometric parameters and inertia coefficients
G_a	actuator dynamics transfer function
G_{TT}	throttle to thrust transfer function
G_{vt}	throttle to velocity transfer function
G_{VT}	thrust to velocity transfer function
h	lateral clearance error between leader and wingman's aircraft
h_c	predefined vertical clearance between leader and wingman's aircraft
H	altitude
I	inertia coefficient (kgm²)
K	control gain
l	lateral clearance error between leader and wingman's aircraft
l_c	predefined lateral clearance between leader and wingman's aircraft
m	mass (Kg)
M_A	aerodynamic moments acting on the aircraft (N*m)
p	roll rate (deg/s)
q	pitch rate (deg/s)
q	dynamic pressure (psi)
r	yaw rate (deg/s)
S	wing platform area (m²)
T	thrust (N)
u	input vector of a dynamic system
V	speed
x	state vector of a dynamic system
x	Longitudinal axes of a reference frame/position of an

object along the x axes.

y output vector of a dynamic system

y lateral axes of a reference frame/position of an object along the y axes.

z vertical axes of a reference frame/position of an object along the z axes.

α attack angle (deg)

β sideslip angle (deg)

δ vector containing δ_E, δ_A, δ_R, δ_T

δ_E elevators deflection (deg)

δ_A ailerons deflection (deg)

δ_R rudders deflection (deg)

δ_T throttle input (μV)

Δ difference

φ roll angle (deg)

θ pitch angle (deg)

Ω vertical component of the trajectory-induced angular velocity

0 trimmed condition

d desired value

L leader

W wingman

x projection along the longitudinal axis

xy projection along the horizontal plane

y projection along the lateral axis

z projection along the vertical axis

1.0 INTRODUCTION

Autonomous formation flight is an important research area in the aerospace community. The aerodynamic benefits of formation flight, and in particular close formation flight, have been well documented[1-3]. The control of the leader-wingman formation has been investigated extensively[4,5], leading to the introduction of different types of compensation-type controllers[4-6].

In Ref. 7 a formation flight control scheme was proposed based on the concept of Formation Geometry Center, also known as the Formation Virtual Leader. Reference 8 describes the application of an 'extremum seeking' algorithm to the formation control problem. More complex control laws based upon Linear Quadratic Regulator and Dynamic Inversion (DI) approaches have also been proposed[9-11]. Particularly, in Ref. 10, the DI-based approach has been augmented with neural networks to cancel the dynamic inversion error, following the methodology outlined in Ref. 12.

A variety of research efforts are currently on-going within the activities of the AFF (Autonomous Formation Flight) program at NASA Dryden[13-15]. The Boeing Company, UCLA, and NASA Ames are also involved in the AFF program. References 13-15 — from the AFF program — describe in detail the current efforts in modeling the aerodynamic interference between the different aircraft within the formation. Of particular interest from a control point of view are the efforts described in Refs 16,17 where baseline constant-gain compensation-type control laws to maintain formation geometry are compared through simulation studies with adaptive control techniques to achieve robustness to un-modeled portions of the aerodynamic interference. Finally Ref. 18 presents initial flight results of the testing of a formation flight autopilot designed with a compensation-type approach.

This paper presents design results of the formation control laws to be implemented on a set of three YF-22 aircraft models that are designed, built, and instrumented at West Virginia University (WVU). One of the three WVU YF-22 models is shown in Figure 1. The model features an 8ft fuselage length with a 6·5ft wingspan for an approximate take-off weight of 48lb, including a 12lbs electronic

Figure 1. WVU YF-22 aircraft model.

payload consisting on a PC-104 flight computer, a complete set of sensors, a GPS receiver and a set of RF modems used for data transmission. The aircraft models are currently undergoing individual flight-tests with flight-testing of the formation control laws to be performed in 2003-2004. Due to the limitations on the flight range, the WVU YF-22 models will be expected to perform fairly tight maneuvers at high Euler angles and moderately high angular rates. Therefore, a specific issue is the design of a control scheme allowing for formation control under these flight conditions. Another objective is to design a formation control scheme with a limited amount of information exchange (between leader and wingman) needed to maintain the predefined formation geometry.

The paper is organised as follows. The second section describes the identification of a linear and nonlinear single aircraft model from collected flight data. The third section outlines the geometric characteristics of the formation. The fourth section outlines the design of the formation control laws. The final sections will present the simulation and visualisation environment, together with the main results.

2.0 SYSTEM IDENTIFICATION AND MODELING OF THE WVU YF-22

The availability of an accurate mathematical model of the aircraft system for designing the formation control laws was a fundamental issue.

2.1 Linear Identification: theoretical background and available tools

The problem of identifying a linear model of a system from its measured input and output data is well known[19,20,21]. In the particular case in which all the states — and their time derivatives for the continuous time system identification — are available for measurement, the system identification problem reduces itself to a multiple linear regression problem[21,22]. In these cases, the problem consists essentially in solving an over-determined linear system in the least squares sense (leading to the well known 'Batch Least Squares' (BLS) method), which is simply solved by pseudo-inverting a large matrix. This methodology can be also easily adapted to the case when some elements of the solution are fixed a-priori.

2.2 Flight data measurement and recording

Flight data for several maneuvers were collected for parameter identification purposes using the following on-board instrumentation.:

- Absolute and differential pressure sensors: (SenSym ASCX15AN and SenSym ASCX01DN) to measure H and V (altitude and speed).
- Inertial measurement unit (Crossbow DMU-VGX) to measure A_x, A_y, A_z, p, q, r, φ, θ, (accelerations, roll pitch and yaw rates, roll and pitch angles).
- Custom designed nose probe to measure α and β (attack and sideslip angles).
- Potentiometers on the control surfaces to measure δ_E, δ_A, δ_R (elevators, ailerons and rudders deflections).

During the flight, the PC-104 based on-board computer collects in real time (at a rate of 100Hz) all of the above signals using the integrated data acquisition card (Diamond MM 32), and stores them on a flash-card for post-flight downloading. A set of flight data was used for the actual parameter estimation process, while a second set of data was used for validation purposes.

2.3 Linear identification process and resulting linear

The model identification was performed with a 3-step process. First, the flight data time histories were inputted to a Simulink scheme providing smoothing and rearrangement of the signals. Next, a batch Matlab file performed a number of identification algorithms either based on the Matlab System Identification Toolbox or on general BLS methods. Each method gave as a result a linear (affine) system.

The last step of the model identification process was the validation of the linear models. Essentially, the linear models were presented with the time histories of the control surface deflections from the validation flight data, and their outputs were compared with the corresponding signals from the actual flight data. The model produced by the BLS method provided the best fit with the flight data. Following the identification study, the estimated (short period) linear lateral-directional model is given by:

$$\begin{bmatrix} \dot\beta \\ \dot p \\ \dot r \end{bmatrix} = \begin{bmatrix} 0.4299 & 0.0938 & -1.0300 \\ -67.3341 & -7.9485 & 5.6402 \\ 20.5333 & -0.6553 & -1.9955 \end{bmatrix} \begin{bmatrix} \beta \\ p \\ r \end{bmatrix} + \begin{bmatrix} 0.2724 & -0.7713 \\ -101.8446 & 33.4738 \\ -6.2609 & -24.3627 \end{bmatrix} \begin{bmatrix} \delta_A \\ \delta_R \end{bmatrix} \quad \dots (1)$$

The estimated (short period) longitudinal model is given by:

$$\begin{bmatrix} \dot\alpha \\ \dot q \end{bmatrix} = \begin{bmatrix} -4.1172 & 0.7781 \\ -3.5129 & \end{bmatrix} \begin{bmatrix} \alpha \\ q \end{bmatrix} + \begin{bmatrix} 0.5435 \\ -59.0847 \end{bmatrix} \delta_E \quad \dots (2)$$

More details on the different identification approaches leading to the determination of the mathematical model of the WVU YF-22 models are available in Ref. 23.

2.4 Nonlinear identification process and resulting nonlinear model

The identification of the mathematical model of a nonlinear system is a more challenging issue[19,24]. Most of the nonlinear identification efforts rely on both good physical insight[19] and some form of optimisation algorithm like Steepest descent or Newton-Raphson[24]. The general nonlinear model of an aircraft system can be expressed as[25]:

$$\dot x = f(x, \delta, G, F_A(x, \delta), M_A(x, \delta));$$
$$y = g(x, \delta, G, F_A(x, \delta), M_A(x, \delta)); \quad \dots (3)$$

where x is the state vector (linear and angular positions and velocity), y is the output vector (linear and angular accelerations), δ is the input vector (surface deflections), G is a vector of geometric parameters and inertia coefficients, F_A and M_A are aerodynamic forces and moments acting on the aircraft; finally, f and g are the known analytic

functions that express the dynamics and kinematics of a rigid body. The aerodynamic forces and moments are expressed using the aerodynamic coefficients C_D, C_Y, C_L, C_l, C_m, C_n:

$$F_A = \bar q S \begin{bmatrix} C_D(x, \delta) \\ C_Y(x, \delta) \\ C_L(x, \delta) \end{bmatrix}, M_A = \bar q S \begin{bmatrix} bC_l(x, \delta) \\ \bar c C_m(x, \delta) \\ bC_n(x, \delta) \end{bmatrix} \quad \dots (4)$$

where S is the wing platform area, $\bar q$ the dynamic pressure, b the wingspan, and $\bar c$ the mean aerodynamic chord. The aerodynamic coefficients are often approximated by affine functions in x and δ; for example, for the lift coefficient:

$$C_L(x, \delta) = c_{L0} + c_{L\alpha}\alpha + c_{Lq}q + c_{L\delta}\delta_e \quad \dots (5)$$

where, c_{L0} and the other three coefficients are usually called the 'derivatives' of C_L.

When the above approximations are considered satisfactory, the nonlinear aircraft model is completely determined by its aerodynamic derivatives as well as by its inertial and geometric coefficients (which can typically be evaluated experimentally). In this effort, the inertial and geometric characteristics of the WVU YF-22 model were determined with an experimental set-up; thus, the remaining critical issue was the determination of the aerodynamic derivatives.

Formulas to calculate the entries of the matrices of the linear model in Equations (1) and (2) from the values of the aerodynamic derivatives and geometric-inertial parameters are well known[25]. By inverting such formulas, an initial value for all the main aircraft aerodynamic derivatives was then calculated from the matrices in Equations (1) and (2) together with the measured geometric and inertial parameters.

Next, a parameter optimisation routine based on routines available with the Matlab Optimization Toolbox® was set up. Specifically, a Matlab routine was written such that it could take as an input the aerodynamic derivatives to be estimated, perform a simulation with the nonlinear model resulting from those derivatives, compare the outputs with the real data, and return the difference (to be minimised) to the caller function. The "fmincon" function — which features the constrained optimisation of a multivariable function using a Sequential Quadratic Programming (SQP) technique[27] — was then used to find the set of aerodynamic derivatives providing the best fit with the flight data starting from the initial set of aerodynamic derivatives calculated from the linear models. The importance of starting the minimization from a set of already accurate derivatives should be emphasised; in fact, this last optimisation can be considered a refinement of the parameters.

A final validation of the nonlinear model was then conducted using the validation flight data set, similarly to what was done for the linear model. As shown in Fig. 2, the agreement between simulated and real data is substantial. The resulting aircraft nonlinear model is given by:

Geometric and inertial data (60% fuel load):
$\bar c = 0.7649$m, $b = 1.9622$m, $S = 1.3682$m^2,
$I_{xx} = 1.6073$kg m^2, $I_{yy} = 7.5085$kg m^2,
$I_{zz} = 7.1865$kg m^2 $I_{xz} = -0.3075$kg m^2
mass $= 20.6384$kg, T(engine thrust force) $= 54.6175$N

Longitudinal aerodynamic derivatives:

$C_{D0} = 0.0085$,	$C_{D\alpha} = 0.50794$,	$C_{Dq} = 0$,
$C_{D\delta E} = -0.03$,		
$C_{L0} = -0.0491$,	$C_{L\alpha} = 3.258$,	$C_{Lq} = 0$,
$C_{L\delta E} = 0.189$,		
$C_{m0} = 0.0226$,	$C_{m\alpha} = -0.47$,	$C_{mq} = -3.449$,
$C_{m\delta E} = -0.364$,		
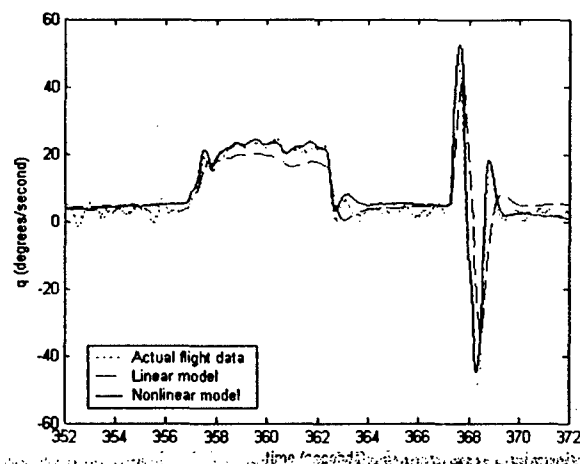
Figure 2. Linear and nonlinear model prediction versus real flight data.

Figure 3. Level plane formation geometry.

Lateral-directional aerodynamic derivatives:

$C_{Y0} = 0.015$, $C_{Yb} = 0.2725$, $C_{Yp} = 1.2151$, $C_{Yr} = -1.1618$,
$C_{Y\delta A} = 0.18363$, $C_{Y\delta R} = -0.4591$,
$C_{l0} = -0.001$, $C_{lb} = -0.037$, $C_{lp} = -0.2134$, $C_{lr} = 0.11474$,
$C_{l\delta A} = -0.055929$, $C_{l\delta R} = 0.0141$,
$C_{n0} = 0$, $C_{nb} = 0.0361$, $C_{np} = -0.151$, $C_{nr} = -0.19583$,
$C_{n\delta A} = -0.0358$, $C_{n\delta R} = -0.0554$,

The above parameters uniquely define the nonlinear aircraft model in Equation (3), and could easily be used within standard rigid body 6DOF aircraft dynamics simulation tools such as FDC or Airlib[26].

As a final note, it should be emphasised that the wake effects from the leader on the wingman have not been modeled and are assumed to be negligible in a preliminary analysis due to the limited size and airspeed of the models. The net effects of modeling the aerodynamic interference between the different aircraft in the formation can be modeled as 'Δ' terms to the above aerodynamic coefficients. A more refined model could include the wake effects as described in Refs 27 and 28. A procedure based on 'Multiple Shoe-Vortex Theory' for modelling the wake effects is outlined in Ref. 28.

3.0 Geometry of the formation control problem

The main purpose of this research effort is to design, simulate, and test a formation controller that allows the wingman aircraft to follow the leader — remotely flown by a pilot with a radio control — at predefined vertical, forward, and lateral distances during the flight phases when formation flight is engaged. From a geometric point of view the formation flight control problem can be naturally decomposed into two independent problems: a level plane tracking problem and a vertical plane tracking problem, to be described in the following sections.

3.1 Level plane formation definition

Figure 3 shows the level plane formation geometry. All trajectory measurements, i.e., leader/wingman position and velocity, are defined with respect to a pre-defined Earth-Fixed Reference x–o–y plane and are measured by the on-board GPSs. The pre-defined formation geometric parameters are the forward clearance f_c and lateral clearance l_c. The forward distance error f and lateral distance error l

can be calculated from the trajectory measurements and formation geometric parameters using the relationships:

$$l = \frac{V_{Ly}(x_L - x_W) - V_{Lx}(y_L - y_W)}{V_{Lxy}} - l_c \qquad \ldots (6)$$

$$f = \frac{V_{Ly}(y_L - y_W) + V_{Lx}(x_L - x_W)}{V_{Lxy}} - f_c \qquad \ldots (7)$$

where $V_{Lxy} = \sqrt{V_{Lx}^2 + V_{Ly}^2}$ is the projection of the leader's velocity onto the x–y plane. Accordingly, the relative forward and lateral speed of the wingman are defined as the time derivatives of the forward and lateral distance respectively and are needed for formation control purposes which can be calculated as:

$$\dot{l} = \frac{V_{Lx}V_{Wy} - V_{Ly}V_{Wx}}{V_{Lxy}} + (f + f_c)\dot{\Omega}_L \qquad \ldots (8)$$

$$\dot{f} = V_{Lxy} - \frac{V_{Lx}V_{Wx} + V_{Ly}V_{Wy}}{V_{Lxy}} - (l + l_c)\dot{\Omega}_L \qquad \ldots (9)$$

There are two methods to obtain the trajectory-induced angular velocity in the x–y plane (around the vertical axis) $\dot{\Omega}_L$. The first method is based on the use of the velocity vector (V_{Lx}, V_{Ly}), as measured by the on-board GPS, and its time derivative:

$$\dot{\Omega}_L = \frac{\dot{V}_{Ly}V_{Lx} - V_{Ly}\dot{V}_{Lx}}{V_{Lx}^2 + V_{Ly}^2} \qquad \ldots (10)$$

A problem with this approach is that the numerical derivative of the velocity vector is sensitive to measurement noise. A second approach is based on using additional measurements from the leader

aircraft along with the following kinematic relation (assuming $\dot{\beta}_L = 0$):

$$\dot{\Omega}_L \equiv \dot{\psi}_L = (q_L \sin\phi_L + r_L \cos\phi_L)/\cos\theta_L \qquad \ldots (11)$$

This second approach not only requires the vertical gyro (to measure bank angle ϕ_L and pitch angle θ_L) but also the angular rate gyros (to measure pitch rate q_L and yaw rate r_L) to be installed on the leader aircraft.

The level plane formation control problem has been further divided into a lateral distance control problem and a forward distance control problem, to be addressed in Sections 4.1-4.4.

3.2 Vertical plane formation definition

At nominal conditions, the leader and the wingman aircraft are separated by a vertical clearance h_c. The vertical distance error h, can then be calculated by:

$$h = z_L - z_W - h_c \qquad \ldots (12)$$

while its time derivative is given by:

$$\dot{h} = V_{Lz} - V_{Wz} \qquad \ldots (13)$$

The "vertical control problem" is reduced to the issue of maintaining the vertical clearance h_c.

Based on the above subdivision of the formation geometry, the design of the control laws are separated into three channels to control respectively the lateral, forward, and vertical distance. The resulting design is outlined in Sections 4.5 and 4.6.

4.0 DESIGN OF THE FORMATION CONTROL LAWS

During the formation flight testing, all aircrafts will be individually flown for take-off and landing; the formation will be engaged when all aircraft have reached a certain meeting point within the flight range. A specific constraint for this project is that the aircraft need to remain within a visual range. This, in turn, implies that frequent tight maneuvers will have to be performed. In conventional formation control schemes[6], only the relative position and the velocity vector of the wingman with respect to the leader are required by the 'formation-autopilot' of the wingman to maintain the desired formation. The use of this amount of information has shown to be sufficient for formation control with mild maneuvers by the leader. However, under substantial maneuvering conditions, additional aircraft variables from the leader, such as Euler angles, were found to be necessary for the wingman to maintain the formation geometry.

The formation control problem can be classified as a 'target-tracking' problem as opposed to a more conventional 'trajectory-following' problem. In the latter case the trajectory is typically pre-defined and stored within the on-board computer while in the former the trajectory to be followed by the controlled aircraft (i.e. the wingman) is 'dynamically produced' by target (i.e. the leader aircraft). Ideally, to achieve the best trajectory tracking performance, the formation flight control laws, — that is, the wingman flight control laws — should be based on a 'full information' tracking strategy. This concept can be expressed as:

Wingman's control inputs = Leader's control inputs + State error feedback   ... (14)

where the control inputs include deflections for the throttle, elevator, aileron and rudder, while state error feedback consists of 'internal' state variable errors (such as errors in angular rate and Euler angles) and 'trajectory' state variable errors (such as forward distance, lateral distance, and vertical distance) between the leader and wingman.

The rationale behind this approach is the fact that if the wingman was flying at the same position as the leader, a perfect asymptotic tracking (in position and attitude) could be achieved through a state error feedback, since the leader and wingman aircraft would share the same dynamics (assuming same type of aircraft) and the same control inputs. In other words, the leader acts as a reference system for the wingman, so the state feedback control measures the differences between the leader (reference) state and the wingman state, and provides corrections to the wingman control inputs in order to correct these differences. In reality, the *desired* wingman position is shifted with respect to the leader's position; therefore, extra compensation might be needed to account for the difference in the trajectory variables between the leader and the (ideal) wingman.

It should be noted that in this 'full information' approach all the leader's states and control inputs are needed to calculate the wingman control inputs; therefore, a high communication bandwidth between the leader and wingman is required. An additional goal was to formulate a criteria for limiting the amount of data to be exchanged from leader and wingman aircraft while maintaining the geometry of the formation. This issue has direct implications on the required performance — and, therefore, the cost — of commercially available RF modems. Therefore only a few of the leader outputs and states are actually used to calculate the wingman's control inputs, in lieu of the 'full information' approach outlined in Equation (14).

4.1 Lateral distance control

The objective of the lateral distance control is to minimize the lateral distance error l. The basic physical principle of the lateral distance control can be expressed by the following logic:
aileron → roll rate → bank angle → lateral speed → lateral distance

In addition, the function of the rudder command is to augment the lateral-directional stability, by increasing the Dutch Roll damping. Since bank angle rate changes are substantially higher than rate changes in the lateral position, the lateral dynamics exhibit a typical two-time-scale feature. Therefore, the design of the control system can be decomposed into two successive phases, that is, the design of an inner loop controlling the bank angle and augmenting the lateral-directional stability, and the design of an outer loop which tries to maintain a desired lateral clearance with respect to the leader.

The resulting linear control law is given below and shown in Fig. 4, where the subscripts L and W indicate respectively the wingman and leader aircraft.

Inner loop control law:

$$\delta_{AW} = \delta_{AL} + K_p p_W + K_\phi(\phi_W - \phi_d) \qquad \ldots (15)$$

$$\delta_{RW} = \delta_{RL} + K_r r_W \qquad \ldots (16)$$
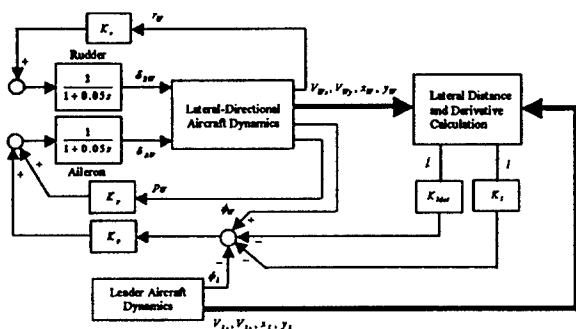
Figure 4. Lateral control law.
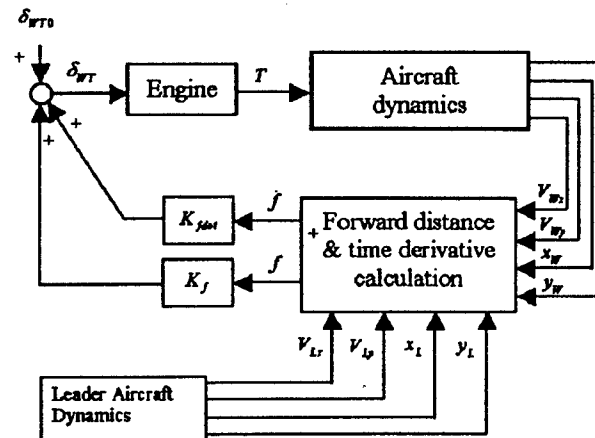
Figure 5 Forward control law.

$$\phi_d = \phi_L + K_i \dot{i} + K_i i \qquad \qquad \dots (17)$$

4.2 Lateral-directional model and determination of the controller parameters

The basic lateral-directional linear model of the aircraft is shown in Equation (1). The actuators dynamics are modeled using the following 1st order transfer function:

$$G_a(s) = \frac{1}{1 + 0.05s} \qquad \qquad \dots (18)$$

As discussed in the previous section, the determination of the parameters of the controller is divided into two phases, that is, inner loop and outer loop design. Given the variables involved in Equations (15), (16) and (17), the inner loop controller can be designed based on the aircraft lateral-directional linear model, but the outer loop design requires a suitable kinematic reference model. Such a model can be obtained by considering that a wing performing a steady-state co-ordinated turn where the lift force balance and centrifugal force balance equations apply. This leads to the following expression:

$$\dot{\Omega}_W = \frac{g}{V_{Wxy}} \mathrm{Tan}\,\phi_W \qquad \qquad \dots (19)$$

Additionally, by assuming a straight and level flight condition of the leader and identical speed for the wingman and the leader, it results that $\Delta\dot{\Omega} = \dot{\Omega}_W$ while Equation (8) takes on the following simple form:

$$\dot{i} = V_{Wxy} \mathrm{Sin}(\Delta\Omega) \qquad \qquad \dots (20)$$

where $\Delta\Omega = \Omega_W - \Omega_L$. The linearisation of the above two equations (around the standard level-straight flight condition) of the wingman provides the following model of the trajectory dynamics:

$$\begin{cases} \Delta\dot{\Omega} = \dfrac{g}{V_{Wxy}}\phi_W \\ \dot{i} = V_{Wxy}\Delta\Omega \end{cases} \qquad \dots (21)$$

Thus, the full linear model for lateral distance controller design is the combination of Equations (1), (18), and (21). Classic root-locus based compensation design tools can then be applied to the model for evaluating the controller gains[26]. The basic design specification is to assign the damping ratio of the dominant poles a value around 0·7. The resulting values for the parameters of the different control laws are given by:

$$K_r = 0.16, \quad K_p = 0.04, \quad K_\phi = 0.35$$
$$K_i = 0.29, \quad K_i = 1.43 \qquad \qquad \dots (22)$$

4.3 Forward distance control

The objective of the forward distance control is to minimise the forward distance error f. This task can only be accomplished through the use of the throttle control channel. In fact, by increasing/decreasing the throttle, the thrust of the engine and therefore the speed of the aircraft is increased/decreased. This, in turn, allows control of the forward distance between the leader and wingman. The basic physical principle of the forward distance control can be expressed by the following logic:

throttle $\rightarrow$ thrust $\rightarrow$ forward speed $\rightarrow$ forward distance

The forward distance control law, shown in Fig. 5, is given by:

$$\delta_{TW} = \delta_{TL} + K_{\dot{f}}\dot{f} + K_f f \qquad \qquad \dots (23)$$

4.4 Forward model and determination of the controller parameters

The cascade of two first order linear models can approximate the forward dynamics. The 1st model represents the engine response in terms of throttle to thrust; this model has been obtained through an experimental analysis of the performance of the jet engines installed on the WVU YF-22 aircraft; a 2nd model represents the airspeed response in terms of thrust to airspeed, which is approximately derived from the knowledge of nominal thrust, airspeed, mass, and the assumption that the change of aerodynamic drag is in proportional to the change of airspeed.

The following equation represents the resulting complete transfer function of throttle to airspeed:
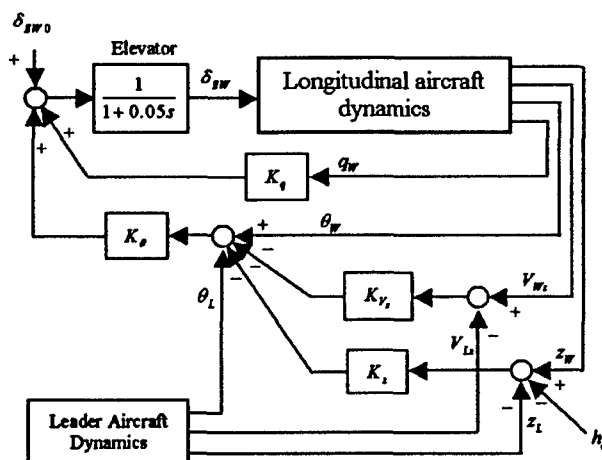
Figure 6. Vertical control law.

Figure 7. VRT visualisation (behind wingman).

Outer loop control law:

$$\theta_{ac} = \theta_L + K_z \dot{\delta}z + K_z \delta z \qquad \ldots (27)$$

The block diagram of the resulting scheme is shown in Fig. 6.

$$G_u(s) = G_{VT}(s)\,G_{TT}(s) = \frac{0 \cdot 315}{1 + 6 \cdot 5s} \bullet \frac{0 \cdot 2}{1 + s} \qquad \ldots (24)$$

It should be noted that this model also represents the transfer function from throttle (of wingman) to forward velocity of Equation (9) under the assumed level-straight constant speed flight condition. The parameters of the forward distance controller outlined in Equation (23) were then determined through a root locus-based compensator design. The resulting parameters are:

$$K_f = 0 \cdot 4, \quad K_f = 1 \cdot 7 \qquad \ldots (25)$$

4.5 Vertical distance control

The objective of the vertical distance control is to minimise the vertical distance error h. This task is accomplished through the use of the elevator control channel. The basic physical principle of the vertical distance control can be expressed by the following logic:

elevator → pitch rate → pitch angle → vertical speed → vertical distance

The vertical distance control law is similar to the conventional altitude-hold autopilot with the only difference being that the altitude reference may vary according to the leader's altitude. As with the lateral distance case, the problem exhibits a two time scale structure; thus, the control scheme can be designed using an inner loop controller — which is basically a pitch angle controller — and an outer loop controller providing altitude control.

A linear control law that accomplishes the above scheme is given by the following formulas.

Inner loop control law:

$$\delta_{EW} = \delta_{EL} + K_q q_W + K_\theta(\theta_W - \theta_d) \qquad \ldots (26)$$

4.6 Vertical model and determination of the controller parameters

The design is based on the linear short period model in Equation (2) in addition to a kinematic model. The linearised kinematic model is given by:

$$\begin{cases} \dot{\theta} = q \\ \dot{h} = V_{Wz}\theta \end{cases} \qquad \ldots (28)$$

With a root locus-based design[20] the parameters of the vertical controller are found to be:

$$K_q = 0 \cdot 12, \quad K_\theta = 0 \cdot 50, \quad K_z = 5, \quad K_z = 3 \qquad \ldots (29)$$

5.0 SIMULATION & RESULTS

A Simulink scheme featuring the models of the WVU YF-22 aircrafts and the formation controller was developed and implemented. Given the multi-object nature of the problem, the design of a visualization environment fully integrated with the simulation was considered to be critical. The Virtual Reality Toolbox (VRT) was selected as the visualisation environment since it allows for objects and events of a virtual world (coded in VRML 2.0 or higher[29]) to be driven by signals from Matlab/Simulink. A VRML world including two YF-22 graphical models and a simple landscape which was then implemented and connected with the simulation using the VRT Simulink Blocks. The resulting scenery from a view behind the wingman is shown in Fig. 7.

A preliminary analysis was conducted to assess if deflections of the control surfaces from the leader in Equations (15), (16), (23) and (26) were actually necessary to have desirable tracking performance. This analysis showed that the elimination of these signals from the leader aircraft did not significantly decrease the performance of the control scheme. Consequently, these signals were no longer used (in Equations (23) and (26) two constant trim values were used instead) therefore saving communication bandwidth for flight testing.

Next, two simulation studies were conducted. The purpose of the first study was to assess the need for the bank angle from the leader
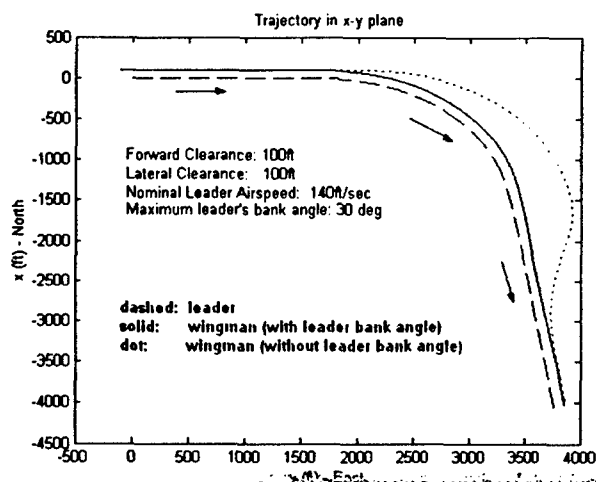
Figure 8. Simulation study #1: trajectories with/without the bank angle from leader aircraft.

Figure 10. Simulation study #2: trajectories in vertical plane.

Figure 9. Simulation study #1: lateral distance with/without the bank angle from leader aircraft.
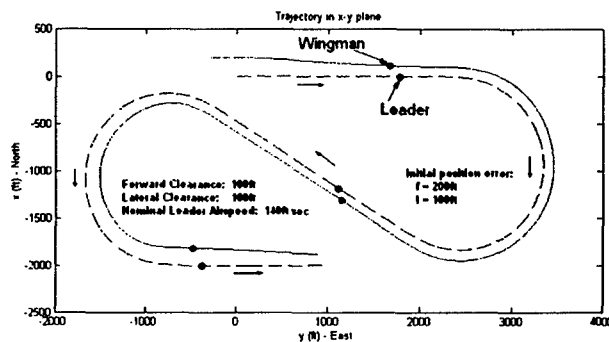
Figure 11. Simulation study #2: trajectories in level plane.

in the wingman control laws in Equation (17). The main results for this study are shown in Figs 8 and 9 where the leader's lateral maneuvering bank angle is about 30°. It can be seen from the simulation that the 'deformation' of the formation in terms of the lateral distance of the wingman from the leader is unacceptably large (as much as 450ft), when the leader's bank angle is not available for formation control purposes. Based on the above considerations, it was decided that the electronic instrumentation of the wingman models will be required to include a three-axis angular rate gyro measuring roll rate p_W, pitch rate q_W and yaw rate r_W, a vertical gyro measuring pitch angle θ_W and bank angle ϕ_W and a GPS receiver measuring the position of the wingman aircraft (with reference to a pre-defined earth-fixed reference) x_W, y_W and z_W, and velocity vector V_{Wx}, V_{Wy} and V_{Wz}. In addition, it was concluded that the pitch angle θ_L and bank angle ϕ_L of the leader aircraft, along with the positions (with reference to a pre-defined earth-fixed reference) x_L, y_L, and z_L, and velocity vector V_{Lx}, V_{Ly} and V_{Lz} are required by the wingman's control system.

The second simulation study was conducted to asses the performance of the formation controller under the following assumptions

and boundary conditions:

● Leader bank and pitch angles are available to the wingman control system;
● 'S' shape flight trajectory in level plane with a maximum leader bank angle of approx. 50° (as recorded in typical flight tests of the WVU YF-22 models);
● 'Level → climb → level' trajectory in vertical plane;
● Formation geometry: f_c = 100ft; l_c = 100ft, h_c = 0ft (level formation);
● Initial position error: f = 300ft, l = 300ft, h = 0ft;
● Nominal level of atmospheric turbulence.

The simulations were conducted with and without the modeling of wind gusts acting in specific flight segments. Figures 10-12 and Figs 13,14 illustrate the results from this study with and without the wind gust respectively. Table 1 summarizes the performance in terms of maximum tracking errors for different values of the leader maximum bank angle at different configurations (with the wingman flying inside/outside the leader). As expected, a detailed analysis of the results shows that the control scheme provides better performance in terms of maximum forward, lateral and vertical errors with lower leader's bank angles. The large difference between the lateral distance error when the wingman is flying outside/inside the trajectory of the leader is due to the fact that when the wingman is flying inside the leader trajectory the formation control scheme requires a larger bank angle; on the other side, the effectiveness of the lateral distance control is very sensitive to the nonlinear effects due to large increases in the wingman's bank angles.
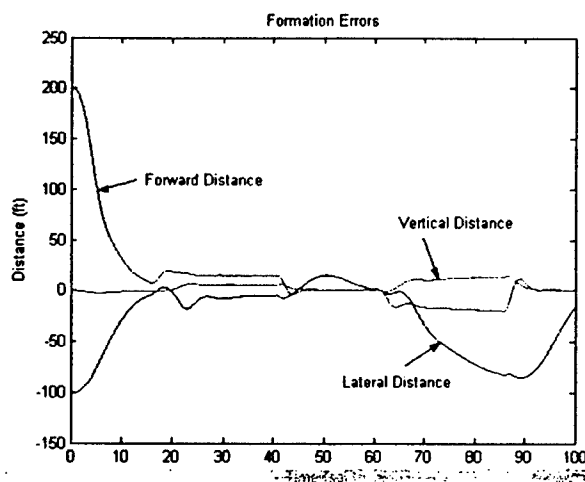
Figure 12. Simulation study #2: formation errors.
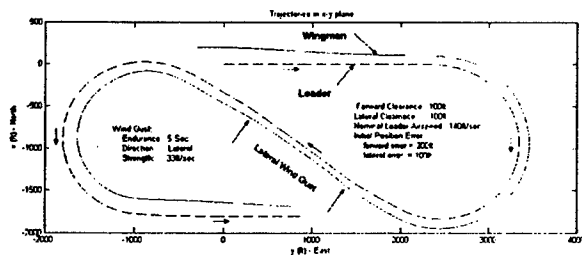
Figure 13. Simulation study #2: trajectories in level plane with lateral wind gusts.

Table 1
Tracking errors for different configurations at different bank angles

Leader airspeed: 140ft/sec, Formation geometry: f_c = 100ft, l_c = 100ft, h_c = 0ft

Wingman's position w.r.t leader F_L	Maximum lateral distance l (ft)		Maximum forward distance f (ft)		Maximum vertical distance h (ft)	
	Outer Turn	Inner Turn	Outer Turn	Inner Turn	Outer Turn	Inner Turn
20°	7·7	18·5	11·0	11·1	0·6	2·1
25°	9·1	25·8	12·6	12·7	1·1	3·1
30°	10·4	34·5	14·0	14·1	1·9	4·5
35°	11·5	45·5	15·7	15·9	2·8	6·2
40°	12·7	58·7	17·4	18·1	3·9	8·6
45°	14·0	77·7	19·4	21·9	5·4	11·9
50°	16·6	105·9	21·8	27·3	7·2	17·2
55°	20·0	166·2	26·7	37·0	9·5	28·6

6.0 CONCLUSIONS

This paper presents an approach for the design of linear control laws to maintain specified geometry for a formation of research aircraft models. The design is based on compensation-type controllers for minimising tracking errors along the forward, lateral, and vertical axes. The analysis shows that the availability of the Euler angles from the leader aircraft is critical for the wingman to maintain the assigned formation geometry throughout the maneuvered flight. An additional goal was to evaluate the criteria to limit the necessary data communication between the leader and the wingman. The design has been verified through a set of simulation studies interfacing the aircraft models and the control schemes in Simulink with a VRT environment. The results of the simulation show a desirable performance of the formation control schemes.

ACKNOWLEDGEMENTS

REFERENCES

1. BLAKE, W. and MULTHOPP, D. Design, performance, and modeling considerations for close formation flight, Proceedings of the 1999 AIAA GNC Conference, AIAA paper 1999-4343, Portland, OR, August 1999.

2. PACHTER, M., D'AZZO, J.J. and PROUD, A.W. Tight formation flight control, *J Guidance, Control, and Dynamics*, March-April 2001, **24**, (2), pp 246-254.

3. GIULIETTI, F., POLLINI, L. and INNOCENTI, M. Autonomous formation flight, *IEEE Control Systems Magazine*, 2000, **20**, (6), pp 34-44.

4. PROUD, A.W. Close Formation Flight Control, MS Thesis, AFIT/GE/ENG/99M-24, School of Engineering, Air Force Institute of Technology (AU), Wright-Patterson AFB, OH, March 1999.

5. HALL, J.K. Three Dimensional Formation Flight Control, MS Thesis, AFIT/GE/ENG/00M-06, School of Engineering, Air Force Institute of Technology (AU), Wright-Patterson AFB, OH, March 2000.

6. PACHTER, M., D'AZZO, J.J. and DARGAN, J.L. Automatic formation flight control, *J Guidance, Control, and Dynamics*, 1994, **17**, (6), pp 1380-1383.

7. GIULIETTI, F., POLLINI, L. and INNOCENTI, M. Formation flight control: A behavioral approach, Proceedings of the 2001 AIAA GNC Conference, AIAA Paper 2001-4239, Montreal, Canada, August 2001.

8. BINETTI, P., ARIYUR, K.B., KRSTIC, M. and BERNELLI, F. Control of formation flight via extremum seeking, Proceedings of the 2002 America Control Conference, Anchorage, AK, May 2002.

9. SCHUMACHER, C.J. and KUMAR, R. Adaptive control of UAVs in close-coupled formation flight, Proceedings of the 2000 American Control Conference, Chicago, IL, June 2000.

10. SCHUMACHER, C.J. AND SINGH, S.N. Non linear control of multiple UAVs in close-coupled formation flight, Proceedings of the 2000 AIAA GNC Conference, AIAA paper 2000-4373, Denver, CO, August 2000.

11. SINGH, S.N., PACHTER, M., CHANDLER, P., BANDA, S., RASMUSSEN, S. and SCHUMACHER, C.J. Input-output invertibility and sliding mode control for close formation flying of multiple UAVs, Proceedings of the 2000 AIAA GNC Conference, Denver, CO, August 2000.

12. CALISE, A.J. and RYSDYK, R.T. Nonlinear adaptive flight control using neural networks, *IEEE Control Systems Magazine*, 1998, **18**, (6).

13. RAY, R.J., COBLEIGH, B., VACHON, M.J., and ST JOHN, C. Flight test techniques used to evaluate performance benefits during formation flight, Proceedings of the 2002 AIAA GNC Conference, AIAA paper 2002-4492, Monterey, CA, August 2002.

14. HANSEN, J.L. and COBLEIGH, B.R. Induced moment effects of formation flight using two F/A-18 aircraft, Proceedings of the 2002 AIAA GNC Conference, AIAA paper 2002-4489, Monterey, CA, August 2002.

15. VACHON, M.J., RAY, R.J., WALSH, K.R. and ENNIX, K. F/A-18 aircraft performance benefits measured during the autonomous formation flight project, Proceedings of the 2002 AIAA GNC Conference, AIAA paper 2002-4491, Monterey, CA, August 2002.

16. MISOVEC, K. Applied adaptive techniques for F/A-18 formation flight, Proceedings of the 2002 AIAA GNC Conference, AIAA paper 2002-4550, Monterey, CA, August 2002.

17. LAVRETSKY, E. F/A-18 Autonomous formation flight control system design, Proceedings of the 2002 AIAA GNC Conference, AIAA Paper 2002-4757, Monterey, CA, August 2002.

18. HANSON, C.E., RYAN, J., ALLEN, M.J. and JACOBSON, S.R. An overview of flight test results for a formation flight autopilot, Proceedings of the 2002 AIAA GNC Conference, AIAA paper 2002-4755, Monterey, CA, August 2002.

19. LJUNG, L. *System Identification: Theory for the User*, 2nd Ed, PTR Prentice Hall, Upper Saddle River, Englewood Cliffs, NJ, 1999.

20. VAN OVERSCHEE, DE MOOR B. *Subspace Identification for Linear Systems: Theory, Implementation, Applications.* Kluwer Academic Publishers, 1996.

21. STENGEL, R.F. *Optimal control and estimation*, Dover Publication, New York, 1994.

22. DOBSON, A.J. *An Introduction to Generalized Linear Models*, 1990, CRC Press.

23. NAPOLITANO, M.R., West Virginia University, Air Force Office of Scientific Research (AFOSR) Grant F49620-98-1-0136 Final Report, March 2002.

24. MAINE, R.E. and ILIFF, K.W. Identification of dynamic systems: theory and formulation, NASA RF 1168, June 1986.

25. STEVENS, B. and LEWIS, F. *Aircraft Control and Simulation*, John Wiley & Sons, NY, 1992.

26. CAMPA, G, 'Airlib', (February 2003), http://www.mathworks.com/matlabcentral/fileexchange/

27. HOCK, W. and SCHITTOWSKI, K. A Comparative performance evaluation of 27 nonlinear programming codes, *Computing*, 1983, 30, p 335.

28. GIULIETTI, F., NAPOLITANO, M.R., CAPETTA, B. and INNOCENTI, M. The complete aircraft model within a formation flight, Proceedings of the 2002 AIAA Atmospheric Flight Mechanics Conference, August 2002

29. The VRML Web Repository (December. 2002): http://www.web3d.org/vrml/vrml.htm

A Synthetic Environment for Simulation of Vision-Based Formation Flight

*Lorenzo Pollini, *Roberto Mati, *Mario Innocenti, †Giampiero Campa, †Marcello Napolitano,

This paper describes the design of autopilots and formation control laws and then the simulation setup and the first results of a novel architecture for close formation flight based on computer vision. The reference aircraft model is the West Virginia University YF-22 model aircraft. The simulation setup includes aircraft dynamics, autopilots and formation keeping controller and a module that creates a synthetic environment for the simulation of the vision equipment based on a commercial software called Dyna-WORLDS. DynaWORLDS is capable of generating synthetic images as if were captured by the camera onboard the wingman. Uniquely identifiable infrared light markers (light emitters each with different wavelength) are applied to the Leader aircraft and a recent iterative, globally convergent, pose estimation algorithm (LHM) is adopted to reconstruct the leader position and attitude. The formation control laws, designed with GPS measurements in mind, have been applied successfully with the Leader position, velocity and Heading estimates obtained from the vision system alone. A more feasible and less expensive solution using light markers with unique wavelength is then introduced and evaluated yielding the same performance of the previous case.

1 Introduction

Autonomous formation flight is an important research area in the aerospace community. The aerodynamic benefits of formation flight, and in particular close formation flight, have been well documented[1,2,3]. The control of the leader-wingman formation has been investigated extensively[4,5], leading to the introduction of different types of compensation-type controllers[4,5,6]. In Ref.[7] a formation flight control scheme was proposed based on the concept of Formation Geometry Center, a variant of the Formation Virtual Leader.[3] More complex control laws based upon Linear Quadratic Regulator (LQR) and Dynamic Inversion (DI) approache s have also been proposed[8,9,10]. Particularly, in Ref.,[9] the DI-based approach has been augmented with neural networks to cancel the dynamic inversion error, following the methodology outlined in Ref.[11] Of particular interest from a control point of view are the efforts described in Refs.[12,13] where baseline constant-gain compensation-type control laws are compared through simulation studies with adaptive control techniques to achieve robustness to un-modeled portions of the aerodynamic interference. Finally Ref.[14] presents initial flight results of the testing of a formation flight autopilot designed with a compensation-type approach.

All the control approaches described in the literature above assume that some measurements of Leader position and flight path or euler angles are available as input to the formation controller. To this end, at least one radio communication channel is needed to send Leader data to the Wingman. In some particular

applications field, as in stealth missions, active radio communications from the vehicles should be avoided. In absence of radio communications, even if all formation vehicles know leader's mission, it is impossible for the wingmen to know the formation/mission leader actual position respect to commanded one. For gaining benefits from flying in formation, the relative distances must be very short, so even mild atmospheric disturbances constitute a serious risk to formation safety. An alternative to radio communication is using a vision system that must be capable of acquiring the leader image with a camera and of estimating its relative position and attitude.

The estimation of wingman-leader relative displacement (translation and rotation) using images from the wingman-mounted camera is very similar to a common problem in robotics, computer graphics, and computer vision: pose estimation. In computer graphics, it plays a central role in tasks that combine computer-generated objects with photographic scenese.g., landmark tracking for determining head pose in augmented reality or interactive manipulation of objects. In computer vision, pose estimation is central to many approaches to object recognition.

This article first presents the mathematical model of the reference aircraft, then shows the design procedure for its autopilots and a formation controller based on generic position and attitude measurements (as coming from a GPS-like system). Then it presents the synthetic environment that simulates the vision system and the algorithm that estimates relative displacement. Finally simulation results are shown that compare the results of the exact measurements (GPS) and the vision-based control systems.

*Electrical Systems & Automation Dept. University of Pisa, via Diotisalvi, 2 , 56126 Pisa (PI) Italy.
†West Virginia University, Morgantown, WV

2 Aircraft Model

The aircraft taken as a reference is the YF-22 aircraft model that is designed, built, and instrumented at West Virginia University (WVU). One of the WVU YF-22 models is shown in Figure 11. The model features an 8 ft. fuselage length with a 6.5 ft. wingspan for an approximate take-off weight of 48 lbs, including a 12 lbs electronic payload consisting on a PC-104 flight computer, a complete set of sensors, a GPS receiver and a set of RF modems used for data transmission. The aircraft models are currently undergoing individual flight-tests with flight-testing of the formation control laws to be performed in 2003-2004.

Fig. 1   The WVU YF-22 Aircraft Model

The mathematical model of the aircraft has been identified with a 3-step process. First, the flight data time histories were inputted to a Simulink scheme providing smoothing and rearrangement of the signals. Next, a batch Matlab file performed a number of identification algorithms either based on the Matlab System Identification Toolbox or on general "Batch Least Squares" (BLS) methods. Identification was initially performed in discrete-time; thus, a discrete time model was derived. Next, an equivalent continuous model was obtained using a zero-order-hold based conversion from the discrete model. This allowed bypassing the continuous time identification, which would have required a direct numerical computation of the time derivatives of the state vector. Each method gave as a result a linear (affine) system. The last step of the model identification process consisted in the validation of the linear models. Essentially, the linear models were presented with the time histories of the control surface deflections from the validation flight data, and their outputs were compared with the corresponding signals from the actual flight data. The model produced by the BLS method provided the best fit with the flight data. Following the parameter identification study, the estimated linear lateral-directional aerodynamic model is given by:

$$\begin{bmatrix} \dot{\beta} \\ \dot{p} \\ \dot{r} \\ \dot{\phi} \end{bmatrix} = \begin{bmatrix} -1.462 & -0.07 & -1.19 & 0.23 \\ -17.86 & -0.57 & 8.46 & 0 \\ 11.55 & -1.30 & -2.71 & 0 \\ 0 & 1 & 0 & 0 \end{bmatrix} \begin{bmatrix} \beta \\ p \\ r \\ \phi \end{bmatrix} + \begin{bmatrix} -0.22 & 1.56 \\ 11.59 & 23.17 \\ 14.40 & -26.41 \\ 0 & 0 \end{bmatrix} \begin{bmatrix} \delta_a \\ \delta_r \end{bmatrix}$$
(1)

And the estimated (short period) longitudinal model of the dynamics is given by:

$$\begin{bmatrix} \dot{\alpha} \\ \dot{q} \end{bmatrix} = \begin{bmatrix} -1.73 & 0.52 \\ -17.97 & -1.53 \end{bmatrix} \begin{bmatrix} \alpha \\ q \end{bmatrix} + \begin{bmatrix} 0.38 \\ -20.15 \end{bmatrix} \begin{bmatrix} \delta_e \end{bmatrix}$$
(2)

where p, q, r are the roll, pitch and yaw rates, α, β are the attack and side-slip angles, ϕ is the bank angle and $\delta_a, \delta_e, \delta_r$ are aileron, elevator and rudder surface deflections.

The transfer function from the throttle command δ_T (in millivolts) to velocity V is:

$$\frac{V(s)}{\delta_T(S)} = \frac{0.63}{(s+1)(6.5s+1)}$$
(3)

More details on the PID approaches leading to the determination of the mathematical model of the WVU YF-22 models are available in Ref.[15]

2.1   The Non Linear Model

The identification of the mathematical model of a nonlinear system is a more challenging issue. When the aerodynamic coefficients can be approximated by affine functions in aircraft state and input, the nonlinear aircraft model is completely determined by its aerodynamic derivatives as well as by its inertial and geometric coefficients (which can typically be experimentally evaluated). In this effort, the inertial and geometric characteristics of the WVU YF-22 model were determined with an experimental set-up; thus, the remaining critical issue was the determination of the aerodynamic derivatives. It has been performed by direct comparison of the linear and nonlinear linearized model and by validation with real flight data. A non linear parameter optimization routine based on Sequential Quadratic Programming (SQP) technique was used to find the set of aerodynamic derivatives providing the best fit with the flight data, starting from the set of derivative from the first step of the nonlinear optimization problem.

The resulting nonlinear model has been used in all our simulations to validate the performance and robustness of the linear controllers.

3 Aircraft Autopilots

The autopilot design goal was to design three servo mechanisms on the heading angle, Altitude and Velocity. The linear systems have been augmented with integrators to obtain the missing dynamics for the lateral model:

$$\dot{\psi} = r \tag{4}$$

and the longitudinal model:

$$\begin{aligned} \dot{\theta} &= q \\ \dot{h} &= V_0(\theta - \alpha) \end{aligned} \tag{5}$$

where V_0 is the linearization velocity.

The control system design has been performed using LQG-LTR[16] to obtain robustness respect to modelling errors and noisy measurements. The outputs of the system available for measurement have been selected depending on available sensors: p, q, r (from the Inertial Measurement Unit (IMU)) α, β from the air-data sensor and V, h and $\chi = \psi + \beta$ from the GPS receiver. The adopted IMU has shown very little reliability on the estimation of the euler angles: these are obtained by integration of the angular rates, and due to non-linearities and saturation in the rate sensors the estimation error tends to drift in time (approx. 15 deg/hr) and, in case of steep maneuvers that get near to the sensor saturation level, the estimation may become corrupted by large errors (tens of degrees) that are impossible to recover. Thus, it has been decided not to use estimated euler angles and to rely only on the heading from the GPS that is quite reliable when the aircraft is flying at its cruise speed: $140 ft/sec$.

The augmented systems with the outputs selected above is controllable and observable. The initial weight matrices have been chosen depending on desired aircraft performance and estimated sensors disturbances and have been updated with the classical iterative LTR procedure.

The resulting control systems have been tested with the linear and the nonlinear models of the WVU-YF22 aircraft, using the same sensor noise levels recorded during real flight tests.

3.1 Lateral Controller

The goal of the lateral controller is to track the desired heading angle ψ_d and to keep the side-slip angle β as low as possible. To achieve side-slip angle and heading tracking with zero steady-state error the LQ-Servo design procedure has been applied adding two integrators over the two state variables β, ψ yielding the new state vector: $[\beta, p, r, \phi, \psi, \int\beta, \int\psi]$.

Given the cost index:

$$\int_0^\infty x^T Q x + u^T R u \tag{6}$$

with the diagonal weight matrices:

$$\begin{aligned} Q &= diag[0.01\ 1\ 1\ 1\ 50\ 1\ 0.7] \\ R &= diag[1\ 1] \end{aligned} \tag{7}$$

and given the unstructured multiplicative uncertainty $L(s)$:

$$L(s) \leq \frac{1}{4}(4s + 1) \tag{8}$$

The Loop Transfer Recovery step ended with the process and measurements noise covariance matrices: $W = I_{2X2}$ and $V = \rho * I_{4X4}$ with $\rho = 0.121$ yielding a controller with the following poles:

$$Poles = \begin{bmatrix} -112.5 \\ -61.1 \\ -0.3 \pm 0.19i \\ -0.01 \\ 0 \end{bmatrix} \tag{9}$$

that are easily realizable with a digital controller running at a sampling rate of $100Hz$.

The controller robustness and performance have been evaluated with simulation tests over the linear and nonlinear models. The following describes the result of one of the tests: sensor noise with the same spectral power as that recorded over real flight tests, first order actuators dynamics with the pole in -20, random modification of the system matrix A with 25% variation of all coefficients.
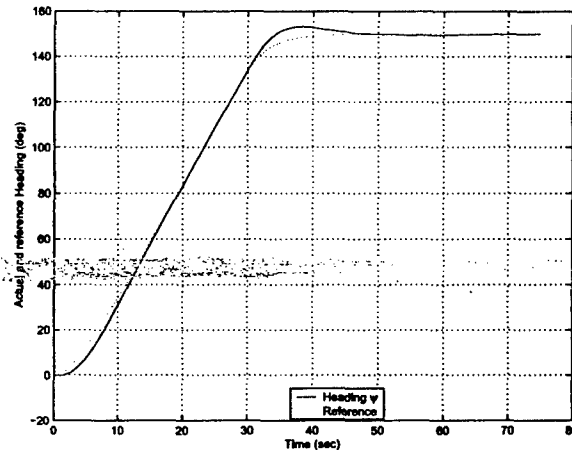
Fig. 2 Heading Angle Tracking

3.2 Longitudinal Controller

As stated before, the pitch angle θ sensor has been considered unreliable; the longitudinal model with outputs α, q, h results observable and to track an altitude reference with zero steady-state error it is necessary to add an integrator at the system's input. We then proceeded to the LQG/LTR synthesis at the input using $W = I_{5X5}$ and $V = 1000$ as estimates of process and measurement noise. The unstructured multiplicative uncertainty $L(s)$ is larger in this case:
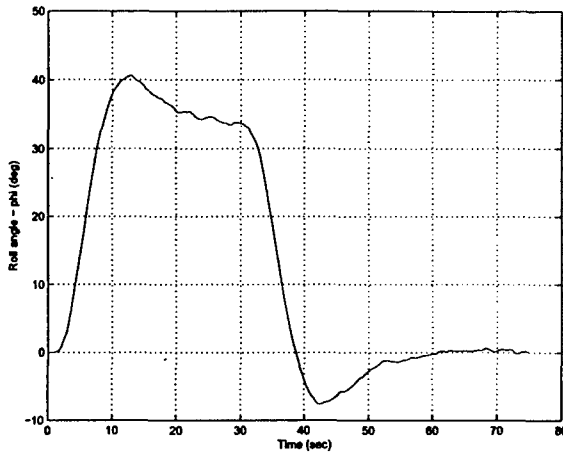
Fig. 3 Roll Angle During Heading Tracking
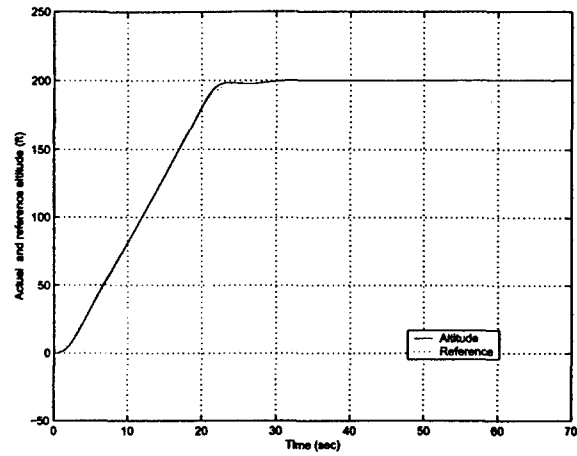
Fig. 5 Altitude Tracking
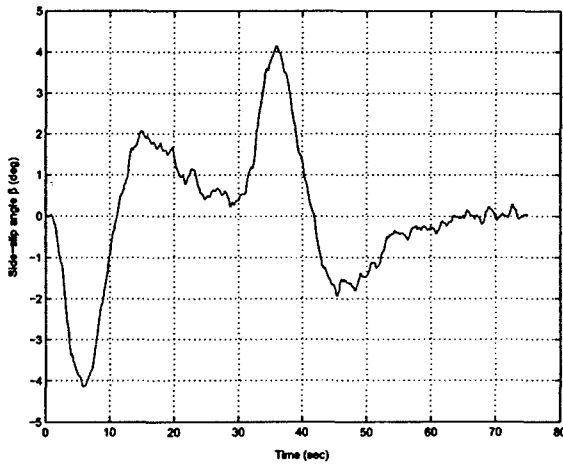
Fig. 4 Side-slip Angle During Heading Tracking
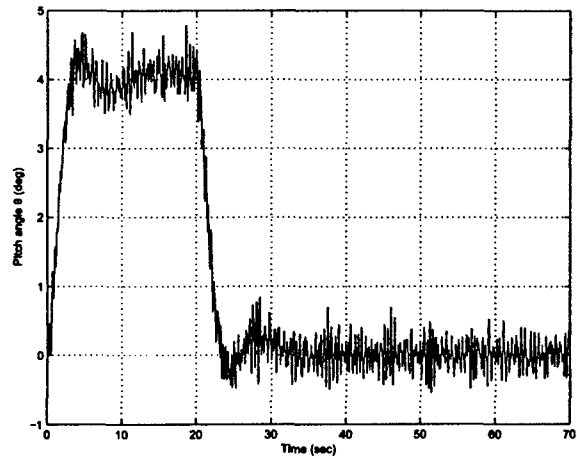
Fig. 6 Pitch Angle During Altitude Tracking

$$L(s) \leq \frac{1}{2}(4s + 1) \qquad (10)$$

The Loop Transfer Recovery steps ended with the the following LQR weight matrices: $Q = C^t C$ and $R = \rho$ with $\rho = 10^{-10}$ yielding a controller with the following poles:

$$Poles = \begin{bmatrix} -66.0 \\ -32.3 \pm 55.5i \\ -1.9 \pm 13.0i \end{bmatrix} \qquad (11)$$

The controller robustness and performance have been evaluated with simulation tests over the linear and nonlinear models. The test conditions are the same of the Lateral controller except that the random modification of the system matrix A is done with a 50% variation of all coefficients.

3.3 Velocity Controller

In our linear decoupled approximation the velocity dynamics and altitude and pitch angle dynamics are decoupled, then a simple Proportional-Integral-Derivative (PID) controller is sufficient to control the dynamics described by (8):

$$\delta_T(s) = K_{PID}(s)(V_d - V(s)) = K_p + \frac{K_I}{s} + \frac{K_d s}{(0.1s + 1)} \qquad (12)$$

where V_d is desired velocity and the aircraft velocity $V(s)$ is obtained from the GPS.

The root locus design procedure led to $K_p = 3$, $K_I = 2.25$ and $K_d = 1$ as a trade-off between performance and maximum thrust request at the maximum allowed velocity change.

4 Formation Flight Control

The main purpose of this research effort is to design, simulate, and test a formation controller that
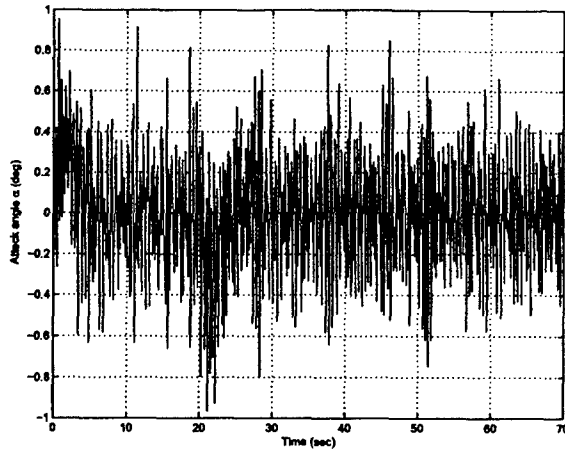
Fig. 7 Attack Angle During Altitude Tracking
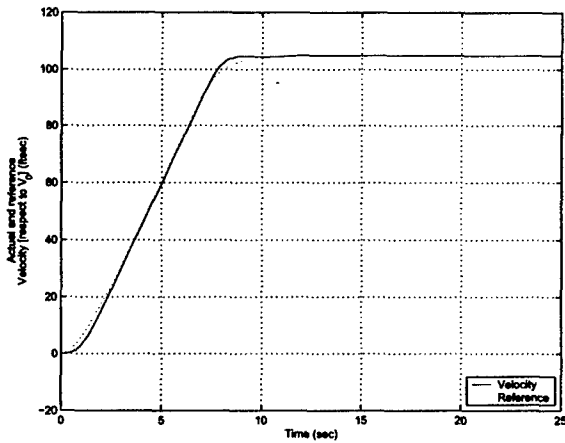
Fig. 9 Formation Flight Geometry

Fig. 8 Velocity tracking

distance $z*$. The forward distance error e_x, lateral distance error e_y and altitude error can be calculated from the trajectory measurements and formation geometric parameters using the relationships:

$$\begin{bmatrix} e_x \\ e_y \\ e_z \end{bmatrix} = R^t(\psi_W) \begin{bmatrix} x_L - x_W \\ y_L - y_W \\ z_L - z_W \end{bmatrix} - \begin{bmatrix} x* \\ y* \\ z* \end{bmatrix} \quad (13)$$

where the rotation matrix $R^t(\psi_W)$ rotates earth frame position error into the wingman frame using the wingman heading angle ψ_W; rotating only around the Z-axis decouples the altitude and horizontal plane errors from the wingman attitude (roll and pitch). This is needed especially during turns or altitude changes to keep all the aircraft of the formation at the same altitude.

allows the wingman aircraft to follow the leader - remotely flown by a pilot with a Radio Control - at pre-defined vertical, forward, and lateral distances during the flight phases when formation flight is engaged. From a geometric point of view the formation flight control problem can be naturally decomposed into two independent problems: a horizontal plane tracking problem and a vertical plane tracking problem. The latter is quite simple because it is sufficient to track leader altitude, while the former needs a little coordinate transformations.

Figure 9 shows the horizontal plane formation geometry. All trajectory measurements: Leader/Wingman position (x_L, y_L, z_L) (x_W, y_W, z_W) are defined with respect to a pre-defined Earth-Fixed Reference frame if they are measured by the on-board GPSs. With the vision system, the relative distance will be measured directly in the wingman reference frame. The pre-defined formation geometric parameters are the forward distance $x*$, lateral distance $y*$ and vertical

4.1 Horizontal Plane Formation Control

The horizontal plane formation controller uses $x*$ and $y*$ as a set point to generate references for the lateral and velocity autopilots: χ_d and V_d. Two Proportional-Integral-Derivative (PID) controllers have been designed using two second order models of velocity and heading dynamics of the autopiloted aircraft. In most papers it assumed that the autopiloted aircraft have a first order dynamics and, often, the simulation and theoretical results remain valid with first order systems only. First order dynamics in velocity and heading is difficult to achieve in the real case; thus, in this paper, it has been used a second order dynamics identified from data simulated with the LQG-LTR autopilots controlling the nonlinear aircraft simulator:

$$\frac{\chi}{\chi_d} = \omega_{N\psi}^2 \frac{s/z1 + 1}{s^2 + 2\xi_p si\omega_{N\psi} + \omega_{N\psi}^2} \quad (14)$$

$$\frac{V}{V_d} = \omega_{NV}^2 \frac{s/z2 + 1}{s^2 + 2\xi_V \omega_{NV} + \omega_{NV}^2} \qquad (15)$$

with $\omega_{N\psi} = 0.5$, $\xi_p si = 0.5$, $z1 = 1$ and $\omega_{NV} = 1$, $\xi_V = 0.33$, $z2 = 2$.

To increase the controller performance, the position errors e_x and e_y have been augmented with velocity and heading errors respectively:

$$
\begin{aligned}
e_x' &= K_x(R^t(\psi_W)(x_L - x_W) - x*) + K_V(V_L - V_W) \\
&= K_x e_x + K_V(V_L - V_W) \qquad (16) \\
e_y' &= K_y(R^t(\psi_W)(y_L - y_W) - x*) + K_\psi(\psi_L - \psi_W) \\
&= K_y e_y + K_\psi(\psi_L - \psi_W) \qquad (17)
\end{aligned}
$$

where K_x, K_Y, K_V and K_ψ has been selected to balance accurately the two errors.

The reference velocity and heading are then generated with the two PID controller:

$$\frac{V_d}{e_x'} = K_1 \frac{(s + a_1)^2}{s} \qquad (18)$$

$$\frac{\chi_d}{e_y'} = K_2 \frac{(s + a_2)^2}{s} \qquad (19)$$

The gains have been selected as:

$K_x = 1.0$ $K_V = 0.83$ $K_1 = 1.4$ $a_1 = 1.2$
$K_y = 1.5$ $K_\chi = 15 * 180/\pi$ $K_2 = 0.035$ $a_2 = 4$

The amount of information needed from the leader is thus very limited: Position in the Earth fixed reference frame, Velocity and Heading; all quantities that can be obtained from the GPS. The choice of the leader outputs to be fed back into the formation controller is crucial: formation flight control based on vision must be capable to reconstruct them with approximately the same accuracy as the GPS system.

4.2 Vertical Plane Formation Control

The vertical plane formation controller uses $z*$ as a set point to generate the reference for the altitude autopilot: h_d. As in the horizontal plane case, a Proportional-Integral (PI) controller is designed based on a second order model of altitude dynamics of the autopiloted aircraft. In fact, it could be sufficient to feed the Leader altitude into the wingman altitude autopilot ($h_d = z_W - z*$), but the leader altitude signal may be very noisy and could stress to much the wingman altitude autopilot. Thus the closed loop control is a better solution. The identified second order model of altitude dynamics is:

$$\frac{h}{h_d} = \omega_{Nh}^2 \frac{s/z3 + 1}{s^2 + 2\xi_h \omega_{Nh} + \omega_{Nh}^2} \qquad (20)$$

where $\omega_{Nh} = 1$, $\xi_h = 0.42$, $z3 = 1.2$. The resulting PI controller is:

$$\frac{h_d}{e_z} = K_h \frac{s + a_3}{s} \qquad (21)$$

with: $K_h = 1$ and $a_3 = 3$.

5 Computer Vision Simulation

The control laws described above assume that the leader absolute position, velocity and heading are available to the Wingman as noisy measurements. In absence of radio communications, a vision system, capable of acquiring the leader image with a camera and of estimating its relative position and attitude, can be used.

The first step in evaluation of such a system feasibility is simulation. To simulate the vision system for a leader-wingman configuration, a computer program must recreate the environment of the mission with all possible visual disturbances, get the aircraft positions and attitudes from a simulator of aircraft dynamics, place accordingly the various vehicles and generate synthetic images as they were acquired from a camera onboard the wingman. This Visual Simulation System (VSS) must be part of the simulation loop and generate frames at the desired camera acquisition frame rate.

At the present time no real flight has been carried on with cameras on board the YF-22 models. In the first real flight test, the vision sensor will be used in open loop to validate the image processing software and to state vision sensor reliability and noise characteristics. In these tests the camera will be probably a light weight and low cost pc camera (often used as web cams) that commonly have a resolution of 640x480 pixels. The algorithm described in the next section will need as input an image with a set of known Markers on the leader aircraft to be identified. A possible solution to this is using infrared light emitting diodes (LEDs) as markers. The low cost PC cameras have CCDs sensors are quite sensible to infrared light thus can be used, with appropriate filters, to detect the infrared LEDs positioned onboard the leader aircraft. because the leader aircraft is a rigid body, the LEDs can be placed onto the aircraft fuselage, wingtips etc and assume then that their geometry is fixed and exactly known. With this configuration the main source of optical disturbance will be the aircraft engine. The use of that type of camera however is not exclusive and is meant as a first very low cost trial solution only to be verified.

The simulation setup used in this work is realized with Commercial Off The Shelf (COTS) software; it includes aircraft dynamics, autopilots and formation keeping controller and the VSS. The simulation of the dynamics systems and the execution of the image processing routines is performed with Mathwork's Simulink. The VSS, that creates the synthetic

environment for the simulation of the vision equipment is based on a commercial software called Dyna-WORLDS.[17] This module is capable to create a synthetic image as if acquired from the cameras on board the follower aircraft. Figure 10 shows the conceptual diagram of Simulink-DynaWORLDS interaction.

The synthetic environment has been interfaced to Simulink to allow a pseudo-real-time simulation of vision: Simulink simulates one step of aircraft dynamics, and sends aircraft position and attitudes to the vision module that renders the scene and sends the image back to Simulink; this triggers an image processing routine that estimates relative displacement between the aircraft for use as feedback in the formation control loop. The size of the image can be varied accordingly to the camera type that has to be simulated. Currently our test are carried or with a resolution of 640x480 pixels.
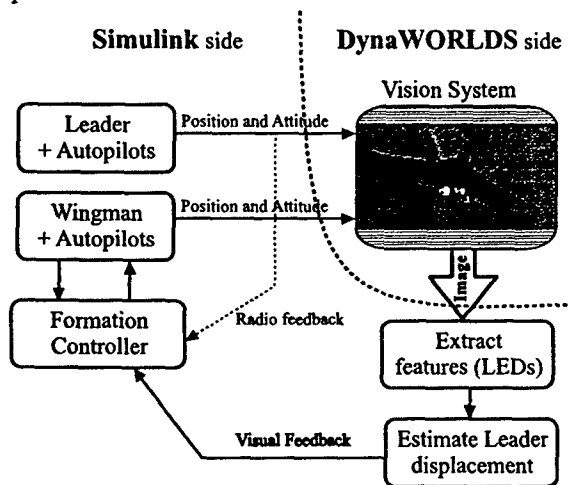
Fig. 10   Conceptual Simulation Environment

The interface between the two softwares is done with inter-process communications based on shared memory. Two buffers have been set-up; one buffer is used to send the simulation data to DynaWORLDS: leader and wingman position and attitude, LEDs positions and camera position and orientation respect to the wingman reference frame. DynaWORLDS receives that data, renders the image as acquired from the wingman camera and uses the second buffer to transfer the image to Simulink. The image is transferred as a $n * m * 3$ matrix that contains the Red Green and Blue (RGB) planes of the image.

The communications are synchronized so that the simulation of image processing delays can be managed entirely from the Simulink side.

Camera lens distortion can be simulated, from the Simulink side, as well, by application of a post-processing filter that warps the image. The synthetic environment can be used to simulate environmental disturbances such as the landscape, the direct sun light

together with fog, rain and clouds. For the simulation of the camera perspective the pin-hole camera model is used, that is also quite appropriate for PC cameras. A pre-filtering process is applied to the image acquired by the camera to reduce noise and extract a least square approximation of the 2-D position of the LEDs to be used as input of the leader position and attitude estimation algorithm.

6   Estimation of Leader Position and Attitude

The goal of the vision system is to estimate the relative displacement and rotations of the leader aircraft respect to the wingman. A Camera is mounted onboard the wingman and it captures two-dimensional (2D) images of the leader aircraft and estimates its position and attitude in the camera frame (a three-dimensional (3D) coordinate system). This relative position, if translated into the wingman frame and then in the earth frame, gives the leader's position and attitude.

Determining the rigid transformation relating 2D images to known geometry, the pose estimation problem, is one of the central problems in photogrammetry, robotics, computer graphics, and computer vision. In robotics, pose estimation is commonly used in hand-eye coordination systems. The information available for solving the pose estimation problem is usually given in the form of a set of point correspondences, each composed of a 3D reference point expressed in object coordinates and its 2D projection expressed in image coordinates. As an anticipation, it is necessary to know exactly the correspondence between any known/recognized 3D point $p_i = (x_i \ y_i \ z_i)^t$ and its projection (2D) on the camera image $c_i = (u_i \ v_i)^t$. Failure in this makes impossible the use of any of the algorithms named below. It is then necessary to put unique optical markers on the Leader aircraft that can be easily recognized by the wingman and associated with the known position of each marker in the Leader reference frame.

For three or four non-collinear points, exact solutions can be computed: A fourth- or fifth-degree polynomial system can be formulated using geometrical invariants of the observed points and the problem can be solved by finding roots of the polynomial system,[18],[19].[20] However, the resulting methods can only be applied to a limited number of points and are thus sensitive to additive noise and possible outliers. For more than four points, closed form solutions do not exist. The classical approach used in photogrammetry is to formulate pose estimation as a nonlinear least-squares most typically, the Gauss-Newton method.[21] In the vision literature, the work by Lowe[22] and its variants is an example of applying the Gauss-Newton method to the pose estimation problem. As with most nonlinear optimizations, these methods rely on a good

initial guess to converge to the correct solution. There is no guarantee that the algorithm will eventually converge or that it will converge to the correct solution. Haralick et al.[23] introduced a pose estimation algorithm which simultaneously computes both object pose and the depths of the observed points. The algorithm seems to be globally convergent, although a complete proof was not given. However, this algorithm has not received much attention, probably due its slow local convergence rate (hundreds of iterations), as indicated by the authors themselves. Lu, Hager and Mjolsness[24] (LHM) show that the pose estimation problem can be formulated as that of minimizing an error metric based on collinearity in object (as opposed to image) space. Using object space collinearity error, they derive an iterative algorithm which directly computes orthogonal rotation matrices and prove that is globally convergent, that is, the solution is always found independently of initial guess. In[25] a comparison of known algorithms and a new one is performed. The LHM algorithm[24] is used as a benchmark and it performs better than all the others in the whole test suite.

For application to the formation flight problem we have selected the algorithm by Lu, Hager and Mjolsness,[24] that we will refer later as LHM algorithm. In general real time systems need tasks that have deterministic execution time. In fact the LHM algorithm is an iterative algorithm that, although proven to be globally convergent, gives no guarantee on the number of iterations needed for convergence, but, in our tests the algorithm has shown a very fast convergence, as reported also by the authors of LHM themselves. In all our simulations the number of iterations remained very low.

6.1 The LHM Algorithm

Lu, Hager and Mjolsness formulate the pose estimation problem as that of minimizing an object-space collinearity error. From this new objective function, they derive an algorithm that operates by successively improving an estimate of the rotation portion of the pose and then estimates an associated translation. The intermediate rotation estimates are always the best orthogonal solution for each iteration. The orthogonality constraint is enforced by using singular value decomposition. They further prove that the proposed algorithm is globally convergent. Empirical results suggest that the algorithm is also extremely efficient and usually converges in five to 10 iterations from very general geometrical configurations. In addition, the same experiments suggest that the LHM method outperforms the Levenberg-Marquardt method, one of the most reliable optimization method currently in use, in terms of both accuracy against noise and robustness against outliers.

It is now tacitly assumed that the correspondence of each 2D point in the video image with the corresponding 3D point on the leader body/frame is known. This assumptions implies that the camera system must be able to tell, by the image only, this correspondence; hence each LED used as marker must be uniquely recognizable from the others. To this end a quite expensive video system could be needed using light emitters each one with different wavelength and a video system capable to recognize the various wavelengths and then establish the 2D-3D correspondence, probably not a simple CCD camera.

The mapping from 3D reference points to 2D image coordinates can be formalized as follows: Given a set of non-collinear 3D coordinates of reference points $p_i = (x_i \ y_i \ z_i)^t$ with $i = 1..n, n \geq 3$ expressed in an object-centered reference frame, the corresponding camera-space coordinates $q_i = (x'_i \ y'_i \ z'_i)^t$ are related by a rigid transformation as:

$$q_i = R p_i + t \qquad (22)$$

where

$$R = \begin{bmatrix} r_1^t \\ r_2^t \\ r_3^t \end{bmatrix} \quad t = \begin{bmatrix} t_x \\ t_y \\ t_z \end{bmatrix} \qquad (23)$$

are the rotation matrix and the translation vector of the object frame respect to the camera frame, respectively.

In computer graphics, the camera reference frame is chosen so that the center of projection of the camera is at the origin of the axis and the optical axis points in the positive z direction. The reference points p_i are projected to the plane with $z' =$, referred to as the normalized image plane, in the camera reference frame.

Let the image point $v_i = (x''_i \ y''_i \ 1)^t$ be the projection of p_i on the normalized image plane. Under the idealized pinhole imaging model, v_i, q_i and the center of projection are collinear. This fact is expressed by the following equation:

$$x''_i = \frac{r_1^t p_i + t_x}{r_3^t p_i + t_z} \qquad (24)$$

$$x''_i = \frac{r_2^t p_i + t_y}{r_3^t p_i + t_z} \qquad (25)$$

or

$$v_i = \frac{1}{r_3^t p_i + t_z}(R p_i + t) \qquad (26)$$

which is known as the collinearity equation. However, another way of formulating collinearity is that the following must hold:

$$R p_i + t = V_i (R p_i + t) \qquad (27)$$

where

$$V_i = \frac{v_i v_i^t}{v_i^t v_i} \qquad (28)$$

is the projection matrix that projects a scene point orthogonally to the line of sight defined by the image point vi.

Given observed image points $\hat{v}_i = (\hat{x}_i \ \hat{y}_i \ 1)^t$, the pose estimation problem is formulated as the problem of minimizing the sum of the squared error

$$E(R,t) = \sum_{i=1}^{n} |||e_i||^2 \qquad (29)$$

where the object-space collinearity error vectors e_i, from equation (27) are:

$$e_i = (I - \hat{V}_i)(Rn_i + t) \qquad (30)$$

and

$$\hat{V}_i = \frac{\hat{v}_i \hat{v}_i^t}{\hat{v}_i^t \hat{v}_i} \qquad (31)$$

The LHM does this minimization solving first the absolute orientation problem, determining an estimated rotation matrix R_k for $k - th$ step; then, from equation (22) estimates the translation vector t_k and then iterates. This algorithm has been proven to be globally convergent (that is finds a solution for any initial guess R_0 and t_0), that $E(R_{k+1}, t_{k+1}) < E(R_k, t_k)$, and has shown that in few iterations: 5 to 10, it reaches the solution.

6.2 Application of LHM to Formation Flight

To apply the LHM algorithm to formation flight, the Leader aircraft must carry a set of uniquely identifiable markers. As introduced above, n LEDs will be placed onto the aircraft body in positions easily viewable from the wingman flying behind of it. The two wing tips, the two rudder's tips and three point on the rear part of the fuselage has been selected to place the markers. Since each led must be identifiable from the others, 7 different colors have been chosen. This choice is quite unrealistic but will be relaxed in the next section.

Figure 11 shows a sample image as taken from the wingman camera; it is possible to see the Leader aircraft, 7 LEDs with different colors each and a superimposed wireframe image of the Leader that shows its reconstructed position.

6.3 The Modified LHM

Having n uniquely identifiable markers is a need for the application of the LHM algorithm. In this section it is shown how it is possible to use the LHM algorithm in a much less structured environment where the LEDs have all the same color. This choice is consistent with the use of single wave length infrared LEDs and an infrared camera or a low cost PC camera with an infrared optical filter.

Fig. 11 Sample image with 7 colored leds

The important fact to note is that the LHM algorithm always converge to a solution even if the correspondence of 2D image points to 3D markers is wrong. In this case the final value of the collinearity error $E(R,t)$ is quite high respect to the case in which that correspondence is correct.

A first approach to the use of undistinguished markers would be to run the LHM algorithm over all possible permutations of the 2D-3D correspondence and choose the solution R^*, t^* which gives the minimum collinearity error $E(R^*, t^*)$. With n LEDs there are n! possible permutations and, even if one run of the LHM requires few milliseconds on a Pentium PC, with, for example 7 leds, the LHM process throughput would become as low as one estimation every 1-2 seconds, surely too low for formation flight.

The idea at the basis of our solution is to place the LEDs over the Leader body appropriately so that their 2D projection on the camera plane, that is their image on the camera, creates a polygon whose sides never intersect for typical formation flight leader-wingman displacements and relative attitudes. This is a feasible assumption because during the whole formation flight mission the relative displacement must be kept approximately constant and relative attitude cannot be more than few degrees in roll, pitch and yaw, otherwise the formation would break in very littel time. As a matter of fact, if the two aircraft are flying in formation they have approximately the same roll, pitch and heading angle.

Figure 12 shows an image of the leader aircraft with 5 identical color LEDs, corresponding to 5 numbered markers, and the unique polygon that connects them. Once the polygon is determined, for each camera image, the unknown of the problem is the numbering of the LEDs, that is the correspondence with the 3D markers. The algorithm starts assigning the index 1 to one randomly chosen LED, then numbers the others clockwise following the polygon sides. The second tentative correspondence set is generated quickly from the previous shifting the LEDs clockwise (from [1 2 3 4 5]

to [5 1 2 3 4] for example). With n markers there are only n 2D-3D correspondences to test.

Fig. 12   Sample image with 5 red LEDs and polygon reconstruction

As a measures of the estimation reliability it is possible to use the ratio ρ between the the minimum value $E(R^*, t^*)$ and the second best result:

$$\rho = \frac{E(R^*, t^*)}{\min_{R_i, t_i \neq R*, t*} E(R_i, t_i)} \quad (32)$$

In all our tests ρ has shown a difference between the best and second best result of 2/3 orders of magnitude.
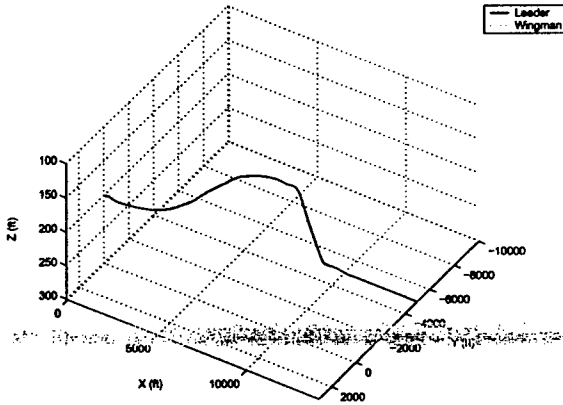
Fig. 13   Comparison of Vision and Radio Feedback - Trajectories

7   Simulations

This section shows the comparison of simulation results for Radio/GPS based and Vision based formation flight performed with the nonlinear aircraft model. The communication rate for position and flight path angle in the former case has been selected to $10Hz$, thus the same rate has been chosen for the image processing algorithm. In the former simulation, the GPS-like position sensor has been modelled as an exact sensor without any noise. In both simulations the leader and wingman aircraft dynamics have been simulated with identical noise on the feedback path of the autopilots.

The leader trajectory contains a first turn right, a short straight path and a turn left followed by a altitude change as shown in Figure 13. The desired relative distance vector $[x * \; y * \; z*]$ is $[70\ 10\ 0]$ ft. The trajectory of the leader aircraft is absolutely unknown to the wingman; they start flying in formation and at time $t = 2$ seconds, the Vision feedback path is turned on.

Figures 14 and 15 show the forward and lateral distance between Leader and Wingman respect to the desired values.
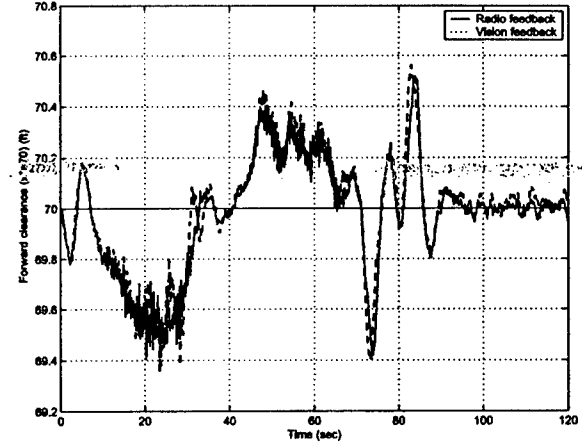
Fig. 14   Comparison of Vision and Radio Feedback - Forward distance
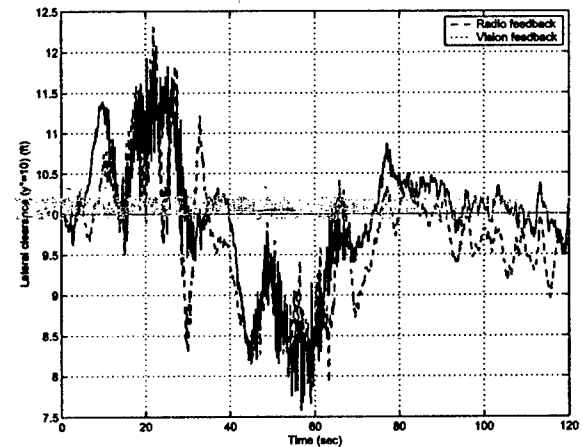
Fig. 15   Comparison of Vision and Radio Feedback - Lateral Distance

The Vision feedback simulations highlights the capability of the Vision system to reconstruct accurately the Leader position; the LHM algorithm has been designed to work on static images rather than on movies but its behavior appears very good in a dynamic environment as well. The position and attitude estimates accuracy could, very probably, benefit from the introduction of some kind of model based filtering scheme

that smoothes estimates and adds the missing link of the dynamic environment.

8 Conclusions

This paper has shown how a vision system for formation flight application can be simulated with COTS software. The autopilots and formation control laws, designed with a GPS-like feedback in mind, has been successfully applied in the vision feedback environment using the same feedback variables estimated by the Vision system rather than received by radio. This work represents a preliminary study on the feasibility of formation flight without radio communications. Open loop real flight tests are expected to be performed in 2004 when the autopilots and formation control laws will be evaluated successfully with radio feedback. Some issues are still open and object of current and future work: reliability of markers identification, identification and exclusion of outliers, extended Kalman filtering to smooth measurements and interpolate missing data, a protocol to request a GPS fix to the leader aircraft in case of accuracy loss in the vision feedback.

References

[1]Blake, W. and Multhopp, D., "Design, Performance, and Modeling Considerations for Close Formation Flight," *Proceedings of the 1999 AIAA GNC Conference, AIAA paper 1999-4343, Portland, OR*, August 1999.

[2]Pachter, M., D'Azzo, J., and Proud, A., "Tight Formation Flight Control," *Journal of Guidance, Control, and Dynamics*, Vol. 24, No. 2, March-April 2001, pp. 246–254.

[3]Giulietti, F., Pollini, L., and Innocenti, M., "Autonomous Formation Flight," *IEEE Control Systems Magazine*, Vol. 20, No. 6, December 2000, pp. 34–44.

[4]Proud, A., "Close Formation Flight Control," *MS Thesis, AFIT/GE/ENG/99M-24, School of Engineering, Air Force Institute of technology (AU), Wright-Patterson AFB, OH*, 1999.

[5]Hall, J., "Three Dimensional Formation Flight Control," *MS Thesis, AFIT/GE/ENG/00M-03, School of Engineering, Air Force Institute of technology (AU), Wright-Patterson AFB, OH*, 2000.

[6]Pachter, M., D'Azzo, J., and Dargan, J., "Automatic Formation Flight Control," *Journal of Guidance, Control, and Dynamics*, Vol. 17, No. 6, 1994, pp. 1380–1383.

[7]Giulietti, F., Pollini, L., and Innocenti, M., "Formation Flight control: A Behavioral Approach," *Proceedings of the 2001 AIAA GNC Conference, AIAA Paper 2001-4239, Montreal, Canada*, August 2001.

[8]Schumacher, C. and Kumar, R., "Adaptive Control of UAVs in Close-Coupled Formation Flight," *Proceedings of the 2000 American Control Conference, Chicago, IL*, June 2000.

[9]Schumacher, C. and Singh, S., "Non Linear Control of Multiple UAVs in Close-Coupled Formation Flight," *Proceedings of the 2000 AIAA GNC Conference, AIAA paper 2000-4373, Denver, CO*, August 2000.

[10]Singh, S., Pachter, N., Chandler, M., Banda, S., Rassmussen, S., and Schumacher, C., "Input-Output Invertibility and Sliding Mode Control for Close Formation Flying of Multiple UAVs," *Proceedings of the 2000 AIAA GNC Conference, AIAA paper 2000-4373, Denver, CO*, August 2000.

[11]Calise, A. and Rysdyk, R., "Nonlinear Adaptive Flight Control Using Neural Networks," *IEEE Control Systems Magazine*, Vol. 18, No. 6, 1998.

[12]Misovec, K., "Applied Adaptive Techniques for F/A-18 Formation Flight," *Proceedings of the 2002 AIAA GNC Conference, AIAA paper 2002-4550, Monterey, CA*, August 2002.

[13]Lavretsky, E., "F/A-18 Autonomous Formation Flight Control System Design," *Proceedings of the 2002 AIAA GNC Conference, AIAA paper 2002-4757, Monterey, CA*, August 2002.

[14]Hanson, C., Ryan, J., Allen, M., and Jacobson, S., "An Overview of Flight Test Results for a Formation Flight Autopilot," *Proceedings of the 2002 AIAA GNC Conference, AIAA paper 2002-4755, Monterey, CA*, August 2002.

[15]Napolitano, M., "West Virginia University, Air Force Office of Scientific Research (AFOSR) Grant F49620-98-1-0136 Final Report," March 2002.

[16]Stein, G. and Athans, M., "The LQG/LTR Procedure for Multivariable Feedback Control Design," *IEEE Transaction on Automatic Control*, Vol. AC, No. 32, Feb. 1987, pp. 105–114.

[17]DynaWORLDS, "www.dynamitechs.com," .

[18]Horaud, R., Canio, B., and Leboullenx, O., "An Analytic Solution for the Perspective 4-Point Problem," *Computer Vision, Graphics, and Image Processing*, No. 1, 1989, pp. 33–44.

[19]Haralick, R., Lee, C., Ottenberg, K., and Nolle, M., "Analysis and Solutions of the Three Point Perspective Pose Estimation Problem," *Proc. IEEE Conf. Computer Vision and Pattern Recognition*, 1991, pp. 592–598.

[20]Dhome, M., Richetin, M., Lapreste, J., and Rives, G., "Determination of the Attitude of 3D Objects from a Single Perspective View," *IEEE Trans. Pattern Analysis and Machine Intelligence*, Vol. 11, No. 12, December 1989, pp. 1265–1278.

[21]Haralick, R. and Shapiro, L., *Computer and Robot Vision*, 1993.

[22]Lowe, D., "Three-Dimensional Object Recognition from Single Two-Dimensional Image," *Artificial Intelligence*, Vol. 31, 1987, pp. 355–395.

[23]Harlalick, R. and et al., "Pose Estimation from Corresponding Point Data," *IEEE Trans. Systems, Man, and Cybernetics*, Vol. 19, No. 6, 1989, pp. 1426–1446.

[24]Lu, C., Hager, G., and Mjolsness, E., "Fast and globally convergent pose estimation from video images," *IEEE Transaction on Pattern Analysis and Machine Intelligence*, Vol. 22, 2000, pp. 610–622.

[25]Ansar, A. and Daniilidis, K., "Linear Pose Estimation from point or Lines," *A.Heyden et al. - Springer-Verlag Berlin*, Vol. ECCV 2002, No. LNCS 2353, 2002, pp. 282–296.

DESIGN OF FORMATION CONTROL LAWS FOR RESEARCH AIRCRAFT MODELS

Sheng Wan[*], Giampiero Campa[*], Marcello R. Napolitano[*§], Brad Seanor[*¶], Yu Gu[*]
*Department of Mechanical and Aerospace Engineering
West Virginia University, Morgantown, WV 26506-6106

Abstract

This paper presents the design approach and simulation results of the preliminary design of the formation control laws for YF-22 aircraft models designed and built at WVU. In the planned configuration, a pilot on the ground controls the leader aircraft while the wingman is required to maintain a pre-defined position and orientation with respect to the leader during flight. The modeling and the design of the control scheme are presented and discussed, with emphasis on the amount of information relative to the leader needed by the wingman to maintain formation. For this purpose, a critical issue is the availability of Euler angle measurements from the leader aircraft. The necessity of identifying a non-linear mathematical model of the aircraft is also discussed. Using the developed nonlinear model, the control of the formation has been simulated within Simulink® and displayed with the Virtual Reality Toolbox® (VRT).

Nomenclature

b	Wingspan, ft
$\bar{c}$	Mean aerodynamic chord, ft
f	Forward distance, ft
f_c	Pre-defined forward clearance, ft
h	Pre-defined vertical clearance, ft
l	Lateral distance, ft
l_c	Pre-defined lateral clearance, ft
m	Aircraft weight, lb
p	Roll rate, deg/sec
q	Pitch rate, deg/sec
$\bar{q}$	Dynamic pressure, lb/ft^2
r	Yaw rate, deg/sec
S	Wing platform area, ft^2
T	Thrust, lb
V	Airspeed, ft/sec
V_x	Projection of x velocity (north), ft/sec
V_y	Projection of y velocity (east), ft/sec
V_z	Vertical velocity, ft/sec
x	Position on x-axis (north), ft
y	Position on y-axis (east), ft
z	Position on z-axis (vertical), ft
α	Angle of attack, deg
β	Angle of sideslip, deg
θ	Pitch angle, deg
ϕ	Bank angle, deg
ψ	Heading angle, deg
δ_A	Aileron deflection, deg
δ_E	Elevator deflection, deg
δ_R	Rudder deflection, deg
δ_T	Throttle command, mV
δz	Vertical distance, ft
Ω	Flight path angle in level plane, deg

Subscripts

L	Leader
W	Wingman
0	Trimmed condition

Introduction

Autonomous formation flight is currently an important research area in the aerospace community. The aerodynamic benefits of formation and, in particular, close formation flight, have been well documented (Ref. [1], [2]). In earlier efforts [3], a leader-wingman formation flight control problem was investigated and a PID-type of formation controller was developed. Ref. [4] describes the application of an "extremum seeking" algorithm to the formation control problem. In Ref. [5] a formation flight control scheme was proposed based on the concept of Formation Geometry Center, also known as Formation Virtual Leader. Some of the initial experimental results of formation flight were reported in Ref [6]. However, in all the previous efforts, the formation control problem is considered with the aircraft flying at straight level flight conditions and/or under mild maneuvering. To the best of the knowledge by the authors, formation control has yet to be attempted experimentally for highly maneuvered flight conditions.

Graduate Research Assistant
Research Assistant Professor
§Professor, AIAA Member
¶Research Assistant Professor, AIAA Member

This paper presents preliminary results from the design of the formation control laws for YF-22 aircraft models designed, built, and instrumented at WVU. One of the 3 WVU YF-22 models is shown in Figure 1. The aircraft has a 8 ft length with a 6.5 ft wing span with an approximate 48 lbs take-off weight, including a 12 lbs electronic payload customized for formation flight with a GPS system and a set of RF modems for data transmission. Figures 2 and 3 show a general and a more detailed block diagram of the electronic payload. The aircraft models are now undergoing individual flight-testing with formation control flight-testing scheduled to start in 2003. Due to the limitations on the flight range, the WVU YF-22 models will be expected to perform fairly tight maneuvers at high Euler angles and moderately high angular rates. Therefore, a specific challenge is to design a control scheme capable of handling non-linear dynamic effects. Another objective is to introduce a formation control scheme with the least amount of information to be exchanged from wingman to leader and maintain a pre-defined formation geometry.

Formation control configuration for the WVU YF-22 models

The main objective is to test the formation controller with the leader aircraft being remotely piloted and the wingman aircraft capable of following the leader at selected vertical, forward, and lateral distances during the flight. All aircraft used in the formation are manually flown for take-off and landing with the formation engaged after all aircraft have reached a certain meeting point within the flight range. A specific constraint for this project is that the aircrafts need to remain within a visual range. This, in turn, implies that frequent maneuvers have to be performed.

In conventional formation control schemes, only the relative position and the velocity vector of the wingman with respect to the leader are required by the "formation-autopilot" of the wingman to maintain the desired formation. The use of this amount of information has shown to be sufficient for formation control with mild maneuvers by the leader. However, under substantial maneuvering conditions, additional dynamic variables from the leader – such as, Euler angles and angular rates – are needed by the wingman for formation control purposes.

Based on the above considerations, the electronic instrumentation of the WVU YF-22 wingman models includes:

- A three-axis angular rate gyro measuring p_W (roll rate), q_W (pitch rate), and r_W (yaw rate);
- A vertical gyro measuring θ_W (pitch angle) and ϕ_W (bank angle);
- A GPS receiver measuring the position of the wingman aircraft (with reference to a pre-defined earth-fixed reference) x_W, y_W, and z_W, and velocity vector V_{Wx}, V_{Wy} and V_{Wz}.

In addition, the following measurements from the leader are available via a 10 Hz data link for formation flight control purposes:

- θ_L (pitch angle) and ϕ_L (bank angle), (from leader's vertical gyro);
- Aircraft position (with reference to a pre-defined earth-fixed reference) x_L, y_L, and z_L, and velocity vector V_{Lx}, V_{Ly} and V_{Lz} (from leader's GPS).

Control strategy

The formation control problem can be basically classified as a *Dynamic 3-D Target-Tracking* problem, where the objective is to track a certain point (desired position) dynamically specified by the leader. The main difference between conventional 'trajectory-following' flight and formation flight is that in the first case the trajectory is typically pre-defined and stored within the on-board computer while in the second case the trajectory to be followed is 'produced' on-line by the leader aircraft flown under remote control; thus, the trajectory information has to be obtained in real time from some of the relevant states of the leader aircraft (position, velocity, etc.). Ideally, to achieve desirable trajectory tracking performance, the formation flight control strategy should be based on full state tracking strategy. This concept can be concisely expressed as:

Wingman's control inputs = Leader's control inputs + State error feedback

where the control inputs include deflections for the throttle, elevator, aileron and rudder, while state error feedback consists of internal state variable errors and trajectory state variable errors between leader and wingman. Particularly, internal state variable errors are angular rate errors and Euler angle errors (pitch and bank angles); trajectory state variable error are instead given by projected 3-D position and velocity errors (i.e., forward

2

distance, lateral distance and vertical distance, and their time derivatives, as defined in next section).

This approach is based on the fact that, if the wingman flies at the same position of the leader, a perfect position tracking could be achieved under any reasonable maneuvering the leader aircraft might execute, since the leader and wingman aircraft are sharing very similar dynamics (assuming same type of aircraft). In reality, extra compensation might be needed to account for the trajectory variable difference between the leader and the ideal wingman. This is because the desired wingman position is shifted with respect to the leader's position. Since both the leader's state and input vectors are needed to calculate the wingman input, a high communication bandwidth between the leader and wingman is required.

Among conventional formation control schemes, the simplest scheme in terms of the minimum amount of information from leader is based upon an existing autopilot (functioning as an "inner loop" controller) with an additional "formation-autopilot" added on to an "outer loop" controller. This outer loop controller uses only trajectory measurements from the leader available from GPS. Unfortunately, this simple formation control scheme has shown desirable performance only if the leader is flying at level straight and/or performing mild maneuvers.

A reasonable tradeoff between the simplest and the most complete schemes introduced above is given by the use of Euler angles error feedback along with trajectory error feedback by the wingman. The control strategy discussed in this paper is based on this approach.

Controller design

Since formation control is a 3-D tracking problem, the control task can be decomposed into three sub-tasks: vertical distance (height) control, lateral distance control, and forward distance control. On the other hand, since the dynamics of the aircraft attitude (angular movement) is much faster than the trajectory dynamics (translational movement), the whole dynamics exhibit a typical two-time-scale feature. Therefore, the design of the control system can be decomposed into two separate phases, that is, the inner loop and the outer loop design. The function of the inner loop controller is to maintain and/or track the desired pitch/bank angle command; the outer loop controller – which is based on the designed inner loop controller and uses the desired pitch/bank angle command as its output – tries to maintain and/or track the desired formation flight.

Formation geometry and trajectory variables

As described above, formation flight control problem can be decomposed as a level plane and a vertical plane dynamic trajectory-tracking problem.

Level plane formation definition

Figure 4 shows the level plane formation geometry. All the trajectory measurements, i.e., leader/wingman position and velocity, are defined with respect to a pre-defined Earth-Fixed Reference x-o-y plane and are measured by the on-board GPS's. The pre-defined formation geometric parameters are the forward clearance, f_c, and the lateral clearance, l_c. The formation trajectory variables in level plane – the forward distance, f, and lateral distance, l, can be calculated from the trajectory measurements and formation geometric parameters as:

$$l = \frac{V_{Ly}(x_L - x_F) - V_{Lx}(y_L - y_F)}{V_{Lxy}} - l_c \qquad (1)$$

$$f = \frac{V_{Ly}(y_L - y_F) + V_{Lx}(x_L - x_F)}{V_{Lxy}} - f_c \qquad (2)$$

where $V_{Lxy} = \sqrt{V_{Lx}^2 + V_{Ly}^2}$ is the projection of the leader's velocity onto x-y plane. Accordingly, the relative forward speed and relative lateral speed of the wingman are defined as the time derivatives of the forward distance and lateral distance respectively and are needed for formation control purposes which can be calculated as:

$$\dot{l} = \frac{V_{Lx}V_{Fy} - V_{Ly}V_{Fx}}{V_{Lxy}} + (f + f_c)\dot{\Omega}_L \qquad (3)$$

$$\dot{f} = V_{Lxy} - \frac{V_{Lx}V_{Fx} + V_{Ly}V_{Fy}}{V_{Lxy}} - (l + l_c)\dot{\Omega}_L \qquad (4)$$

There are basically two methods to obtain the angular velocity (around the vertical axis) $\dot{\Omega}_L$. One method is to first calculate Ω_L from the GPS measurement (V_{Lx}, V_{Ly}), then apply conventional numerical derivative techniques to estimate the time derivatives of Ω_L; within this approach particular caution should be exercised due to the sensitivity of the numerical derivative with respect to measurement noise. A second approach consists in using additional measurements from the leader aircraft, that is, using the following kinematic relation (assuming $\dot{\beta}_L = 0$):

$$\dot{\Omega}_L \cong \dot{\psi}_L = (q_L \sin\phi_L + r_L \cos\phi_L)/\cos\theta_L \qquad (5)$$

This second approach requires not only the vertical gyro (to measure bank angle ϕ_L and pitch angle θ_L) but also the angular rate gyros (to measure

3

pitch rate q_L and yaw rate r_L) on the leader aircraft.

In this study the first approach was used with the definitions provided above. The level plane formation control problem can be sub-divided into a lateral distance control problem and a forward distance control problem.

Vertical plane formation definition

At nominal conditions, the leader and the wingman aircraft are separated by a vertical clearance h. The vertical distance, δz, can then be calculated by:

$$\delta z = z_L - z_W - h \qquad (6)$$

while its time derivative is given by:

$$\dot{\delta z} = V_{Lz} - V_{Wz} \qquad (7)$$

Control laws

Lateral Distance Control

The objective of the lateral distance control is to minimize the lateral distance l. The basic physical principle of the lateral distance control can be expressed by the following action-consequence logic:

aileron $\rightarrow$ roll rate $\rightarrow$ bank angle $\rightarrow$
lateral speed $\rightarrow$ lateral distance

In addition, the function of the rudder is to augment the lateral-directional stability (by increasing the Dutch Roll damping). Therefore, the lateral formation control law consists of an inner loop controller – controlling the bank angle and augmenting the lateral-directional stability - and an outer loop controller - maintaining the pre-defined flight formation with respect to the leader. The control law, represented in Figure 5, can be expressed as:

Inner loop control law:

$$\delta_{WA} = K_p p_W + K_\phi (\phi_W - \phi_g) \qquad (8)$$

$$\delta_{WR} = K_r r_W \qquad (9)$$

Outer loop control law:

$$\phi_g = \phi_L + K_{ldot}\dot{l} + K_l l \qquad (10)$$

Forward Distance Control

The objective of the forward distance control is to minimize the forward distance, f. This task can only be accomplished through the involvement of the throttle control channel. In fact, by increasing/decreasing the throttle, the thrust of the engine and therefore the speed of the aircraft is increased/decreased; this, in turn, allows to control the forward distance between leader and wingman. The forward distance control law, represented in Figure 6, is given by:

$$\delta_T = \delta_{T0} + K_{fdot}\dot{f} + K_f f \qquad (11)$$

Vertical Distance Control

The objective of the vertical distance control is to minimize the vertical distance, δz. This task is accomplished through the use of the elevator control channel. The vertical distance control law is similar to the conventional altitude-hold autopilot with the only difference being that the altitude reference may vary according to the leader's altitude. Similar to the lateral distance controller, the vertical distance control scheme can be designed using an inner loop control scheme - which is basically a pitch angle controller - and an outer loop controller which provide an altitude control capabilities:

Inner loop control law:

$$\delta_E = \delta_{E0} + K_q q_W + K_\theta (\theta_W - \theta_g) \qquad (12)$$

Outer loop control law:

$$\theta_g = \theta_L + K_{zdot}\dot{\delta z} + K_z \delta z \qquad (13)$$

This control law is represented in Figure 7

Linear model and controller parameter design

For the purpose of conducting a preliminary design of the formation control laws for the current WVU YF-22 models, a linear mathematical model of a *previous* YF-22 model was used. The earlier WVU YF-22 research model was slightly smaller and carried a lighter electronic payload but has similar dynamic and aerodynamic characteristics. The linear mathematical model was obtained from a Parameter IDentification (PID) analysis using actual flight test data collected around a flight condition with airspeed of 140 ft/sec and altitude of approximately 1000 ft. The actuator dynamics is modeled using the following 1st order transfer function:

$$G_a(s) = \frac{1}{1 + 0.05s} \qquad (14)$$

Lateral-directional model and controller parameter design

The controller design process was divided into two phases, that is, inner loop and outer loop design. Typically, the inner loop controller can be designed based on a linear lateral-directional aerodynamic model. The linear lateral-directional aerodynamic state variable model obtained from the PID analysis is given by:

4

$$\begin{bmatrix} \dot{\beta} \\ \dot{p} \\ \dot{r} \\ \dot{\phi} \end{bmatrix} = \begin{bmatrix} -1.462 & -0.07 & -1.19 & 0.23 \\ -17.86 & -0.57 & 8.46 & 0 \\ 11.55 & -1.30 & -2.71 & 0 \\ 0 & 1 & 0 & 0 \end{bmatrix} \begin{bmatrix} \beta \\ p \\ r \\ \phi \end{bmatrix} +$$

$$\begin{bmatrix} -0.22 & 1.56 \\ 11.59 & 23.17 \\ 14.40 & -26.41 \\ 0 & 0 \end{bmatrix} \begin{bmatrix} \delta_A \\ \delta_R \end{bmatrix} \quad (15)$$

To design the outer loop control parameters a suitable reference model is needed. A suitable model for the lateral trajectory controller design can be obtained by considering the aircraft performing a steady state coordinated turn where the lift force balance and centrifugal force balance equations can apply. This leads to the following expression:

$$\dot{\Omega}_W = \frac{g}{V_{W_{xy}}} \tan \phi_W \quad (16)$$

On the other hand, by assuming a straight and level flight condition of the leader and (constant) identical speed by the wingman and the leader, equation (3) takes on the following simple form:

$$\dot{d} = V_{W_{xy}} \sin(\Delta\Omega) \quad (17)$$

where $\Delta\Omega = \Omega_W - \Omega_L$. The linearization of the above two equations around the level-straight flight condition of the wingman (note that $\Delta\dot{\Omega} = \dot{\Omega}_W$ under the assumed condition) provides the following model of the trajectory dynamics:

$$\begin{cases} \Delta\dot{\Omega} = \dfrac{g}{V_{W_{xy}}} \phi_W \\ \dot{d} = V_{W_{xy}} \Delta\Omega \end{cases} \quad (18)$$

Thus, the full linear model for lateral distance controller design is the combination of Eqs. (14), (15), and (18). Classic root-locus based compensation design tools can then be applied to the model for evaluating the controller gains (Ref. [7]). The final design parameters are given by:

$$K_p = 0.12, \quad K_\phi = 0.25, \quad K_r = 0.4 \quad (19)$$
$$K_{ldot} = 0.6, \quad K_l = 0.086$$

Forward model and controller parameter design

The cascade of two first order linear models can approximate the forward dynamics. The 1st model represents the engine response in terms of throttle to thrust; this model has been obtained through an experimental analysis of the performance of the jet engines installed on the WVU YF-22 aircraft; the 2nd model represents the airspeed response in terms of thrust to airspeed.

The following transfer function represents the resulting complete transfer function of throttle to airspeed:

$$G_{VT}(s) = G_{VT}(s)G_{TT}(s) = \frac{0.2}{1+s} \times \frac{0.315}{1+6.5s} \quad (20)$$

It is noted that this model also represents the transfer function from throttle (of wingman) to forward velocity of (4) under the assumed level-straight constant speed flight condition. The parameters of the forward distance controller outlined in Eq. (11) were then determined through root locus-based compensator design. The resulting parameters are:

$$K_{fdot} = 4.76, \quad K_f = 1.19 \quad (21)$$

Vertical model and controller parameter design

The design is based on a model consisting of short period model plus a kinematic model. The state variable model of the short period dynamics of the WVU YF-22 model obtained from PID analysis is given by:

$$\begin{bmatrix} \dot{\alpha} \\ \dot{q} \end{bmatrix} = \begin{bmatrix} -1.73 & 0.52 \\ -17.97 & -1.53 \end{bmatrix} \begin{bmatrix} \alpha \\ q \end{bmatrix} + \begin{bmatrix} 0.38 \\ -20.15 \end{bmatrix} \delta_E \quad (22)$$

The linearized kinematic model is given by:

$$\begin{cases} \dot{\theta} = q \\ \delta\dot{z} = V_{W_z}\theta \end{cases} \quad (23)$$

With a similar root locos – based compensation design, the parameters of the vertical controller were evaluated and given by:

$$K_q = 0.2, \quad K_\theta = 0.4, \quad K_{zdot} = 0.5, \quad K_z = 0.75 \quad (24)$$

Nonlinear simulation model

The formation control law developed in the previous section was based on a linear aircraft model. Such a controller, if properly designed, can be guaranteed to perform nominally only when the system is operating around the design point where the linear model was derived from. However, non-linear dynamic effects, particularly those associated with the kinematics, cannot be ignored when the aircraft is undergoing a significant trajectory maneuver, i.e., flying at a large bank angle. Thus, it is necessary that the designed controller be validated through simulation using a nonlinear model so that any major non-linearities in terms of trajectory dynamics, such as non-linear reference transformation and kinematic non-linearity, can be accounted for.

The non-linear aircraft model of dynamics can be described by the following 6 DOF equations plus kinematic equations:

5

6 DOF Dynamics equations
Rotational acceleration equations:

$$I_x \dot{p} - I_{xz}\dot{r} + (I_z - I_x)qr - I_{xz}pq = L \quad (25)$$

$$I_y \dot{q} + (I_x - I_z)rp + I_{xz}(p^2 - r^2) = M \quad (26)$$

$$I_z \dot{r} - I_{xz}\dot{p} + (I_y - I_x)pq + I_{xz}qr = N \quad (27)$$

Translational acceleration equations:

$$\dot{V} = \frac{1}{m}(-D\cos\beta + Y\sin\beta + T\cos\alpha\cos\beta)$$
$$-g(\sin\theta\cos\alpha\cos\beta - \cos\theta\sin\phi\sin\beta \quad (28)$$
$$-\cos\theta\cos\phi\sin\alpha\cos\beta)$$

$$\dot{\alpha} = \frac{1}{mV\cos\beta}(-L_f - T\sin\alpha)$$
$$+\frac{g}{V\cos\beta}(\cos\theta\cos\phi\cos\alpha + \sin\theta\sin\alpha)] \quad (29)$$
$$+q - (p\cos\alpha + r\sin\alpha)\tan\beta$$

$$\dot{\beta} = \frac{1}{mV}(D\sin\beta + Y\cos\beta - T\cos\alpha\sin\beta)$$
$$+p\sin\alpha - r\cos\alpha \frac{g}{V}(\sin\theta\cos\alpha\sin\beta \quad (30)$$
$$+\cos\theta\sin\phi\cos\beta - \cos\theta\cos\phi\sin\alpha\sin\beta)$$

In the above equations,

$$L = \bar{q}SbC_l, \quad M = \bar{q}S\bar{c}C_m, \quad N = \bar{q}SbC_n \quad (31)$$

$$D = \bar{q}SC_D, \quad L_f = \bar{q}SC_L, \quad Y = \bar{q}SC_Y \quad (32)$$

are aerodynamic moments and forces along x, y, z body axis respectively, where C_l, $\cdots$, C_Y are aerodynamic moment/force coefficients that are functions of state and input variables.

6 DOF Kinematic equations
Attitude rate equations:

$$\dot{\phi} = p + q\sin\phi\tan\theta + r\cos\phi\tan\theta \quad (33)$$

$$\dot{\theta} = q\cos\phi - r\sin\phi \quad (34)$$

$$\dot{\psi} = q\sin\phi\sec\theta + r\cos\phi\sec\theta \quad (35)$$

Earth-relative velocity equations:

$$\dot{x} = V[\cos\beta\cos\alpha\cos\theta\cos\psi$$
$$+\sin\beta(\sin\phi\sin\theta\cos\psi - \cos\phi\sin\psi) \quad (36)$$
$$+\cos\beta\sin\alpha(\cos\phi\sin\theta\cos\psi + \sin\phi\sin\psi)]$$

$$\dot{y} = V[\cos\beta\cos\alpha\cos\theta\sin\psi$$
$$+\sin\beta(\sin\phi\sin\theta\sin\psi + \cos\phi\cos\psi) \quad (37)$$
$$+\cos\beta\sin\alpha(\cos\phi\sin\theta\sin\psi - \sin\phi\cos\psi)]$$

$$\dot{h} = V(\cos\beta\cos\alpha\sin\theta - \sin\beta\sin\phi\cos\theta$$
$$-\cos\beta\sin\alpha\cos\phi\cos\theta) \quad (38)$$

The mass/inertia and geometric characteristics of the WVU YF-22 model were evaluated with an experimental set-up. Thus, the remaining critical issue was the determination of the aerodynamic force/moment coefficient C_l, $\cdots$, C_Y. These coefficients are usually obtained through wind-tunnel test. In this study, however, wind-tunnel testing was not feasible. Thus, to calculate these coefficients, the 6 DOF nonlinear aircraft model expressed by equations (25) through (32) was linearized around the given nominal flight condition and compared with the identified linear model in Eqs. (22) and (15). The underlying assumption is that non-dimensional aerodynamic forces and moments were approximately linear in the state variables; this approach allowed the evaluation of the aerodynamic coefficients. The maximum

Simulation & Visualization Environment

A Simulink scheme featuring the developed non-linear models of the WVU YF-22 aircrafts and the designed formation controller was implemented and shown in Figure 8. In this scheme, the complete non-linear models of two WVU YF-22 aircrafts are enclosed in separate blocks. These blocks are essentially based on the available libraries from the Flight Dynamics and Control (FDC) Toolbox [8]. The aircraft geometric, inertial, and aerodynamic data have been modified to allow the modeling of the WVU YF-22 aircraft models (Figure 9). Figure 10 shows in more detail the controller block.

Given the multi-object nature of the problem, the design of a visualization environment fully integrated with the simulation was considered to be critical. The Virtual Reality Toolbox (VRT), was chosen as visualization environment since it allowed for object and events of a virtual world (usually coded in VRML 2.0 or higher [9]) to be driven by signals coming from Matlab or Simulink. A VRML world including two YF-22 graphical models and a simple landscape was then implemented and connected with the simulation using the VRT Simulink Blocks. The resulting scenery from a view behind the wingman and in front of the leader is shown in Figures 11 and 12. The option of selecting between different views such as side, rear or top of a given vehicle was also very helpful for analyzing the aircrafts trajectories and evaluating the controller's performance.

Simulation results

The simulations were conducted based on the following assumptions and boundary conditions:
- Oval flight trajectory in level plane with maximum leader bank angle of approx. 55

6

deg (as recorded in typical flight tests of the models)

- "Level → climb → level" trajectory in vertical plane
- Airspeed: 140ft/sec
- Jointly simulated with lateral, forward and vertical distance control
- Formation geometry: $f_c = 100$ ft; $l_c = 100$ ft, $h = 0$ ft
- Initial position error: $f = 300$ ft , $l = 300$ ft, $\delta z = 0$ ft
- Simulation length: 70 sec

Figure 13 shows the initial positions of the two aircrafts. Figures 14 through Figure 19 illustrate the results from the simulation. It can be seen that the maximum tracking error occurs when the leader is executing "hard" rolling maneuvers at an approx. 55° bank angle. An analysis of the errors shows that the control scheme is providing desirable performance with maximum forward, lateral and vertical errors about 21ft, 30 ft, and 10 ft respectively. Smaller errors could be achieved through selection of stricter specifications during the design of the compensation-based control laws; however, smaller error ranges are associated with even higher angular velocities and, therefore, structural loads.

Conclusions
This paper presented results of a formation flight control law design for later implementation and flight testing using YF-22 aircraft models designed and built at WVU. These aircraft models feature a specific electronic instrumentation to provide formation flight capabilities. A procedure for obtaining a non-linear model of the aircraft from partial information is discussed, along with some other critical issues. The analysis shows that knowledge of the Euler angles of the leader aircraft is critical for the wingman to maintain the assigned formation geometry throughout the maneuvered flight.

References
[1] Meir Pachter, John J. D'Azzo, and Andrew W. Proud, "Tight Formation Flight Control," Journal of Guidance, Control, and Dynamics, Vol. 24, No. 2, March-April 2001, pp. 246-254.
[2] Fabrizio Giulietti, Lorenzo Pollini, and Mario Innocenti, "Autonomous Formation Flight," IEEE Control Systems Magazine, Vol. 20, No. 6, pp. 34-44, Dec. 2000.
[3] Meir Pachter, John J. D'Azzo, and J. L. Dargan, "Automatic Formation Flight Control," Journal of Guidance, Control, and Dynamics, Vol. 17, No. 6, 1994, pp. 1380-1383.
[4] Paolo Binetti, Kartik B. Ariyur, Miroslav Krstic and Franco Bernelli, "Control of Formation Flight via Extremum Seeking," Proceedings of the America Control Conference, Anchorage, 2002.
[5] Fabrizio Giulietti, Lorenzo Pollini, and Mario Innocenti, "Formation Flight control: A Behavioral Approach," AIAA Paper 2001-4239, Proceedings of the AIAA Guidance, Navigation, and Control Conference and Exhibit, August 2001, Montreal.
[6] Eugene Lavretsky, "F/A-18 Autonomous Formation Flight Control System Design," AIAA Paper 2002-4757, Proceedings of the AIAA Guidance, Navigation, and Control Conference and Exhibit, August 2002, Monterey, California.
[7] Stevens, B. and Lewis, F. "Aircraft Control and Simulation," John Wiley & Sons, NY, 1992.
[8] M. O. Rauw, FDC 1.2 – A Simulink Toolbox for Flight Dynamics and Control Analysis, Delft, The Netherlands: Delft University, 1998.
[9] The VRML Web Repository (Dec. 2002): http://www.web3d.org/vrml/vrml.htm
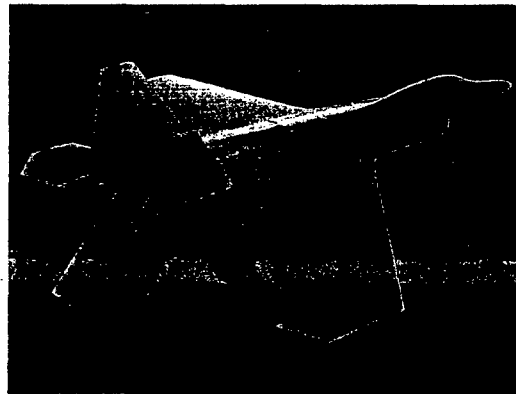
Figure 1 - WVU YF-22 aircraft model
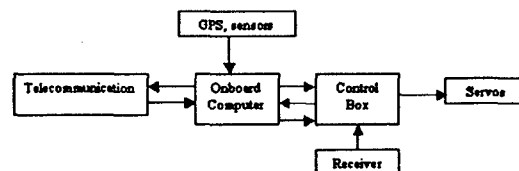
Figure 2 - General Block diagram of the payload

7
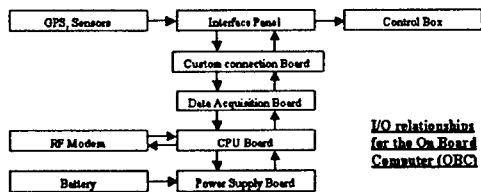
Figure 3 – Payload detailed block diagram
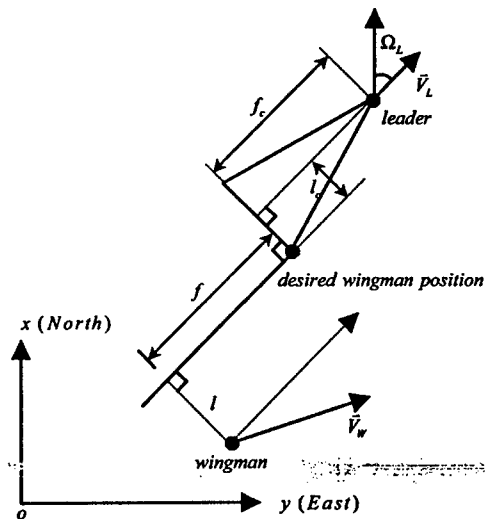
Figure 4 - Level Plane formation geometry
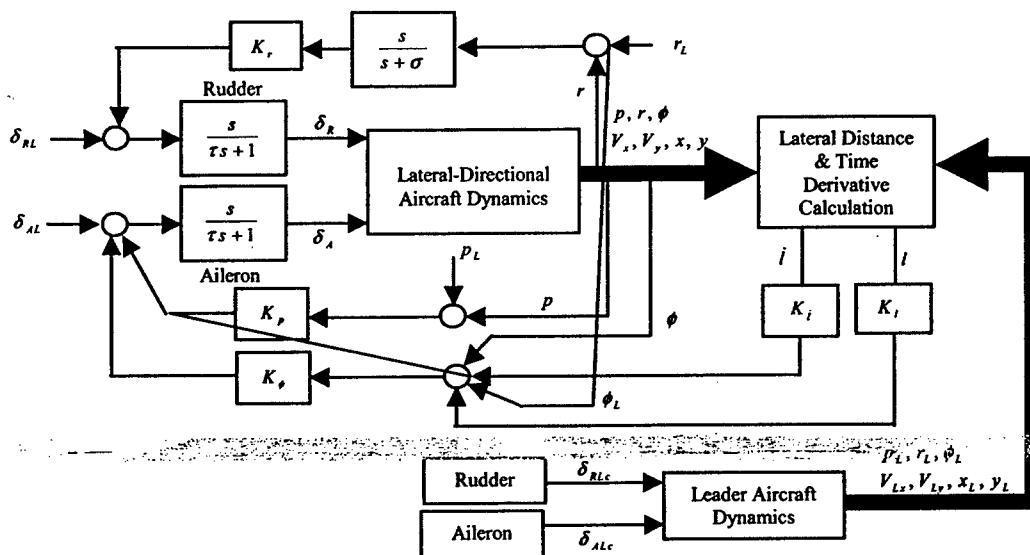
Figure 5 - Lateral-Directional Control Law
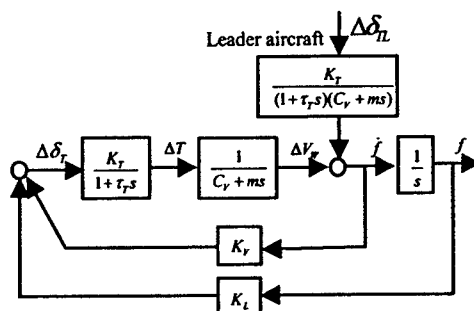
Figure 6 - Forward Control Law

8
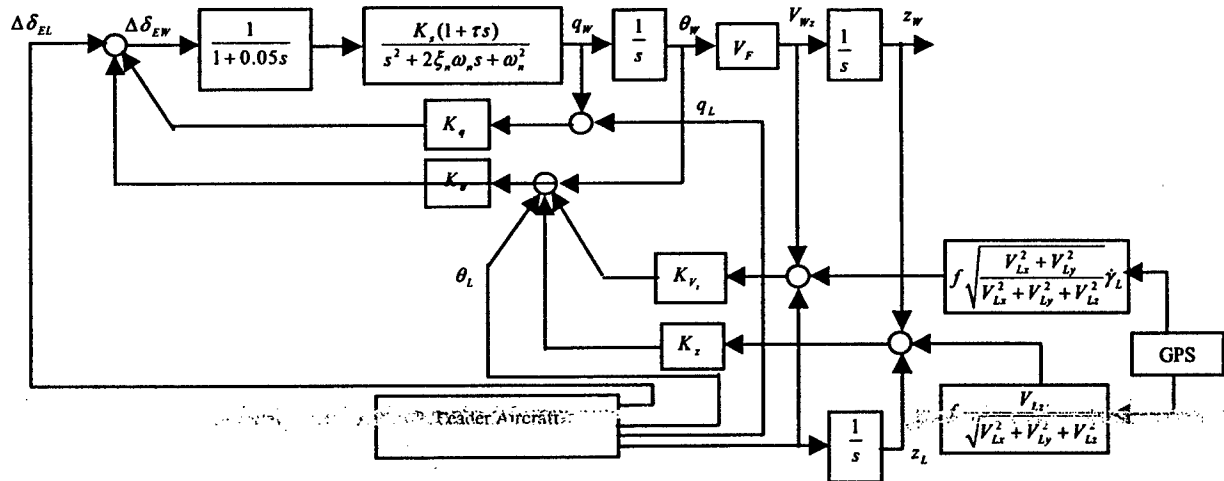
Figure 7-Vertical Control Law
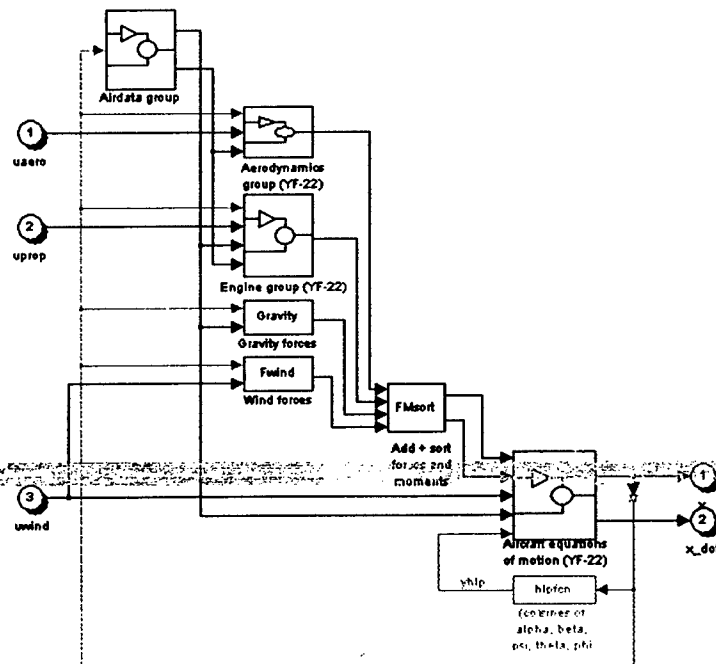
Figure 8 - Aircraft model architecture

9
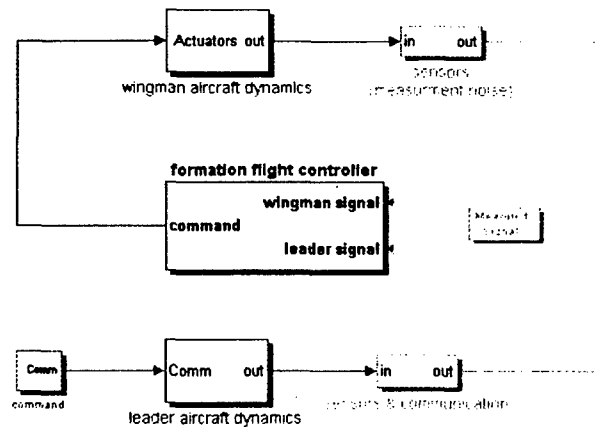
Figure 9 - Main Simulink scheme
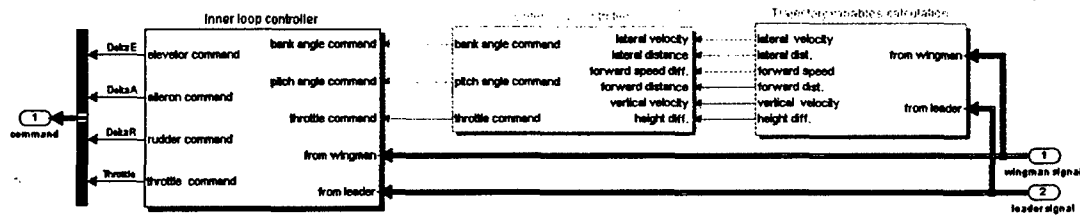
Figure 10 - Formation flight controller block

Figure 11 – Visualization (behind wingman)

Figure 12 - Visualization (in front of leader)

trajectory in x-y plane (red: wingman; blue: leader)
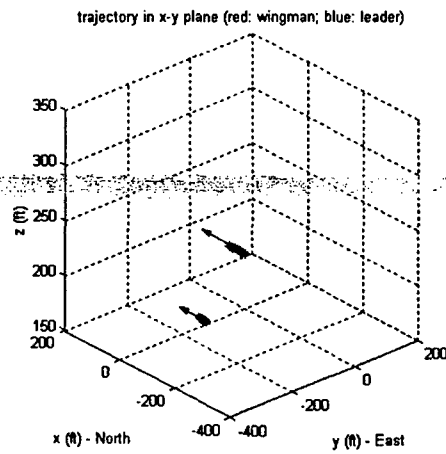
Figure 13 - Initial condition

10
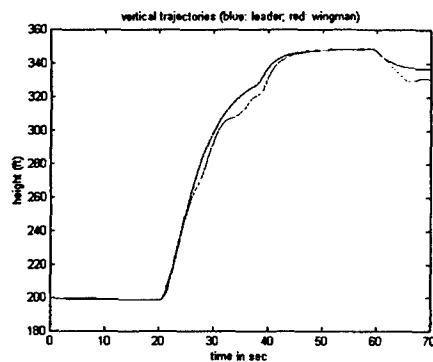
Figure 14 - Trajectories in vertical plane
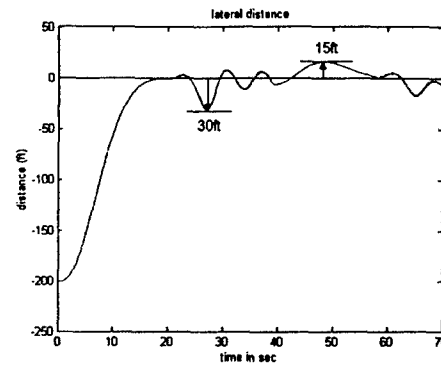
Figure 17 - Lateral distance

Figure 15 - Trajectories in level plane

Forward Clearance: 100ft
Lateral Clearance: 100ft
Airspeed: 140ft/sec

Leader
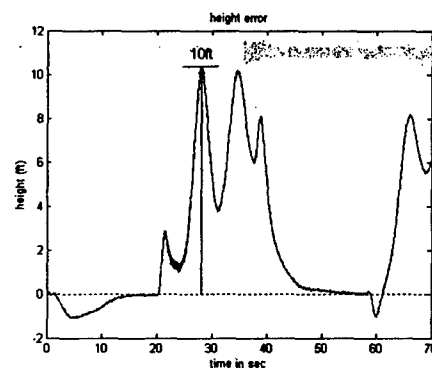
Figure 18 - Vertical distance

Figure 19 - Bank angles
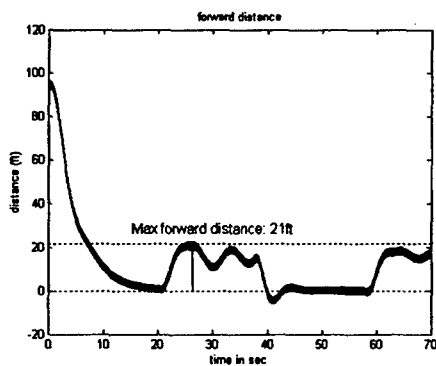
Figure 16 - Forward distance

11

DESIGN OF CONTROL LAWS
FOR MANEUVERED FORMATION FLIGHT

Giampiero Campa^, Marcello R. Napolitano@, Brad Seanor^, Mario G. Perhinschi^

Department of Mechanical and Aerospace Engineering, West Virginia University, Morgantown, WV 26506/6106,

Abstract

This paper presents identification, control synthesis and simulation results for an YF-22 aircraft model designed, built, and instrumented at West Virginia University. The goal of the project is the experimental demonstration of formation flight for a set of 3 of the above models. In the planned flight configuration, a pilot on the ground controls the controls of the leader aircraft while a wingman aircraft is required to maintain a pre-defined position and orientation with respect to the leader. The identification of both a linear model and a nonlinear model of the aircraft from flight data is discussed first. Then, the design of the control scheme is presented and discussed. Using the developed nonlinear model, the control laws for a maneuvered flight of the formation are then simulated with Simulink® and displayed with the Virtual Reality Toolbox®. Simulation studies have been performed to evaluate the effects of specific parameters and the system robustness to atmospheric turbulence. The results of this analysis have allowed the formulation of specific guidelines for the design of the electronic payload for formation flight.

1 Introduction

Autonomous formation flight is an important research area in the aerospace community. The aerodynamic benefits of formation flight, and in particular close formation flight, have been well documented [1]. The investigation of control issues related to a leader-wingman formation has lead to the introduction of different types of compensation-type controllers [2]. In Ref. [3] a formation flight control scheme was proposed based on the concept of Formation Geometry Center, also known as the Formation Virtual Leader. More complex control laws based upon Linear Quadratic Regulator and Dynamic Inversion (DI) approaches have also been proposed [4].

This paper presents design results of the formation control laws to be implemented on a set of 3 YF-22 aircraft models that are designed, built, and instrumented at West Virginia University (WVU). One of the 3 WVU YF-22 models is shown in Figure 1. The model features an 8 ft. fuselage length with a 6.5 ft. wingspan for an approximate take-off weight of 48 lbs, including 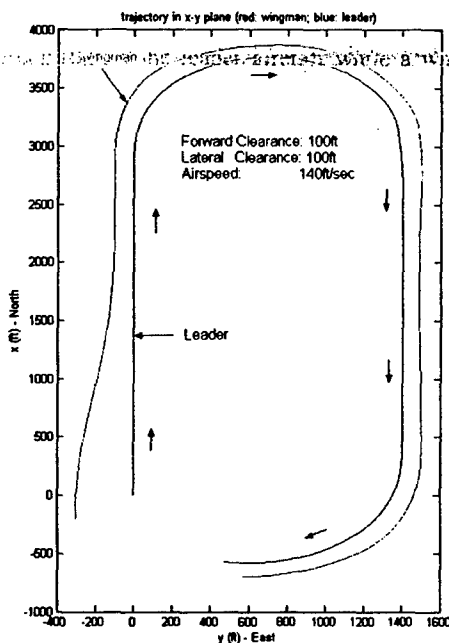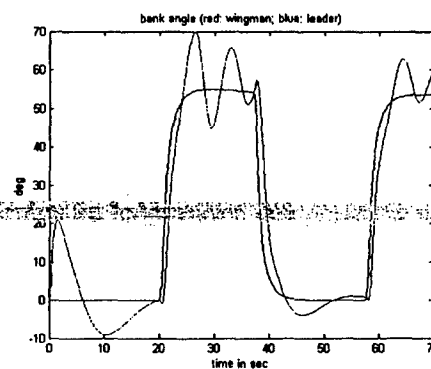a 12 lbs electronic payload consisting on a PC-104 flight computer, a complete set of sensors, a GPS receiver and a set of RF modems used for data transmission.

Figure 1 - WVU YF-22 aircraft model

The aircraft models are currently undergoing individual flight-tests with flight-testing of the formation control laws to be performed in the early 2005. Due to the limitations on the flight range, the WVU YF-22 models will be expected to perform fairly tight maneuvers at high Euler angles and moderately high angular rates. Therefore, a specific issue is the design of a control scheme allowing for formation control under these flight conditions. Another objective is to design a formation control scheme with a limited amount of information exchange (between leader and wingman) needed to maintain the predefined formation geometry.

The paper is organized as follows. The second section describes the identification of a linear and nonlinear single aircraft model from collected flight data. The third section outlines the geometric characteristics of the formation. The fourth section outlines the design of the formation control laws. The final sections will present the simulation and visualization environments, together with the main results. The symbols used throughout the paper are very standard, but readers less familiar with flight mechanics could consult [7] or download the FDC manual [10] as a reference.

2 System Identification of the WVU YF-22

Flight data for several maneuvers were collected for parameter identification purposes using the following on-board instrumentation:

- Absolute and differential pressure sensors: (SenSym ASCX15AN and SenSym ASCX01DN) to measure H and V (altitude and speed).

@ Professor, ^ Research Assistant Professor

- Inertial Measurement Unit (Crossbow DMU-VGX) to measure Ax, Ay, Az, p, q, r, φ, θ, (accelerations, roll pitch and yaw rates, roll and pitch angles).
- Custom designed nose probe to measure α and β (attack and sideslip angles).
- Potentiometers on the control surfaces to measure δE, δA, δR (elevators, ailerons and rudders deflections).

During the flight, the PC-104 based on-board computer collects in real time (at a rate of 100Hz) all of the above signals using the integrated data acquisition card (Diamond MM 32), and stores them on a flash-card for post-flight downloading. A set of flight data was used for the actual parameter estimation process, while a second set of data was used for validation purposes. Turn maneuvers, plus doublets on each control surfaces, (typical for collecting data for parameter identification purposes), were periodic.

2.1 Linear Model Identification

The linear model identification was performed with a 3-step process. First, the flight data time histories were inputted to a Simulink scheme providing smoothing and rearrangement of the signals. Next, a batch Matlab file performed the actual identification algorithm. The last step of the model identification process was the validation of the linear model using time histories of the control surface deflections from the validation flight data Following the identification study, the estimated linear lateral-directional aerodynamic model is given by:

$$
\begin{bmatrix} \dot{\beta} \\ \dot{p} \\ \dot{r} \\ \dot{\phi} \end{bmatrix} = \begin{bmatrix} 0.4299 & 0.0938 & -1.0300 & 0.2366 \\ -67.3341 & -7.9485 & 5.6402 & 0 \\ 20.5333 & -0.6553 & -1.9955 & 0 \\ 0 & 1 & 0 & 0 \end{bmatrix} \begin{bmatrix} \beta \\ p \\ r \\ \phi \end{bmatrix}
$$
$$
+ \begin{bmatrix} 0.2724 & -0.7713 \\ 10.8446 & 33.4738 \\ -6.2609 & -24.3627 \\ 0 & 0 \end{bmatrix} \begin{bmatrix} \delta_A \\ \delta_R \end{bmatrix}
\tag{1}
$$

The estimated longitudinal model is given by:

$$
\begin{bmatrix} \dot{v} \\ \dot{\alpha} \\ \dot{q} \\ \dot{\theta} \end{bmatrix} = \begin{bmatrix} -0.2835 & -23.0959 & 0 & -0.1711 \\ 0 & -4.1172 & 0.7781 & 0 \\ 0 & -33.8836 & -3.5729 & 0 \\ 0 & 0 & 1 & 0 \end{bmatrix} \begin{bmatrix} v \\ \alpha \\ q \\ \theta \end{bmatrix}
$$
$$
+ \begin{bmatrix} 20.1681 \\ 0.5435 \\ -39.0847 \\ 0 \end{bmatrix} \delta_E
\tag{2}
$$

This model represent the aircraft in a steady and level flight at 42 m/s, 336m of altitude, with alpha and theta of 3 deg. This linear model was mainly used for control synthesis.

For simulation purposes, a full nonlinear aircraft model was considered highly desirable if not necessary.

2.2 Linear Model Identification

The identification of the mathematical model of a nonlinear system is a more challenging issue [5,6]. Most of the nonlinear identification efforts rely on both good physical insight [5] and some form of optimization algorithm like Steepest descent or Newton-Raphson [6]. The general nonlinear model of an aircraft system can be expressed (see for example [7]) as:

$$
\dot{x} = f(x, \delta, G, F_A(x, \delta), M_A(x, \delta));
$$
$$
y = g(x, \delta, G, F_A(x, \delta), M_A(x, \delta));
\tag{3}
$$

where x is the state vector (linear and angular positions and velocity), y is the output vector (linear and angular accelerations), δ is the input vector (surface deflections), G is a vector of geometric parameters and inertia coefficients, F_A and M_A are aerodynamic forces and moments acting on the aircraft; finally, f and g are the known analytic functions that express the dynamics and kinematics of a rigid body. The aerodynamic forces and moments are expressed using the aerodynamic coefficients C_D, C_Y, C_L, C_l, C_m, C_n :

$$
F_A = \bar{q}S \begin{bmatrix} C_D(x, \delta) \\ C_Y(x, \delta) \\ C_L(x, \delta) \end{bmatrix}, M_A = \bar{q}S \begin{bmatrix} bC_l(x, \delta) \\ \bar{c}C_m(x, \delta) \\ bC_n(x, \delta) \end{bmatrix}
\tag{4}
$$

where S is the wing platform area, $\bar{q}$ the dynamic pressure, b the wingspan, and $\bar{c}$ the mean aerodynamic chord. The aerodynamic coefficients are often approximated by affine functions in x and δ; for example, for the lift coefficient:

$$
C_L(x, \delta) = c_{L0} + c_{L\alpha}\alpha + c_{Lq}q + c_{L\delta_e}\delta_e
\tag{5}
$$

where, c_{L0} and the other three coefficients are usually called the "derivatives" of C_L.

When the above approximations are considered satisfactory, the nonlinear aircraft model is completely determined by its aerodynamic derivatives as well as by its inertial and geometric coefficients (which can typically be evaluated experimentally). In this effort, the inertial and geometric characteristics of the WVU YF-22 model were determined with an experimental set-up; thus, the remaining critical issue was the determination of the aerodynamic derivatives. Formulas to calculate the entries of the matrices of the linear model in (1) and (2) from the values of the aerodynamic derivatives and geometric-inertial parameters are well known [7]. By inverting such formulas, an initial value for all the main aircraft aerodynamic derivatives was then calculated from the matrices in (1) and (2) together with the measured geometric and inertial parameters.

Next, a parameter optimization routine based on routines available with the Matlab Optimization Toolbox® was set up. Specifically, a Matlab routine was written such that it could take as an input the aerodynamic derivatives to be estimated, perform a simulation with the nonlinear model resulting from those derivatives, compare the outputs with the real data, and return the difference (to be minimized) to

the caller function. The "*fmincon*" function – which features the constrained optimization of a multivariable function using a Sequential Quadratic Programming (SQP) technique [8] - was then used to find the set of aerodynamic derivatives providing the best fit with the flight data, starting from the initial set of aerodynamics derivatives calculated from the linear models. The importance of starting the minimization from a set of already accurate derivatives should be emphasized; in fact, this last optimization can be considered a refinement of the parameters. A lesson learned was that in order for such an optimization to avoid local minima and converge successfully, care must be taken in the selection of the cost function. Specifically, the selected cost function contained 3 terms, a term expressing the RMS of the deviation between real and predicted output, a frequency based term expressing the lowest spectral components of the deviation, and a term expressing the difference between the current linearized model (obtained by performing a numerical linearization algorithm on the current nonlinear model) and the base linear model in equations (1) and (2).

A final validation of the nonlinear model was then conducted using the validation flight data set, similarly to what was done for the linear model. As shown in Figure 2, the agreement between simulated and real data is substantial.

Figure 2 – Linear and nonlinear model prediction versus real flight data

The resulting aircraft nonlinear model is given by:

Geometric and Inertial Data (60% fuel load):
$\bar{c}$ = 0.7649 m, b = 1.9622 m, S= 1.3682 m^2, I_{xx} = 1.6073 Kg m^2, I_{yy} = 7.5085 Kg m^2, I_{zz} = 7.1865 Kg m^2, Ixz = - 0.2441 Kg m^2, mass = 20.6384 Kg, T (engine thrust force) = 54.6175 N

Longitudinal Aerodynamic derivatives:
C_{D0} = 0.0069, $C_{D\alpha}$ = 0.4345, C_{Dq} = 0, $C_{D\delta E}$ = -0.2477,

C_{L0} = 0.0038, $C_{L\alpha}$ = 2.4554, C_{Lq} = 0.0358, $C_{L\delta E}$ = -0.3291, C_{m0} = 0.0063, $C_{m\alpha}$ = -0.2324, C_{mq} = -2.6913, $C_{m\delta E}$ = -0.2681.

Lateral-Directional Aerodynamic derivatives:
C_{Y0} = 0.0208, C_{Yb} = 0.3073, C_{Yp} = 0.8345, C_{Yr} = -1.0777, $C_{Y\delta A}$ = 0.2115, $C_{Y\delta R}$ = -0.4466, C_{l0} = -0.0016, C_{lb} = -0.0453, C_{lp} = -0.2260, C_{lr} = 0.0994, $C_{l\delta A}$ = -0.0543, $C_{l\delta R}$ = 0.0175, C_{n0} = 0, C_{nb} = 0.0546, C_{np} = -0.1106, C_{nr} = -0.2629, $C_{n\delta A}$ = -0.0228, $C_{n\delta R}$ = -0.0638.

3   Formation Control Problem : Geometry

From a geometric point of view the formation flight control problem can be naturally decomposed into two independent problems: a level plane tracking problem and a vertical plane tracking problem.
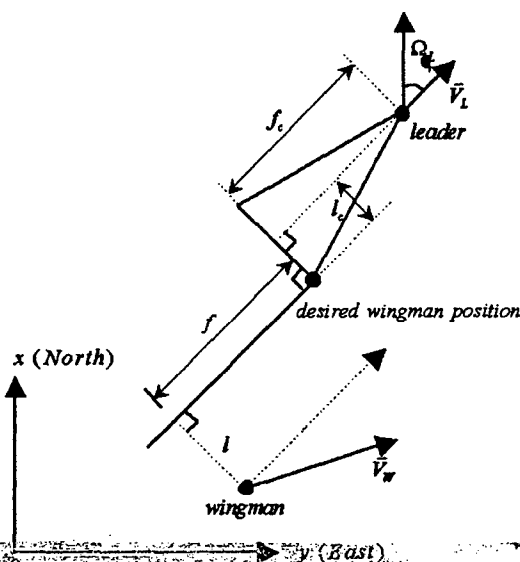
Figure 3 – Formation Geometry

Figure 3 shows the level plane formation geometry. All trajectory measurements, *i.e.*, leader/wingman position and velocity, are defined with respect to a pre-defined Earth-Fixed Reference $x - o - y$ plane and are measured by the on-board GPSs. The pre-defined formation geometric parameters are the forward clearance f_c and lateral clearance l_c. The forward distance error f and lateral distance error l can be calculated from the trajectory measurements and formation geometric parameters using the relationships:

$$l = \frac{V_{Ly}(x_L - x_W) - V_{Lx}(y_L - y_W)}{V_{Lxy}} - l_c \qquad (6)$$

$$f = \frac{V_{Ly}(y_L - y_W) + V_{Lx}(x_L - x_W)}{V_{Lxy}} - f_c \qquad (7)$$

where $V_{Lxy} = \sqrt{V_{Lx}^2 + V_{Ly}^2}$ is the projection of the leader's velocity onto the $x-y$ plane. Accordingly, the relative forward and lateral speed of the wingman are defined as the time derivatives of the forward and lateral distance respectively and are needed for formation control purposes which can be calculated as:

$$l = \frac{V_{Lx}V_{Wy} - V_{Ly}V_{Wx}}{V_{Lxy}} + (f + f_c)\dot{\Omega}_L \qquad (8)$$

$$\dot{f} = V_{Lxy} - \frac{V_{Lx}V_{Wx} + V_{Ly}V_{Wy}}{V_{Lxy}} - (l + l_c)\dot{\Omega}_L \qquad (9)$$

The trajectory-induced angular velocity in the $x-y$ plane (around the vertical axis) $\dot{\Omega}_L$ is computed as:

$$\dot{\Omega}_L \equiv \dot{\psi}_L = (q_L \sin\phi_L + r_L \cos\phi_L)/\cos\theta_L \qquad (10)$$

At nominal conditions, the leader and wingman aircraft are separated by a vertical clearance h_c. The vertical distance error h, can then be calculated by:

$$h = z_L - z_W - h_c \qquad (11)$$

while its time derivative is given by:

$$\dot{h} = V_{Lz} - V_{Wz} \qquad (12)$$

The "vertical control problem" is reduced to the issue of maintaining the vertical clearance h_c. Based on the above subdivision of the formation geometry, the design of the control laws are separated into 3 channels to control respectively the lateral, forward, and vertical distance. The resulting design is outlined in the following sections.

4 Design of the Formation Control Laws

Ideally, to achieve the best trajectory tracking performance, the formation flight control laws, - that is, the wingman flight control laws - should be based on a "full information" tracking strategy. This concept can be expressed as:

Wingman's control inputs = Leader's control inputs + State error feedback

where the control inputs include deflections for the throttle, elevator, aileron and rudder, while state error feedback consists of "internal" state variable errors (such as errors in angular rate and Euler angles) and "trajectory" state variable errors (such as forward distance, lateral distance, and vertical distance) between the leader and wingman.

The rationale behind this approach is the fact that if both aircraft were flying in the same position then the leader acts as a reference system for the wingman, so the state feedback control measures the differences between the leader (reference) state and the wingman state, and provides corrections to the wingman control inputs in order to correct these differences. In reality, the *desired* wingman position is shifted with respect to the leader's position; therefore, extra compensation might be needed to account for the difference in the trajectory variables between the leader and the (ideal) wingman.

It should be noted that in this "full information" approach all the leader's states and control inputs are needed to calculate the wingman control inputs; therefore, a high communication bandwidth between the leader and wingman is required. An additional goal was to formulate a criteria for limiting the amount of data to be exchanged from leader and wingman aircraft while maintaining the geometry of the formation. This issue has direct implications on the required performance – and, therefore, the cost – of commercially available RF modems. Therefore only a few of the leader outputs and states are actually used to calculate the wingman's control inputs.

4.1 Lateral Distance Control

The objective of the lateral distance control is to minimize the lateral distance error l. Since bank angle rate changes are substantially higher than rate changes in the lateral position, the lateral dynamics exhibit a typical two-time-scale feature. Therefore, the design of the control system can be decomposed into two successive phases, that is, the design of an inner loop controlling the bank angle and augmenting the lateral-directional stability, and the design of an outer loop which tries to maintain a desired lateral clearance with respect to the leader.

The resulting linear control law is given below and shown in Figure 4, where the subscripts L and W indicate respectively the wingman and leader aircraft.

Inner loop control law:

$$\delta_{AW} = \delta_{AL} + K_p p_W + K_\phi(\phi_W - \phi_d) \qquad (13)$$

$$\delta_{RW} = \delta_{RL} + K_r r_W \qquad (14)$$

Outer loop control law:

$$\phi_d = \phi_L + K_{\dot{l}}\dot{l} + K_l l \qquad (15)$$

At this point, given the basic lateral-directional linear model of the aircraft (1), and the actuators dynamics:

$$G_a(s) = \frac{1}{1 + 0.05s} \qquad (16)$$

the inner loop controller can be designed based on the aircraft lateral-directional linear model.

The outer loop design requires a suitable kinematic reference model. Such a model can be obtained by considering the aircraft performing a steady state coordinated turn where the lift force balance and centrifugal force balance equations apply. This leads to the following expression:

$$\dot{\Omega}_W = \frac{g}{V_{Wxy}}\tan\phi_W \qquad (17)$$

Additionally, by assuming a straight and level flight condition of the leader and identical speed for the wingman and the leader, it results that $\Delta\dot{\Omega} = \dot{\Omega}_W$ while (8) takes on the following simple form:

$$l = V_{Wxy}\sin(\Delta\Omega) \qquad (18)$$

where $\Delta\Omega = \Omega_W - \Omega_L$. The linearization of the above two equations (around the standard level-straight flight

condition) of the wingman provides the following model of the trajectory dynamics:

$$\begin{cases} \Delta\dot{\Omega} = \dfrac{g}{V_{W_{xy}}}\phi_W \\ \dot{l} = V_{W_{xy}}\Delta\Omega \end{cases} \qquad (19)$$

Thus, the full linear model for lateral distance controller design is the combination of equations (1), (16), and (19). Classic root-locus based compensation design tools can then be applied to the model for evaluating the controller gains [26]. The basic design specification is to assign the damping ratio of the dominant poles a value around 0.7. The resulting values for the parameters of the different control laws are given by:

$$K_p = 0.05, \quad K_\phi = 0.312, \quad K_r = 0.3$$
$$K_i = 1.76, \quad K_l = 0.256 \qquad (20)$$

4.2 Forward Distance Control

The objective of the forward distance control is to minimize the forward distance error f. The forward distance control law, shown in Figure 5, is given by:

$$\delta_{TW} = \delta_{TL} + K_f \dot{f} + K_f f \qquad (21)$$

The cascade of two first order linear models can approximate the forward dynamics. The 1st model represents the engine response in terms of throttle to thrust; this model has been obtained through an experimental analysis of the performance of the jet engines installed on the WVU YF-22 aircraft; a 2nd model represents the airspeed response in terms of thrust to airspeed, which is approximately derived from the knowledge of nominal thrust, airspeed, mass, and the assumption that the change of aerodynamic drag is in proportional to the change of airspeed.

The following equation represents the resulting complete transfer function of throttle to airspeed:

$$G_{W}(s) = G_{YT}(s)\,G_{TT}(s) = \frac{0.315}{1+6.5s}\bullet\frac{0.2}{1+s} \qquad (22)$$

It should be noted that this model also represents the transfer function from throttle (of wingman) to forward velocity of (9) under the assumed level-straight constant speed flight condition. The parameters of the forward distance controller outlined in (21) were then determined through a root locus-based compensator design:

$$K_f = 4.76, \quad K_f = 1.19 \qquad (23)$$

4.3 Vertical Distance Control

The objective of the vertical distance control is to minimize the vertical distance error h. As with the lateral distance case, the problem exhibits a two time scale structure; thus, the control scheme can be designed using an inner loop controller - which is basically a pitch angle controller - and an outer loop controller providing altitude control.

A linear control law that accomplishes the above scheme is given by the following formulas.
Inner loop control law:

$$\delta_{EW} = \delta_{EL} + K_q q_W + K_\theta(\theta_W - \theta_d) \qquad (24)$$

Outer loop control law:

$$\theta_d = \theta_L + K_i \dot{\delta}z + K_z \delta z \qquad (25)$$

The design is based on the linear short period model in (2) in addition to a linearized kinematic model:

$$\begin{cases} \dot{\theta} = q \\ \dot{h} = V_{W_z}\theta \end{cases} \qquad (26)$$

With a root locus-based design[20] the parameters of the vertical controller are found to be:

$$K_q = 0.56, \quad K_\theta = 1.66, \quad K_i = 1.59, \quad K_z = 5.22 \qquad (27)$$

5 Simulation Results

A Simulink scheme featuring the models of the WVU YF-22 aircraft and the formation controller was developed and implemented. Given the multi-object nature of the problem, the design of a visualization environment fully integrated with the simulation was considered to be critical. The Virtual Reality Toolbox (VRT) was selected as the visualization environment since it allows for objects and events of a virtual world (coded in VRML 2.0 or higher [9]) to be driven by signals from Matlab/Simulink. The resulting scenery from a view behind the wingman is shown in Figure 4.
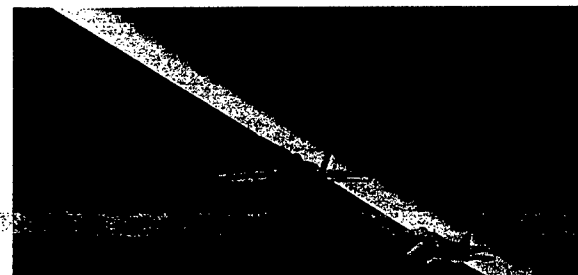
Figure 4 – VRT visualization (behind wingman)

A preliminary analysis was conducted to assess if deflections of the control surfaces from the leader in (13), (14), and (24) were actually necessary to have desirable tracking performance. This analysis showed that the elimination of these signals from the leader aircraft did not significantly decrease the performance of the control scheme. Consequently, these signals were no longer used (constant trim values were used instead of them) therefore saving communication bandwidth for flight testing.
Next, a simulation study was conducted to assess the need for the bank angle from the leader in the wingman control laws in (15). The main results for this study is shown in Figure 5 where the leader's lateral maneuvering bank angle is about 30°.
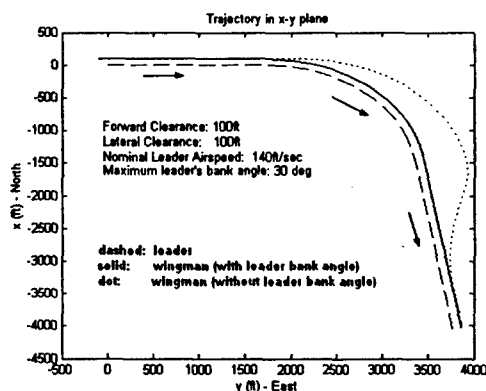
Figure 5 –Trajectories with/without the
bank angle from leader aircraft

It can be seen from the simulation that the "deformation" of
the formation in terms of the lateral distance of the
wingman from the leader is unacceptably large (as much as
450 feet), when the leader's bank angle is not available for
formation control purposes. Based on the above
considerations, it was decided that the electronic
instrumentation of the wingman models will be required to
include a three-axis angular rate gyro measuring roll rate
p_w, pitch rate q_w and yaw rate q_w, a vertical gyro measuring
pitch angle θ_w and bank angle φ_w and a GPS receiver
measuring the position of the wingman aircraft x_w, y_w, z_w
and its velocity vector, V_{wx}, V_{wy}, V_{wz}. In addition, it was
concluded that the pitch angle θ_L and bank angle φ_L of the
leader aircraft, along with its positions and velocity vector
$(x_L, y_L, z_L$ and its velocity vector, V_{Lx}, V_{Ly}, $V_{Lz})$ are required
by the wingman's control system.

Figure 6 -Trajectories in level plane

Another simulation study was conducted to assess the
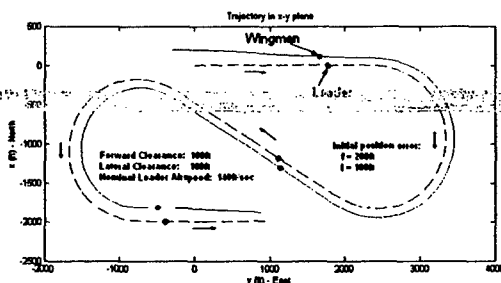performance of the formation controller following of an 'S'
shape flight trajectory in level plane (Figure 6) with a
maximum leader bank angle of approx. 50 deg (as recorded
in typical flight tests of the WVU YF-22 models);
The formation geometry was: $f_c = 100$ ft; $l_c = 100$ ft, $h_c = 0$
ft, with initial position error $f = 300$ ft, $l = 300$ ft, $h = 0$ ft.
The simulations were conducted with and without the
modeling of wind gusts acting in specific flight segments.
A more detailed analysis of the results shows that, as
expected, the control scheme provides better performance

in terms of maximum forward, lateral and vertical errors
with lower leader's bank angles.

Conclusions

This paper presents an approach for the design of linear
control laws to maintain specified geometry for a formation
of research aircraft models. The design is based on
compensation-type controllers for minimizing tracking
errors along the forward, lateral, and vertical axes. The
analysis shows that the availability of the Euler angles from
the leader aircraft is critical for the wingman to maintain the
assigned formation geometry throughout the maneuvered
flight. An additional goal was to evaluate the criteria to
limit the necessary data communication between the leader
and the wingman. The design has been verified through a
set of simulation studies interfacing the aircraft models and
the control schemes in Simulink with a VRT environment.
The results of the simulation show a desirable performance
of the formation control schemes.

References

1 - Pachter M., D'Azzo J.J., Proud A. W., "Tight Formation
Flight Control," Journal of Guidance, Control, and
Dynamics, Vol. 24, No. 2, March-April 2001, pp. 246-254
2 – Proud A.W. "Close Formation Flight Control", MS
Thesis, AFIT/GE/ENG/99M-24, School of Engineering, Air
Force Institute of technology (AU), Wright-Patterson AFB,
OH, March 1999
3 - Giulietti F., Pollini L., Innocenti M. , "Formation Flight
control: A Behavioral Approach," Proceedings of the 2001
AIAA GNC Conference, AIAA Paper 2001-4239,
Montreal, Canada, August 2001
4 – Singh S.N., Pachter M., Chandler P., Banda S.,
Rasmussen S., Schumacher, C.J. "Input-Output Invertibility
and Sliding Mode Control for Close Formation Flying of
Multiple UAVs", Proceedings of the 2000 AIAA GNC
Conference, Denver, CO, August 2000
5 - Ljung, L.,: *System Identification: Theory for the User*,
2nd *Ed.*, PTR Prentice Hall, Upper Saddle River, Englewood
Cliffs, NJ, 1999.
6 - Maine, R.E., Iliff, K.W., "Identification of Dynamic
Systems: Theory and Formulation", NASA RF 1168, June
1986
7 - Stevens, B. and Lewis, F. "Aircraft Control and
Simulation," John Wiley & Sons, NY, 1992.
8 - Hock, W. and K. Schittowski, "A Comparative
Performance Evaluation of 27 Nonlinear Programming
Codes," *Computing*, Vol. 30, p. 335, 1983.
9 - The VRML Web Repository (Dec. 2002):
http://www.web3d.org/vrml/vrml.htm
10 - Rauw, M.O.: *"FDC 1.2 - A Simulink Toolbox for Flight
Dynamics and Control Analysis"*. Zeist, The Netherlands,
1997. ISBN: 90-807177-1-1, http://www.dutchroll.com/

Formation Flight Test Results for
UAV Research Aircraft Models

Brad Seanor[*], Giampiero Campa[†], Yu Gu[‡], Marcello Napolitano[§], Larry Rowe[**] and Mario Perhinschi[††]
West Virginia University, Morgantown, WV 26506

This paper presents experimental results for a research program using research UAVs built and developed at West Virginia University. The main objective of this effort was to provide a flight demonstration of a formation control scheme using three YF-22 research aircraft models. For several years formation flight research has been an important topic for the aerospace community. The benefits of formation flight and development of formation control problems have been investigated and well documented. A detailed mathematical model was obtained using parameter identification techniques from previously recorded flight data of the WVU YF-22 aircraft. From this data, a Simulink® based simulation environment was developed and used to test the formation control laws. Simulation results used this mathematical model to design and refine a set of control laws to maintain desired formation geometry during maneuvered flight. The formation control law consists of a set of inner and outer loop control schemes executed by an on-board computer system on the "Follower" aircraft. Performance of the "Follower" inner-loop control laws has been assessed through a series of flight tests. Flight-testing activities focusing on the formation control laws initially used a "virtual leader" scenario. Results of the "virtual leader" testing validated the overall design of the formation controller and confirmed the performance of the on-board computer system. Formation flight with two aircraft was then performed during the 2004 flight season. This paper will first describe the UAV models along with their customized electronic computer systems. Next, the aircraft mathematical model as well as the formation control schemes will be presented. The overall control design process, with emphasis on the controller implementation on the on-board computer, will also be described. Finally, the flight-testing operations and experimental results obtained to date will be presented and discussed.

Nomenclature

English:

C_D	=	aerodynamic drag force coefficient
C_Y	=	aerodynamic side force coefficient
f	=	forward distance between "leader" and "follower" aircrafts, m
g	=	gravitational acceleration, m/s^2
h	=	altitude, m
k	=	control gain
l	=	lateral distance between "leader" and "follower" aircraft
m	=	aircraft mass, kg
p	=	roll rate, deg/s
q	=	pitch rate, deg/s
r	=	yaw rate, deg/s
S	=	wing platform area, m^2

[*] Research Assistant Professor, Department of Mechanical and Aerospace Engineering, AIAA Member
[†] Research Assistant Professor, Department of Mechanical and Aerospace Engineering
[‡] Graduate Research Assistant, Department of Mechanical and Aerospace Engineering
[§] Professor, Department of Mechanical and Aerospace Engineering
[**] Graduate Research Assistant, Department of Mechanical and Aerospace Engineering
[††] Assistant Professor, Department of Mechanical and Aerospace Engineering, AIAA Senior Member

I. Introduction

The main objective of this research effort is to provide a flight demonstration of formation control using the West Virginia University (WVU) YF-22 research aircraft models. These vehicles were not designed to be scaled replicas, but to serve as research platforms with a relatively high payload volume capacity with the capability of fulfilling a variety of mission roles. For several years formation flight research has been an important topic for the aerospace community. Benefits of close formation flight and development of formation control problems have been investigated and well documented.[1-3] Previous research of automatic control and experimental test results of formation flight have been reported.[4,5] The main focus of this research program was to develop a set of control laws to be applied on a low-cost "off-the-shelf" hardware system, and provide a flight demonstration. The demonstration consists of a single "leader" aircraft controlled by a ground Radio Controlled (R/C) transmitter with two "follower" aircraft flying autonomously at a pre assigned relative position. Flight tests were completed to assess the handling qualities of each aircraft model, followed by a performance assessment of the electronic payload, and testing of the hardware controller interface used for formation control. A detailed mathematical model was derived using Parameter Identification (PID) techniques from flight data. Simulation work used this mathematical model to design and refine a set of control laws with the goal of maintaining a desired formation geometry during maneuvered flight. The development of a Simulink® based simulation environment used to initially test the formation control laws has been presented in recent publications.[6-8] A Non-linear Dynamic Inversion (NLDI) formation controller has been designed, simulated, and flight tested. For flight operations, all aircraft models are flown within visual range of the R/C pilots, which restrict the flight envelope to a circular pattern. This, in turn, implies the need for "high bank angle" maneuvers, which increases the complexity of the design for the formation control laws. To date, extensive flight testing activities including Virtual Leader (VL) flights with a single aircraft and actual formation flight with two research aircraft has been performed.

II. Design of the Research Aircraft Models

Each of the WVU YF-22 research models, shown in Fig. 1 and 2, has been designed to carry a minimum 12 lb. electronic payload for formation flight purposes. A jet-based propulsion system provides approximately 28 lbs. of thrust with a typical takeoff weight range of approximately 46-49 lbs. depending on the sensor configuration. In this context, 'configuration' refers to whether or not the vehicle was set-up as a "leader" or as a "follower".
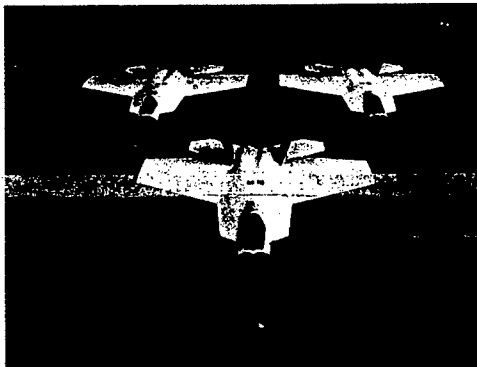

Figure 1. WVU YF-22 formation research aircraft

Figure 2. Close up photo during take-off

The general specifications for the WVU YF-22 research aircraft are shown in Table 1.

Wingspan	78"
Length	10 ft with probe
Height	24"
Wing Area	14.7 ft^2
Fuel Capability	7 lbs
Maximum Flight Duration	12 minutes
Maximum Airspeed	Approximately 130 mph
Cruse Airspeed	90 mph
Takeoff Speed	60 mph
Radio	JR 10X 10 channel SPCM
Engine / Thrust	RAM1000 / 28 lbs

Table 1. WVU YF-22 model specifications

On board sensors included a GPS for position and velocity, IMU for 3-axis acceleration and angular rate, air-data probe for measurement of flow angles and air pressures, a vertical gyro for the Euler angles, and potentiometers for individual main control surfaces (δ_E, δ_A, δ_R) deflections. Typical mission durations are approximately (10 to 12) minutes with flights performed within visual range at the WVU Jackson Mill flight-testing facility. For the take-off and landing phases, both the "leader" and "follower" aircraft are piloted remotely using a 10-channel R/C transmitter. After the development and construction of the aircraft test beds, flight-testing operations were conducted on each vehicle to assess their individual handling qualities. The payload design criteria involved producing a small, lightweight hardware system with low power consumption. A PC/104 based computer was selected to perform these tasks. The components/modules of the OBC include: CPU card, Data Acquisition (DAQ) card, power supply card, and custom interface boards for aircraft control and sensor interfaces.

III. Hardware and Software Design

A. Hardware Design

The WVU YF-22 research models have been developed to carry an electronic package specifically designed for formation flight purposes. The main component of the electronic payload is a PC-104 based flight computer interfaced with custom boards – shown in Fig. 3 – which houses the control laws on a compact flash card.
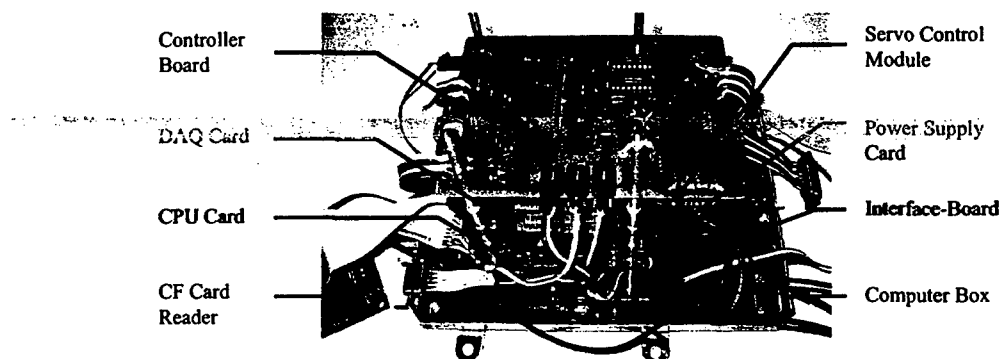
Figure 3. OBC stack with custom electronic boards

The CPU card is a low-power system with a 300 MHz processor. The DAQ card collects signals from the aircraft sensors and, in turn, relays commands to the controller board through the digital output capability. The accuracy of the flight control laws depends directly on the accuracy and speed of the DAQ card. The DAQ card has the capability of 32 analog input channels with 16 bits resolution and provides a 24 channel digital I/O, which is then used to send the channel selection signal to the controller board. The general architecture used for the DAQ system is shown in Fig. 4.

Figure 4. Data acquisition system

A Control Signal Distribution System (CSDS) was designed to execute the controller command to the control surface and propulsion system. The controller board acts as the main component of the CSDS, which is the hub for the entire flight control system. The functions of the CSDS include:

1. Receive control signals from the receiver;
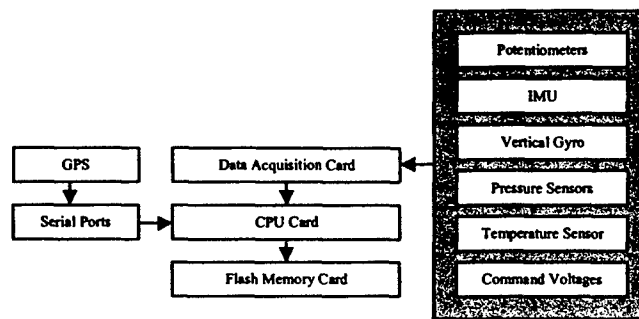2. Receive control signals from the OBC;
3. Translate commands from the OBC into Pulse Width Modulation (PWM) signals;
4. Select the current operation mode of the aircraft (Manual or Autonomous);
5. Selection of control channels to be executed by the OBC;
6. Distribute control signals to the individual servos.

The controller board receives signals from both the pilot (R/C receiver) and the OBC (converting to a PWM signal). The controller board is required to be extremely reliable and was considered to be the most critical component of the flight control hardware. A block diagram for the CSDS is shown in Fig. 5.
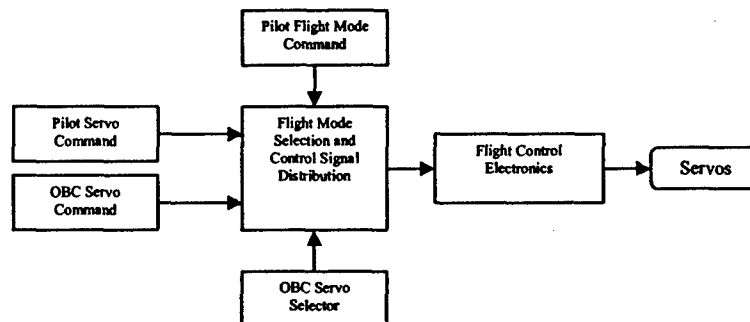
Figure 5. Control signal distribution system

The "custom-designed" and "custom-built" interface board is a signal connection board designed to connect individual sensor outputs to a specific data acquisition channel. This board also provides power to the sensors (except vertical gyro and GPS powered separately) and gives out reference voltages for controller use.

Two flight-mode switching mechanisms have been designed to improve flight safety of the UAV – providing both hardware and software switching. Hardware switching gives R/C pilots the ability to switch off the entire controller instantly at any circumstance, even if the on-board payload power is lost. The software switching provides a dual redundancy and the flexibility to selectively control all (or a subset) of the major aircraft surfaces (δ_E, δ_A, δ_R) and propulsion system.

An overview photo of the main payload is shown in Fig. 6. Figure 7 shows additional hardware components including key instruments for the formation flight control consisting of the GPS and communication RF modems.

Figure 6. Payload system (main bay)

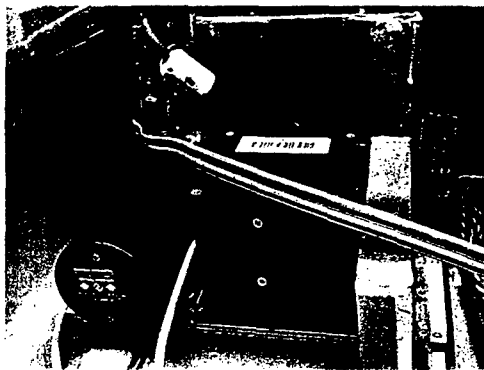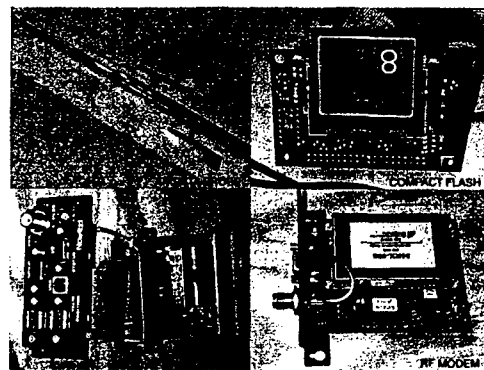Figure 7. Additional hardware components

The general architecture of the OBC is shown in Fig. 8.
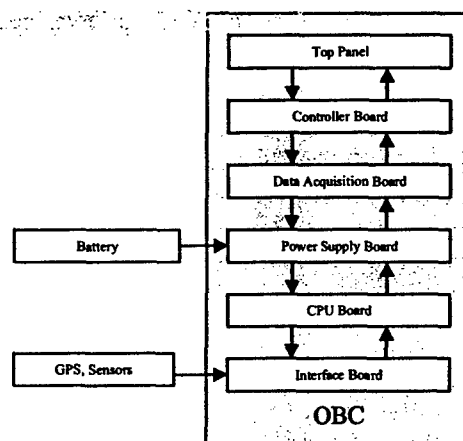
Figure 8. Layout of the OBC

The overall hardware payload was designed in such a way that it can be configured to accommodate various flight testing research activities.

B. Software Design

As for any flight control software, the on-board software must be executable in real time. Matlab Real-Time Workshop® has been selected to provide the real time environment. All software is programmed with C-language as Matlab® S-functions and Simulink® provides the simulation environment. Flight test software is compiled with real-time workshop and generated as a real-time DOS target. DOS is used as the operating system of the OBC. Both the operating system and on-board software are stored within a compact flash card, which is a self-supporting bootable device. All of the software components were designed as individual modules and are easily configured for different tasks. The following requirements were used to define the software architecture:

1. Reliability;
2. Performance in real time;
3. System sampling rate no slower than 25Hz;
4. Acquire data from all sensors and convert into engineering units;
5. Execute control laws on-board;
6. Provide control command and control channel selection signal;
7. Store data for post analysis;
8. Automatic update calibration data at field (without recompile).

A diagram of the on-board software is shown in Fig. 9.

Figure 9. On-Board Software Architecture

IV. Development of a Mathematical Model using Flight Test Data
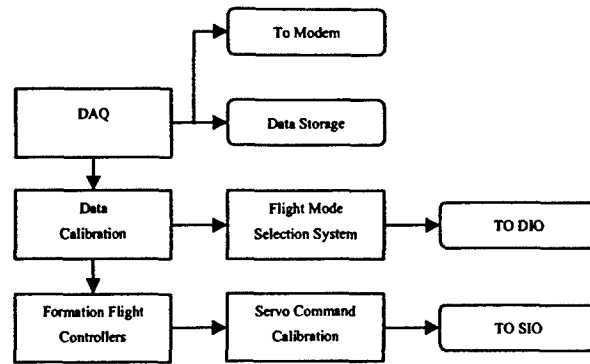
Flight data was collected to provide sensor information so that a PID scheme could then be used to obtain a mathematical representation of the formation flight aircraft. Typical PID maneuvers included standard elevator, aileron, and rudder doublets to produce suitable flight data for model analysis. Linear model identification was performed using a three-step process. First, the flight data time histories were provided to a Simulink® scheme providing smoothing and rearrangement of aircraft signals. Second, a batch Matlab® file performed the actual identification algorithm. The third step of the model identification process was to then validate a linear model using time histories from a different set of flight data. Following the identification study, the estimated longitudinal model is given as:

$$\begin{bmatrix} \dot{v} \\ \dot{\alpha} \\ \dot{q} \\ \dot{\theta} \end{bmatrix} = \begin{bmatrix} -0.2835 & -23.0959 & 0 & -0.1711 \\ 0 & -4.1172 & 0.7781 & 0 \\ 0 & -33.8836 & -3.5729 & 0 \\ 0 & 0 & 1 & 0 \end{bmatrix} \begin{bmatrix} v \\ \alpha \\ q \\ \theta \end{bmatrix} + \begin{bmatrix} 20.1681 \\ 0.5435 \\ -39.0847 \\ 0 \end{bmatrix} \delta_E \qquad (1)$$

and the estimated linear lateral-directional model is given as:

$$\begin{bmatrix} \dot{\beta} \\ \dot{p} \\ \dot{r} \\ \dot{\phi} \end{bmatrix} = \begin{bmatrix} 0.4299 & 0.0938 & -1.0300 & 0.2366 \\ -67.3341 & -7.9485 & 5.6402 & 0 \\ 20.5333 & -0.6553 & -1.9955 & 0 \\ 0 & 1 & 0 & 0 \end{bmatrix} \begin{bmatrix} \beta \\ p \\ r \\ \phi \end{bmatrix} + \begin{bmatrix} 0.2724 & -0.7713 \\ -101.8446 & 33.4738 \\ -6.2609 & -24.3627 \\ 0 & 0 \end{bmatrix} \begin{bmatrix} \delta_A \\ \delta_R \end{bmatrix} \qquad (2)$$

The linear model in Eq. (1) and (2) represent the aircraft in a reference flight condition and was mainly used for controller design. A full non-linear aircraft model was necessary for simulation and validation of the control laws. The development of the nonlinear aircraft model is discussed in Ref. 3.

V. Formation Flight Controller Design

The formation controller was designed to allow the "follower" vehicle to position itself at a pre-defined vertical, forward, and lateral distance from the "leader" after formation is engaged. From a geometric point of view, see Fig. 10, the control problem can be divided into two independent problems: a level plane tracking problem (horizontal geometry) and a vertical plane tracking problem (vertical geometry).
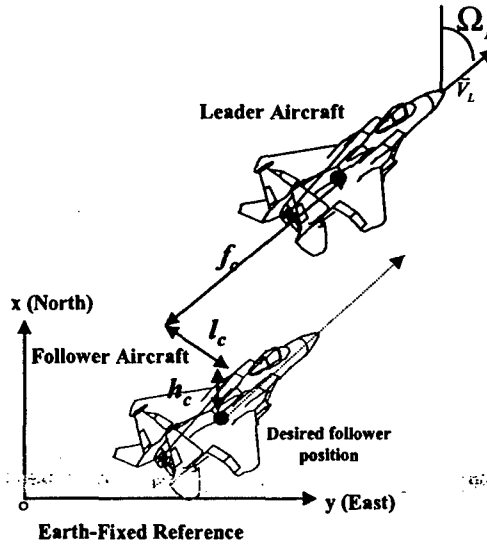
Figure 10. Formation geometry

The actuator response, engine response, and aircraft inertial characteristics were evaluated experimentally. The actuator model was identified using a Batch Least Squares (BLS) technique as a generic first order model.

$$G_{ACTUATOR}(s) = \frac{K}{s+K} \tag{3}$$

Similarly, the throttle signal and force were measured and recorded. As with the actuators, a BLS technique was used to identify an engine model containing a time delay, where δ_T is the throttle command and T is the thrust force:

$$\frac{T-T_b}{\delta_T} = \frac{K_T}{(1+\tau_T s)} e^{-\tau_d s} \tag{4}$$

For control purposes, the relationship between the throttle command and thrust can be approximated by a much simpler formula:

$$T = T_b + K_T \delta_T \tag{5}$$

A. Horizontal Geometry

The pre-defined formation geometric parameters are the forward clearance f_c and lateral clearance l_c. The forward distance error f and lateral distance error l can be calculated from positions and velocities using the following formulas:

$$\begin{bmatrix} l \\ f \end{bmatrix} = \begin{bmatrix} \sin(\chi_L) & -\cos(\chi_L) \\ \cos(\chi_L) & \sin(\chi_L) \end{bmatrix} \begin{bmatrix} x_L - x \\ y_L - y \end{bmatrix} - \begin{bmatrix} l_c \\ f_c \end{bmatrix} \tag{6}$$

where χ_L is the azimuth angle for the "leader":

$$\cos(\chi_L) = \frac{V_{Lx}}{\sqrt{V_{Lx}^2 + V_{Ly}^2}}, \text{ and } \sin(\chi_L) = \frac{V_{Ly}}{\sqrt{V_{Lx}^2 + V_{Ly}^2}} \tag{7}$$

Note that the (2 x 2) matrix in Eq. (6) is simply a rotation matrix that rotates the error from an earth fixed reference frame to a reference frame oriented as the velocity of the "leader".

B. Vertical Geometry

The vertical distance error, h, can be simply defined as:

$$h = z_L - z - h_c \qquad (8)$$

VI. Controller Structure

The whole formation control problem is ultimately a non-linear control problem in which the controller has to act on throttle and control surface commands to minimize the three error parameters f, l and h. However, it is useful to note that this problem, like other conventional flight trajectory control problems, exhibits a two-time-scale feature because the trajectory dynamics (relative position and velocity) is slower than the attitude dynamics (angular velocity and orientation). This is why, usually, both lateral-directional and vertical controllers consist of an inner loop (pitch and roll angle tracking) and outer loop controller (lateral-directional and height tracking).

A. Outer Loop Controller

The outer loop controller is divided in two parts. The "vertical" part is a simple linear altitude control that takes the vertical error as input and commands the desired pitch angle to the inner loop:

$$\theta_d = K_{zi} \dot{h} + K_z h \qquad (9)$$

The "horizontal" part is a nonlinear dynamic inversion (NLDI) based controller that takes lateral and forward error as inputs and commands the throttle (directly) and the desired bank angle to the inner loop:

$$\begin{bmatrix} \delta_T \\ \phi_d \end{bmatrix} = f(\chi - \chi_L, \begin{bmatrix} f \\ l \end{bmatrix}) \qquad (10)$$

B. Design of the NLDI Outer Loop Horizontal Controller

The control technique used aims at canceling the non-linearities of the plant dynamics using feedback linearization, which, under some assumptions, reduces a nonlinear system to a series of integrators, which are then controlled by linear techniques. The nonlinear system has both the forward and lateral distance errors (f and l) as outputs; the desired bank angle ϕ_d and the throttle command δ_T as inputs; and all the states that belong to the lateral dynamics of the "follower".

According to the feedback linearization technique, we must derive the outputs until the inputs explicitly appear in the expression, and try to invert the relationship among inputs and derivatives of the outputs. In our case, the first and second derivatives of the outputs are:

$$\begin{bmatrix} \dot{l} \\ \dot{f} \end{bmatrix} = \begin{bmatrix} V_{xy} \sin(\chi - \chi_L) \\ V_{Ly} - V_{xy} \cos(\chi - \chi_L) \end{bmatrix} + \Omega_L \begin{bmatrix} f \\ -l \end{bmatrix} \qquad (11)$$

$$\begin{bmatrix} \ddot{l} \\ \ddot{f} \end{bmatrix} = \begin{bmatrix} V_{xy} \cos(\chi - \chi_L) & \dfrac{V_{xy}}{V} \omega_1 \sin(\chi - \chi_L) \\ V_{xy} \sin(\chi - \chi_L) & -\dfrac{V_{xy}}{V} \omega_1 \cos(\chi - \chi_L) \end{bmatrix} \begin{bmatrix} \dfrac{g}{V} \tan(\phi_d) \\ T_b + K_T \delta_T \end{bmatrix}$$

$$+ \dfrac{V_{xy}}{V} \omega_2 \begin{bmatrix} -\sin(\chi - \chi_L) \\ \cos(\chi - \chi_L) \end{bmatrix} - \Omega_L V_{xy} \begin{bmatrix} \cos(\chi - \chi_L) \\ \sin(\chi - \chi_L) \end{bmatrix} + \dot{\Omega}_L \begin{bmatrix} f \\ -l \end{bmatrix} + \Omega_L \begin{bmatrix} \dot{f} \\ -\dot{l} \end{bmatrix} \qquad (12)$$

where:

$$\omega_1 = \frac{1}{m}\cos\alpha\cos\beta, \qquad \omega_2 = \frac{\bar{q}S}{m}(C_D\cos\beta - C_Y\sin\beta) + g\sin\gamma \tag{13}$$

and the coordinated turn condition is assumed for both "leader" and "follower":

$$\Omega = \dot{\chi} \cong \dot{\psi} \cong \frac{g}{V}\tan\phi \tag{14}$$

In practice, keeping both a constant altitude and zero sideslip angle ($\beta\cong0$) during the turn imposes the coordinated turn condition in Eq. (14). Since the 2 by 2 matrix that relates inputs and second derivatives of the output in Eq. (12) is invertible, we can express the inputs as a function of the (desired) second derivatives of the outputs. By considering $\alpha=\alpha_0$, $\beta=0$, and Ω_L constant (quasi steady state turn), we have the following feedback linearization laws:

Lateral NLDI Control Law:

$$\phi_d = \arctan\left\{\frac{1}{g\cos\gamma}\left[\ddot{\ell}_d\cos(\chi-\chi_L) + \ddot{f}_d\sin(\chi-\chi_L)\right] + \frac{V}{g}\Omega_L + \left[\ell\sin(\chi-\chi_L) - f\cos(\chi-\chi_L)\right]\frac{\Omega_L}{g\cos\gamma}\right\} \tag{15}$$

Forward NLDI Control Law:

$$\begin{aligned}\delta_T = &\frac{m}{K_T\cos\gamma}\left[\ddot{\ell}_d\sin(\chi-\chi_L) - \ddot{f}_d\cos(\chi-\chi_L)\right] + \frac{1}{K_T}\left(\frac{1}{2}\rho_0 V^2 S\left(C_{D0} + C_{D\alpha}\alpha_0\right) + m\sin\gamma - T_b\right)\\ &- \frac{m}{K_T\cos\gamma}\Omega_L\left[\ell\cos(\chi-\chi_L) + f\sin(\chi-\chi_L)\right]\end{aligned} \tag{16}$$

The application of the inputs ϕ_d and δ_T obtained from Eq. (15) and (16) to the system in Eq. (12) completely cancels the nonlinearities leading to:

$$\begin{bmatrix}\ddot{\ell}\\\ddot{f}\end{bmatrix} = \begin{bmatrix}\ddot{\ell}_d\\\ddot{f}_d\end{bmatrix} \tag{17}$$

which is a linear system consisting of two channels, each containing two integrators in series. This can be controlled by a standard linear control, in our case, the chosen controller was:

$$\begin{aligned}\ddot{\ell}_d &= -\bar{K}_{\ell_s}\dot{\ell} - \bar{K}_\ell\ell\\ \ddot{f}_d &= -\bar{K}_{f_s}\dot{f} - \bar{K}_f f\end{aligned} \tag{18}$$

where a set of controller gains were selected to be:

$$\begin{aligned}\bar{K}_\ell &= 0.2027, \quad \bar{K}_{\ell_s} = 0.8894\\ \bar{K}_{f_s} &= 2.0560, \quad \bar{K}_f = 0.2419\end{aligned} \tag{19}$$

C. Inner Loop Lateral Controller

The lateral inner loop controller is a simple linear controller that tracks the desired bank angle (supplied by the outer loop controller) and augments the lateral-directional stability of the aircraft using the commands described by:

$$\delta_A = K_p p + K_\phi(\phi - \phi_d); \qquad \delta_R = K_r r \tag{20}$$

Classic root-locus based compensation design tools has been applied to the model for evaluating the controller gains. The basic design specification is to assign the damping ratio of the dominant poles to a value around 0.7. The resulting values for the parameters are:

$$K_p = 0.05, \quad K_\phi = 0.312, \quad K_r = 0.3 \tag{21}$$

D. Inner Loop Longitudinal Controller

The longitudinal inner loop controller is a simple linear controller that tracks the desired pitch angle (supplied by the outer loop controller):

$$\delta_E = K_q q + K_\theta (\theta - \theta_d) \tag{22}$$

As for the lateral controller, the resulting parameters of the longitudinal controller have been calculated using a root locus-based approach:

$$K_q = 0.56, \quad K_\theta = 1.66 \tag{23}$$

VII. Experimental Flight Testing Results

The overall scenario of the formation flight testing experiments is a "leader/follower" combination where all aircraft are manually controlled during the takeoff and landing phases. After each aircraft reaches a nominal flight condition, the "leader" and "follower" aircraft perform a rendezvous maneuver where the "follower" attempts to get within 150 m and the "follower" pilot can then engage the autonomous formation control. In the event of unsafe flight conditions, the pilot can manually disengage from formation control and regain individual control of the aircraft. "leader" information is passed to the "follower" aircraft via RF modems, including GPS position, GPS velocity and Euler angles (pitch/roll). After landing, the ground crew is able to download the data stored in the flash card(s), re-play the flight data, and – if necessary – change the existing software configuration (re-compile with real time workshop) and perform a different task within the same flight session.

To reduce the risk associated with initially flight testing of multiple UAVs, a "Virtual Leader" (VL) method was employed to evaluate the formation controller prior to actual formation flight testing. This configuration consisted of a single aircraft tracking the trajectories of a VL, which was essentially a flight path of previously recorded flight data. This VL data could either be preinstalled in the OBC or beamed directly to the RF modem so that only one aircraft was necessary for the experiment. Results from the VL configuration confirmed a desirable performance of the formation control laws. A sample of VL flight data showing the aircraft altitude and GPS XY trajectories are presented in Fig. 11 and 12.
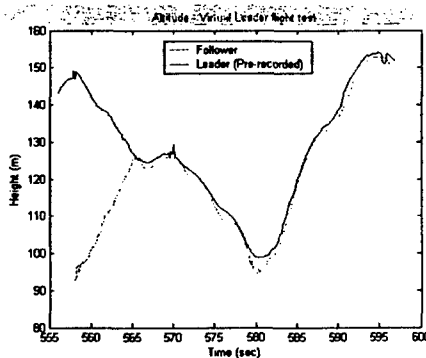

| Figure 11. Virtual leader: altitude plot | Figure 12. Virtual leader: XY plot |
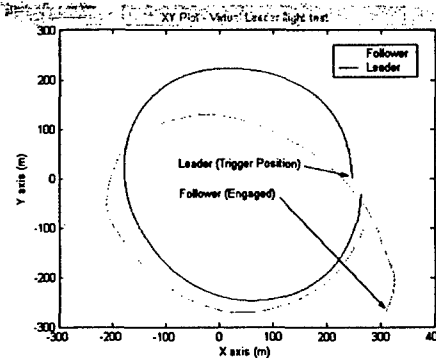
The blue line represents a pre-recorded flight path stored on-board the "follower" aircraft computer, which was then used by the control laws. The green line represents the actual response of the "follower" aircraft. In this particular flight test, the "follower" was designed to track the altitude of the VL with a predefined offset in the X and Y direction. After the performance of the formation control law was established and demonstrated with the testing of different VL configurations, actual flight testing with two aircraft in formation was performed. Figures 13 and 14

show the Simulink® schemes for both the "leader" and "follower" on-board software. These schemes were compiled with real time workshop to generate DOS executables, which were uploaded to both flight computers.
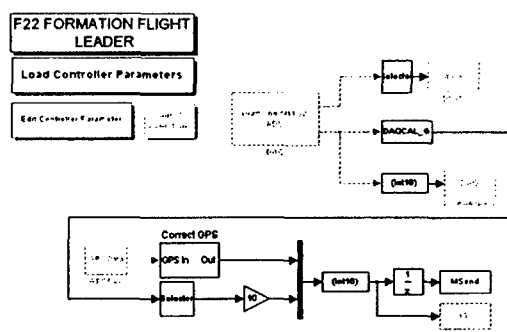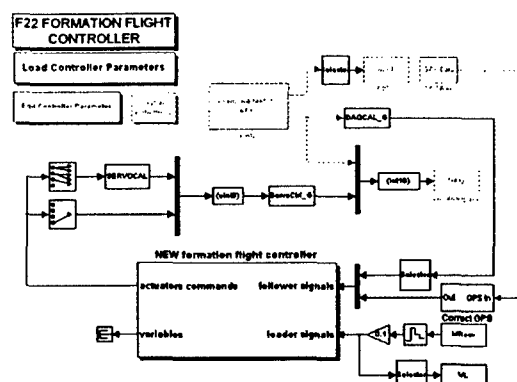

Figure 13. "Leader" on-board software scheme   Figure 14. "Follower" on-board software scheme

The flight testing of two aircraft in formation began in summer 2004. The "leader" takes off first followed by the second aircraft. Once the "leader" aircraft reached a nominal height (approximately 130-150 m), the pilot then began flying a circular pattern until landing. The pilot of the "follower" aircraft then maneuvered to a position behind the "leader" aircraft. Once the "follower" reached within approximately 150 m behind the "leader", the "follower" pilot then engage the formation control. Once engaged, the on-board controller assumes control over all aircraft functions while the R/C pilot remained in a standby mode in case of an emergency. Note, the hardware system allows for the pilot can disengage the formation control at any time and regain full control of the aircraft instantly. Once formation is then disengaged, both aircraft return to R/C mode in preparation for landing.

The planned flight test was for two aircraft to complete several circular pattern laps with the formation controller engaged. The "follower" controller was designed to track the "leader" trajectory with a predefined offset in the X, Y, and Z direction. The on-board DAQ for each aircraft runs at 50Hz, while the communication between the "leader" and "follower" aircraft are updated at a rate of 20Hz. The formation control (for the data presented in this paper) with two aircraft was engaged for approximately 3 laps (~108 seconds) where the "leader" pilot provided a circular pattern for the "follower" controller to track. Figure 15 shows a captured video image from the ground camera once formation was engaged. Figure 16 shows a screen shot from the on-board "follower" video camera mounted in the canopy of the aircraft during formation.

Figure 15. Screen shot from ground video   Figure 16. Screen shot from in-flight video

Analysis of the flight data with two aircraft is shown in Fig. 17-19. For clarity purposes, only 2 laps of formation flight data are shown indicating the initial aircraft positions in Fig. 18.
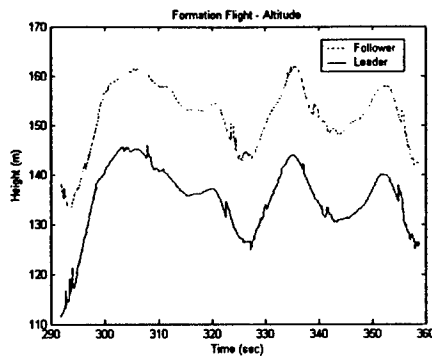
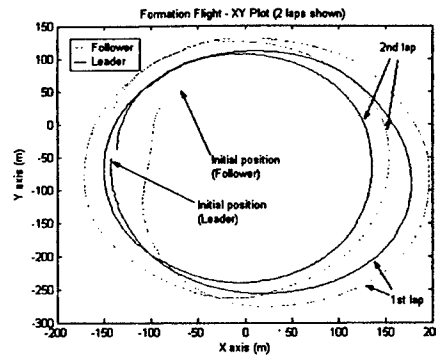**Figure 17. Formation flight: altitude plot**

Figure 18. Formation flight: XY plot

Figure 17 shows the altitude information from both the "leader" and "follower" aircraft during the engagement. For this particular flight test, the preset distances were set at 30 m forward, 30 m lateral, and 20 m in the vertical plane. Specifically, the "follower" was commanded to be above and to the right of the "leader" aircraft on an outside circular path. Figure 18 presents the vehicle trajectories in the XY (horizontal) plane. The initial positions for both aircraft are indicated on the figure. This graph clear shows the XY trajectory taken by the "follower" aircraft once the controller was engaged. Figure 19 shows the same trajectory information within a 3D plot.
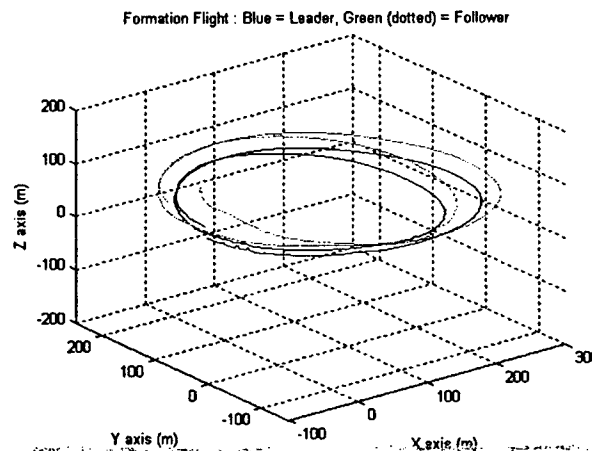

Figure 19. Formation flight: 3D plot

VIII.   Conclusions

A formation flight controller was designed and flight tested using research UAVs. The aircraft and on-board electronic payloads were designed, manufactured, and instrumented at WVU; and extensive flight testing has been performed in 2003 and 2004. Flight testing has started from initial vehicle handling qualities, to payload testing, use of a VL test scenario of the formation control, and actual flight testing of multiple aircraft. The VL scenario provided a low risk way of initially testing the control laws. Initial formation flight testing results have shown desirable performance for a formation control design based on inner and outer loop control. The outer loop features a nonlinear dynamic inversion (NLDI) approach while the inner loop features a conventional (proportional) controller. Additional flight testing activities are planned for involving a third aircraft into the formation.

Acknowledgments

13
American Institute of Aeronautics and Astronautics

NLDI GUIDANCE CONTROL LAWS
FOR CLOSE FORMATION FLIGHT

Giampiero Campa^, Brad Seanor^, Yu Gu^, Marcello R. Napolitano@,
Department of Mechanical and Aerospace Engineering, West Virginia University, Morgantown, WV 26506/6106,

Abstract

This paper presents identification, control synthesis and simulation results for an YF-22 aircraft model designed, built, and instrumented at West Virginia University. The goal of the project was the experimental demonstration of formation flight for a set of 3 of the above models. In the planned flight configuration, a pilot on the ground maintained controls of the leader aircraft while a follower aircraft was required to maintain a pre-defined position and orientation with respect to the leader. In this paper, the identification of both a linear model and a nonlinear model of the aircraft from flight data is shown first. Then, the control laws, that feature a linear inner loop controller and a NLDI (nonlinear dynamic inversion) based outer loop guidance controller, are discussed in detail. Finally, both simulation and flight test results are presented.

1   Introduction

Autonomous formation flight is an important research area in the aerospace community. The investigation of control issues related to a leader-follower formation has lead to the introduction of different types of compensation-type controllers [1]. In Ref. [2] a formation flight control scheme was proposed based on the concept of Formation Geometry Center, also known as the Formation Virtual Leader. This paper presents design and results of a formation control project performed on a set of 3 YF-22 aircraft models that were designed, built, and instrumented at West Virginia University (WVU). One of the 3 WVU YF-22 models is shown in Figure 1. The model features an 3 m fuselage length with a 2 m wingspan for an approximate take-off weight of 23 Kg, including a 5 Kg electronic payload consisting on a PC-104 flight computer, a complete set of sensors, a GPS receiver and a set of RF modems used for data transmission.

Due to the limitations on the flight range, the WVU YF-22 models were expected to perform fairly tight maneuvers at high Euler angles and moderately high angular rates. Therefore, a specific issue in the design of a control scheme was to allow for formation control under these flight conditions. Another objective was to limit the amount of information exchange (between leader and follower) needed to maintain the predefined formation geometry.
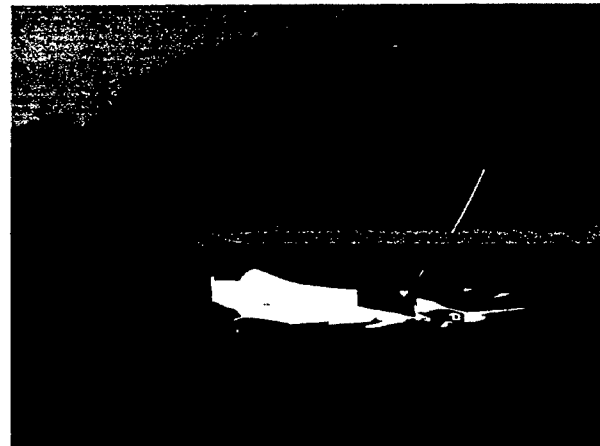

Figure 1 - WVU YF-22 aircraft model

The paper is organized as follows. The second section describes the identification of a linear and nonlinear single aircraft model from collected flight data. The third section outlines the geometric characteristics of the formation. The fourth section outlines the design of the formation control laws. The final sections will present the simulation and visualization environments, together with the main formation flight experimental results. The symbols used throughout the paper are very standard, but readers less familiar with flight mechanics could consult [3] or download the FDC manual [4] as a reference.

2   System Identification of the WVU YF-22

Flight data for several maneuvers were collected for parameter identification purposes using the following on-board instrumentation:

- Absolute and differential pressure sensors: (SenSym ASCX15AN and SenSym ASCX01DN), used to calculate H and V (altitude and speed).
- Inertial Measurement Unit (Crossbow IMU-400) to measure Ax, Ay, Az, p, q, r, (accelerations, roll pitch and yaw rates).
- Vertical Gyro (Goodrich Sensor System VG34) to measure φ, θ, (roll and pitch angles).
- Nose probe (Space Age) to measure α and β (attack and sideslip angles).
- Potentiometers on the control surfaces to measure δ_E, δ_A, δ_R (elevators, ailerons and rudders deflections).

@ Professor, ^ Research Assistant Professor

Turn maneuvers, plus doublets on each control surface, were performed during the flights. A PC-104 based on-board computer collected in real time (at a rate of 100Hz) all of the above signals using the integrated data acquisition card (Diamond MM 32). The data were stored on a flash-card for post-flight downloading. A set of flight data was selected for the actual parameter estimation process, while a second set of data was selected for validation purposes.

2.1 Linear Model Identification

The linear model identification was performed with a 3-step process. First, the flight data time histories were smoothed and rearranged using simulink-based filters. Next, a batch Matlab file performed the actual identification algorithm. The last step of the model identification process was the validation of the linear model using time histories of the control surface deflections from the validation flight data. In other words, the simulated and true responses to the time histories of the control surface deflections (in the validation data set) were compared. Following the identification study, the estimated linear lateral-directional aerodynamic model was given by:

$$\begin{bmatrix} \dot{\beta} \\ \dot{p} \\ \dot{r} \\ \dot{\phi} \end{bmatrix} = \begin{bmatrix} 0.4299 & 0.0938 & -1.0300 & 0.2366 \\ -67.3341 & -7.9485 & 5.6402 & 0 \\ 20.5333 & -0.6553 & -1.9955 & 0 \\ 0 & 1 & 0 & 0 \end{bmatrix} \begin{bmatrix} \beta \\ p \\ r \\ \phi \end{bmatrix}$$
$$+ \begin{bmatrix} 0.2724 & -0.7713 \\ -101.8446 & 33.4738 \\ -6.2609 & -24.3627 \\ 0 & 0 \end{bmatrix} \begin{bmatrix} \delta_A \\ \delta_R \end{bmatrix} \quad (1)$$

The estimated longitudinal model was given by:

$$\begin{bmatrix} \dot{v} \\ \dot{\alpha} \\ \dot{q} \\ \dot{\theta} \end{bmatrix} = \begin{bmatrix} -0.2835 & -23.0959 & 0 & -0.1711 \\ 0 & -4.1172 & 0.7781 & 0 \\ 0 & -33.8836 & -3.5729 & 0 \\ 0 & 0 & 1 & 0 \end{bmatrix} \begin{bmatrix} v \\ \alpha \\ q \\ \theta \end{bmatrix}$$
$$+ \begin{bmatrix} 20.1681 \\ 0.5435 \\ -39.0847 \\ 0 \end{bmatrix} \delta_E \quad (2)$$

This model represents the aircraft in a steady and level flight at 42 m/s, 336m of altitude, with alpha and theta of 3 deg. This linear model was mainly used for control synthesis. For simulation purposes, a full nonlinear aircraft model was considered highly desirable if not necessary.

2.2 Nonlinear Model Identification

The identification of the mathematical model of a nonlinear system is a more challenging issue [5,6]. Most of the nonlinear identification efforts rely on both good physical

insight [5] and some form of optimization algorithm like Steepest descent or Newton-Raphson [6]. The general nonlinear model of an aircraft system can be expressed (see for example [3]) as:

$$\dot{x} = f(x,\delta,G,F_A(x,\delta),M_A(x,\delta));$$
$$y = g(x,\delta,G,F_A(x,\delta),M_A(x,\delta)); \quad (3)$$

where x is the state vector (linear and angular positions and velocity), y is the output vector (linear and angular accelerations), δ is the input vector (surface deflections), G is a vector of geometric parameters and inertia coefficients, F_A and M_A are aerodynamic forces and moments acting on the aircraft; finally, f and g are the known analytic functions that express the dynamics and kinematics of a rigid body. The aerodynamic forces and moments are expressed using the aerodynamic coefficients C_D, C_Y, C_L, C_l, C_m, C_n:

$$F_A = \bar{q}S \begin{bmatrix} C_D(x,\delta) \\ C_Y(x,\delta) \\ C_L(x,\delta) \end{bmatrix}, M_A = \bar{q}S \begin{bmatrix} bC_l(x,\delta) \\ \bar{c}C_m(x,\delta) \\ bC_n(x,\delta) \end{bmatrix} \quad (4)$$

where S is the wing platform area, $\bar{q}$ the dynamic pressure, b the wingspan, and $\bar{c}$ the mean aerodynamic chord. The aerodynamic coefficients are often approximated by affine functions in x and δ; for example, for the lift coefficient:

$$C_L(x,\delta) = c_{L0} + c_{L\alpha}\alpha + c_{L_q}q + c_{L\delta_e}\delta_e \quad (5)$$

where, c_{L0} and the other three coefficients are usually called the "derivatives" of C_L.

Under the above assumptions, the nonlinear aircraft model is completely determined by its aerodynamic derivatives as well as by its inertial and geometric coefficients (which can typically be evaluated experimentally). In this effort, the inertial and geometric characteristics of the WVU YF-22 model were determined with an experimental "swing pendulum" set-up [7]; thus, the remaining critical issue was the determination of the aerodynamic derivatives. Formulas to calculate the entries of the matrices of the linear model in (1) and (2) from the values of the aerodynamic derivatives and geometric-inertial parameters are well known [3]. By inverting such formulas, an initial value for all the main aircraft aerodynamic derivatives was then calculated from the matrices in (1) and (2).

Next, a parameter optimization routine based on routines available within the Matlab Optimization Toolbox® was set up. Specifically, a Matlab routine was written such that it could take as an input the aerodynamic derivatives to be estimated, perform a simulation with the nonlinear model resulting from those derivatives, compare the outputs with the real data, and return the difference (to be minimized) to the caller function. The "fmincon" function – which features the constrained optimization of a multivariable function using a Sequential Quadratic Programming (SQP) technique [8] - was then used to find the set of aerodynamic derivatives providing the best fit with the flight data, starting from the initial set of aerodynamics derivatives calculated from the linear models. The importance of starting the minimization from a set of already accurate derivatives should be emphasized; in fact, this last

optimization can be considered a refinement of the parameters. A lesson learned was that in order for such an optimization to avoid local minima and converge successfully, care must be taken in the selection of the cost function. Specifically, the selected cost function contained 3 terms, a term expressing the RMS of the deviation between real and predicted output, a frequency based term expressing the lowest spectral components of the deviation, and, finally, a term expressing the difference between the current linearized model (obtained by performing a numerical linearization algorithm on the current nonlinear model) and the base linear model in equations (1) and (2).

A final validation of the nonlinear model was then conducted using the validation flight data set, similarly to what was done for the linear model. As shown in Figure 2, the agreement between simulated and real data is substantial.
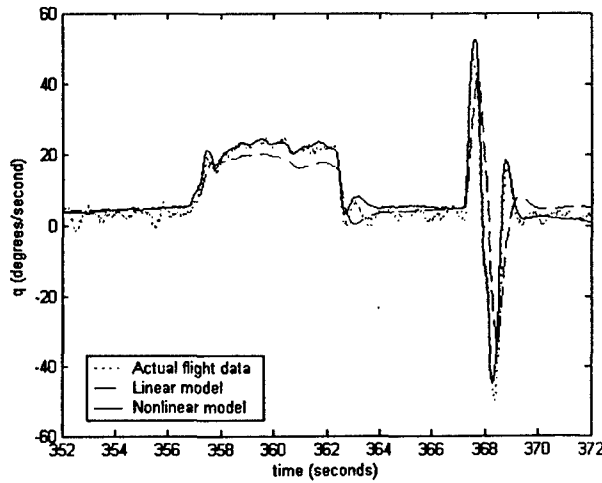

Figure 2 – Linear and nonlinear model prediction versus real flight data

The resulting aircraft nonlinear model is given by:

Geometric and Inertial Data (60% fuel load):
$\bar{c} = 0.765$ m, $b = 1.962$ m, S= 1.368 m^2, $I_{xx} = 1.607$ Kg m^2, $I_{yy} = 7.508$ Kg m^2, $I_{zz} = 7.186$ Kg m^2, $Ixz = -0.244$ Kg m^2, mass = 20.638 Kg, T (engine thrust force) = 54.617 N

Longitudinal Aerodynamic derivatives:
$C_{D0} = 0.008$, $C_{D\alpha} = 0.507$, $C_{Dq} = 0$, $C_{D\delta E} = -0.033$, $C_{L0} = -0.049$, $C_{L\alpha} = 3.258$, $C_{Lq} = 0$, $C_{L\delta E} = 0.189$, $C_{m0} = 0.022$, $C_{m\alpha} = -0.473$, $C_{mq} = -3.449$, $C_{m\delta E} = -0.364$.

Lateral-Directional Aerodynamic derivatives:
$C_{Y0} = 0.016$, $C_{Yb} = 0.272$, $C_{Yp} = 1.215$, $C_{Yr} = -1.161$, $C_{Y\delta A} = 0.183$, $C_{Y\delta R} = -0.459$, $C_{l0} = -0.001$, $C_{lb} = -0.038$, $C_{lp} = -0.213$, $C_{lr} = 0.114$, $C_{l\delta A} = -0.056$, $C_{l\delta R} = 0.014$, $C_{n0} = 0$, $C_{nb} = 0.036$, $C_{np} = -0.151$, $C_{nr} = -0.195$, $C_{n\delta A} = -0.035$, $C_{n\delta R} = -0.055$.

2.3 Actuators and Engine Model Identification

Both signals to the actuators and deflection were measured and recorded. The actuator model was then identified by simple Batch Least Squares (BLS) technique:

$$G_{ACTUATOR}(s) = \frac{23}{s+23} \qquad (6)$$

Similarly, and both throttle signal and force (a force measuring device was appositely designed and built) were measured and recorded. As for the actuator case, a simple Batch Least Squares (BLS) technique was used to identify a simple engine model containing a time delay, where δ_T is the throttle command and T is the thrust force:

$$\frac{T-T_b}{\delta_T} = \frac{K_T}{(1+\tau_T s)}e^{-\tau_d s} \qquad (7)$$

where $T_b = -25.86N$, $K_T = 0.624$, $\tau_T = 0.25s$, $\tau_d = 0.26s$. For control synthesis purposes the relationship between throttle command and thrust force can be approximated by a much simpler static affine formula:

$$T = T_b + K_T\delta_T \qquad (8)$$

where δ_T is a digital command between 70 and 255.

3 Formation Geometry

Since flight paths mostly lie on a horizontal plane, (and since gravitational force is perpendicular to such plane), a formation flight control problem can be naturally decomposed into two (almost) independent problems: horizontal (planar) tracking and a vertical tracking.

Note that position and velocity of both leader and follower are expressed with respect to a pre-defined earth-fixed reference frame and are measured by the on-board GPSs.

3.1 Horizontal geometry

The pre-defined formation geometric parameters are the forward clearance f_c and lateral clearance l_c (Figure 3). The forward distance error f and lateral distance error l can be calculated from positions and velocities using the following formulas:

$$\begin{bmatrix} l \\ f \end{bmatrix} = \begin{bmatrix} \sin(\chi_L) & -\cos(\chi_L) \\ \cos(\chi_L) & \sin(\chi_L) \end{bmatrix}\begin{bmatrix} x_L - x \\ y_L - y \end{bmatrix} - \begin{bmatrix} l_c \\ f_c \end{bmatrix} \qquad (9)$$

where χ_L is the azimuth angle for the leader:

$$\cos(\chi_L) = \frac{V_{Lx}}{\sqrt{V_{Lx}^2 + V_{Ly}^2}}, \text{ and } \sin(\chi_L) = \frac{V_{Ly}}{\sqrt{V_{Lx}^2 + V_{Ly}^2}} \qquad (10)$$

Note that the 2 by 2 matrix in (9) is simply a rotation matrix that rotates the error from an earth fixed reference frame to a reference frame oriented as the velocity of the leader.

3.2 Vertical geometry

The vertical distance error h, can be simply obtained as:
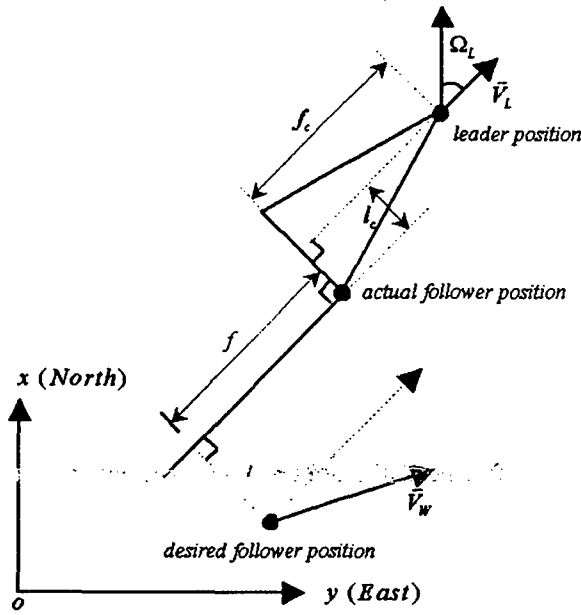$$h = z_L - z - h_c \qquad (11)$$

Figure 3 – Horizontal formation geometry

4 Controller Structure

The whole formation control problem is ultimately a nonlinear control problem in which the controller has to act on throttle and elevator commands to minimize the three errors l, f, and h. It is however useful to note that this problem, like other conventional flight trajectory control problems, exhibits a two-time-scale feature because the trajectory dynamics (relative position and velocity) is slower than the attitude dynamics (angular velocity and orientation). This is why usually both lateral-directional and vertical controllers consist of an inner loop controller (pitch and roll angle tracking) and outer loop controller (lateral-directional and height tracking).

4.1 Outer loop controller

The outer loop controller consists of two parts.

The "vertical" part is a simple linear altitude control. It takes the vertical error (and its derivative) as inputs. The outputs is the desired pitch angle (theta):

$$\theta_d = K_z h + K_{zz} \dot{h} \tag{12}$$

This desired pitch angle is then taken as a reference signal by the inner loop controller.

The "horizontal" part is a nonlinear dynamic inversion (NLDI) based controller that takes lateral and forward errors (and their derivatives) as inputs. The outputs are the throttle and the desired roll angle (phi).

$$\begin{bmatrix} \delta_T \\ \phi_d \end{bmatrix} = f(\chi - \chi_L, \begin{bmatrix} f \\ l \end{bmatrix}, \begin{bmatrix} \dot{f} \\ \dot{l} \end{bmatrix}) \tag{13}$$

The desired roll angle is taken as a reference signal by the inner loop controller; the throttle is instead directly used as a control command.

4.2 NLDI Outer Loop horizontal controller: design

This control technique aims at canceling the nonlinearities in the plant dynamics using (output) feedback linearization [9], which, under some assumption, reduces a nonlinear system to a series of integrators that can be then controlled by simple linear techniques. In our case, the nonlinear system is the one that has the forward and lateral distance errors f and l as outputs, the desired bank angle ϕ_d and the throttle command δ_T as inputs, and all the states that belong to the lateral dynamics of the follower as states.

According to the feedback linearization technique, we must derive the outputs until the inputs explicitly appear in the expression, and then try to invert the relationship among inputs and derivatives of the outputs. For this problem, the second derivatives of the output are:

$$\begin{bmatrix} \ddot{l} \\ \ddot{f} \end{bmatrix} = \begin{bmatrix} V_{xy}\cos(\chi - \chi_L) & \dfrac{V_{xy}}{V}\omega_1\sin(\chi - \chi_L) \\ V_{xy}\sin(\chi - \chi_L) & -\dfrac{V_{xy}}{V}\omega_1\cos(\chi - \chi_L) \end{bmatrix} \begin{bmatrix} \dfrac{g}{V}\tan(\phi_d) \\ T_b + K_T\delta_T \end{bmatrix}$$

$$+ \dfrac{V_{xy}}{V}\omega_2 \begin{bmatrix} -\sin(\chi - \chi_L) \\ \cos(\chi - \chi_L) \end{bmatrix} - \Omega_L V_{xy} \begin{bmatrix} \cos(\chi - \chi_L) \\ \sin(\chi - \chi_L) \end{bmatrix} + \dot{\Omega}_L \begin{bmatrix} f \\ -l \end{bmatrix}$$

$$+ \Omega_L \begin{bmatrix} \dot{f} \\ -\dot{l} \end{bmatrix} \tag{14}$$

where:

$$\omega_1 = \frac{1}{m}\cos\alpha\cos\beta, \quad \omega_2 = \frac{\bar{q}S}{m}(C_D\cos\beta - C_Y\sin\beta) + g\sin\gamma$$

and the coordinated turn condition is assumed for both leader and wingman:

$$\Omega = \dot{\chi} \cong \dot{\psi} \cong \frac{g}{V}\tan\phi \tag{15}$$

In practice the coordinated turn condition (15), is imposed by trying to keep both a constant altitude and a zero sideslip angle $(\beta\equiv 0)$ during the turn. In the following, the simplifying assumptions $\alpha=\alpha_0$, $\beta=0$, and $\Omega_L=constant$ have also been made (quasi steady state turn).

Note that both ϕ_d and δ_T appear as inputs in (14) and the 2 x 2 matrix that relates inputs and second derivatives of the output is invertible. Therefore, by inverting Eq. (14), and then replacing $\ddot{f}$ and $\ddot{l}$ respectively with $\ddot{f}_d$ and $\ddot{l}_d$, (which are the *desired* values for the double derivatives of f and l) we have the following laws.

- Lateral NLDI Control Law:

$$\phi_d = \arctan\left\{\frac{1}{g\cos\gamma}\left[\ddot{l}_d\cos(\chi - \chi_L) + \ddot{f}_d\sin(\chi - \chi_L)\right]\right.$$

$$\left. + \frac{V}{g}\Omega_L + \left[\dot{l}\sin(\chi - \chi_L) - \dot{f}\cos(\chi - \chi_L)\right]\frac{\Omega_L}{g\cos\gamma}\right\} \tag{16}$$

- Forward NLDI Control Law:

$$\delta_T = \frac{m}{K_T \cos\gamma}\left[\ddot{\ell}_d \sin(\chi-\chi_L) - \ddot{f}_d \cos(\chi-\chi_L)\right]$$

$$+ \frac{1}{K_T}\left(\frac{1}{2}\rho_0 V^2 S\left(C_{D0}+C_{D\alpha}\alpha_0\right)+m\sin\gamma-T_b\right)$$

$$-\frac{m}{K_T \cos\gamma}\Omega_L\left[\dot{\ell}\cos(\chi-\chi_L)+\dot{f}\sin(\chi-\chi_L)\right]$$

(17)

Applying the inputs ϕ_d and δ_T in (17) and (18) to the system in (14) completely cancels the nonlinearities, yielding:

$$\begin{bmatrix}\ddot{\ell}\\\ddot{f}\end{bmatrix}=\begin{bmatrix}\ddot{\ell}_d\\\ddot{f}_d\end{bmatrix}$$

(18)

that is a linear system consisting of two channels each containing two integrators in series:
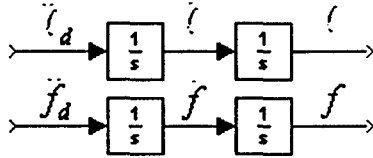

Figure 4 – Feedback linearized system

The above system can be easily controlled by a standard linear control, in our case, the chosen controller was:

$$\ddot{\ell}_d = -\tilde{K}_\ell \ell - \tilde{K}_{\ell_s}\dot{\ell}$$

$$\ddot{\ell}_d = -\tilde{K}_f f - \tilde{K}_{f_s}\dot{f}$$

(19)

where the gains were selected so that the controller could be locally equivalent to a previous designed linear one [10]:

$$\tilde{K}_\ell = 0.2027, \quad \tilde{K}_{\ell_s} = 0.8894$$

$$\tilde{K}_f = 0.2419, \quad \tilde{K}_{f_s} = 2.0560$$

(20)

$$K_z = 3.2254, \quad K_{zs} = 1.7593$$

4.3 Inner Loop Lateral Controller

The lateral inner loop controller is a simple linear controller that tracks the desired bank angle (supplied by the outer loop controller) and augments the lateral-directional stability of the aircraft:

$$\delta_A = K_p p + K_\phi(\phi - \phi_d)$$

(21)

$$\delta_R = K_r r$$

(22)

Classic root-locus based compensation design tools can then be applied to the model for evaluating the controller gains [3]. The basic design specification is to assign the damping ratio of the dominant poles a value around 0.7. The resulting values for the parameters are:

$$K_p = 0.04, \quad K_\phi = 0.35, \quad K_r = 0.16$$

(23)

4.4 Inner loop Longitudinal Controller

The longitudinal inner loop controller is a simple linear controller that tracks the desired pitch angle (supplied by the outer loop controller):

$$\delta_E = K_q q + K_\theta(\theta - \theta_d)$$

(24)

The parameters of the controller were calculated using a root locus-based approach [3]:

$$K_q = 0.12, \quad K_\theta = 0.50$$

(25)

5 Simulation Environment

A Simulink scheme featuring the models of the WVU YF-22 aircraft and the formation controller was developed and implemented. Given the multi-object nature of the problem, the use of a fully integrated visualization environment was highly desirable. The Virtual Reality Toolbox was used because it allowed for objects and events of a virtual world (coded in VRML 2.0 or higher [11]) to be driven by signals from Matlab/Simulink
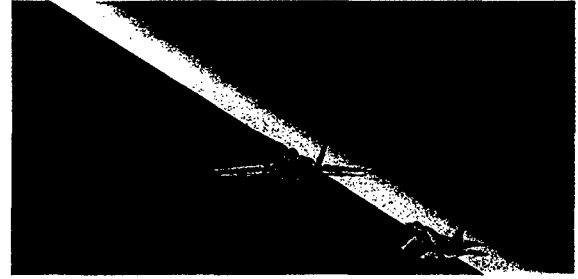

Figure 5 – VRT visualization (behind wingman)

Several simulation studies were conducted to evaluate, test, and optimize several controller and flight configuration parameters. The fact that the controller was coded in Simulink, (using C s-functions) allowed for it to be easily compiled with Real Time Workshop to generate an executable to be uploaded to the flight computer.

6 Flight Test Results

The overall scenario of the formation fight testing experiments is a "leader/follower" combination where initially all aircraft are manually controlled during the takeoff and landing phases. After each aircraft reaches a nominal fight condition, the follower pilot can then engage the autonomous formation controller. Once engaged, the onboard controller takes over all aircraft control functions and the pilot remains in a standby mode in case of an emergency. Both aircrafts are then landed manually using the R/C mode. The planned flight test was for 2 aircraft to complete several circular pattern laps with the formation controller engaged. The follower controller was designed to track the leaders trajectory with a predefined offset in the X, Y, and Z directions. For this particular flight test, the preset distance was 30 m forward, 30 m lateral, and 20 m vertical. Figure 6 shows a captured video image from the ground camera.

Figure 6. Screen shot from ground video

In the initial flight-testing sessions, summer 2004, formation control with 2 aircraft was engaged for approximately 3 laps (~108 seconds), with the leader pilot flying in a circular pattern. For clarity purposes, only the first lap is shown in the following figures. These plots also feature a simulated follower aircraft, which was set to follow the position of the real leader starting from the same initial condition as the real follower.
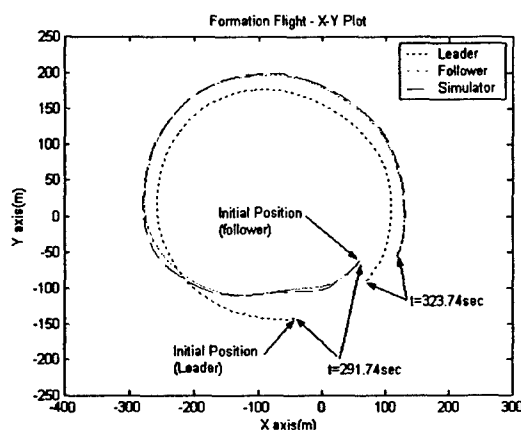

Figure 7. Formation Flight: XY plot

Figure 7 shows the vehicle trajectories in the XY (horizontal) plane. Figure 8 shows the same trajectory within a 3D plot.
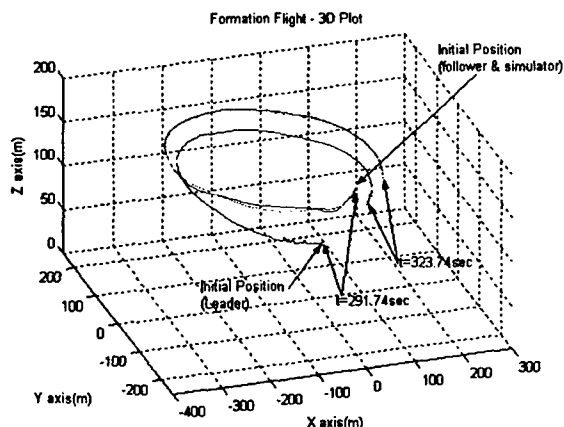

Figure 8. Formation Flight: 3D plot

The above plots show a satisfactory tracking. They also show that the track of the simulated follower remains remarkably close to the track generated by the real follower.

Conclusions

This paper presents a formation flight project that used YF-22 research aircraft developed and built at West Virginia University. Particular emphasis is placed on the design of control laws to maintain the formation of aircraft. The resulting controller has an inner-outer loop structure in which the horizontal outer loop guidance laws rely on feedback linearization. The inner loop controllers are instead linear, and were designed using classical root locus methods. Results of the formation flight test in June 2004 validated the overall design of the formation controller.

Acknowledgement

References

1 – Proud A.W. "Close Formation Flight Control", MS Thesis, AFIT/GE/ENG/99M-24, School of Engineering, Air Force Institute of technology (AU), Wright-Patterson AFB, OH, March 1999

2 - Giulietti F., Pollini L., Innocenti M. , "Formation Flight control: A Behavioral Approach," AIAA GNC Conference 2001, AIAA Paper 2001-4239, Montreal, Canada.

3 - Stevens, B. and Lewis, F. "Aircraft Control and Simulation," John Wiley & Sons, NY, 1992.

4 - Rauw, M.O.: "*FDC 1.2 - A Simulink Toolbox for Flight Dynamics and Control Analysis*". Zeist, The Netherlands, 1997. ISBN: 90-807177-1-1, (http://www.dutchroll.com/)

5 - Ljung, L.,: *System Identification: Theory for the User*, *2nd Ed*., PTR Prentice Hall, Upper Saddle River, Englewood Cliffs, NJ, 1999.

6 - Maine, R.E., Iliff, K.W., "Identification of Dynamic Systems: Theory and Formulation", NASA RF 1168, June 1986

7 - Soule, H. A., Miller, M. P., "The experimental determination of the moments of inertia of airplanes", (http://naca.larc.nasa.gov/reports/1934/). NACA Report 467, 1934

8 - Hock, W. and K. Schittowski, "A Comparative Performance Evaluation of 27 Nonlinear Programming Codes," *Computing*, Vol. 30, p. 335, 1983.

9 - Isidori, A., "*Nonlinear Control Systems*", Springer-Verlag, London, Third edition, 1995.

10 – Campa, G, Napolitano, M. R., Seanor, B, Perhinschi, M. G. "Design of Control Laws For Maneuvered Formation Flight", American Control Conference 2004.

11 - The VRML Web Repository, Dec. 2002: (http://www.web3d.org/x3d/vrml/)